



HAL
open science

Error estimators and adaptive anisotropic remeshing in 3D coupled electromagnetic modelling: Application to electromagnetic material processing

Jesus Garcia Carrero

► **To cite this version:**

Jesus Garcia Carrero. Error estimators and adaptive anisotropic remeshing in 3D coupled electromagnetic modelling: Application to electromagnetic material processing. Mechanics of materials [physics.class-ph]. Université Paris sciences et lettres, 2023. English. NNT : 2023UPSLM059 . tel-04546802

HAL Id: tel-04546802

<https://pastel.hal.science/tel-04546802v1>

Submitted on 15 Apr 2024

HAL is a multi-disciplinary open access archive for the deposit and dissemination of scientific research documents, whether they are published or not. The documents may come from teaching and research institutions in France or abroad, or from public or private research centers.

L'archive ouverte pluridisciplinaire **HAL**, est destinée au dépôt et à la diffusion de documents scientifiques de niveau recherche, publiés ou non, émanant des établissements d'enseignement et de recherche français ou étrangers, des laboratoires publics ou privés.



THÈSE DE DOCTORAT
DE L'UNIVERSITÉ PSL

Préparée à Mines Paris-PSL

Estimateurs d'erreurs et remaillage anisotrope adaptatif en modélisation électromagnétique couplée 3D – Application aux procédés de fabrication avec couplage électromagnétique.

Error estimators and adaptive anisotropic remeshing in 3D coupled electromagnetic modelling - Application to electromagnetic material processing.

Soutenue par

**Jesus Oswaldo GARCIA
CARRERO**

Le 11 octobre 2023

Ecole doctorale n° 364

**Sciences fondamentales et
appliquées**

Spécialité

**Mécanique Numérique et
Matériaux**

Composition du jury :

Frédéric, MAGOULES Professeur, CentraleSupélec	<i>Président</i>
Annie, GAGNOUD Directeur de Recherche, SIMAP/EPM Grenoble	<i>Rapporteur</i>
Marco, PICASSO Professeur, EPFL Lausanne	<i>Rapporteur</i>
Maria del Pilar, SALGADO Professeur, USC Santiago de Compostela	<i>Examineur</i>
Simon, THIBAUT Docteur, Ingénieur Innovation Procédés, NTN-SNR	<i>Examineur</i>
José R., ALVES Z. Docteur, Développeur scientifique, Transvalor	<i>Examineur</i>
François, BAY Directeur de Recherche, Mines Paristech	<i>Directeur de thèse</i>

Acknowledgements

I would like to express my gratitude to the Centre de Mise en Forme de Matériaux (CEMEF) and Transvalor SA for their support throughout my research journey. I am so grateful for their expertise and resources, which have played a crucial role in making this work a success.

I am deeply thankful to my advisor, François Bay, for giving me the opportunity to take on this project. His guidance and continuous support have been truly invaluable.

I would also like to thank the Forge team at Transvalor: Etienne, Christine, Stéphane, Guillaume, Grégory. A special thanks goes to Julien Barlier for his assistance and support throughout this research endeavour. I also want to mention Ugo Ripert, the master of meshes, for his tremendous help. I am particularly grateful to José Alves, who has been a mentor and a big brother to me during these years. Thank you for your patience, guidance, and for always being available, even when you had a ton of other things to do.

Lastly, I want to dedicate this thesis to my parents, Benilde and Osbaldo, whose love, support, and sacrifices have been the driving force behind my academic journey. I am also grateful to my siblings: Ramon, Guadalupe, and Golfan for their constant encouragement and support. And to Chantal, responsible for my trip to France, thank you for all you have done and for believing in me.

Contents

1	Introduction	9
1.1	Electromagnetic based industrial process	9
1.1.1	Induction heating	10
1.1.2	Magnetic pulse forming	12
1.1.3	Electromagnetic Stirring	13
1.2	Physical phenomena	15
1.2.1	Electromagnetic properties of materials	15
1.2.2	Skin effect	18
1.2.3	Proximity effect	20
1.2.4	Ring effect	21
1.3	Numerical modelling and automatic remeshing for industrial applications.....	22
2	Multiphysics computational modelling	28
2.1	Multiphysics model.....	28
2.1.1	Electromagnetic problem	28
2.1.2	Heat transfer problem	30
2.1.3	Solid Mechanics problem	33
2.1.4	Fluids Mechanics problem	35
2.2	Electromagnetic model.....	36
2.2.1	Potential formulation	36
2.2.2	Boundary conditions	39
2.2.3	Edge elements	40
2.2.4	Weak formulation.....	42
2.2.5	Discretised formulation	45
2.2.6	Boundary element method (BEM)	45
2.2.7	Fully immersed finite elements approach	46
2.2.8	Time integration	47
2.3	Multiphysics coupling.....	50
2.3.1	Characteristic times involved	50
2.3.2	Coupling scheme	52
2.4	R-adaptation.....	54

2.5	Field transport procedure in electromagnetic modelling	54
2.5.1	Transport strategies	55
2.6	Parallel paradigm	57
3	Error estimators	62
3.1	Introduction	62
3.2	Electromagnetic-coupled processes modelling	62
3.3	Finite elements and a posteriori error estimators	62
3.3.1	<i>A priori</i> error estimators	65
3.3.2	<i>A posteriori</i> error estimates	65
3.4	Recovery based – Galerkin method	68
3.4.1	Superconvergent Patch Recovery vs Galerkin-based Recovery for building a smoothed solution	68
3.4.2	Estimator based on a recovered smooth vector field	70
3.5	Physics-specific estimators alternatives	71
3.5.1	Estimator based on the derived current density	72
3.5.2	Estimator based on the verification of Faraday’s Induction Law	72
3.5.3	Estimator based on the verification of Amperé’s Law	72
3.5.4	Estimator based on fundamental conservation principle	74
3.6	Analysing, scaling, and normalizing estimator results	76
3.7	Validation and analysis on semi-analytical cases	78
3.7.1	Validation by comparison with an analytical solution	78
3.7.2	Convergence rate analysis	79
3.7.3	Application to the TEAM7 benchmark case	81
3.7.4	Heat treatment case	91
3.7.5	Magnetic pulse forming case	93
3.7.6	Electromagnetic stirring case	95
3.8	Conclusions	97
4	Mesh adaptation	101
4.1	Introduction	101
4.1.1	Electromagnetic-coupled processes and modelling	101
4.1.2	Metric based anisotropic mesh adaptation - basic principles	101
4.2	Anisotropic mesh adaptation	103
4.2.1	Metric based methods	103
4.2.2	Algorithms proposed	112
4.3	Anisotropy Capturing Comparison	113

4.3.1	Symmetrisation procedure.....	114
4.3.2	Anisotropic behaviour	115
4.4	Application to electromagnetic processing of materials	118
4.4.1	Intrinsic anisotropy	119
4.4.2	Isotropic vs Anisotropic performance comparison (model size/error distribution/etc)	120
4.4.3	Skin effect case.....	123
4.4.4	Industrial processes	125
4.4.5	Magnetic and electric fields duality	130
4.5	Relation between the Hessian and the Jacobian	132
4.6	Conclusions.....	134
5	Fully coupled multi-physical implementation	138
5.1	Coupling procedure	138
5.1.1	Current procedure.....	138
5.1.2	Proposed procedure	139
5.1.3	Geometrical metric	140
5.2	Performance test	141
5.2.1	Simple induction case.....	141
5.2.2	A more complex induction case	144
5.3	Industrial applications	146
5.3.1	Wheel bearing Induction heating	146
5.3.2	Magnetic Pulse Forming	149
5.4	Conclusions.....	154
6	Conclusions	156
7	Appendices	161
7.1	Solid mechanics problem	161
7.1.1	Mass conservation	161
7.1.2	Linear momentum conservation	162
7.1.3	Angular momentum conservation	163
7.1.4	Constitutive laws	165
7.2	Fluids Mechanics problem	167
7.2.1	Mass continuity equation	168
7.2.2	Momentum conservation	168
7.2.3	Constitutive laws	169
7.3	Edge element – Coulomb gauge demonstration.....	170

7.4	Hessian – Jacobian analytical and numerical test	171
7.4.1	Numerical solution	173
7.4.2	Analytical solution	178
7.4.3	Analytical vs numerical solution.....	179
Bibliography.....	182

Chapter 1

Introduction

1.1	Electromagnetic based industrial process	9
1.1.1	Induction heating	10
1.1.2	Magnetic pulse forming	12
1.1.3	Electromagnetic Stirring	13
1.2	Physical phenomena	15
1.2.1	Electromagnetic properties of materials	15
1.2.1.1	Relative Permittivity	15
1.2.1.2	Magnetic Permeability	16
1.2.1.3	Electrical Conductivity	18
1.2.2	Skin effect	18
1.2.3	Proximity effect	20
1.2.4	Ring effect	21
1.3	Numerical modelling and automatic remeshing for industrial applications.....	22

Résumé : Introduction

Chapitre 1 présente une introduction aux procédés de fabrication basés sur l'électromagnétisme, tels que le chauffage par induction, la mise en forme par impulsion magnétique et le brassage électromagnétique. De plus, nous abordons les phénomènes physiques sous-jacents associés à ces procédés, en mettant l'accent sur des effets importants tels que l'effet de profondeur de peau, l'effet de proximité et l'influence des champs magnétiques sur les propriétés des matériaux.

En outre, nous étudions le comportement des matériaux ferromagnétiques et paramagnétiques en relation avec la température de Curie.

Finalement, nous discutons également de l'importance de l'utilisation de remaillages automatiques sur les modèles d'éléments finis, en mettant particulièrement en évidence les avantages de l'utilisation de maillages adaptés en fonction de l'anisotropie du phénomène étudié.

1 Introduction

Electromagnetic processing of materials (EPM) cover an ever-increasing range of processes. Beyond being more environment-friendly, they offer many other advantages, such as rapid heat-up and production start-up speed, minimal material waste and high energy transfer efficiency. They include, among others, induction heating (IH) or induction hardening processes, magnetic pulse forming processes (MPF), electromagnetic stirring processes (EMS).

However, their design needs to rely on accurate and efficient computational models as these processes involve multi-physics couplings of several phenomena – among which the continuous interaction of electromagnetic wave scattering with heat transfer, mechanical deformation or fluid flows, etc. Finite element method (FEM) has been very successful due to the flexibility it offers to model complex geometries and integrate different physical phenomena with each other. Therefore, the main objective is to make these tools more accurate, efficient, reliable, and ergonomic for use in industrial contexts.

One of the main challenges is to automatize the mesh generation and adaptation. If a fine triangulation is considered, a large number of elements is obtained, and the computation will require a significant amount of memory and CPU time. To overcome this situation, mesh adaptation methods consist of locating the areas where the numerical solution is not sufficiently accurate and proposing local refinements, while increasing the mesh size in the areas where the solution does not need to be sufficiently accurate. The result is a more accurate and less costly numerical solution.

The research techniques and results developed in this work will be introduced in the induction module of Forge® software. It is a finite element-based tool in which the electromagnetic model was the result of several PhD works; we can mention among other the work of Cardinaux D [1] dealing with induction heat treatment process of stamped sheets, subsequently the work Alves J [2] dealing with extension to magnetic pulse forming processes and the work of Marioni L [3] who pursued the electromagnetic-CFD coupling in casting processes, precisely to the modelling of electromagnetic stirring. Following previous work on modelling electromagnetic coupled manufacturing processes, this thesis aims to develop a mesh adaptation procedure that can be used in a general way for each of these processes.

This section provides an overview of electromagnetically based processes and the physical phenomena involved.

1.1 Electromagnetic based industrial process

Electromagnetic processing of materials (EPM) has gained popularity in recent decades, opening the way to a large family of industrial technologies due to its many advantages. These processes are often more energy efficient than purely thermo-mechanical processing methods.

They offer many advantages, including rapid heat-up and production start-up speed, minimal material waste and high energy transfer efficiency. Among the most popular we can mention induction heating (IH) [4], [5] which is nowadays one of the most widely used, allows heat treatment of difficult shapes, which is a major problem in standard processes, as well as surface hardening or preheating of metal parts before forming, stamping or bending. Magnetic Pulse Forming/Crimping/Welding [6](MPF), is one of the most industrially used high-speed processes. As the large magnetic forces induce a specific mechanical behaviour of the material and are applied without any mechanical contact, it allows the creation of complex parts with fine details an increased surface characteristics; it is also possible to join diverse materials that cannot normally be joined by classical welding, allowing the creation of high-quality joints between dissimilar materials, reducing to almost zero the elastic spring-back [7]. Electromagnetic Stirring (EMS) [8], which is a well-known method to improve the quality of casted products, is used in continuous casting of metals to remove inclusions and gas bubbles, in order to especially avoid dendrite pre-growth to homogenise the composition and temperature of the melt, and thus refine the microstructure.

The following implemented electromagnetic processes to be modelled and discussed here therefore include:

- Induction heating [1]
- Magnetic pulse forming [2]
- Electromagnetic stirring [3]

1.1.1 Induction heating

Induction heating is a powerful and efficient non-contact heating process that is widely used in various industrial processes. The process occurs when an alternating voltage is applied to an induction coil, such as a solenoid multiturn coil, it generates an alternating current in the coil circuit. This current creates a time-varying magnetic field around the coil, which has the same frequency as the coil current. This magnetic field induces eddy currents in any conductive material placed within or near the coil. These eddy currents flow in the opposite direction to the coil current, but at the same frequency. As a result, they generate heat through the Joule effect. This phenomenon is displayed in Fig. 1.1.

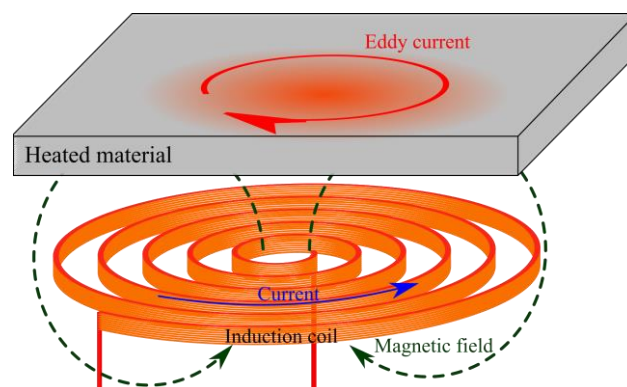


Fig. 1.1 Induction phenomenon

It's important to note that the direction and magnitude of eddy currents depend on the material's electrical conductivity, magnetic permeability, and geometry. Hence, the design of the induction coil and the choice of operating parameters are critical factors in optimizing the heating process.

One of the key advantages of induction heating is its high efficiency, as it heats only the material being processed and not the surrounding environment. This leads to reduced energy waste and cost savings. Moreover, induction heating allows for precise temperature control, which is critical in industrial applications where accurate heating is necessary to achieve the desired results. For example, by allowing precise control of temperature evolution in parts at specific locations; this can enable, for instance, in heat treatment processes, to control the grain size according to the required final properties (as a prescribed hardness at the surface). It can also heat materials at very fast rates, which increases productivity and reduces processing times. Additionally, induction heating is a clean process that does not produce any emissions, making it an environmentally friendly heating method.

Induction heating has a wide range of industrial applications, including metal processing, heat treatment, semiconductor manufacturing, and medical device manufacturing. In metal processing, induction heating is commonly used for forging, hardening, annealing, and brazing applications. Forging involves heating metal billets to a malleable state, allowing them to be shaped into a variety of forms. Hardening is used to create a hard, wear-resistant surface on a metal part. Annealing is used to soften metal and improve its ductility. Brazing is used to join two metal parts together using a filler material that melts at a lower temperature than the base metal. In heat treatment, induction heating is used to enhance the properties of various materials, such as hardness, ductility, and strength. It is also used in semiconductor manufacturing to create thin films of material, and in food processing for cooking and sterilization applications. Additionally, induction heating is used in the manufacturing of medical devices such as catheters and stents.



Fig. 1.2 Some induction heating industrial applications.

1.1.2 Magnetic pulse forming

Magnetic pulse forming (MPF) is a metalworking process that uses a high-energy magnetic field to shape metal parts. In this process, a high-voltage electrical pulse is applied to a coil, which generates a magnetic field that rapidly deforms a metal workpiece, enabling the creation of complex parts with fine details while preserving surface integrity.

The MPF process involves the following steps:

- A metal workpiece is placed between two flat dies, which are aligned with the desired shape of the finished part.
- A coil is wrapped around the dies and the workpiece, and a high-voltage electrical pulse is applied to the coil.
- The electrical pulse generates a magnetic field that rapidly compresses the workpiece, causing it to conform to the shape of the dies.
- The dies are then removed, and the finished part is removed from the workpiece.

The scheme of how a common MPF application works is displayed in Fig. 1.3

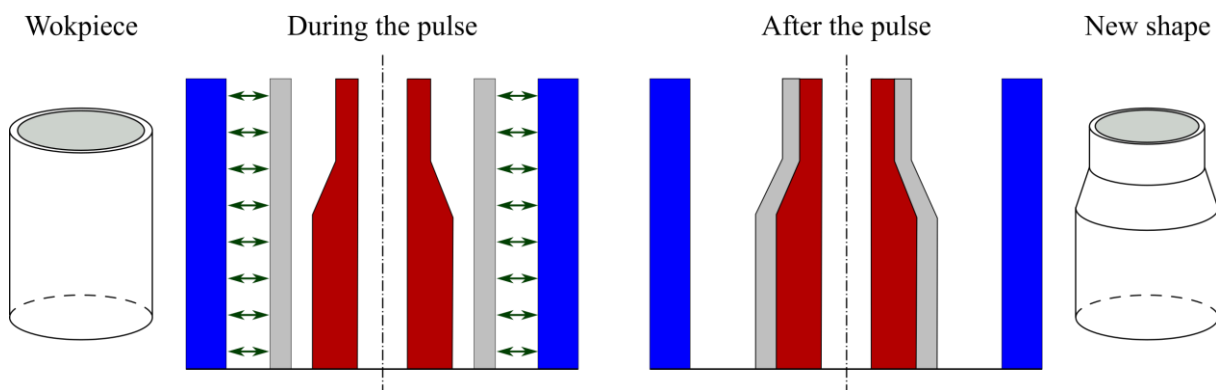


Fig. 1.3 MPF scheme: coil (dark blue), magnetic field pressure (green arrows), workpiece (grey) and the die (dark red).

In addition to its applications in shaping processes in MPF, the technique can also be used for joining different materials that are typically challenging to weld using conventional methods. This opens up possibilities for creating high-quality joints between dissimilar materials while minimizing elastic spring-back. Various variants of this technique exist, including interference-fit joints, which rely on elastic-plastic bracing, form-fit joints, which involve the formation of an undercut, and metallic bonding, which utilizes a microstructural joining mechanism. And another one, referred as electromagnetic pulse welding, utilizes electromagnetic pulses to achieve the joining process.

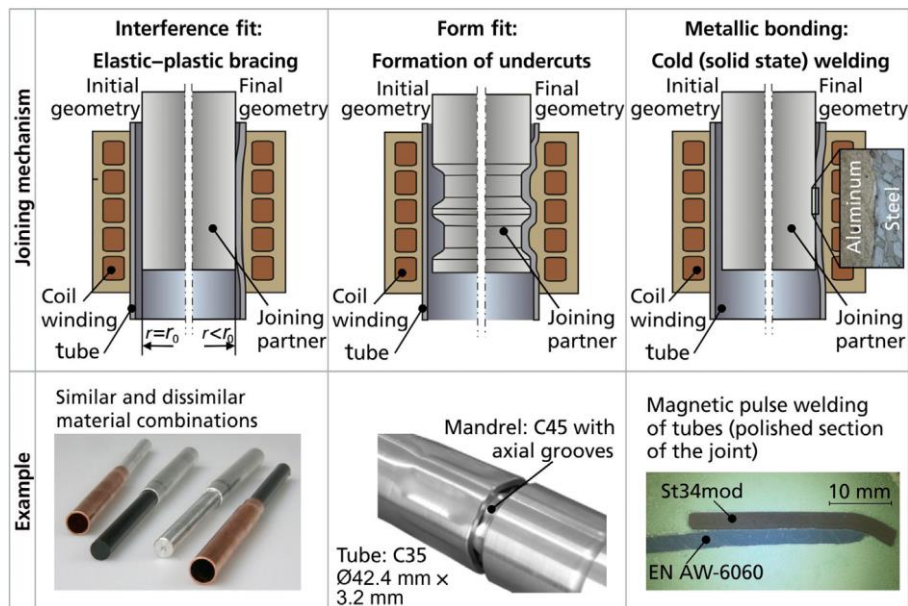


Fig. 1.4 Joining mechanism for electromagnetic pulse joining and examples [9].

The MPF process offers several advantages over other metalworking processes, including:

- High forming speeds: MPF can form parts at very high speeds, which reduces cycle times and increases productivity.
- High precision: MPF can form parts with high precision and accuracy, making it ideal for applications that require tight tolerances.
- Material savings: MPF can form parts using less material than other metal working processes, which can result in material cost savings.
- Flexibility: MPF can be used to form a wide range of materials, including metals, plastics, and composites (under the condition of using a metallic flyer such as an aluminium ring to transform the magnetic energy into kinetic energy.).

The MPF process is commonly used in the automotive, aerospace, and electronics industries for forming complex parts with high precision and accuracy. Some specific applications of MPF include forming metal casings for electronic devices, forming complex engine components for the automotive industry, and forming intricate parts for aerospace applications.

1.1.3 Electromagnetic Stirring

Electromagnetic Stirring (EMS) [8] is a powerful process used in the manufacturing of metallic materials to enhance mixing and homogenization of the melt during casting, solidification, and/or subsequent heat treatments. The process involves applying an alternating

current (AC) to an electromagnet, which generates a magnetic field that interacts with the electrically conductive melt.

During the EMS process, the magnetic field induces an electromagnetic force that causes the melt to circulate and mix, resulting in a more homogeneous and refined microstructure. It consists of using the time-varying electromagnetic field to control the fluid flow between the liquid steel and the stirrer without any physical contact. This process is used to disrupt the molten metal's fluid flow by means of the Lorentz force provided by a linear induction motor allowing a more homogeneous solidification, avoiding premature growth of dendrites during the casting process and resulting in a better quality of the final ingot. The strength and direction of the electromagnetic force can be finely controlled by adjusting the frequency, amplitude, and orientation of the magnetic field. This allows for precise tuning of the stirring effect, resulting in greater control over the final properties of the material. Fig. 1.5 shows a scheme presented by Zhang et al. [10] for a typical configuration of an EMS process.

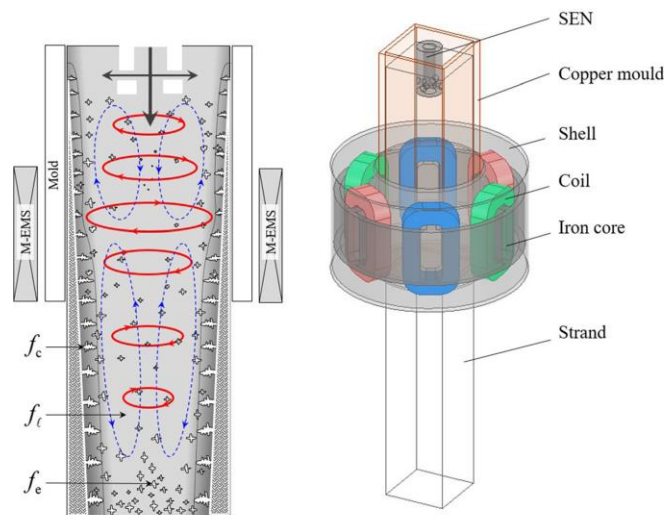


Fig. 1.5 EMS scheme [10]: magnetic field (red arrows), Lorentz force (blue arrows), dendrites: fraction of columnar phase (f_c) and equiaxed phase (f_e)

EMS has several advantages in metal processing, including:

- Improved homogenization: EMS can significantly improve the homogeneity and refinement of metallic materials, leading to improved properties and performance.
- Reduced segregation: EMS can help reduce the formation of segregation in castings, which can improve the quality and consistency of the final product.
- Reduced porosity: EMS can also reduce the formation of porosity in castings, which can improve the strength and ductility of the material.
- Increased yield: The improved homogeneity and reduced segregation and porosity achieved with EMS can increase the yield of the manufacturing process, resulting in cost savings.

EMS is widely used in the casting and solidification of metals, including aluminium, copper, and steel. It is also used in the production of semi-solid metal alloys and in the

processing of metallic powders. Some specific applications of EMS include the production of high-performance aluminium alloy components for aerospace and automotive applications, as well as the production of high-quality steel billets for forging and rolling.

1.2 Physical phenomena

Most electromagnetic-coupled processes deal with time-varying electrical loadings (harmonic or pulsed). As a time-dependent current runs through the coils, a time-varying electromagnetic field is induced in the surrounding domain. This electromagnetic field generates eddy currents in the conductive work piece. These currents dissipate heat through the Joule effect and produce Lorentz forces, thus allowing the workpiece to be heated and deformed.

These processes represent an interplay of multi-physics phenomena, involving electromagnetic, heat transfer, metallurgical and circuit analysis. This interaction is highly non-linear due to the dependence of the physical properties of the material on magnetic field strength, temperature and microstructure.

There are several electromagnetic phenomena that cause non-uniform current distribution. These are responsible for the temperature gradients experienced by parts during electromagnetic-based processes. This is associated, among other things, with:

- Skin effect
- Proximity effect
- Ring effect

1.2.1 Electromagnetic properties of materials

Electromagnetic properties refer to the way materials interact with electromagnetic waves. Electromagnetic waves are a combination of electric and magnetic fields propagating through space. When electromagnetic waves interact with materials, they can be absorbed, reflected, transmitted or refracted. This depends on their electromagnetic properties, which can be described by a number of different parameters. Understanding these properties is important for a wide range of applications, such as the design of electronic devices or the development of new materials for energy storage and transmission.

Some important electromagnetic properties of materials are:

1.2.1.1 Relative Permittivity

This parameter, also known as the dielectric constant, describes the ability of a material to store electric charge. Materials with a high dielectric constant are good insulators, while those with a low dielectric constant are good conductors. In fact, it is a measure of how easily a

material can be polarized by an electric field. It is defined as the ratio of the electric flux density to the electric field strength. This parameter is important in the design of capacitors and other electrical components that rely on storing electric charge.

1.2.1.2 Magnetic Permeability

Magnetic permeability refers to the ability of a material to become magnetized when it is placed in a magnetic field. It is defined as the ratio of the magnetic flux density to the magnetic field strength. This parameter is important in the design of electrical and electronic devices such as transformers, inductors, and electromagnets.

$$\mu = B/H \quad (1.1)$$

The magnetic permeability depends on the temperature, as well as on the magnetic field itself. This material non-linearity is due to the physical characteristics of the material and can be studied through the magnetization law. The magnetization law is a fundamental relationship that links the magnetic field strength (H), the magnetization (M) of the material, and the resulting magnetic field density (B). This law can be expressed as

$$B = \mu_0 H + M \quad (1.2)$$

Where μ_0 represents the magnetic permeability of vacuum with a constant value of $4\pi \times 10^{-7} \text{H/m}$, and M represents the magnetic dipole moment per unit volume, which characterizes the material's magnetization.

The magnetization of the material is influenced by the magnetic susceptibility χ , which is a dimensionless quantity that describes the degree to which a material can be magnetized. It is a measure of the material's ability to develop a magnetic moment in response to an applied magnetic field. the magnetization can then be expressed as

$$M = \mu_0 \chi H \quad (1.3)$$

By substituting this expression into the magnetization law, the following expression is found:

$$B = \mu_0 (1 + \chi) H \quad (1.4)$$

We can introduce the concept of relative magnetic permeability

$$\mu_r = 1 + \chi \quad (1.5)$$

Which characterizes the magnetic behaviour of the material. The value and evolution of the relative magnetic permeability depend on the specific physics of the material. Different classes of materials exhibit varying behaviours when subjected to an external magnetic field, and the most common classes are ferromagnetic and paramagnetic materials.

Ferromagnetic materials exhibit a strong magnetic moment and have a high magnetic permeability due to the alignment of the magnetic moments of their atoms in the same direction; the induced structured subdomains are called magnetic domains or Weiss domains. In the absence of an external magnetic field, these magnetic moments domains are randomly oriented, resulting in no net magnetization. However, when exposed to an external magnetic field, the magnetic moments of the atoms align with the field, leading to a net magnetization of the material. This magnetization remains even after the external magnetic field is removed due to the presence of domains within the material where the magnetic moments remain aligned. However, above a certain temperature known as the Curie temperature, the thermal energy in the material is sufficient to overcome the magnetic interactions between the atoms, causing the domains to break up and the material to lose its magnetization.

Paramagnetic materials have a weak magnetic moment and exhibit a magnetic permeability that is slightly higher than that of vacuum. This magnetic moment arises from the presence of unpaired electrons in their atomic structure, which generate a small magnetic field. When an external magnetic field is applied, these magnetic moments align themselves in the same direction as the field, resulting in a net magnetization of the material. However, when the external magnetic field is removed, the magnetization disappears. Unlike ferromagnetic materials, the Curie temperature does not significantly affect the magnetic properties of paramagnetic materials.

Fig. 1.6 Magnetic moments of a ferromagnetic material (right) and a paramagnetic material (left) Fig. 1.6 and Fig. 1.7 show the magnetic moments and the magnetization curve respectively of ferromagnetic and paramagnetic materials.

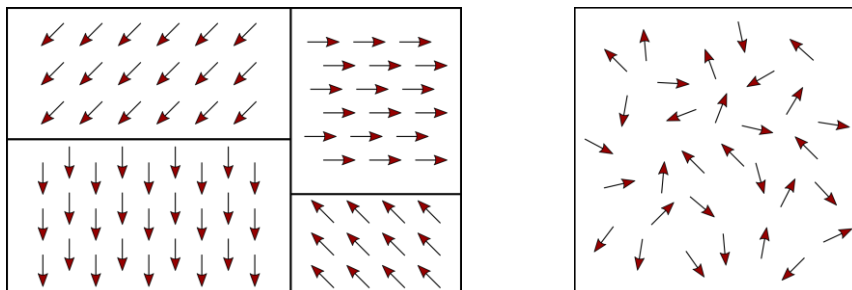


Fig. 1.6 Magnetic moments of a ferromagnetic material (right) and a paramagnetic material (left)

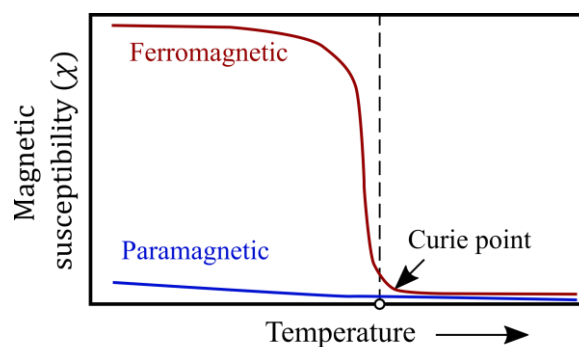


Fig. 1.7 Magnetization curve of ferromagnetic and paramagnetic materials

1.2.1.3 Electrical Conductivity

Electrical conductivity refers to the ability of a material to conduct an electric current and is determined by the ease with which electrons can move through the material in response to an applied electric field. Materials with high electrical conductivity are considered good conductors, while those with low electrical conductivity are good insulators.

Normally, the electrical conductivity of most materials decreases with increasing temperature. This is due to the increased thermal motion of the atoms and electrons in the material, which makes it more difficult for electrons to move freely. At low temperatures, electrons are usually in their lowest energy state, or ground state, which means that they are tightly bound to the atoms of the material and move more slowly.

As the temperature increases, the thermal energy of the electrons also increases, causing them to move faster and collide with other electrons, impurities and defects in the material. These collisions increase the material's resistance to current flow, leading to a decrease in electrical conductivity and an increase in electrical resistivity.

The relationship between electrical conductivity and resistivity can be expressed mathematically by the formula:

$$\sigma = 1/\rho \quad (1.6)$$

where σ represents electrical conductivity and ρ represents electrical resistivity. The formula indicates that as the resistivity of a material increases, its conductivity decreases.

1.2.2 Skin effect

The skin effect is a phenomenon which occurs in conductors carrying alternating currents (AC). At high frequencies, the current tends to flow near the surface, rather than through the entire cross-section. This happens due to the interaction between the AC magnetic field and the electrical conductivity. The magnetic field induces an opposing electric field, which causes the current to be pushed towards the surface, where the magnetic field is strongest. Consequently, the effective cross-sectional area available for current flow is reduced, leading to an increase in the equivalent resistance of the conductor.

The skin depth is a measure of how deep the current penetrates into the conductor. At a distance of one skin depth ($y = \delta$) from the surface, the current density drops to about 37% of its surface value, while the power density decreases to about 14% of its surface value. This means that the majority of the current (63%) and power (86%) is concentrated within a surface layer with a thickness equal to the skin depth, this can be seen in Fig. 1.8

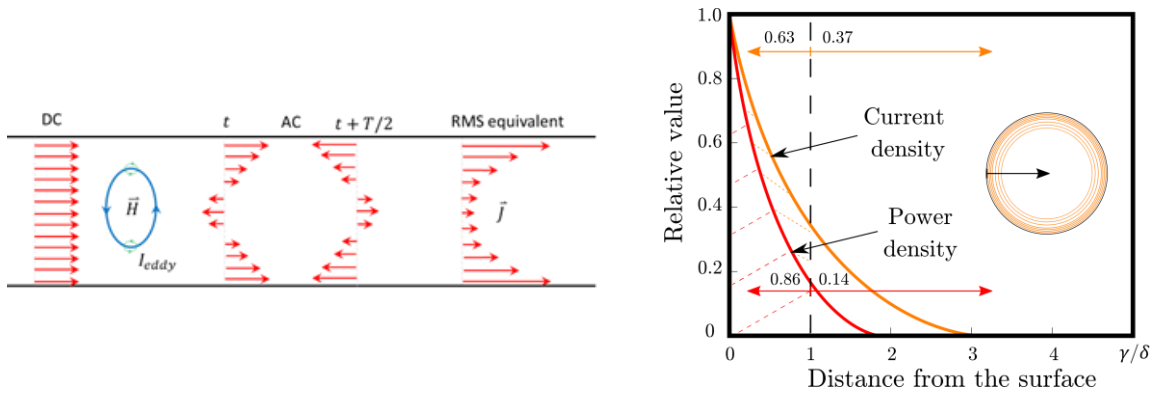


Fig. 1.8 Skin effect in a circular cross-sectional area.

Which is determined by the square root of the ratio between the electrical resistivity, frequency of the AC current, and magnetic permeability of the material.

$$\delta(f) = \sqrt{\frac{2\rho}{2\pi f \mu_r \mu_0}} \quad (1.7)$$

Where f represents the signal frequency, ρ the material electrical resistivity and μ the magnetic permeability (index 0 stands for void absolute permeability and r the material's relative value). The skin effect can be used in heat treatment processes to selectively heat the surface layer of a metal part, thus enabling induction surface hardening.

In induction surface hardening, a high-frequency alternating current is passed through a coil, generating a magnetic field. The metal part is then placed inside the coil, and the magnetic field induces eddy currents on the surface of the part due to the skin effect. These eddy currents generate heat, which causes the surface layer of the part to reach a high temperature. The depth of the heated layer is determined by the frequency of the AC and the electrical resistivity of the material as expressed in (1.7). Higher frequencies and higher resistivity materials result in a shallower skin depth, which can be useful for selectively heating only the surface layer. Once the surface layer reaches the desired temperature, the part is quickly quenched to harden the surface layer. The core of the part remains relatively unaffected by the heat treatment, which can result in a part with a hard and wear-resistant surface layer and a tough and ductile core.

However, it is important to note that the skin effect in ferromagnetic materials like carbon steel is also influenced by the magnetic permeability of the material, which can change with temperature. Below the Curie temperature, carbon steel is ferromagnetic, and its magnetic permeability is high, which can reduce the depth of the eddy currents and the amount of heat generated by the skin effect. Above the Curie temperature, carbon steel becomes paramagnetic, and its magnetic permeability decreases, which can increase the depth of the eddy currents and the amount of heat generated by the skin effect (see Fig. 1.9)

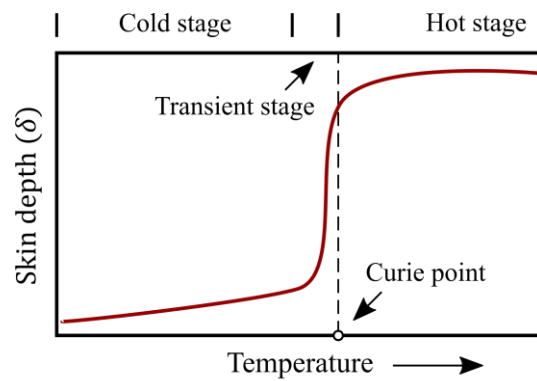


Fig. 1.9 Skin depth behaviour in ferromagnetic materials

1.2.3 Proximity effect

In the skin effect definition, it was assumed that a conductor stands alone and that there are no other current-carrying conductors in the surrounding area. In this case the induced current flows uniformly on the surface as shown in (Fig. 1.10(a)). In practical applications, conductors and cables rarely stand alone, with other current-carrying conductors often in close proximity. The proximity effect is a phenomenon that occurs when alternating currents flow through two or more conductors. It results in a non-uniform distribution of current, increasing the effective resistance of each conductor.

This effect is more pronounced at higher frequencies, where the skin effect also becomes significant. Both effects can lead to a significant increase in the effective resistance of the conductors, affecting the design and operation of electrical systems.

The proximity effect occurs due to magnetic fields generated by the currents in one conductor induce eddy currents in nearby conductors, which produce their own magnetic fields. These fields interact with the original magnetic fields and create a non-uniform distribution of current. Current tends to concentrate near the surface of the conductors closest to each other or on their opposite side, leading to an increase in effective resistance.

The proximity effect is influenced by several factors, including the distance between conductors, the frequency of the current, and the relative orientation of the conductors. The closer the conductors are to each other, the more pronounced the proximity effect becomes, causing the current distribution to become more non-uniform. When the currents in the conductors flow in opposite directions, the magnetic fields induced for both conductors reinforce each other, leading to a stronger proximity effect. This results in a concentration of the current near the surface of the conductors closest to each other (Fig. 1.10(b)). On the other hand, when the currents flow in the same direction, the magnetic fields tend to cancel each other out, reducing the magnitude of the proximity effect. In this case, the current is concentrated in the opposite sides of the conductors (Fig. 1.10(c)).

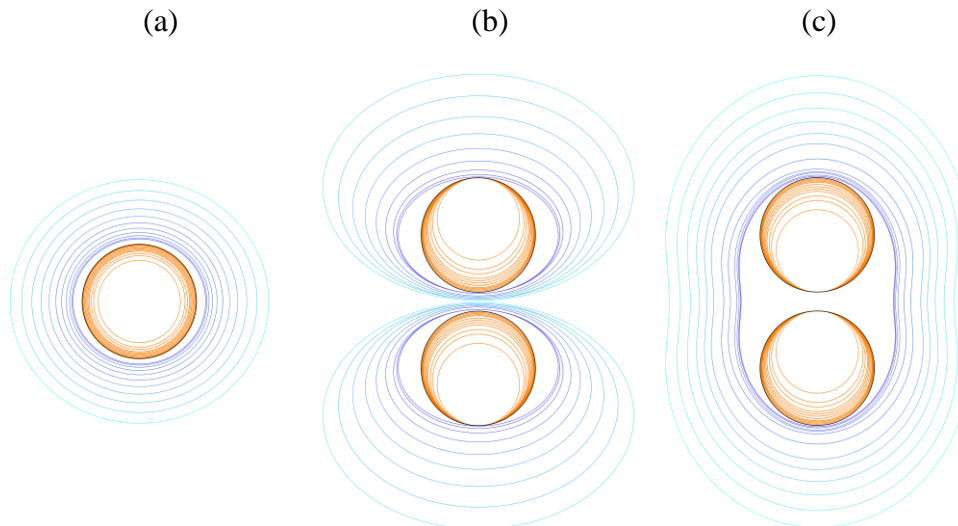


Fig. 1.10 Magnetic field (blue) and current density (orange) distributions in circular cross-sectional area displaying: (a) stand-alone conductor and the proximity effect when the currents are flowing: (b) in the opposite directions and (c) in the same direction (right)

1.2.4 Ring effect

The focus was previously on current density distribution in straight conductors. However, when a cylinder with a current-carrying bar is bent into a ring, the current distribution is affected. The magnetic flux lines concentrate inside the ring, leading to an increase in magnetic flux density. Consequently, the majority of the current flows in the thin internal surface layer of the ring, where the path of least impedance exists. This phenomenon is referred to as the ring effect, and it is similar to the proximity effect because currents flowing on the internal surfaces of opposite sides of the ring's circumference are oriented in opposite directions and attract each other.

Fig. 1.11 illustrates the electromagnetic ring effect, which causes current to concentrate on the inside surface of an induction coil. It's worth noting that this effect isn't restricted to single-turn inductors and can also be observed in multturn coils.

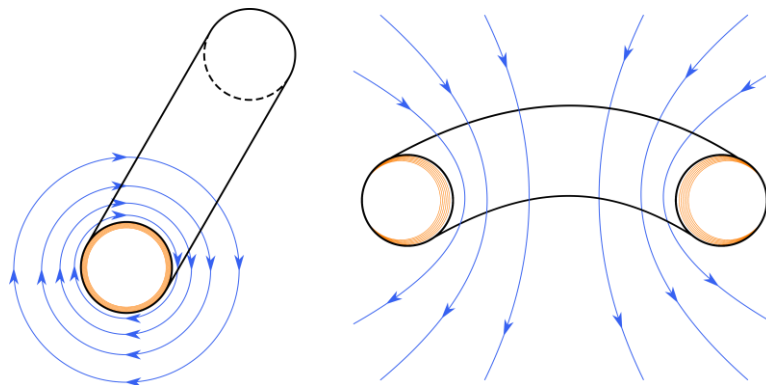


Fig. 1.11 Ring effect in a cylindrical conductor

The ring effect can have a significant impact on heating and process efficiency, either positively or negatively. When performing conventional induction heating with a solid cylinder workpiece inside a solenoid induction coil, the ring effect plays a positive role. It works in conjunction with the skin and proximity effects to concentrate the coil current on the internal surface of the coil, leading to improved coil-to-workpiece electromagnetic coupling and an increase in coil efficiency.

1.3 Numerical modelling and automatic remeshing for industrial applications

Numerical modelling is essential for understanding and optimizing Electromagnetic-coupled manufacturing processes (EMP) due to several reasons:

- Predicting process outcomes: EMP involves the interaction of multiple physical phenomena, making it a complex process. Computational modelling can simulate the EMP process and predict the outcomes, including the shape and dimensions of the formed part. This enables engineers and scientists to optimize the process parameters and achieve the desired outcomes.
- Designing and optimizing equipment: The design of EMP equipment, such as the capacitor bank and coil, can have a significant impact on the process outcomes. Simulation can optimize the design of the equipment and ensure that it is capable of delivering the required magnetic field and electrical current.
- Understanding the underlying physics: EMP involves several physical phenomena, including electromagnetic induction, Joule heating, heat transfer, and plastic deformation. Numerical modelling can help understand the underlying physics and identify the key parameters affecting the process outcomes.
- Reducing experimentation cost and time: EMP experiments can be time-consuming and expensive. Computer-aided analysis can reduce the number of experiments required to optimize the process parameters and identify optimal operating conditions, thereby reducing experimentation costs and time.

Finite element analysis (FEA) is a widely used numerical method for solving complex problems in engineering and science. To perform a successful FEA, it is essential to consider the following points:

- Problem definition: Define the problem and objectives of the analysis by specifying the system's geometry, material properties, boundary conditions, and loads.
- Mesh generation: Generate a suitable finite element mesh that accurately represents the geometry and captures the system's relevant physical behaviour.
- Element type and properties: Select appropriate finite element types and material properties that accurately describe the system's physical behaviour, taking into account the problem's geometry, material properties, and loading conditions.

- Solver selection: Choose an appropriate solver based on the problem's complexity and required level of accuracy. The solver should be capable of handling the analysis type and have sufficient computational resources to complete the analysis efficiently.
- Results interpretation: Analyse the results to understand the system's behaviour and identify areas for improvement. This involves analysing the results for trends, patterns, and anomalies and validating them against experimental data or analytical solutions.

Mesh adaptation is a crucial step in finite element analysis that plays a key role in improving the accuracy and efficiency of the solution. The quality of the finite element analysis results is highly dependent on the mesh used. A coarse mesh can be unfit to provide insight into important smaller-scale details and result in an inaccurate solution, while a fine mesh can increase the computational cost of the analysis to an unmanageable level. Therefore, mesh adaptation helps to find a balance between accuracy and computational efficiency.

Mesh adaptation can be carried out by refining or coarsening the existing mesh or by generating a completely new mesh. One of the methods to achieve mesh adaptation is to take into account the anisotropy of the analysed field. Anisotropy refers to the directional dependence of physical properties such as electrical conductivity, thermal conductivity and mechanical properties. Anisotropy can significantly affect the accuracy of finite element results, especially when the solution varies significantly in certain directions. Therefore, to ensure accuracy, it is essential to adapt the mesh according to the anisotropy of the analysed field.

Mesh adaptation based on anisotropy consists in refining or coarsening the mesh in specific directions to better capture the behaviour of the solution. For example, regions with rapid changes in the solution or strong gradients require a finer mesh to accurately capture the solution behaviour, while smoother regions may be modelled using a coarser mesh. By adapting the mesh according to the anisotropy of the analysed field, FEA can accurately capture the behaviour of the system, leading to more reliable results.

The importance of mesh adaptation as a function of anisotropy can be demonstrated with an example. When analysing eddy currents induced in a part, the current density near the surface due to the skin effect can be underestimated if the mesh used in the FEA is not adapted to the anisotropy of the physical phenomenon. By adapting the mesh according to the anisotropy, FEA can accurately capture the behaviour of the system, leading to more reliable results. This, in turn, can help optimise system design and operation, resulting in improved performance and reduced costs.

Chapter 2

Multiphysics computational modelling

2.1	Multiphysics model.....	28
2.1.1	Electromagnetic problem	28
2.1.1.1	Maxwell equations.....	28
2.1.1.2	Constitutive laws	29
2.1.2	Heat transfer problem.....	30
2.1.2.1	Energy conservation	30
2.1.2.2	Constitutive laws	31
2.1.2.3	Heat transfer equation.....	32
2.1.2.4	Boundary conditions.....	32
2.1.3	Solid Mechanics problem.....	33
2.1.3.1	Mass conservation	33
2.1.3.2	Linear momentum conservation	33
2.1.3.3	Angular momentum conservation	34
2.1.4	Fluids Mechanics problem	35
2.1.4.1	Mass continuity equation.....	35
2.1.4.2	Momentum conservation	35
2.2	Electromagnetic model.....	36
2.2.1	Potential formulation.....	36
2.2.1.1	$(\mathbf{A} - \phi)$ formulation	36
2.2.1.1.1	The gauge condition.....	37
2.2.1.2	$\mathbf{T} - \mathbf{\Omega}$ formulation	38
2.2.1.2.1	The gauge condition.....	39
2.2.2	Boundary conditions	39
2.2.3	Edge elements	40
2.2.4	Weak formulation.....	42
2.2.5	Discretised formulation	45
2.2.6	Boundary element method (BEM)	45
2.2.7	Fully immersed finite elements approach	46
2.2.8	Time integration	47
2.2.8.1	Electromagnetic resolution	47

2.2.8.2	Time integration schema	48
2.3	Multiphysics coupling.....	50
2.3.1	Characteristic times involved	50
2.3.2	Coupling scheme	52
2.4	R-adaptation.....	54
2.5	Field transport procedure in electromagnetic modelling	54
2.5.1	Transport strategies	55
2.5.1.1	Transformation from edges to integration points.	56
2.5.1.2	Transport from the old mesh to the new mesh.	56
2.5.1.3	Transformation from integration points to edges.	57
2.6	Parallel paradigm	57

Résumé : Modélisation numérique multiphysique.

Ce chapitre se concentre sur la modélisation et la résolution des problèmes électromagnétiques couplés à d'autres phénomènes physiques tels que le transfert de chaleur, la mécanique des solides et la mécanique des fluides.

En premier lieu, nous aborderons le transfert de chaleur, qui est associé aux phénomènes électromagnétiques dans des applications pratiques telles que le chauffage par induction. Ensuite, nous étudierons la mécanique des solides, qui est couplée à des applications telles que la mise en forme par impulsion magnétique. Enfin, nous aborderons la mécanique des fluides, qui est utilisée pour modéliser le brassage électromagnétique.

Pour approfondir la résolution numérique du modèle électromagnétique, une attention particulière sera accordée à la formulation potentielle et à sa résolution variationnelle. Nous discuterons également de l'utilisation courante des éléments d'arêtes dans les méthodes numériques pour les problèmes électromagnétiques.

En dernier lieu, nous explorerons le schéma de couplage multiphysique et examinerons les stratégies de résolution utilisées dans le domaine de la forge pour gérer le transport et le parallélisme.

2 Multiphysics computational modelling

2.1 Multiphysics model

Modelling multiphysics electromagnetic coupled processes involves integrating various physical models, each representing a different aspect of the phenomenon. These models are typically based on partial differential equations (PDEs) and rely on the coupling of:

- **Electromagnetism:** This aspect deals with the behavior of electromagnetic fields, governed by Maxwell's equations, which describe how electric and magnetic fields interact and propagate.
- **Heat transfer:** It focuses on the flow of thermal energy within the system. It considers thermal conductivity and temperature gradients to describe how heat is transferred through materials.
- **Solid/fluid mechanics:** These models are used to understand the mechanical behaviour of solid and fluids under the influence of electromagnetic forces, as in Magnetic Pulse Forming and Electromagnetic Stirring respectively.

These models are interconnected, as physical processes don't occur in isolation but influence each other. The coupling occurs through:

- **General Conservation Laws:** These laws describe fundamental principles such as the conservation of mass, energy, momentum, and charge. They ensure that the physical quantities involved remain conserved across system.
- **Constitutive Models:** These models incorporate material properties and characteristics into the equations.

In the following sections, these models will be presented for the various physical problems involved.

2.1.1 Electromagnetic problem

In this section, we introduce the fundamental equations that describe electromagnetic phenomena.

2.1.1.1 Maxwell equations

Models describing the propagation of electromagnetic waves, which capture the spatial and temporal evolution of electric and magnetic fields, are grounded in the Maxwell equations:

Faraday's Induction Law
$$\vec{\nabla} \times \vec{E} = -\partial_t \vec{B} \quad (2.1)$$

$$\text{Ampere's Law} \quad \vec{\nabla} \times \vec{H} = \vec{J} + \partial_t \vec{D} \quad (2.2)$$

$$\text{Gauss's Law} \quad \vec{\nabla} \cdot \vec{D} = \rho \quad (2.3)$$

$$\text{Gauss's Law for the magnetic field} \quad \vec{\nabla} \cdot \vec{B} = 0 \quad (2.4)$$

Where: E: electric field intensity

D: electric flux density

H: magnetic field intensity

B: magnetic flux density

J: electric current density

ρ : electric charge density

In this system of equations, the relations (2.1) and (2.2) express the interaction between the electric (\vec{E}, \vec{D}) and magnetic (\vec{B}, \vec{H}) fields. In many electromagnetic-based materials processes, typically occurring at low to medium frequencies ($< 1\text{MHz}$), the current displacements density term $\partial_t \vec{D}$ can be neglected, leading to a quasi-steady state approximation. Under these conditions, Maxwell equations can be re-written as follows:

$$\vec{\nabla} \times \vec{E} = -\partial_t \vec{B} \quad (2.5)$$

$$\vec{\nabla} \times \vec{H} = \vec{J} \quad (2.6)$$

$$\vec{\nabla} \cdot \vec{B} = 0 \quad (2.7)$$

From the Ampere's law expression, the current density conservation is derived:

$$\vec{\nabla} \cdot \vec{J} = 0 \quad (2.8)$$

2.1.1.2 Constitutive laws

The Maxwell equations presented earlier provide an essential foundation, encompassing only the fields and their sources. Similar to solid mechanics, constitutive relations that describe the electromagnetic properties of various materials at a macroscopic level need to be incorporated. These relationships are detailed below:

Electrical permittivity (ϵ):

$$\vec{D} = \epsilon_0 \epsilon_r \vec{E} \quad (2.9)$$

Here, ϵ_0 denotes the void's electric permittivity and ϵ_r the relative electric permittivity.

Magnetic permeability (μ):

$$\vec{B} = \mu_0 \mu_r(\|\vec{H}\|, T) \vec{H} \quad (2.10)$$

Where μ_0 denotes the void's magnetic permeability and μ_r the relative magnetic permeability, which can be a function of magnetic field strength (\vec{H}) and temperature (T).

Electrical conductivity (Ohm's law):

$$\vec{J} = \sigma(T) \vec{E} \quad (2.11)$$

The parameter $\sigma(T)$ is the electrical conductivity, indicating the proportionality between current density (\vec{J}) and electric field (\vec{E}), and it can depend on temperature (T).

2.1.2 Heat transfer problem

In electromagnetic-based industrial processes, particularly in induction heating, a significant coupling occurs between electromagnetism and heat transfer. The thermal problem at hand is unsteady. It is governed by the heat transfer equation, completed by boundary conditions applying on both free and contact surfaces.

2.1.2.1 Energy conservation

The first law of thermodynamics defines the rate of change of internal thermal energy of a system (Ω) as the sum of two factors: the net energy flow across its boundaries (Γ) and the heat generated internally. This fundamental principle of thermal energy conservation is expressed through the following global balance equation:

$$\int_{\Omega} \rho \frac{\partial e}{\partial t} dV = - \int_{\Gamma} \vec{q} \cdot \hat{n} dS + \int_{\Omega} f dV \quad (2.12)$$

Here, ρ represents the mass density, e denotes the specific internal energy, \vec{q} the heat flux vector, \hat{n} the outward normal vector and f the rate of heat production per unit volume. By applying the divergence theorem to the surface integral involving the heat flux, the global form of the thermal energy is rewritten as:

$$\int_{\Omega} \rho \frac{\partial e}{\partial t} dV = - \int_{\Omega} \vec{\nabla} \cdot \vec{q} dV + \int_{\Omega} f dV \quad (2.13)$$

Subsequently, assuming the continuity of the above expression and recognizing that this equality holds not only for the entire system Ω , but also for each individual subdomain, the following PDE is obtained:

$$\rho \frac{\partial e}{\partial t} + \vec{\nabla} \cdot \vec{q} = f \quad \text{in } \Omega \quad (2.14)$$

2.1.2.2 Constitutive laws

For a wide range of materials and temperatures, it can be assumed that the specific thermal energy is linearly related to temperature (T), leading to the following expression:

$$\frac{\partial e}{\partial t} = C \frac{\partial T}{\partial t} \quad (2.15)$$

Here, C represents the specific heat capacity.

Similarly, as heat naturally flows from areas of high temperature to low temperature, a linear relationship between these quantities was established by Fourier:

$$\vec{q} = -k(T)\vec{\nabla}T \quad (2.16)$$

Where $k(T)$ is the thermal conductivity, which can vary with temperature. This temperature-dependent relationship introduces non-linearity into the problem.

The rate of heat production, denoted as f , is expressed in electromagnetic material processing modelling as the sum of two components:

$$f = \dot{Q}_e + \dot{Q}_m \quad (2.17)$$

Where \dot{Q}_e represents the volumetric heat source generated by the Joule heating effect phenomenon, expressed as:

$$\dot{Q}_e = \vec{j} \cdot \vec{E} \quad (2.18)$$

And \dot{Q}_m is the mechanical heat term resulting from the transformation of dissipated mechanical work into heat, expressed as:

$$\dot{Q}_m = \underline{\underline{\dot{\epsilon}}} : \underline{\underline{\sigma}} \quad (2.19)$$

Here, $\underline{\underline{\dot{\epsilon}}}$ and $\underline{\underline{\sigma}}$ represent the strain rate tensor and the stress tensor, respectively.

The heat source term can thus be expressed as:

$$f = \vec{j} \cdot \vec{E} + \underline{\underline{\dot{\epsilon}}} : \underline{\underline{\sigma}} \quad (2.20)$$

2.1.2.3 Heat transfer equation

The heat transfer equation, which allows us to calculate the temperature within conductive components, is expressed as follows:

$$\rho C \frac{\partial T}{\partial t} - \nabla \cdot (k \nabla T) = \vec{j} \cdot \vec{E} + \underline{\underline{\dot{\epsilon}}} : \underline{\underline{\sigma}} \quad \text{in } \Omega \quad (2.21)$$

2.1.2.4 Boundary conditions

The various boundary conditions that apply to heat transfer are summarized in Fig. 2.1

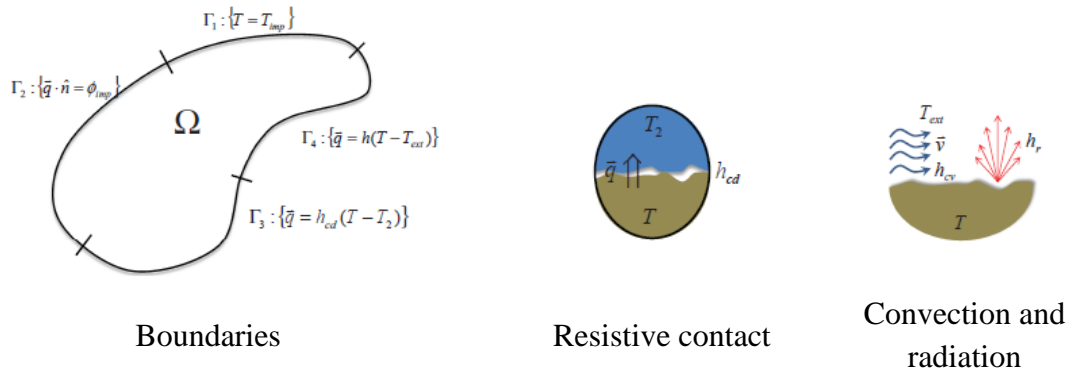


Fig. 2.1 Boundary conditions for heat transfer problem. After Alves [2]

In this context, the boundary conditions can be defined as follows:

1. Temperature is set to a prescribed value:

$$T = T_{prescribed} \quad \text{on } \Gamma_1 \quad (2.22)$$

2. Heat flux is set to a prescribed value:

$$-k \nabla T \cdot \hat{n} = \phi_{prescribed} \quad \text{on } \Gamma_2 \quad (2.23)$$

3. Convection and Radiation: pure convection and radiation are modelled using a single convection coefficient h , which is expressed as:

$$h = h_{cv} + h_r$$

Where h_{cv} is related to external condition (such as air or any fluid) and h_r is approximated by:

$$h_r \approx \epsilon_r \sigma_r (T + T_{ext})(T^2 + T_{ext}^2)$$

Where ϵ_r is the surface emissivity coefficient and $\sigma_r = 5.67 \times 10^{-8} [W m^{-2} K]$ is the Stefan-Boltzman constant. Then, expressed as:

$$-k \nabla T \cdot \hat{n} = h(T - T_{ext}) \quad \text{on } \Gamma_4 \quad (2.24)$$

4. Heat exchange between two solids is controlled by a resistive surface contact. An equivalent convection coefficient for surface conduction h_{cd} is employed to deal with this situation. This coefficient considers the conductivity of both bodies as well as the surface rugosity, which can trap air between them.

2.1.3 Solid Mechanics problem

In solid mechanics, we consider the mechanical behaviour of materials at a macroscopic scale. Here, materials are assumed to be continuous and homogeneous, allowing us to describe them using the principles of mass and momentum conservation. These fundamental equations require further refinement through appropriate initial and boundary conditions, as well as the incorporation of constitutive laws that describe the specific mechanical properties of the material. This section provides a brief introduction to solid mechanics problem; for more detail, refer to APPENDIX 7.1

2.1.3.1 Mass conservation

In solid mechanics, the conservation of mass is expressed as follows:

$$\frac{\partial \rho}{\partial t} + \vec{\nabla} \cdot (\rho \vec{v}) = 0 \quad (2.25)$$

Here, ρ represents the density of matter at any point of Ω and \vec{v} is the material's velocity field. Two specific scenarios arise:

- 1) **Steady State Case:** In this scenario, nothing changes over time, implying that the partial derivative with respect to time is zero. Equation (2.25) simplifies to:

$$\vec{\nabla} \cdot (\rho \vec{v}) = 0 \quad (2.26)$$

- 2) **Incompressible Material:** When the material's density remains constant throughout the domain Ω , it is considered incompressible. Equation (2.25) can then be rewritten as:

$$\vec{\nabla} \cdot \vec{v} = 0 \quad (2.27)$$

2.1.3.2 Linear momentum conservation

The velocity vector \vec{v} featured in the mass conservation equation can be determined through the principle of momentum conservation. Momentum variations primarily arise from volume and contact forces acting upon a body. The equation governing momentum conservation is given by:

$$\frac{\partial}{\partial t}(\rho \vec{v}) + \vec{v} \cdot \vec{\nabla}(\rho \vec{v}) = \vec{\nabla} \cdot \underline{\underline{S}} - \vec{\nabla} p + \rho \vec{b} \quad (2.28)$$

Here, the expression of momentum density ($\rho \vec{v}$) is introduced. In the context of electromagnetic-based industrial processes, the term \vec{b} represents the Lorentz force, which establishes the coupling between the electromagnetic and mechanical model. Additionally, $\underline{\underline{S}}$ and p are introduced:

$$\text{Hydrostatic pressure: } p = -\frac{1}{3} \text{Tr}(\underline{\underline{\sigma}}) \quad (2.29)$$

$$\text{Deviatoric component: } \underline{\underline{S}} = \underline{\underline{\sigma}} + p \underline{\underline{I}} \quad (2.30)$$

2.1.3.3 Angular momentum conservation

For the conservation of angular momentum in a continuum medium, it's a fundamental requirement that the Cauchy stress tensor must be symmetric, as expressed by:

$$\sigma_{ij} = \sigma_{ji} \quad (2.31)$$

Nevertheless, there are specific scenarios where the stress tensor can potentially be asymmetric, one of them is when the material interacts with magnetic fields. This asymmetry arises due to the way the stress field depends on the electromagnetic field.

Given the Lorentz force acting on a distribution of charges:

$$\vec{f} = \rho^e \vec{E} + \vec{J} \times \vec{B} \quad (2.32)$$

Then, this force can be further expressed as:

$$\begin{aligned} \vec{f} &= (\vec{\nabla} \cdot \vec{D}) \vec{E} + \left(\vec{\nabla} \times \vec{H} - \frac{\partial \vec{D}}{\partial t} \right) \times \vec{B} \\ \vec{f} &= (\vec{\nabla} \cdot \vec{D}) \vec{E} - \vec{B} \times \vec{\nabla} \times \vec{H} - \frac{\partial \vec{D}}{\partial t} \times \vec{B} \\ \vec{f} &= (\vec{\nabla} \cdot \vec{D}) \vec{E} - \vec{D} \times \vec{\nabla} \times \vec{E} - \vec{B} \times \vec{\nabla} \times \vec{H} - \frac{\partial}{\partial t} (\vec{D} \times \vec{B}) \\ \vec{f} &= (\vec{\nabla} \cdot \vec{D}) \vec{E} - \vec{D} \times \vec{\nabla} \times \vec{E} + (\vec{\nabla} \cdot \vec{B}) \vec{H} - \vec{B} \times \vec{\nabla} \times \vec{H} - \frac{\partial}{\partial t} (\vec{D} \times \vec{B}) \\ \vec{f} &= \vec{\nabla} \cdot \left[\vec{D} \otimes \vec{E} - \frac{1}{2} (\vec{D} \cdot \vec{E}) \underline{\underline{I}} + \vec{B} \otimes \vec{B} - \frac{1}{2} (\vec{B} \cdot \vec{B}) \underline{\underline{I}} \right] - \frac{\partial}{\partial t} (\vec{D} \times \vec{B}) \\ \vec{f} &= \vec{\nabla} \cdot \underline{\underline{S}} - \frac{\partial \vec{S}}{\partial t} \end{aligned} \quad (2.33)$$

Where $\underline{\underline{\sigma}}$ represents the electromagnetic induced stress tensor and \vec{S} is the Poynting vector. The symmetry of $\underline{\underline{\sigma}}$ is conditioned to $\vec{D}||\vec{E}$ and $\vec{B}||\vec{H}$. It is demonstrated in [11] that an asymmetric case can take place if the microscopic magnetic dipoles in the material do not align with the macroscopic field, which will induce a torque per unit volume. This situation might arise if certain interactions prevent the dipoles from aligning with the field. However, it is generally reasonable to assume aligned dipoles[2]

2.1.4 Fluids Mechanics problem

Describing the motion of a Newtonian fluid within a domain Ω over a time period $[0; T]$ employs a similar approach to that used in solid mechanics. The fluid motion must satisfy the principle of momentum and mass conservation, along with a Newtonian constitutive law that establishes a linear relationship between stress and strain rates tensors based on the fluid viscosity. This section provides a brief introduction to fluid mechanics; for more detail, refer to APPENDIX 7.2

2.1.4.1 Mass continuity equation

The equation governing mass conservation within a domain is expressed as:

$$\frac{\partial \rho}{\partial t} - \vec{v} \cdot \vec{\nabla} \rho + \rho \vec{\nabla} \cdot \vec{v} = s_1 \quad (2.34)$$

Here, ρ represents fluid mass density, \vec{v} is the velocity field, and s_1 is the source term. Assuming constant mass density across the domain simplifies the mass continuity equation to:

$$\rho \vec{\nabla} \cdot \vec{v} = s_1 \quad (2.35)$$

Finally, in the absence of a mass source, the expression for fluid incompressibility becomes:

$$\vec{\nabla} \cdot \vec{v} = 0 \quad (2.36)$$

2.1.4.2 Momentum conservation

The conservation of momentum in fluid mechanics is described by:

$$\rho \left(\frac{\partial \vec{v}}{\partial t} + \vec{u} \cdot \vec{\nabla} \vec{v} \right) = \vec{\nabla} \cdot \underline{\underline{\sigma}} + \vec{f} \quad (2.37)$$

In this equation, $\underline{\underline{\sigma}}$ is the Cauchy stress tensor, and \vec{f} represents an external volumetric force.

2.2 Electromagnetic model

The modeling of electromagnetic problems is grounded in Maxwell's equations, supplemented by the electromagnetic constitutive laws of materials. Let's review Maxwell's equations:

$$\text{Faraday's Induction Law} \quad \vec{\nabla} \times \vec{E} = -\partial_t \vec{B} \quad (2.38)$$

$$\text{Ampere's Law} \quad \vec{\nabla} \times \vec{H} = \vec{J} + \partial_t \vec{D} \quad (2.39)$$

$$\text{Gauss's Law} \quad \vec{\nabla} \cdot \vec{D} = \rho \quad (2.40)$$

$$\text{Gauss's Law for the magnetic field} \quad \vec{\nabla} \cdot \vec{B} = 0 \quad (2.41)$$

2.2.1 Potential formulation

Solving Maxwell's equations can be accomplished either by directly dealing with the magnetic and electric fields (resulting in a complex system of equations involving six unknowns) or by expressing these fields in terms of potentials: one scalar and one vector. We introduce two potential formulations: the electric ($A - \phi$) formulation and the the magnetic ($T - \Omega$) formulation ([12],[13]).

2.2.1.1 ($A - \phi$) formulation

The $A - \phi$ formulation stems from the divergence-free nature of the magnetic flux density \vec{B} , expressed in (2.41). This allows us to express the magnetic flux as the curl of a magnetic vector potential \vec{A} , such that:

$$\vec{B} = \vec{\nabla} \times \vec{A} \quad (2.42)$$

By substituting this expression for \vec{B} into Faraday's induction law (2.38), we derive:

$$\vec{\nabla} \times \vec{E} = -\frac{\partial}{\partial t} (\vec{\nabla} \times \vec{A}) \quad (2.43)$$

Applying the associative property of the differential operator $\vec{\nabla}$ in (2.43), this expression can be rewritten as:

$$\vec{\nabla} \times \left(\vec{E} + \frac{\partial \vec{A}}{\partial t} \right) = 0 \quad (2.44)$$

This results in a new form of Faraday's law [14]:

$$\vec{E} = -\left(\frac{\partial \vec{A}}{\partial t} + \vec{\nabla} \phi \right) \quad (2.45)$$

The current density is naturally calculated by substituting equation (2.45) into Ohm's law (2.11):

$$\vec{J} = -\sigma \left(\frac{\partial \vec{A}}{\partial t} + \vec{\nabla} \phi \right) \quad (2.46)$$

Similarly, the electric flux density can be expressed in terms of electric permittivity and the potential formulation as:

$$\vec{D} = -\varepsilon_0 \varepsilon_r \left(\frac{\partial \vec{A}}{\partial t} + \vec{\nabla} \phi \right) \quad (2.47)$$

Finally, using the expressions (2.10), (2.42) and (2.45) and substituting each term into Ampere's law (2.2), the following expression is found:

$$\vec{\nabla} \times \left(\frac{1}{\mu_0 \mu_r} \vec{\nabla} \times \vec{A} \right) = \frac{\partial}{\partial t} \left(-\varepsilon_0 \varepsilon_r \left(\frac{\partial \vec{A}}{\partial t} + \vec{\nabla} \phi \right) \right) - \sigma \left(\frac{\partial \vec{A}}{\partial t} + \vec{\nabla} \phi \right) \quad (2.48)$$

Reordering this, it yields to the A – ϕ potential formulation of electromagnetism:

$$\varepsilon_0 \varepsilon_r \frac{\partial^2 \vec{A}}{\partial t^2} + \sigma \frac{\partial \vec{A}}{\partial t} + \frac{1}{\mu_0} \left(\vec{\nabla} \times \frac{1}{\mu_r} \vec{\nabla} \times \vec{A} \right) + \varepsilon_0 \varepsilon_r \frac{\partial (\vec{\nabla} \phi)}{\partial t} + \sigma \vec{\nabla} \phi = 0 \quad (2.49)$$

In the same manner, using the current density conservation (2.8), the gradient of the electric scalar potential is calculated as:

$$\vec{\nabla} \cdot \sigma \left(\frac{\partial \vec{A}}{\partial t} + \vec{\nabla} \phi \right) = 0 \quad (2.50)$$

2.2.1.1.1 The gauge condition

To ensure the uniqueness of the potential vector \vec{A} , which is not guaranteed by the previous equations, a gauge condition must be prescribed. One classical condition is the Coulomb gauge:

$$\vec{\nabla} \cdot \vec{A} = 0 \quad (2.51)$$

By imposing the Coulomb gauge on (2.50) and assuming a constant electric conductivity in a finite domain, along with commutability of $\vec{\nabla}$ and $\frac{\partial}{\partial t}$ operators, we obtain:

$$\vec{\nabla} \cdot \sigma(\vec{\nabla}\phi) = 0 \quad (2.52)$$

2.2.1.2 $T - \Omega$ formulation

Similarly to the $(A - \phi)$ formulation, the $T - \Omega$ formulation also derives from the Maxwell equations (2.38) and (2.39) combined with the constitutive laws (2.10) and (2.11). For the sake of simplicity, we employ the quasi-steady state approximation to introduce this formulation. In $T - \Omega$ formulation, we use current density conservation (2.8) to define an electric vector potential \vec{T} , given by:

$$\vec{j} = \vec{\nabla} \times \vec{T} \quad (2.53)$$

Substituting expression (2.53) into Ampere's law (2.6), we obtain:

$$\vec{\nabla} \times \vec{H} = \vec{\nabla} \times \vec{T} \quad (2.54)$$

Applying the associative property of the differential operator $\vec{\nabla}$ in (2.54), this can be rewritten as:

$$\vec{\nabla} \times (\vec{H} - \vec{T}) = 0 \quad (2.55)$$

This leads to the expression:

$$\vec{H} = \vec{T} - \vec{\nabla}\Omega \quad (2.56)$$

Finally, by using equations (2.10), (2.11), (2.53) and (2.56) and substituting them into Faraday's Induction law (2.38), the following expression is found:

$$\vec{\nabla} \times \sigma(\vec{\nabla} \times \vec{T}) = -\frac{\partial}{\partial t} \mu_0 \mu_r (\vec{T} - \vec{\nabla}\Omega) \quad (2.57)$$

Reordering (2.57) yields to the $T - \Omega$ potential formulation for electromagnetism:

$$\mu_0 \mu_r \frac{\partial \vec{T}}{\partial t} + \vec{\nabla} \times \sigma(\vec{\nabla} \times \vec{T}) + \mu_0 \mu_r \vec{\nabla}\Omega = 0 \quad (2.58)$$

The magnetic scalar potential Ω is calculated from the Gauss law of induction, also known as the magnetic induction (2.41):

$$\vec{\nabla} \cdot \mu_0 \mu_r (\vec{T} - \vec{\nabla}\Omega) = 0 \quad (2.59)$$

2.2.1.2.1 The gauge condition

As in the $A - \varphi$ formulation, to ensure the uniqueness of the potential vector \vec{T} , a gauge condition must be specified. For this purpose, the Coulomb gauge is employed:

$$\vec{\nabla} \cdot \vec{T} = 0 \quad (2.60)$$

2.2.2 Boundary conditions

In cases where a global finite element approach is employed to tackle the electromagnetic problem, situations such as the one depicted in Fig. 2.2 arise. In this scenario, the domain Ω encompasses various components, including inductors (Ω_I), workpieces (Ω_p), and the surrounding air (Ω_a).

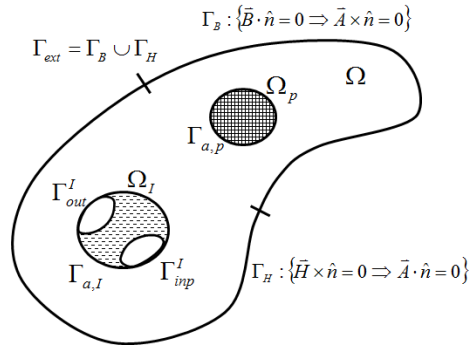


Fig. 2.2 Boundaries for a global electromagnetic case. Ω_p is the work piece, Ω_i is the inductor, Ω represent whole domain (air surroundings + work piece + inductors). Γ_{inp}^I and Γ_{out}^I represent the electrical input and output connections of the inductor. After Biro et al. [14]

There are two types of boundary conditions [14] that are applied to the magnetic field intensity \vec{H} and the magnetic flux density \vec{B} on the boundaries Γ_H and Γ_B respectively.

$$\vec{H} \times \vec{n} = \vec{0} \Rightarrow \mu^{-1} \vec{\nabla} \times \vec{A} \times \hat{n} = 0, \text{ on } \Gamma_H \quad (2.61)$$

$$\vec{B} \cdot \hat{n} = 0 \Rightarrow \hat{n} \cdot \vec{\nabla} \times \vec{A} = 0, \text{ on } \Gamma_B \quad (2.62)$$

The tangential component of the magnetic field is set to zero on Γ_H and the normal component of the magnetic flux is set to zero on Γ_B . These boundary conditions are expressed in terms of the vector potential \vec{A} :

$$\vec{n} \times \mu^{-1} \vec{\nabla} \times \vec{A} = 0 \quad \text{on } \Gamma_H \quad (2.63)$$

$$\vec{A} \times \vec{n} = 0 \quad \text{on } \Gamma_B \quad (2.64)$$

Additionally, the input and output conditions on the inductor are given as follows:

$$\phi = 0, \text{ on } \Gamma_{out}^I \quad (2.65)$$

$$\phi = V(t), \text{ on } \Gamma_{inp}^I \quad (2.66)$$

Finally, the initial boundary condition is given on the magnetic vector potential \vec{A} :

$$\vec{A}(\vec{x}, 0) = 0 \quad \text{and} \quad \frac{\partial}{\partial t} \vec{A}(\vec{x}, 0) = 0, \quad \vec{x} \in \Omega \quad (2.67)$$

2.2.3 Edge elements

In classical finite element analysis, degrees of freedom are typically defined at the nodes for most finite elements, and internal values are derived by interpolating nodal values. However, these conventional elements present several issues when applied to electromagnetic problems. As highlighted in [15], they can produce non-physical or spurious solutions. This issue stems from the fact that nodal elements enforce continuity on the normal components of vector fields. This continuity is well-suited for handling divergence or gradient operators. However, electromagnetic equations primarily rely on the curl operator, which requires continuity only on the tangential components and permits discontinuity on the normal components, in opposition of the divergence or gradient operators. To address these challenges, a different approach for solving of electromagnetic problems using finite element has been developed. This approach involves using vector basis or vector elements that assign degrees of freedom to the edges rather than to the nodes of the element. These specialized elements are referred to as "edge elements" and were introduced by Nédélec ([16],[17]).

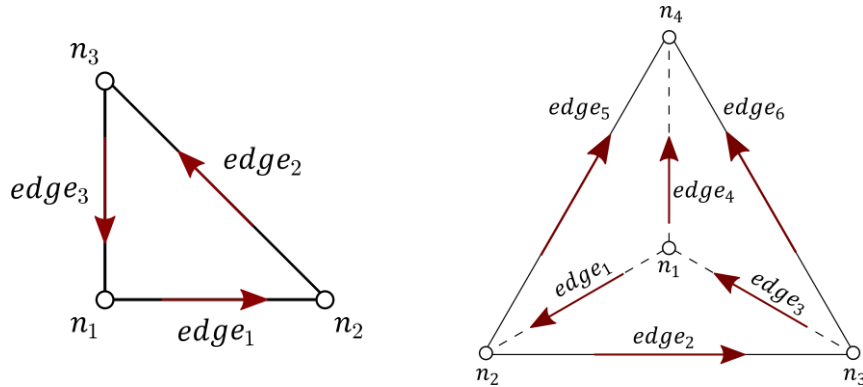


Fig. 2.3 Nedelec elements (2D and 3D)

To construct the edge basis functions in Nédélec elements, we first define nodal basis functions. For a 3D tetrahedral element, as illustrated in Fig. 2.3, the basis functions are defined as:

$$\phi(t, \vec{x}) = \sum_n \phi_n(t) \varphi_n(\vec{x}) \quad (2.68)$$

For this element, the basis functions $\varphi_n(\vec{x})$ are represented by a linear (P1) interpolation function of the coordinates:

$$\varphi_1(\vec{x}) = 1 - x - y - z ; \varphi_2(\vec{x}) = x ; \varphi_3(\vec{x}) = y ; \varphi_4(\vec{x}) = z \quad (2.69)$$

Similarly, a vector field expressed on the edges is defined as:

$$\vec{A}(t, \vec{x}) = \sum_e a_e(t) \vec{\Psi}_e(\vec{x}) \quad (2.70)$$

Here, $a_e = \int_e \vec{A} \cdot \hat{t}$ represents the mean value of the integral of \vec{A} along the edge e , and \hat{t} denotes a vector tangent to the edge. The vector base functions $\vec{\Psi}_e(x)$ are computed from the nodal basis functions using the convention provided in [15].

$$\vec{\Psi}_e(\vec{x}) = \varphi_i(\vec{x}) \vec{\nabla} \varphi_j(\vec{x}) - \varphi_j(\vec{x}) \vec{\nabla} \varphi_i(\vec{x}) \quad (2.71)$$

In this type of element, tangential components conserve continuity, and their constructions on a 3D tetrahedral element (6 edges) are given by:

$$\begin{aligned} \vec{\Psi}_1(\vec{x}) &= \varphi_1(\vec{x}) \vec{\nabla} \varphi_2(\vec{x}) - \varphi_2(\vec{x}) \vec{\nabla} \varphi_1(\vec{x}) \\ \vec{\Psi}_2(\vec{x}) &= \varphi_2(\vec{x}) \vec{\nabla} \varphi_3(\vec{x}) - \varphi_3(\vec{x}) \vec{\nabla} \varphi_2(\vec{x}) \\ \vec{\Psi}_3(\vec{x}) &= \varphi_3(\vec{x}) \vec{\nabla} \varphi_1(\vec{x}) - \varphi_1(\vec{x}) \vec{\nabla} \varphi_3(\vec{x}) \\ \vec{\Psi}_4(\vec{x}) &= \varphi_1(\vec{x}) \vec{\nabla} \varphi_4(\vec{x}) - \varphi_4(\vec{x}) \vec{\nabla} \varphi_1(\vec{x}) \\ \vec{\Psi}_5(\vec{x}) &= \varphi_2(\vec{x}) \vec{\nabla} \varphi_4(\vec{x}) - \varphi_4(\vec{x}) \vec{\nabla} \varphi_2(\vec{x}) \\ \vec{\Psi}_6(\vec{x}) &= \varphi_3(\vec{x}) \vec{\nabla} \varphi_4(\vec{x}) - \varphi_4(\vec{x}) \vec{\nabla} \varphi_3(\vec{x}) \end{aligned} \quad (2.72)$$

The 2D representation of these edge vector basis functions is show in Fig. 2.4.

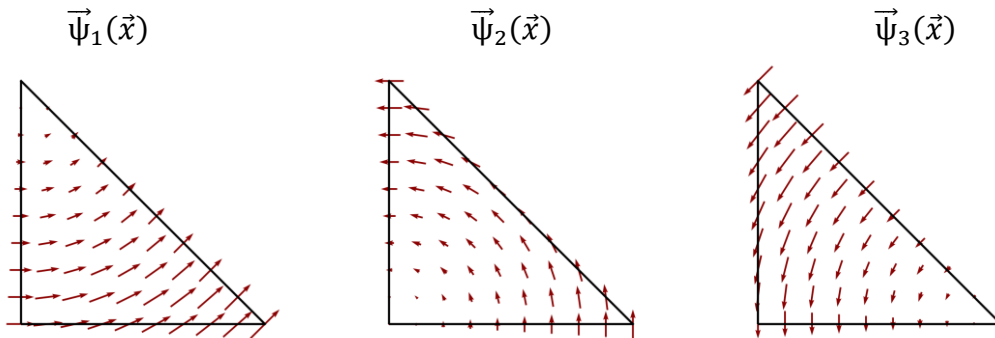


Fig. 2.4 Edge base functions in 2D for P_1 triangular element.

The Nedelec element the notable advantage of inherently ensuring the Coulomb gauge. For a detailed proof, refer to APPENDIX 7.3

$$\vec{\nabla} \cdot \vec{A} = 0 \quad (2.73)$$

The curl of the edges basis functions $\vec{\Psi}_e(\vec{x})$ is computed numerically as:

$$\vec{\nabla} \times \vec{\Psi}_e(\vec{x}) = 2\vec{\nabla}\varphi_i(\vec{x}) \times \vec{\nabla}\varphi_j(\vec{x}) \quad (2.74)$$

2.2.4 Weak formulation

Maxwell equations can be solved analytically for simple geometries and constant material properties. However, when dealing with complex system, analytical solutions become unattainable. Therefore, numerical approximation methods are essential for solving these equations over a discretized domain.

The most widely used method for this purpose is the finite element method, which was initially developed and applied extensively for structural analysis and has since found extensive application in other fields, including electromagnetic [15]. This method begins with the establishment of a weak formulation of the problem.

The first step involves defining functional spaces for gradient, divergence, and curl operators [18]. Let's assume that the domain Ω is closed and convex. The Sobolev spaces are mathematical vector spaces that form the foundation of finite element analysis for solving partial differential equations. These spaces characterize the regularity of the solution function (vector or scalar) and its derivative up to a certain order. They also define scalar product and norms for these functions and their derivatives.

Consider L^2 and \mathbf{L}^2 as the scalar and vector function spaces, respectively, which represents square-integrable functions over the domain Ω . In these spaces, a scalar inner product between two functions is defined as:

$$\int_{\Omega} u \cdot v \, d\Omega \quad \text{with } u \in L^2 \quad \text{et } v \in L^2 \quad (2.75)$$

$$\int_{\Omega} \mathbf{u} \cdot \mathbf{v} \, d\Omega \quad \text{with } \mathbf{u} \in \mathbf{L}^2 \quad \text{et } \mathbf{v} \in \mathbf{L}^2 \quad (2.76)$$

The set of \mathcal{H}^1 Sobolev spaces for scalar functions in the domain Ω , for which the gradient belongs to L^2 , is given by:

$$\mathcal{H}^1(\Omega) = \{u \in L^2(\Omega); \vec{\nabla}u \in \mathbf{L}^2(\Omega)\} \quad (2.77)$$

The \mathcal{H}^{curl} Space for vector functions with square-integrable curl is given by:

$$\mathcal{H}^{curl}(\Omega) = \{\mathbf{u} \in \mathbf{L}^2(\Omega); \vec{\nabla} \times \mathbf{u} \in \mathbf{L}^2(\Omega)\} \quad (2.78)$$

The \mathcal{H}^{div} Space for vector functions with square-integrable divergence is given by:

$$\mathcal{H}^{div}(\Omega) = \{\mathbf{u} \in L^2(\Omega); \vec{\nabla} \cdot \mathbf{u} \in L^2(\Omega)\} \quad (2.79)$$

The finite element method employs an internal approximation method (Galerkin), where the discretised solution is obtained by using a discretised version of the function space from the weak formulation. More specifically, the discretised function space is constructed using specific polynomial functions that go from 1 to 0 at the degrees of freedom associated with the finite element mesh.

After defining these spaces and considering the electromagnetic system given by the $(A - \phi)$ formulation:

$$\varepsilon_0 \varepsilon_r \frac{\partial^2 \vec{A}}{\partial t^2} + \sigma \frac{\partial \vec{A}}{\partial t} + \frac{1}{\mu_0} \left(\vec{\nabla} \times \frac{1}{\mu_r} \vec{\nabla} \times \vec{A} \right) + \varepsilon_0 \varepsilon_r \frac{\partial(\vec{\nabla}\phi)}{\partial t} + \sigma \vec{\nabla}\phi = 0 \quad (2.80)$$

$$\vec{\nabla} \cdot \sigma(\vec{\nabla}\phi) = 0 \quad (2.81)$$

where \vec{A} and ϕ are unknown variables, we can define the discretised quantities of the fields as $\vec{A}_h \in \mathcal{H}_h^{curl}$ and $\phi_h \in \mathcal{H}_h^{div}$. Then, the problem becomes:

Find $\vec{A}_h \in \mathcal{H}_h^{curl}$ and $\phi_h \in \mathcal{H}_h^{div}$, such that:

$$\varepsilon_0 \varepsilon_r \frac{\partial^2 \vec{A}_h}{\partial t^2} + \sigma \frac{\partial \vec{A}_h}{\partial t} + \frac{1}{\mu_0} \left(\vec{\nabla} \times \frac{1}{\mu_r} \vec{\nabla} \times \vec{A}_h \right) + \varepsilon_0 \varepsilon_r \frac{\partial(\vec{\nabla}\phi_h)}{\partial t} + \sigma \vec{\nabla}\phi_h = 0 \quad (2.82)$$

$$\vec{\nabla} \cdot \sigma(\vec{\nabla}\phi_h) = 0 \quad (2.83)$$

For all $\vec{\psi}_e \in \mathcal{H}_h^{curl}$ and $\varphi_n \in \mathcal{H}_h^{div}$ the above expression yield:

$$\langle \vec{\psi}_e, \varepsilon_0 \varepsilon_r \frac{\partial^2 \vec{A}_h}{\partial t^2} + \sigma \frac{\partial \vec{A}_h}{\partial t} + \frac{1}{\mu_0} \left(\vec{\nabla} \times \frac{1}{\mu_r} \vec{\nabla} \times \vec{A}_h \right) + \varepsilon_0 \varepsilon_r \frac{\partial(\vec{\nabla}\phi_h)}{\partial t} + \sigma \vec{\nabla}\phi_h \rangle = 0 \quad (2.84)$$

$$\langle \varphi_n, \vec{\nabla} \cdot \sigma(\vec{\nabla}\phi_h) \rangle = 0 \quad (2.85)$$

Then, by applying the first Green's vector theorem, we can simplify the double curl expression as follows:

$$\langle \vec{\psi}_e, \frac{1}{\mu_0} \vec{\nabla} \times \frac{1}{\mu_r} \vec{\nabla} \times \vec{A}_h \rangle = \frac{1}{\mu_0} \langle \vec{\nabla} \times \vec{\psi}_e, \frac{1}{\mu_r} \vec{\nabla} \times \vec{A}_h \rangle - \frac{1}{\mu_0} \int_{\Gamma} \vec{\psi}_e \cdot \left(\frac{1}{\mu_r} \vec{\nabla} \times \vec{A}_h \times \hat{n} \right) dS \quad (2.86)$$

Similarly, we apply the same principle to the electrical potential term:

$$\langle \varphi_n, \vec{\nabla} \cdot \sigma(\vec{\nabla}\phi_h) \rangle = \langle \vec{\nabla}\varphi_n, \sigma(\vec{\nabla}\phi_h) \rangle - \int_{\Gamma} \varphi_n (\sigma \hat{n} \cdot \vec{\nabla}\phi_h) dS \quad (2.87)$$

Using these transformations, the electromagnetic system can be rewritten as:

$$\begin{aligned} \langle \vec{\Psi}_e, \varepsilon_0 \varepsilon_r \frac{\partial^2 \vec{A}_h}{\partial t^2} \rangle + \langle \vec{\Psi}_e, \sigma \frac{\partial \vec{A}_h}{\partial t} \rangle + \frac{1}{\mu_0} \langle \vec{\nabla} \times \vec{\Psi}_e, \frac{1}{\mu_r} \vec{\nabla} \times \vec{A}_h \rangle - \frac{1}{\mu_0} \int_{\Gamma} \vec{\Psi}_e \cdot \left(\frac{1}{\mu_r} \vec{\nabla} \times \vec{A}_h \times \hat{n} \right) dS \\ + \langle \vec{\Psi}_e, \varepsilon_0 \varepsilon_r \frac{\partial(\vec{\nabla}\phi_h)}{\partial t} \rangle + \langle \vec{\Psi}_e, \sigma \vec{\nabla}\phi_h \rangle = 0 \end{aligned} \quad (2.88)$$

$$\langle \vec{\nabla}\varphi_n, \sigma(\vec{\nabla}\phi_h) \rangle - \int_{\Gamma} \varphi_n (\sigma \hat{n} \cdot \vec{\nabla}\phi_h) dS = 0 \quad (2.89)$$

To solve this problem, we make the following assumptions:

- The electric potential is defined based on the input and output potential conditions, as specified in equations (2.65) and (2.66)
- Electric flow is exclusively allowed on surfaces associated with Γ_{inp}^I and Γ_{out}^I . This restriction is expressed mathematically as:

$$\int_{\Gamma} \varphi_n (\sigma \hat{n} \cdot \vec{\nabla}\phi_h) dS = 0 \quad (2.90)$$

- The boundary condition expressed in (2.61) is the only employed to permit the outward flow of the magnetic field:

$$\frac{1}{\mu_0} \int_{\Gamma} \vec{\Psi}_e \cdot \left(\frac{1}{\mu_r} \vec{\nabla} \times \vec{A}_h \times \hat{n} \right) dS = 0 \quad (2.91)$$

By considering these assumptions, the electromagnetic system is reformulated as follows:

$$\begin{aligned} \langle \vec{\Psi}_e, \varepsilon_0 \varepsilon_r \frac{\partial^2 \vec{A}_h}{\partial t^2} \rangle + \langle \vec{\Psi}_e, \sigma \frac{\partial \vec{A}_h}{\partial t} \rangle + \frac{1}{\mu_0} \langle \vec{\nabla} \times \vec{\Psi}_e, \frac{1}{\mu_r} \vec{\nabla} \times \vec{A}_h \rangle + \langle \vec{\Psi}_e, \varepsilon_0 \varepsilon_r \frac{\partial(\vec{\nabla}\phi_h)}{\partial t} \rangle \\ + \langle \vec{\Psi}_e, \sigma \vec{\nabla}\phi_h \rangle = 0 \end{aligned} \quad (2.92)$$

$$\langle \vec{\nabla}\varphi_n, \sigma(\vec{\nabla}\phi_h) \rangle = 0 \quad (2.93)$$

The expression (2.92) constitutes the general electromagnetic equation employed in this work. Where $\vec{\Psi}_e$ and φ_n are the basis functions of the problem, and equation (2.93) defines the electric potential equation within the coil domain.

2.2.5 Discretised formulation

The weak formulations of the electromagnetic system and the electric potential, as given in equations (2.92) and (2.93) are discretized using the approximation defined in equations (2.94) and (2.95):

$$\phi(t, \vec{x}) \approx \phi_n(t, \vec{x}) = \sum_n \phi_n(t) \varphi_n(\vec{x}) \quad (2.94)$$

$$\vec{A}(t, \vec{x}) \approx \vec{A}_n(t, \vec{x}) = \sum_e a_e(t) \vec{\Psi}_e(\vec{x}) \quad (2.95)$$

The discretized equations for the magnetic and electric potentials can be obtained as follows.

$$\begin{aligned} \langle \vec{\Psi}_e, \epsilon_0 \epsilon_r \vec{\Psi}_e \rangle \frac{\partial^2 \{a_e\}}{\partial t^2} + \langle \vec{\Psi}_e, \sigma \vec{\Psi}_e \rangle \frac{\partial \{a_e\}}{\partial t} + \frac{1}{\mu_0} \langle \vec{\nabla} \times \vec{\Psi}_e, \frac{1}{\mu_r} \vec{\nabla} \times \vec{\Psi}_e \rangle \{a_e\} \\ + \langle \vec{\Psi}_e, \epsilon_0 \epsilon_r \vec{\nabla} \varphi_n \rangle \frac{\partial \{\phi_n\}}{\partial t} + \langle \vec{\Psi}_e, \sigma \vec{\nabla} \varphi_n \rangle \{\phi_n\} = 0 \end{aligned} \quad (2.96)$$

$$\langle \vec{\nabla} \varphi_n, \sigma \vec{\nabla} \varphi_n \rangle \{\phi_n\} = 0 \quad (2.97)$$

2.2.6 Boundary element method (BEM)

The Boundary Element Method (BEM) is a numerical technique employed to solve partial differential equations (PDEs) and integral equations. Unlike the Finite Element Method (FEM) that discretizes the entire domain, BEM specifically focuses on discretizing only the boundaries of the problem domain. It operates on the principle that the solution to a PDE can be expressed as an integral over the domain's boundary. By dividing the boundary into elements and approximating the solution using basis functions, the integral equation can be effectively solved through numerical methods.

One notable advantage of BEM is its ability to reduce the dimensionality of the problem by eliminating the need to discretize the entire domain. This reduction brings significant computational savings. BEM is particularly well-suited for problems featuring homogeneous boundary conditions or when the solution is primarily concentrated on the boundary.

This approach is often used in electromagnetic problems to perform the coupling between the different conductive part avoiding meshing the space in-between (usually air) whilst the other domains are represented using FEM [19]. Although not meshing the air space

simplifies the tracking of solid body movements, it also introduces complexities in the numerical resolution of the electromagnetic problem. One key consideration is that the BEM generates fully connected matrices, which can make them more challenging to solve [20], despite having a smaller number of degrees of freedom. Additionally, managing these matrices becomes even more complicated in parallel computations. Furthermore, the BEM approach can pose difficulties when dealing with symmetry planes.

2.2.7 Fully immersed finite elements approach

The Immersed Finite Element Method (IFEM) is a numerical technique employed in electromagnetic modeling [21] and is currently used in our simulations.

The IFEM approach involves discretizing the computational domain using a single computational mesh that encompasses the entire domain, including conductive parts, inductors, and the air domain. This computational mesh serves as a framework for solving the electromagnetic problem as a unified system. Rather than using separate meshes for each component. The immersed parts, such as conductive parts or inductors, are identified within the computational mesh using their specific material properties.

By solving the entire system as a whole, a sparse symmetric linear system of equations is obtained. This system can be efficiently solved using various Krylov subspace solvers such as PCCG, GMRES, and others. The equations governing electromagnetic fields are solved on the whole mesh, while any discontinuities in material properties or magnetic fields at domain interfaces are naturally handled, as demonstrated in [22] and [23]. Moreover, the IFEM approach enables the consideration of solid body movements, including displacements and deformations, as well as adaptive mesh refinement, as described in [24],[25] and [26]. Fig. 2.5 shows a typical induction heating configuration in IFEM.

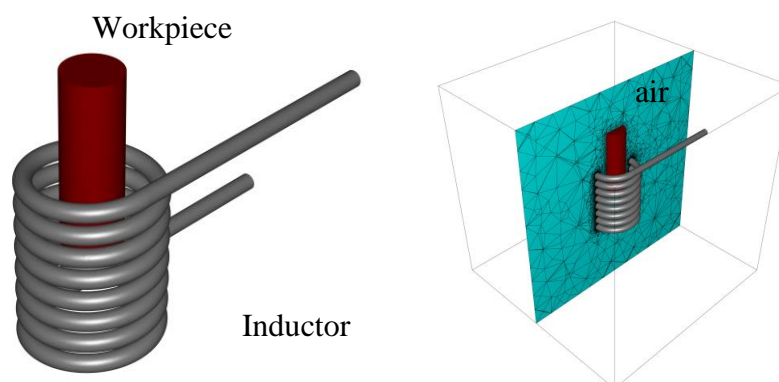


Fig. 2.5 domain simulated: Workpiece-Inductor-Surrounding air

2.2.8 Time integration

2.2.8.1 Electromagnetic resolution

In electromagnetic computations, there are two common approaches to handling the time-dependency of solutions. The first numerical approach employs a harmonic approximation to solve the electromagnetic problem in the frequency domain, which implies transforming all fields into complex-valued representations. This method is suitable for problems involving a single perfectly harmonic sinusoidal signal or a finite summation of harmonic signals with constant material properties, as it does not incur any loss of accuracy ([27],[28],[29],[30]). However, from a physical standpoint, its main drawback lies in the fact that the entire system responds with the same pulsation. Consequently, this approach is not well-suited for scenarios involving magnetic materials. It remains valid for linear magnetic materials and loses accuracy when dealing with non-linear magnetic materials [31], where the electromagnetic field solution can exhibit non-sinusoidal time evolution due to additional harmonics. Moreover, from a numerical standpoint, solving the complex valued problem can be challenging, given that the resulting matrix has a very large sparsity pattern.

The second approach involves a direct time resolution of the Maxwell equations. In this method, any arbitrary input signal is discretised performed discretising the input current signal over time steps by breaking down the input current signal into time steps.

Marioni et al. [30] conducted a comparative analysis of these approaches, specifically examining the computational time required for each. The study revealed that the conditioning of the harmonic problem can significantly impact computational costs. Showing that the time required to solve the harmonic problem alone exceeds the time needed to solve multiple increments in the time approach. Additionally, a time resolution offers some others advantages, especially when dealing with non-linear materials and electromagnetic field distortions [32]. The ability to use arbitrary input signals overcomes the limitations of the harmonic problem, enabling the proper simulation of multi-frequency signals. As a result, the model used in this work is discretized over the time domain.

We can now proceed by starting from the discretised equations (2.96) and (2.97) and defining each individual term as a function of the material properties:

$$M(\varepsilon) = \varepsilon_0 \langle \vec{\Psi}_e, \varepsilon_r \vec{\Psi}_e \rangle \quad (2.98)$$

$$C(\sigma) = \langle \vec{\Psi}_e, \sigma \vec{\Psi}_e \rangle \quad (2.99)$$

$$K(\mu) = \frac{1}{\mu_0} \langle \vec{\nabla} \times \vec{\Psi}_e, \frac{1}{\mu_r} \vec{\nabla} \times \vec{\Psi}_e \rangle \quad (2.100)$$

$$F(\varepsilon) = \langle \vec{\Psi}_e, \varepsilon_0 \varepsilon_r \vec{\nabla} \varphi_n \rangle \quad (2.101)$$

$$Q(\sigma) = \langle \vec{\Psi}_e, \sigma \vec{\nabla} \varphi_n \rangle \quad (2.102)$$

$$G(\sigma) = \langle \vec{\nabla} \varphi_n, \sigma \vec{\nabla} \varphi_n \rangle \quad (2.103)$$

The discretized formulation is reformulated as:

$$M(\varepsilon) \frac{\partial^2 \{a_e\}}{\partial t^2} + C(\sigma) \frac{\partial \{a_e\}}{\partial t} + K(\mu) \{a_e\} + F(\varepsilon) \frac{\partial \{\phi_n\}}{\partial t} + Q(\sigma) \{\phi_n\} = 0 \quad (2.104)$$

$$G(\sigma) \{\phi_n\} = 0 \quad (2.105)$$

As the electric conductivity depends solely on temperature, the electric potential ϕ calculation is independent of the magnetic vector potential \vec{A} . Therefore, the solution of the system (2.104) - (2.105), is computed in a decoupled manner:

1. First, the electric potential is solved only within the inductor domain:

$$\begin{cases} G(\sigma) \{\phi_n\} = 0 & \text{in } \Omega_I^h \\ \phi_i = V & \text{on } \Gamma_{inp}^I \\ \phi_i = 0 & \text{on } \Gamma_{out}^I \end{cases} \quad (2.106)$$

2. Then, the magnetic potential is solved throughout the entire domain, using the electric potential as the source term. By reorganizing expression (2.104) and shifting the source term to the left-hand side of the equation:

$$\begin{cases} M(\varepsilon) \frac{\partial^2 \{a_e\}}{\partial t^2} + C(\sigma) \frac{\partial \{a_e\}}{\partial t} + K(\mu) \{a_e\} = -F(\varepsilon) \frac{\partial \{\phi_n\}}{\partial t} - Q(\sigma) \{\phi_n\} & \text{in } \Omega^h \\ a_i = 0 & \text{on } \Gamma_B \end{cases} \quad (2.107)$$

Typically, most electromagnetic material processes occur at low to medium frequencies ($< 1\text{MHz}$), thus enabling to neglect the current displacements density term $\partial_t \vec{D}$ (quasi-steady state approximation). Then, for this purpose, the discretised equation can be rewritten as:

$$\begin{cases} C(\sigma) \frac{\partial \{a_e\}}{\partial t} + K(\mu) \{a_e\} = -Q(\sigma) \{\phi_n\} & \text{in } \Omega^h \\ a_i = 0 & \text{on } \Gamma_B \end{cases} \quad (2.108)$$

2.2.8.2 Time integration schema

One of the key aspects in modelling evolution problems is the proper discretisation of time dependence. To maintain accuracy and stability and minimize the divergence between the numerical approximation and the “real” solution, it's essential to use a robust time integration method. This work employs a family of second-order time integration schemes, previously introduced for the thermal problems and later extended to electromagnetic problems, as

described in equation (2.109). A detailed description can be found in [33],[34]. Here, a brief overview of the method is provided.

The system of ordinary differential equations is given as:

$$C \frac{\partial X}{\partial t} + KX = Q \quad (2.109)$$

It is required to compute X at a future time t_{n+1} assuming all state and input fields are known at the current time t_n and a past time t_{n-1} , where $t_{n+1} > t_n > t_{n-1}$, $\Delta t = t_{n+1} - t_n$ and $\Delta t_0 = t_n - t_{n-1}$ are the current and previous time steps. An asynchronous time concept is also introduced, as depicted in Fig. 2.6.

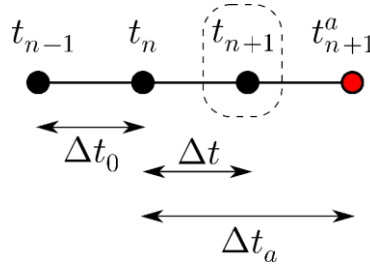


Fig. 2.6 Discretization of time in the asynchronous time-integration approach

The discretization and equilibrium are established at a virtual time as follows:

$$t^* = \alpha_1 t_{n-1} + \alpha_2 t_n + \alpha_3 t_{n+1}^a; \quad \alpha_1 + \alpha_2 + \alpha_3 = 1 \quad (2.110)$$

$$X^* = \alpha_1 X_{n-1} + \alpha_2 X_n + \alpha_3 X_{n+1}^a \quad (2.111)$$

$$C \frac{\partial X}{\partial t} = (1 - \gamma) \frac{X_n - X_{n-1}}{\Delta t_0} + \gamma \frac{X_{n+1}^a - X_n}{\Delta t_a} \quad (2.112)$$

$$C^* \frac{\partial X^*}{\partial t} + K^* X^* = Q^* \quad (2.113)$$

The linear system is assembled as:

$$\left[C^* + \frac{\alpha_3}{\gamma} \Delta t_a K^* \right] X^* = \frac{\alpha_3}{\gamma} \Delta t_a Q^* + C^* \left[\left(\alpha_2 + \frac{\Delta t_a}{\Delta t_0} (\gamma - 1) \frac{\alpha_3}{\gamma} + \alpha_3 \right) X_n + \left(\alpha_1 - \frac{\Delta t_a}{\Delta t_0} (\gamma - 1) \frac{\alpha_3}{\gamma} \right) X_{n-1} \right] \quad (2.114)$$

The actual solution at t_{n+1} is re-interpolated:

$$X_{n+1} = \frac{\Delta t}{\alpha_3 \Delta t_a} X^* + \left(1 - \left(1 + \frac{\alpha_2}{\alpha_3} \right) \frac{\Delta t}{\Delta t_a} \right) X_n - \frac{\alpha_1}{\alpha_3} \frac{\Delta t}{\Delta t_a} X_{n-1} \quad (2.115)$$

For practical purposes, $\Delta t_a = \Delta t$ is used, meaning there are four numerical parameters to define the integration scheme. The method is considered:

- unconditionally stable if

$$\gamma \geq \frac{1}{2}; \alpha_1 > \frac{1}{2}(1 - \gamma) \quad (2.116)$$

- and consistent if

$$\alpha_2 = 1 - \alpha_1 + \left(\frac{1}{2} - \alpha_1\right) \frac{\Delta t_a}{\Delta t} - \frac{\gamma}{2} \left(1 + \frac{\Delta t_a}{\Delta t}\right) \quad (2.117)$$

$$\alpha_3 = \left(\alpha_1 - \frac{1}{2}\right) \frac{\Delta t_a}{\Delta t} + \frac{\gamma}{2} \left(1 + \frac{\Delta t_a}{\Delta t}\right) \quad (2.118)$$

In order to satisfy both conditions, there are only two free numerical parameters from where to choose α_1 and γ . Otherwise, the consistency condition can be violated, as it is the case for the classical Euler implicit method (Table 2.1).

Table 2.1

List of some known time-integration schemes that can be derived from the proposed method.

Name	γ	α_1	α_2	α_3
Euler Implicit	1	0	0	1
Crank-Nicholson	1	0	1/2	1/2
Dupont-Implicit	3/2	0	0	1
Lees	1/2	1/3	1/3	1/3

2.3 Multiphysics coupling

In most electromagnetic coupled processes, the electromagnetic force plays a significant role as the driving force. As a result, most coupling procedures typically initiate by solving the electromagnetic equation as a primary step before coupling it to other physics.

2.3.1 Characteristic times involved

The time scales of electromagnetic phenomena can significantly differ from those of other physics involved in various applications. For instance, in Induction Heating (IH), the electromagnetic period can range from 10^{-2} s to the 10^{-6} s, covering frequencies from 100Hz and 1MHz, while heat diffusion occurs on a much large scale, typically in seconds [1]. In Magnetic Pulse Forming (MPF), shock-wave mechanics operate at nanosecond (10^{-9} s) timescales during impact conditions, whereas the electromagnetic wave problem remains in the microsecond (10^{-6} s) range [35]. In Electromagnetic Stirring (EMS), the frequencies typically range around a few Hertz (from 2Hz to 10Hz), meaning the electromagnetic problem operates on a timescale of about 0.1 seconds, while vorticity issues in fluid flow can occur at orders of magnitude ranging from 10^{-3} s to several seconds.[3]

In order to accuracy model these processes and properly couple the physics involved, considerations regarding the characteristic time scales have to be taken into account. Two main cases can be identified, which are explained in detail in Fig. 2.7.

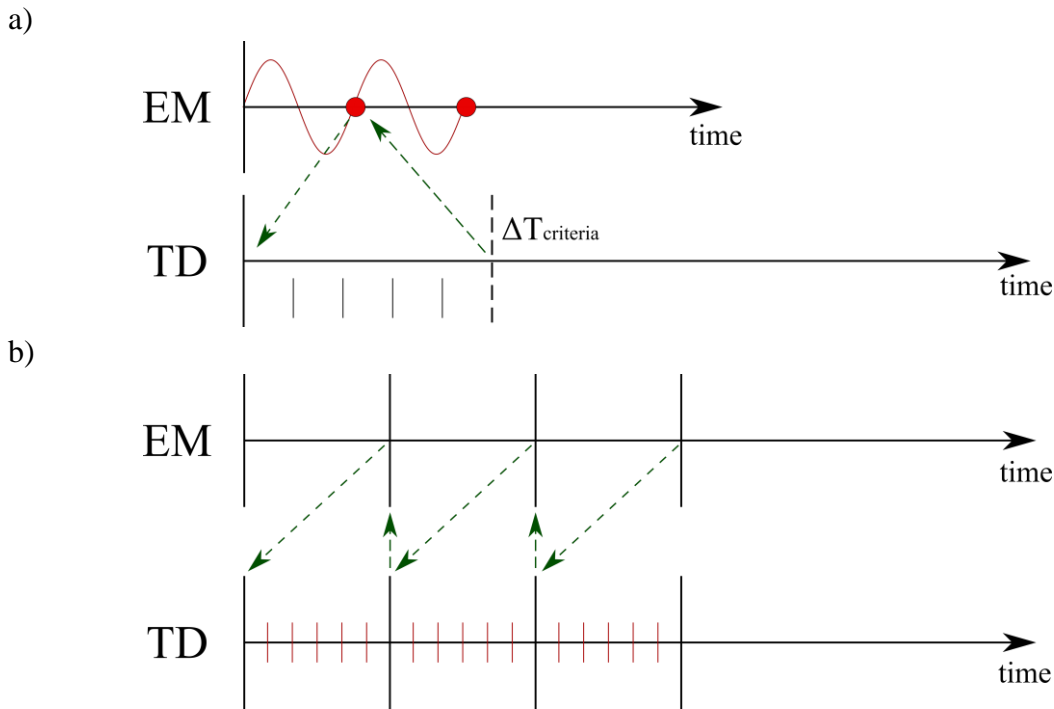


Fig. 2.7 Coupling schemes: a) periodic coupling and b) incremental coupling. EM: electromagnetics and TD: thermo-dynamics

On one hand, the periodic scheme shown in Fig. 2.7.a considers two main factors when solving the coupled problem:

- The temperature remains constant during the electromagnetic period.
- The Joule heating effect phenomenon and the Lorentz force are averaged over the electromagnetic period.

The electromagnetic model is solved periodically using this scheme. The electromagnetic period is divided into time steps, and at each time step, the electromagnetic equation (2.96) is solved using the time integration scheme introduced in section 2.2.8. Computation continues until convergence is achieved over the period. This approach is used to solve the induction heating problem.

On the other hand, the incremental scheme allows for direct coupling of the physics after solving a time increment computation of the electromagnetic solver. This scheme is employed in simulating the magnetic pulse forming process, which enables taking into account the characteristic time scale of the phenomenon.

For EMS, the choice of scheme depends on the relative time scales of the EM force and the turnover time of the turbulent structure. If the period of the EM force is of the same order of magnitude as the turnover time, the transient part will affect the turbulence structure, and an incremental coupling shall be used. Conversely, if the time scale of the EM force is smaller than the turbulence time scale, only the average part of the force will affect the flow, and a periodic coupling scheme is employed.

The power density dissipated through Joule effect and Lorentz force are crucial quantities utilized in the coupling process. In the electromagnetic model, these quantities can be calculated as follows: The power resulting from Joule effect is determined using the equation:

$$\dot{Q}_e = \vec{E} \cdot \vec{J} \quad (2.119)$$

For the periodic scheme, a time average over the period needs to be calculated. This can be computed at each point within the domain by:

$$\dot{Q}_e = \frac{1}{t_p - t_0} \int_{t_0}^{t_p} \vec{E} \cdot \vec{J} dt \quad (2.120)$$

Where t_p represents the period of the electromagnetic wave. Lorentz force is computed using the equation:

$$\vec{F}_L = \rho^e (\vec{E} + \vec{v} \times \vec{B}) \quad (2.121)$$

Where ρ^e represents a distribution of charges. Then, the time average at each point within the domain is given by:

$$\vec{F}_L = \frac{1}{t_p - t_0} \int_{t_0}^{t_p} \rho^e (\vec{E} + \vec{v} \times \vec{B}) dt \quad (2.122)$$

2.3.2 Coupling scheme

The Multiphysics coupled integration scheme is illustrated in Fig. 2.8, depicting the flow of information between the solvers. In this scheme, the EM solver provides the source term for the Solid/Fluid mechanics solver. This source term can be either the power dissipated due to Joule effect or the Lorentz force. Conversely, the EM solver receives input from the Solid/Fluid mechanics solver, which includes temperature data for updating material properties and the new coordinates of the pieces for updating shape and position.

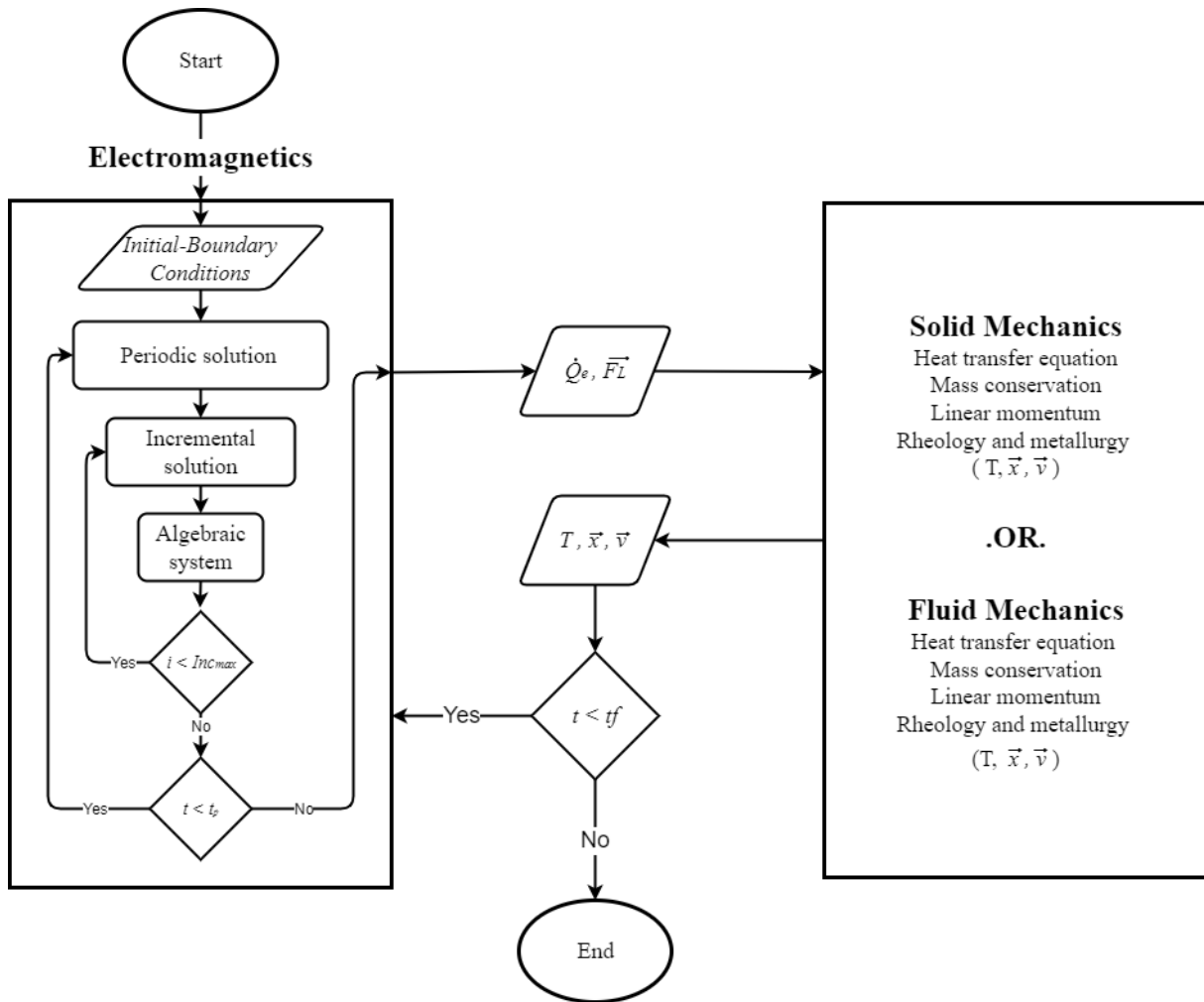


Fig. 2.8 Coupling scheme of the Multiphysics problem.

The temperature plays a key role in terms of material property variations. In fact, magnetic properties of materials often exhibit temperature-dependent behaviour. This dependence can lead significant changes in the electromagnetic characteristics of material, such as transitioning from ferromagnetic to paramagnetic states at the Curie temperature. Additionally, the phases motion, such as free surface fluctuation or phase change, can also exert an influence on electromagnetic properties, resulting in substantial variations within regions undergoing phase/material changes. After each coupling with the solid/fluid mechanics model, the material properties are recalculated for input into the electromagnetic model.

Considering the strong influence of temperature, a coupling criterion is established based on differences in material properties concerning temperature. This criterion is applied to the solid/fluid mechanics model, triggering a re-launch of the EM simulation when necessary.

2.4 R-adaptation

R-adaptation involves adjusting the positions of the nodes within the mesh while preserving the same topology, meaning that no new mesh is generated; rather, only the nodes positions are altered. This approach is suitable for scenarios involving minor deformations, such as thermal expansion or small parts displacements. However, the problem arises when the change is large enough to create a distortion of the mesh elements. In such case, the creation of a new mesh becomes necessary. A common methodology after r-adaptation is to evaluate the quality of the element, and if the quality falls below a predefined threshold, a new mesh will be generated. Fig. 2.9 illustrated the r-adaptation principle, where a displacement is performed in the ring, impacting only the coordinates of the nodes.

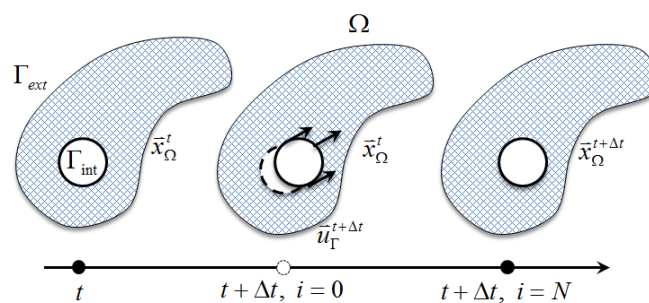


Fig. 2.9 R-adaptation principle [2]

In electromagnetic modelling, when employing a fully immersed finite element approach, the surrounding air must follow the motion applied to the components.

2.5 Field transport procedure in electromagnetic modelling

Field transport is a fundamental step in finite element simulations facing large deformations and hence use remeshing steps. In the current electromagnetic solver implementation, it is used in two different scenarios:

- 1) Remeshing of the AM mesh to recover the information of the previous mesh:
 - a. Magnetic vector potential \vec{A} or electric scalar potential ϕ from previous time steps.
 - b. Other fields such as Magnetic field \vec{H} , magnetic flux density \vec{B} or electric current density \vec{J}
- 2) Coupling step with thermo-mechanics (since different meshes are used for each physics) to recover:
 - a. Temperature
 - b. Displacement
 - c. Velocity

2.5.1 Transport strategies

In finite element methods, when a geometry undergoes topological modifications, it becomes necessary to transfer the information from the old mesh to the new mesh. This process is accomplished through a transport strategy, which is determined based on the type of field being considered and its geometric representation. Fig. 2.10 illustrates the different types of fields available in our finite element library.

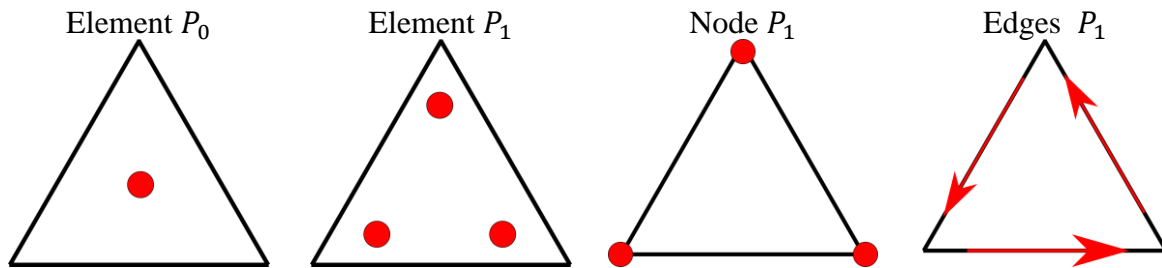


Fig. 2.10 Type of fields in the library

As displayed in Fig. 2.10 fields can be represented in different ways. They can be stored as elementwise values (P_0) at the barycentre of each element or as linear valued (P_1) at Gauss integration points, nodes and edges. For the fields stored in the gauss points and nodes, the transportation of these fields from one mesh to another follows a basic strategy, as depicted in Fig. 2.11. When transporting a P_1 field from the original mesh to a target mesh, a linear interpolation is employed. On the other hand, in the case of P_0 fields, the value of the closest element in the target mesh is assigned to the corresponding element in the original mesh.

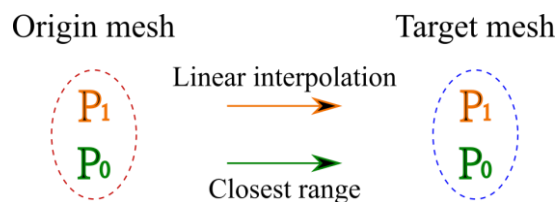


Fig. 2.11 Basic transport method

In the electromagnetic formulation, are computed using edge elements, which presents a challenge when it comes to transporting these values between meshes. This is due to the fact that a single edge in the original mesh may traverse multiple elements in the target mesh. To address this, a mapping procedure is employed, as illustrated in Fig. 2.12. The procedure involves three steps:

- Transformation from edges to integration points: Initially, the edge values are transformed to the corresponding integration points on the elements.
- Transport from the old mesh to the new mesh: The values are then transported from the original mesh to the target mesh, using a linear interpolation method.

- Transformation from integration points to edges: Finally, the transported values are mapped back from the integration points to the edges in the target mesh.

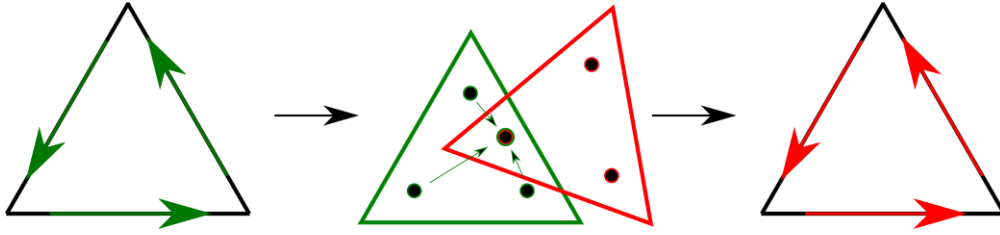


Fig. 2.12 Edges field transport procedure.

In order to perform the last step of the procedure described above, a minimisation problem is solved, involving the field at the integration points in both the target and original mesh. Let $\vec{A}^*(\vec{x})$ represent the field in the new mesh and $\vec{A}(\vec{x})$ the field in the old mesh. The minimisation problem is then expressed as:

$$\min \|\vec{A}^*(\vec{x}) - \vec{A}(\vec{x})\|^2 \quad (2.123)$$

The solution is obtained through the following steps:

2.5.1.1 Transformation from edges to integration points.

This first step involves using the edge basis functions, denoted as $\vec{\psi}_e(\vec{x})$, which were defined in section 2.2.3. Let a_e represent the value of the field at the edge e and $\vec{A}(\vec{x})$ the value at any point inside the element in the original mesh. The values at the Gauss integration points can be then computed as follows:

$$\vec{A}(\vec{x}) = \sum_e a_e \vec{\psi}_e(\vec{x}) \quad (2.124)$$

2.5.1.2 Transport from the old mesh to the new mesh.

The second step involves localizing the integration point of the target element on the original mesh. Once the element in the original mesh is identified, the field in the target element, denoted as $\vec{A}^*(\vec{x})$, can be computed using the following expression:

$$\vec{A}^*(\vec{x}) = \sum_g \omega_g \vec{A}(\vec{x})_g \quad (2.125)$$

Where ω_g represents the weights associated with the integration point of the element in the original mesh. The weights depend on the relative coordinates of the point being calculated in the target element.

2.5.1.3 Transformation from integration points to edges.

The field in the target mesh can be represented by its respective values at the edge of the element using equation (2.124).

$$\vec{A}^*(\vec{x}) = \sum_j a_j^* \psi_j^* \quad (2.126)$$

Where (j) represent the index of the edge in the element. The minimisation problem is then solved projecting it onto the basis function of the target mesh, resulting in the following expression:

$$\left\langle \sum_j a_j^* \psi_j^* - \vec{A}^*(\vec{x}), \psi_k^* \right\rangle = 0 \quad (2.127)$$

By reordering this expression, the following linear system is obtained:

$$\sum_j \langle \psi_j^*, \psi_k^* \rangle a_j^* = \langle \vec{A}^*(\vec{x}), \psi_k^* \rangle \quad (2.128)$$

Solving this linear system allows us to find the values on each edge of the mesh.

2.6 Parallel paradigm

The parallel paradigm used in Forge® is based on the Single Program Multiple Data (SPMD), where the same program runs on different data. This means that for a mesh partition as shown in Fig. 2.13, each processor executes a separate full version of the code. At the same time, information can be shared between processors with specific synchronization operations. In this parallel architecture, the nodes and edges of the element are shared between several processors, while the volumetric element only belongs to a single partition. This can be clearly seen in Fig. 2.13, where the colours represent the different partitions of the mesh. For more information, see [2] and [36]

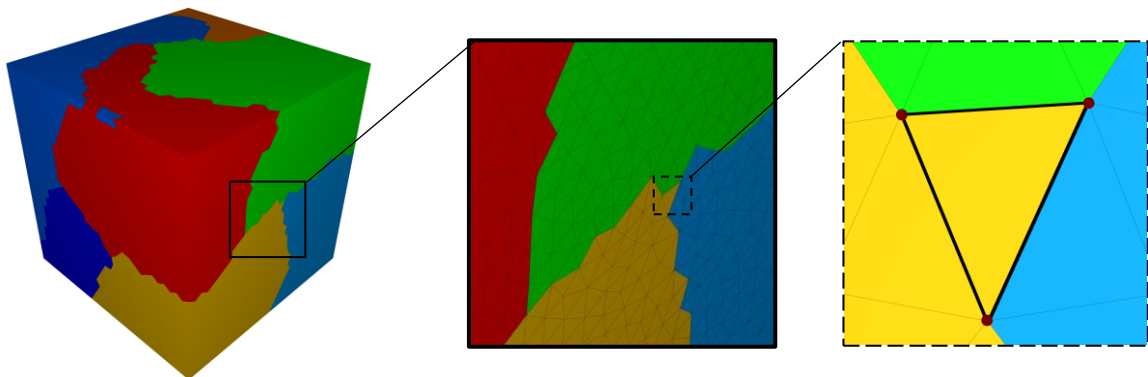


Fig. 2.13 Mesh partitioning in Forge®

Chapter 3

Error estimators

3.1	Introduction	62
3.2	Electromagnetic-coupled processes modelling.....	62
3.3	Finite elements and a posteriori error estimators	62
3.3.1	<i>A priori</i> error estimators	65
3.3.2	<i>A posteriori</i> error estimates	65
3.3.2.1	Residual-based estimators	66
3.3.2.2	Equilibrated estimators	66
3.3.2.3	Recovery-based estimators	66
3.3.2.4	Error based on dual problem	67
3.4	Recovery based – Galerkin method	68
3.4.1	Superconvergent Patch Recovery vs Galerkin-based Recovery for building a smoothed solution	68
3.4.1.1	On the interpolation enrichment potential	69
3.4.1.2	On the geometrical pathologies and convergence risks.....	69
3.4.1.3	On solver implementation	70
3.4.2	Estimator based on a recovered smooth vector field.....	70
3.5	Physics-specific estimators alternatives.....	71
3.5.1	Estimator based on the derived current density	72
3.5.2	Estimator based on the verification of Faraday’s Induction Law	72
3.5.3	Estimator based on the verification of Ampere’s Law.....	72
3.5.4	Estimator based on fundamental conservation principle.....	74
3.6	Analysing, scaling, and normalizing estimator results.....	76
3.7	Validation and analysis on semi-analytical cases.....	78
3.7.1	Validation by comparison with an analytical solution	78
3.7.2	Convergence rate analysis	79
3.7.3	Application to the TEAM7 benchmark case	81
3.7.3.1.1	Convergence with mesh size.....	82
3.7.3.1.2	Comparison of computational times	88
3.7.3.1.3	Considering magnetic permeability variation due to the magnetic field and time-averaging estimator.	89

3.7.4	Heat treatment case	91
3.7.5	Magnetic pulse forming case.....	93
3.7.6	Electromagnetic stirring case	95
3.8	Conclusions.....	97

Résumé : Estimateurs d'erreur a posteriori pour la modélisation électromagnétique.

Ce chapitre se concentre sur le premier pas de l'adaptation de maillage en éléments finis, qui consiste à développer des estimateurs d'erreurs permettant d'identifier les zones à adapter dans le domaine discrétisé.

Tout d'abord, une bibliographie des estimateurs d'erreur a posteriori implémentés dans la modélisation électromagnétique est présentée. Ensuite, un estimateur d'erreur basé sur la méthode variationnelle de Galerkin est développé. À partir de cet estimateur, des estimateurs additionnels sont également développés en se basant sur le comportement physique du phénomène électromagnétique :

- Dérivation de la densité de courant
- Vérification de la loi de Faraday
- Vérification de la loi d'Ampère
- Et enfin, un estimateur basé sur un principe fondamental de conservation du calcul.

De plus, une normalisation est conçue pour comparer les différences entre les estimateurs.

Une validation de l'estimateur par recouvrement est effectuée en résolvant un cas analytique et en comparant l'erreur exacte de la solution numérique avec l'estimateur d'erreur. Finalement, les estimateurs sont testés sur des cas purement électromagnétiques ainsi que sur des cas d'application industrielle.

3 Error estimators

3.1 Introduction

Electromagnetic material processing frequently involves parts with complex geometries and materials with non-linear magnetic properties. Effectively modelling these processes can be computationally intensive, demanding significant CPU time and resources. Furthermore, computer models often lack error information for the final results. Consequently, the development of error estimators capable of handling complex geometries and multiphysics interactions is of utmost importance. These estimators can provide users with information on the accuracy as well as enable to reach a good compromise between the resources available and the accuracy aimed at. This chapter aims at going beyond some of the restrictions commonly found in the error estimators, such as simplified geometries and harmonic approximation. Instead, they will be suited to the fully immersed computational model developed here, enabling remeshing in both the air domain and the involved conducting materials.

3.2 Electromagnetic-coupled processes modelling

Continuous improvement of processing units (CPUs/GPUs) and availability of HPC infrastructures, computational models are expected to become more realistic and accurate. However, this comes at the price of increasingly complex models. In order to reduce the concept-to-production time by improving the engineering design phase, one of the key challenges and opportunities for improvement of numerical methods is to automatize mesh generation and adaptation. Before addressing automatic remeshing, it is required to tackle the error estimation problem for the electromagnetic simulation as from here it will be possible to build the required tools for automatic remeshing. It means that regions with larger than average error estimation will be refined and regions less affected by numerical error will enable coarsening of the mesh to optimize accuracy as well as computational time. Therefore, this chapter will focus on the development of a posteriori error estimators, with an especial focus on electromagnetic fields accuracy.

3.3 Finite elements and a posteriori error estimators

Powerful modern computers and efficient numerical procedures now make it possible to transform any physical phenomenon into engineering simulations to predict real situations. However, even with the best mathematical models, computational results always contain numerical errors. These errors give the information about the accuracy of the solution obtained

with the numerical procedure. For this reason, a mathematical theory for the estimation and quantification of error in numerical simulation is so important. In fact, in finite element method knowledge of the error, its magnitude and its distribution provide the initial basis of adaptive control of the simulation. This adaptive procedure can range from changing the discretization mesh or the choice of the algorithm to improving computation efficiency.

Numerical error in FEM computation has been a major source of research since the beginning of computer simulations of physical phenomena. In finite element methods, partial differential equations involved in mathematical models are first transformed from local equations of physical phenomena into a global weak formulation, and then discretized in space by means of Galerkin method. Nonetheless, the discretisation procedure induces an intrinsic loss of accuracy, and is thus one of the sources for numerical errors. All the information contained in these complex models cannot be accurately captured by the discretization process alone. Consequently, it becomes imperative to estimate, control, and minimize numerical errors, as it enables a first level of uncertainty quantification.

During the numerical simulation of a physical problem, several sources of error can be distinguished, which cause the obtained solution to differ from the exact solution of the studied problem. The main sources of error are:

- Choice of the mathematical model: which may neglect any particular physical phenomena.
- Spatial discretization of the problem: Intrinsic in finite element method, which depends on the mesh size.
- Numerical resolution: numerical integration errors related to the choice of the integration scheme, rounding error, etc.
- Time discretisation: choice of time step and integration methods.

In this section, we shall focus on the space discretization error, which can be defined as:

$$\epsilon = u - u_h \quad (3.1)$$

Where u represents the exact solution, and u_h is the solution computed with the finite element approach. To provide a more comprehensive evaluation, a norm is used to measure the difference of those two functions. Then, for any square-integrable function u or u_h defined on a domain Ω , the L_2 - norm is defined as:

$$\|u\|_{L_2(\Omega)} = \left(\int_{\Omega} |u|^2 dV \right)^{1/2} \quad (3.2)$$

This enables to express the error within an a L_2 - norm as:

$$\epsilon = \|u - u_h\|_{L_2(\Omega)} \quad (3.3)$$

This spatial discretization error is directly related to the convergence of the finite element method. Indeed, different works collected on Babuska and Aziz [37] give as a result the following expression:

$$\|u - u_h\|_{L_2(\Omega)} \leq C \inf_{v_h \in V_h} \|u - v_h\|_{L_2(\Omega)} \quad (3.4)$$

Here, v_h is a variational function within the approximation space V_h , and C is a constant that remains independent of V_h . Under the condition of sufficient regularity on the solution u , it becomes possible to define an upper-bound on right-side of the expression (3.4) as follows:

$$\|u - u_h\|_{L_2(\Omega)} \leq C h^p \|u'\|_{L_2(\Omega)} \quad (3.5)$$

Here, $p = k + 1 - m > 0$ is the rate of convergence, where k represents the order of the finite element basis functions, m stands for the order of the highest derivative of the solution ($m = 0$ in the L_2 - norm), h denotes the discretised element size, and C a positive constant independent of both the solution u and h . This estimate implies that if the size of the element h approaches zero, the error, ϵ , itself also decreases towards zero. This forms the basis of h-adaptive procedures. Additionally, this estimate also highlights the p-adaptive procedure, which asserts that as the degree of the interpolation functions increases, the rate of convergence, p , accelerates. By rearranging expression (3.5), substituting the error, and applying logarithmic properties, the following expression is obtained:

$$\log(\epsilon) = p \log(h) + \log(C) \quad (3.6)$$

This expression leads graphically to a straight line on a “ $\log(\epsilon)$ vs $\log(h)$ ” graph, with the slope of the line equal to the rate of convergence (p).

In order to use an error estimator in a mesh adaptation procedure, it must be reliable and efficient [38]. Reliability is defined as:

$$\epsilon \leq C\eta \quad (3.7)$$

Here, the global estimator (η), calculated within the entire domain, provide an upper bound for the error (ϵ). This implies that the global error estimator is always larger than the exact global error. Therefore, if the global estimator decreases, the error also decreases. This guarantees that the error remains under control based on the estimator's information. The efficiency is being defined by

$$\eta_T \leq C\epsilon_P \quad (3.8)$$

In this definition, the local estimator (η_T), evaluated at mesh element T , offers a lower bound for the local error (ϵ_P) evaluated in the neighbourhood of T . This signifies that locally, the error estimator is consistently smaller than the exact error. Consequently, when the local

estimator is larger in certain elements, it indicates that the exact error is also larger in the vicinity. This capability enables the identification of regions with larger error, and thus to carry out adaptive refinement; in both cases C is a positive constant only dependent on the problem intrinsic data (such as material properties and domain geometry) and remains independent of mesh discretisation.

The global estimator can be obtained using:

$$\eta = \left(\sum \eta_T^2 \right)^{1/2} \quad (3.9)$$

The quality of an estimator is often judged using global (3.10) or local (3.11) scalars:

$$\theta = \frac{\eta}{\|\epsilon\|} \quad (3.10)$$

$$\theta_p = \frac{\eta_T}{\|\epsilon\|_p} \quad (3.11)$$

In order to address the problem of computing numerical errors, two main approaches for error estimation are found in the literature: a priori and a posteriori.

3.3.1 *A priori* error estimators

A priori error estimators rely on exact solution. As shown in expression (3.5), the upper-bound of the error is controlled by u and not u_h .

Their numerical computation may involve extrapolate solutions obtained on sequences of progressively finer meshes (varying the element size) or on sequences of meshes with shape functions of increasing order (degrees of interpolation functions). The, a comparison of these solutions can provide an indication of the error, where the expression in (3.5) can be used to study the convergence of the solution.

3.3.2 *A posteriori* error estimates

A posteriori error estimators, on the other hand, are based on a postprocessing of the numerical solution. The interest in a posteriori error estimation for finite element methods in boundary values problems began with the pioneering work of Babuška and Rheinboldt [39]. A posteriori error estimations techniques were developed to approximate the error in energy or an energy norm on each finite element. This idea laid the basis for adaptive meshing procedures designed to control and minimize the error. A posteriori error estimation for the electromagnetic simulation is directly applied to the solutions contained in H^{curl} and is based on edge (Nédélec)

elements. It has been investigated by several researchers, leading to various types of estimators that can be classified into three main categories:

- Residual based estimators, which include both implicit [40] and explicit([41],[42],[43])¹ approaches
- Equilibrated estimators [44], [45],[46].
- Recovery-based estimators [47].

3.3.2.1 Residual-based estimators

Residual-based estimators are widely employed and involve calculating the residual of the weak formulation locally. These estimators were initially introduced by Babuška and Rheinboldt [48] and have been further developed by several authors ([49],[50],[51]) for elliptic problems. They have since been extended to other types of equations, including those found in various electromagnetic problems, as detailed in [52]. In the modelling of electromagnetic problems using a harmonic approach, Creusé et al. introduced a residual-based estimator [53] for the $A - \phi$ formulation and other one [54] for the $T - \Omega$ formulation. Later, Robert T. [55] extended these works to a temporal $A - \phi$ formulation. The residual method is grounded in the solution of a well-posed variational formulation, where the core concept being to establish a connection between the error norm and the residual norm of the weak formulation being solved. The main limitation of this method is its lack of generalisability. In other words, meaning that if conditions slightly change, the local problem often needs to be reformulated, making it less versatile in handling varying scenarios.

3.3.2.2 Equilibrated estimators

Equilibrated estimators are designed to compute the discontinuity jump between two elements or element patches. In the context of electromagnetic modelling, these estimators are particularly valuable for verifying conditions like the divergence-free current ($\vec{\nabla} \cdot \vec{J} = 0$) or the divergence-free of the magnetic flux ($\vec{\nabla} \cdot \vec{B} = 0$). Several works have explored the equilibrated method; in the case of edge elements some equilibration techniques have been developed and documented in [44],[45],[46]. However, these methods often rely on restrictive assumptions, such as the necessity of piecewise magnetic permeability, which limits their applicability in modelling ferromagnetic materials. Moreover, their computational cost can be relatively high, making them less suitable for efficiently modelling complex industrial electromagnetic material processes.

3.3.2.3 Recovery-based estimators

Recovery estimators are based on constructing a higher interpolation order field compared to the one calculated from FEM. This technique involves post-processing the

¹ By explicit it is meant that the chosen formulation enables posing the problem such that the variable to be computed does not depend on itself (neither its current state (time) nor its neighbouring values (spatial distribution)).

approximation solution u_h , to generate a more enriched representation of its gradient $G(u_h)$. This approach for *a posteriori* estimators was introduced by Ainsworth and Craig[56]. Among the recovery methods, one of the most popular is the Superconvergent Patch Recovery (SPR) method, which has been documented in ([56][57],[58],[59]). In the finite element method, using basis functions of degree p leads to errors in the derivative of order $O(h^p)$. The SPR method is based on the superconvergent property of the Gauss quadrature points, as elaborated in section 4.3 of [38]. These superconvergent points allow for the recovery of the solution's gradient with a higher-order approximation, leading for errors to the order $O(h^{p+1})$. Applications of this method to electromagnetic fields, particularly in addressing $H(\text{curl})$ problem, have been documented in [60]. Due to its versatility and demonstrated effectiveness across various problem domains, this type of estimator has been selected for use in this work.

3.3.2.4 Error based on dual problem

Another field of research has explored estimators based on the dual problem technique. This technique delves into the two potential formulations $(A - \phi)$ and $(T - \Omega)$.

The $A - \phi$ formulation revolves around the magnetic flux density $\vec{B}_{A,\phi}$ and the electric field $\vec{E}_{A,\phi}$. In contrast, the $T - \Omega$ formulation is centered on the magnetic field $\vec{H}_{T,\Omega}$ and the current density $\vec{J}_{T,\Omega}$. Since these fields do not completely satisfy the discretized constitutive laws, it becomes possible to define a local error estimator for each mesh element. This estimator is based on the errors for the constitutive laws governing both magnetic and electric fields. First, an estimator based on the magnetic field (η_{magn}) is formulated as:

$$\eta_{magn} = \left\| \vec{H}_{T,\Omega} - \frac{1}{\mu} \vec{B}_{A,\phi} \right\|_{L^2(\text{norm})} \quad (3.12)$$

Similarly, an estimator based on the electric fields is defined as:

$$\eta_{elec} = \left\| \vec{J}_{T,\Omega} - \sigma \vec{E}_{A,\phi} \right\|_{L^2(\text{norm})} \quad (3.13)$$

It is important to note that η_{elec} is only defined within the conductive domain. Finally, the dual error estimator is computed as:

$$\eta_{dual} = \left(\eta_{magn}^2 + \eta_{elec}^2 \right)^{\frac{1}{2}} \quad (3.14)$$

While this method offers high accuracy, it often comes with a significant computational cost. Despite various strategies employed to mitigate this computational cost, as exemplified in [61], [62], [55], which aim to avoid solving the two formulations simultaneously, the computation cost remains high.

3.4 Recovery based – Galerkin method

As observed earlier, numerous papers have addressed the subject of a posteriori error estimation for finite element computations. However, many of the examples provided involve simple geometries, which facilitates the validation of these estimators. Nevertheless, extending these estimators to cases involving complex geometries can result in substantial demands on CPU time and computational resources. Therefore, the objective here is to introduce a recovery-based technique that combines computational efficiency with the capability to handle industrially complex scenarios.

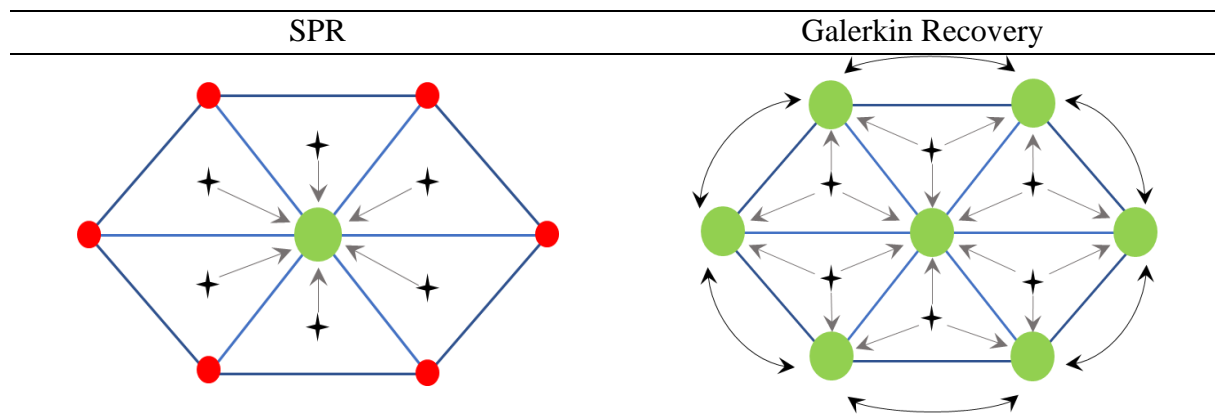
3.4.1 Superconvergent Patch Recovery vs Galerkin-based Recovery for building a smoothed solution

Recovery-based techniques rely on the determination of a smoothed solution. Several strategies can be found in literature for constructing the enriched or smoothed solution; here again, it is important when constructing the smoothed solution to consider robustness and ability to deal with to geometrically complex configurations, such as the ones found in industrial processes, as well as the use of fast and efficient methods.

Two approaches are briefly compared in this section to guide the choice of the implemented strategy and summarised in Table 3.1. The first strategy is the classical implementation of the SPR approach which consists in constructing arbitrary p -order polynomials valid for the neighbourhood of each mesh node using a Least Squares Method locally. The interpolation order p of this new polynomial should be at least one order higher than the original interpolation degree of the field at neighbouring Gauss points. The second strategy is the Galerkin recovery or residual minimization recovery, which follows the same objective, but the order of interpolation is constrained by the interpolation degree of the FE mesh used to represent the original field since it is built using the same mesh than the one required for solving the original PDE.

Table 3.1 Comparison of SPR and Galerkin recovery

(note on figure: green points mean “active” node during iteration, red points mean “unactive” node during iteration)



$\tilde{f}_i(\vec{x}) = a_i + b_i x + c_i y + d_i z$	$\tilde{f}_i(\vec{x}) = \sum_j \varphi_j f_j$
N local linear systems on the polynomial's coefficients per node	1 single global sparse linear system on the field values
Degree of interpolation can be locally adjusted as a function of number of neighboring elements	Degree of interpolation is fixed by elements formulation
Corner nodes (isolated) have ill-conditioned systems	All nodes are simultaneously connected, and the system is always invertible

3.4.1.1 On the interpolation enrichment potential

As mentioned before, the SPR approach enables building polynomials of arbitrary interpolation degrees. The choice is constrained by the number of coefficients resulting from the conjunction of the topological dimension and the interpolation degree p . The number of coefficients will set the size of the local linear systems, ex: for a 1st degree polynomial 4 coefficients are required in 3D for a scalar field, which requires building 4 orthogonally independent linear systems. To guarantee the orthogonality, the node needs to be surrounded by, at least, 4 gauss integration points that do not superpose but also are not perfectly aligned. For sufficiently large FE meshes this limitation can be overcome by using not only the first layer of elements connected to a node but also by incrementing the next layers of elements.

In the Galerkin recovery approach, the unknowns are the values of the enriched field at the nodes instead of the coefficients of the polynomial and the orthogonality is enforced during the construction of the interpolation functions of each node. This implies that the number of unknowns is greatly reduced and that a solution to the linear system should always exist (provided elements are not degenerate or inverted).

3.4.1.2 On the geometrical pathologies and convergence risks

Since in the SPR approach, each node is treated (in principle) individually, many unforeseen geometrical pathologies can appear for arbitrary complex meshes. Fig. 3.1 displays two main kinds of pathologies. They are associated with exterior nodes for which the Least Square matrix will result in an ill-posed problem because they do not have enough neighbors to guarantee orthogonality. One way to overcome this issue is by solving the enrichment in two steps [63]: 1. Compute only interior nodes which have well posed matrices. 2. Carry out an iterative penalized fixed-point resolution on the exterior nodes and include the neighboring nodes as reference points. Some authors also propose the use of phantom elements by mirroring elements on the surface. Such approaches are highly prone to stumble on difficult-to-handle pathologies.

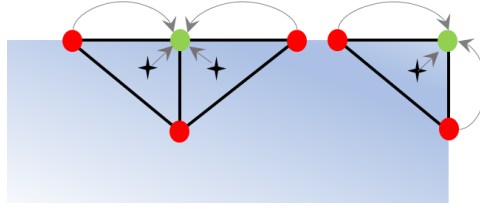


Fig. 3.1 Problematic nodal configurations in typical SPR approaches requiring particular algorithmic treatments: Corner nodes & surface nodes.

3.4.1.3 On solver implementation

By solving all unknowns simultaneously with a well- conditioned linear matrix obtained by the variational approach, the Galerkin recovery procedure clearly is an extremely robust option. The well-posed nature of the matrix comes from the fact that only the identity operator is involved in the residual equation (no presence of derivative operators).

Another key aspect is that the matrix has the same sparsity pattern as the matrix required for the original PDE, which means that the same allocated memory space can be used. Since the matrix is symmetric and positive defined a PCCG Krylov solver with Jacobi preconditioning is sufficient for optimal resolution of the linear system.

3.4.2 Estimator based on a recovered smooth vector field

In the finite element method as in any other numerical procedure, the quantification of the gap between the exact solution and the numerical one needs to be measured and controlled. If the accuracy condition is not reached, it should be able to provide a way to get a new sufficiently enriched solution, using a procedure as economical and efficient as possible. A large number of papers have demonstrated that when using a higher order accuracy enriched solution, the estimated error converges towards zero as the mesh size decreases. A recovery-based a posteriori error estimator is proposed here, which satisfies the above-mentioned conditions. This estimator computes the gap in terms of regularity between the original and the recovered solution.

Implementation: The error estimator relies on a smooth recovery method, involving the construction of a smoothed field [56] based on an already known field. In order to construct the smoothed field for determining the numerical solution error, the Galerkin or residual minimization method have been implemented. This approach ensures stability by framing it as a conservation problem (see detailed in chapter 4 of [2]). Let \vec{X}_{P_0} be the field obtained from the finite element analysis and \vec{X}_{P_1} the recovered or smoothed field, the method consists in solving the following global minimization problem:

$$\min \|\vec{X}_{P_1} - \vec{X}_{P_0}\|_{L^2(\Omega)}^2 \quad (3.15)$$

Now, let's $\vec{\psi}$ be the interpolation function on the edges. Expressing the field in a discrete form becomes:

$$\vec{X}_{P_1} = \sum_j x_{P_{1j}} \vec{\psi}_j \quad \forall j = 1, 2, \dots, 6 \quad (3.16)$$

As \vec{X}_{P_1} is the unknown, the minimisation problem is solved by projecting $\vec{X}_{P_1} - \vec{X}_{P_0}$ onto the basis functions of the edge mesh, leading to:

$$\left\langle \left(\sum_j x_{P_{1j}} \vec{\psi}_j - \vec{X}_{P_0} \right), \vec{\psi}_k \right\rangle = 0 \quad \forall k = 1, 2, \dots, 6 \quad (3.17)$$

$$\sum_j \langle \vec{\psi}_j, \vec{\psi}_k \rangle x_{P_{1j}} = \langle \vec{X}_{P_0}, \vec{\psi}_k \rangle \quad (3.18)$$

This results in the linear system:

$$Ax = b \quad (3.19)$$

The field calculated by system (3.19) is represented by its line integrals along the edges of the elements ($\int \vec{X} \cdot \vec{t}$). To compare it with the initial field stored at the Gauss integration points ($\vec{X}_{P_0}(x_G)$), a transformation is performed using the following expression:

$$\vec{X}_{P_1}(x_g) = \sum_{i=1}^{\text{edges}} (\vec{x}_{P_{1i}} \vec{\psi}_i) \quad (3.20)$$

This linear field has one order of interpolation higher than the initial field. The magnetic field (\vec{H}) is applied in this approach. By comparing the smoothed P_1 field to the P_0 solution, the error can be calculated as:

$$\epsilon_H = \|\vec{H}_{P_1} - \vec{H}_{P_0}\|_{L^2(\Omega)} \quad (3.21)$$

3.5 Physics-specific estimators alternatives

Additional error estimators have been explored, primarily focusing on assessing the accuracy of certain Maxwell equations by comparing fields with different orders of interpolation, specifically P_1 and P_0 . To construct these estimators, the recovered magnetic field computed in section 3.4.2 is used. Bellow, we list and define these estimators:

3.5.1 Estimator based on the derived current density

Current density can be computed using Ampere's law (2.6). Since the smoothed magnetic field (\vec{H}_{P_1}) is linear, it does not vanish under the application of a curl operator. Thus, taking advantage of this property, a electric current density is derived as follows:

$$\vec{J}_{P_0} = \vec{\nabla} \times \vec{H}_{P_1} \quad (3.22)$$

Here, \vec{J}_{P_0} is element-wise constant. The estimator is then defined as the difference with the linear current density obtained from the finite element analysis (\vec{J}_{P_1}). Consequently, the error between these two quantities can be calculated as:

$$\epsilon_J = \|\vec{J}_{P_1} - \vec{J}_{P_0}\|_{L^2(\Omega)} \quad (3.23)$$

3.5.2 Estimator based on the verification of Faraday's Induction Law

Faraday's law of induction (2.5) is a fundamental principle in electromagnetics, and validating it provides crucial insights into the accuracy of the numerical model. To achieve this, the first a posteriori estimator, grounded in the underlying physics, aims to confirm Faraday's law.

Implementation: This estimator's objective is to verify the Faraday's Induction law (2.5), which necessitates the curl of the electric field plus the time derivative of the magnetic flux density to vanish or approach zero:

$$\|\vec{\nabla} \times \vec{E}_{P_1} + \partial_t \vec{B}_{P_1}\|_{L^2(\Omega)} = 0 \quad (3.24)$$

To verify this expression within a single element, the electric field resulting from the finite element analysis, which is linear over the element is used. Additionally, the time-derivative of the magnetic flux density is computed from the recovery procedure (3.20). Since these values are directly stored at the Gauss integration points, the error in the element is computed as:

$$\epsilon_E = \|\vec{\nabla} \times \vec{E}_{P_1} + \partial_t \vec{B}_{P_1}\|_{L^2(\Omega)} \quad (3.25)$$

3.5.3 Estimator based on the verification of Ampere's Law

A second *a posteriori* error based in the underlying physics has been developed. This estimator aims to verify Ampere's law (2.6), one of the fundamental laws of electromagnetics.

Implementation: To assess the verification of Ampere's law (2.6), the objective is to calculate the difference between the magnetic circulation and the current density, aiming for this difference to be as close to zero as possible:

$$\vec{\nabla} \times \vec{H}_{P_1} - \vec{J}_{P_1} = 0 \quad (3.26)$$

To evaluate expression (3.26) for a single element, the Stokes theorem is applied, which relates the surface integral of the curl of a vector field to the line integral of the same vector field over its boundary. Expressing the magnetic field \vec{H} within this theorem results in:

$$\oint_{\Gamma} \vec{H}_{P_1} \cdot d\vec{l} = \iint_S (\vec{\nabla} \times \vec{H}_{P_1}) \cdot \hat{n} dS \quad (3.27)$$

In order to define the Ampere's law-based estimator it's essential to establish the flux directions on each face of the element and determine the circulation direction. The circulation direction is chosen to be counter-clockwise on each face, ensuring that the normal vector \hat{n} points out of the element, as illustrated in Fig. 3.2.

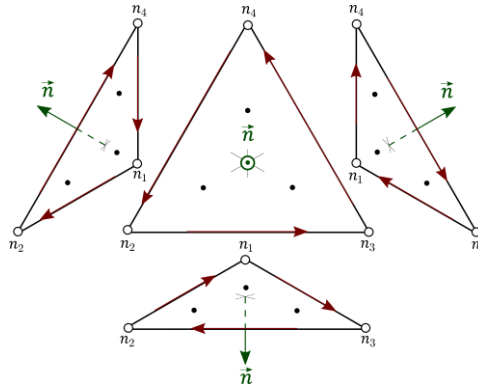


Fig. 3.2 Magnetic circulation across the element's face.

The estimator is computed separately for each face of the tetrahedron. For each face, we compute the line integral of the recovered magnetic field (3.20) and subtract the surface integral of the current density passing through the face. Consequently, the error estimator for each face is defined as:

$$\epsilon_F = \oint_{\partial F} \vec{H}_{P_1} \cdot d\vec{l} - \iint_F \vec{J}_{P_1} \cdot \hat{n} dS \quad (3.28)$$

The line integral along the face is calculated numerically by summing the computed magnetic field at the edges, as shown in the following expression:

$$\oint_{\partial F} \vec{H}_{P_1} \cdot d\vec{l} = \sum_{e=1}^{edges} \vec{H}_{P_1} \cdot \vec{l} \quad (3.29)$$

To compute the current density passing through the face in three-dimensional finite element modelling, it is necessary to interpolate the current density values from the tetrahedron element to its triangular faces. Therefore, the flux is determined by computing the current density at the integration points of the triangular face (pts_f) using the integration points of the element (pts_v). Thus, the flux through a face is calculated as:

$$\iint_F \vec{J}_{P_1} \cdot \hat{n} d\vec{S} = \sum_{i=1}^{pts_f} \omega_i \left(\sum_{k=1}^{pts_v} \omega_k \vec{J}_k \right) \cdot \hat{n} dS \quad (3.30)$$

Where ω_i represents the weight at each integration point. To maintain consistency, the normal vector is considered to be pointing out from each face of the tetrahedron. The face integration points and the normal vector (\vec{n}) are depicted in Fig. 3.3

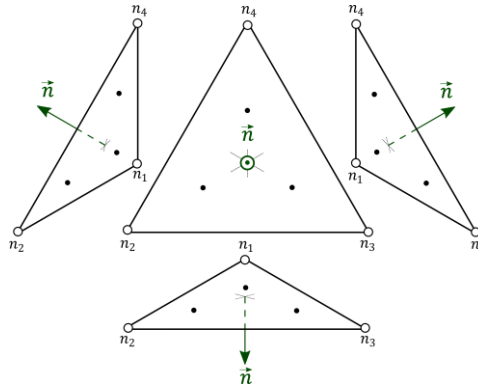


Fig. 3.3 Flux direction from the element's face and face integration points.

Finally, to calculate the error over the entire tetrahedron, we compute the mean error within the element as follows:

$$\epsilon_E^{mean} = \frac{1}{S_E} \sum_{F=1}^{faces} \epsilon_F S_F \quad (3.31)$$

Where S represents the surface of each face.

3.5.4 Estimator based on fundamental conservation principle

A final estimator is developed to validate the fundamental calculus principle of the divergence of curl, which simply states that the divergence of the curl of any vector field is always zero:

$$\nabla \cdot (\nabla \times \vec{X}) = 0 \quad (3.32)$$

Implementation: To test equation (3.32), a linear interpolation field (P_1) is required. In this way, the recovered magnetic field (3.20) is used. To construct this estimator, the Stokes theorem is applied, which states:

$$\iint_S (\vec{\nabla} \times \vec{H}_{P_1}) \cdot \hat{n} d\vec{S} = \oint_C \vec{H}_{P_1} \cdot d\vec{l} \quad (3.33)$$

As shown in Fig. 3.2, the right-hand side of (3.33) can be evaluated on each face of the element. The contribution of each face F is added up, thus the integral on the tetrahedron will be closed, implying:

$$\oiint_S (\vec{\nabla} \times \vec{H}_{P_1}) \cdot \hat{n} d\vec{S} = \sum_{F=1}^{faces} \sum_{e=1}^{edges} \vec{H}_{P_1} \cdot \vec{l} \quad (3.34)$$

In this sense, the divergence theorem is applied to the curl operator. Then, the same left-hand side term is found as in (3.34):

$$\iiint_E (\vec{\nabla} \cdot (\vec{\nabla} \times \vec{H}_{P_1})) dV = \oiint_S (\vec{\nabla} \times \vec{H}_{P_1}) \cdot \hat{n} d\vec{S} \quad (3.35)$$

Finally, expression (3.32) is validated through:

$$\iiint_E (\vec{\nabla} \cdot (\vec{\nabla} \times \vec{H}_{P_1})) dV = \sum_{F=1}^{faces} \sum_{e=1}^{edges} \vec{H}_{P_1} \cdot \vec{l} \quad (3.36)$$

Table 3.2 A posteriori error estimators proposed.

Estimator	Expression	Principle
Based-recovery field	$\epsilon_H = \ \vec{H}_{P_1} - \vec{H}_{P_0}\ _{L^2(\Omega)}$	A higher order interpolation field
Derived from Ampere's law	$\epsilon_J = \ \vec{J}_{P_1} - \vec{J}_{P_0}\ _{L^2(\Omega)}$	$\vec{J} = \vec{\nabla} \times \vec{H}$
Faraday's Induction law	$\epsilon_E = \ \vec{\nabla} \times \vec{E}_{P_1} + \partial_t \vec{B}_{P_1}\ _{L^2(\Omega)}$	$\vec{\nabla} \times \vec{E} + \partial_t \vec{B} = 0$
Ampere's law	$\epsilon_E = \frac{1}{S_E} \sum_{F=1}^{faces} \left(\oint_{\partial F} \vec{H}_{P_1} \cdot d\vec{l} - \iint_F \vec{J}_{P_1} \cdot \hat{n} d\vec{S} \right) S_F$	$\vec{\nabla} \times \vec{H} - \vec{J} = 0$
Fundamental conservation principle	$\epsilon_E = \sum_{F=1}^{faces} \sum_{e=1}^{edges} \vec{H}_{P_1} \cdot \vec{l}$	$\nabla \cdot (\nabla \times \vec{H}) = 0$

3.6 Analysing, scaling, and normalizing estimator results

The results obtained from the previous estimators are often not immediately usable or comparable. This is primarily due to the presence of noise in the results, which can obscure the essential information provided by the estimators, particularly in complex industrial models. Additionally, the estimators described in the previous section have different physical scales, making direct comparisons challenging. Hence, the need for normalize the results.

The oscillatory and discontinuous nature of electromagnetic fields necessitates an appropriate choice of normalization scheme for the error. This scheme be versatile enough to enable comparisons across diverse physical quantities. To address this, a scale-agnostic normalization methodology has been developed to properly quantify the error. This methodology is based on extracting some measure of “noise” from the numerically computed fields. Let S represent as a signal proxy for any given field, and a measure of energy contained in this signal is given by:

$$ES = \int_{t_0}^{t_f} S^2 dt \quad (3.37)$$

As discussed in section 3.4.2, the error estimator calculated a smoothed field based on the original field solution. For the sake of simplicity, let's denote the smoothed solution as (\bar{S}) . Similar to (3.37), the energy of the smoothed signal can be computed as:

$$E\bar{S} = \int_{t_0}^{t_f} \bar{S}^2 dt \quad (3.38)$$

Now, consider S as a simple sinusoidal signal with some noise, as shown in Fig. 3.4(a), and \bar{S} as the smoothed version, as in Fig. 3.4(b). The respective energies are illustrated in Fig. 3.4(c) and (d).

However, it is not only important to measure the energy gap between both signals but also to establish a reference of the error, thereby creating an appropriate normalization for the estimators. To address this, a noise energy normalization approach is proposed. The main idea is to minimize the energy contained in the noise (ENS), which is represented by the energy integral difference between both signals:

$$ENS = \int_{t_0}^{t_f} (S - \bar{S})^2 dt \quad (3.39)$$

In this context, the reference is defined as the accumulation of the total energy contained in the noise, as depicted in the Fig. 3.5.a (coral color). Consequently, the local error is interpreted as a fraction of the noise energy, as illustrated in Fig. 3.5.b. In other words, larger local error will manifest as peaks, as shown in the zoomed-in section of Fig. 3.5.a

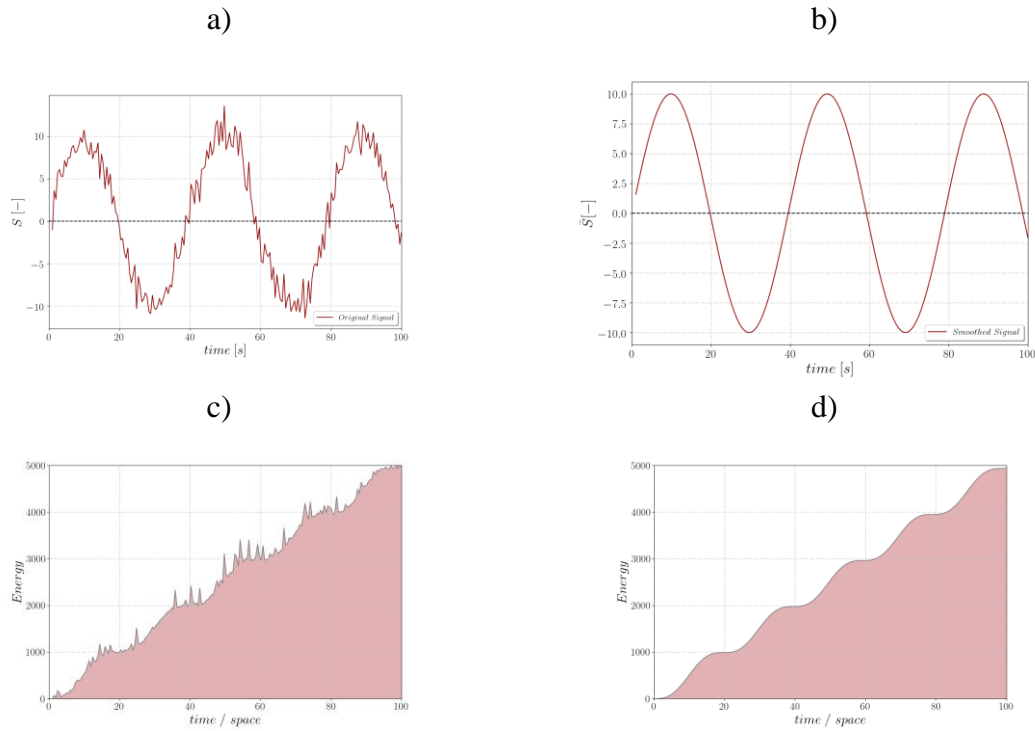


Fig. 3.4 1D analogy; Energy of the signal: a) original signal S . b) Smoothed signal \bar{S} . c) S energy. D) \bar{S} energy.

Therefore, the error normalization of any X field within the Ω domain is calculated using the following expression:

$$\|\epsilon_X\|^2 = \frac{(X - \bar{X})^2}{\sum_{\Omega} (X - \bar{X})^2} \quad (3.40)$$

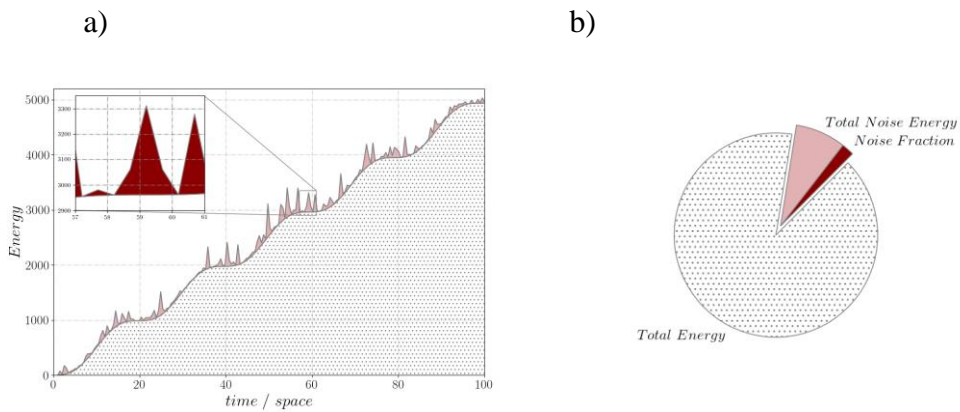


Fig. 3.5 Total energy, total noise energy and noise fraction contained in the signal. a) Schematic representation of the noise energy normalisation. b) Error fraction.

3.7 Validation and analysis on semi-analytical cases

All the estimators presented in previous section have been integrated into the computational model FORGE® within the electromagnetic module.

3.7.1 Validation by comparison with an analytical solution

This section is dedicated to the numerical validation of the recovery-based error estimator. In the initial phase, validation is conducted using an analytical test case. The scenario involves an infinitely long cylindrical wire with diameter of $\phi_C = 1mm$, which is subjected to a sinusoidal time-dependent current, denoted as $I(t)$. This current flows through the wire, inducing a time-varying magnetic field. To analyse the generated magnetic field and evaluate the accuracy of the error estimator, we positioned a ring at a distance $L = 19.5mm$ from the wire. This ring has an external diameter $\phi_R = 5mm$ and an internal diameter $\phi_r = 4mm$. The analytical case is illustrated in Fig. 3.6.

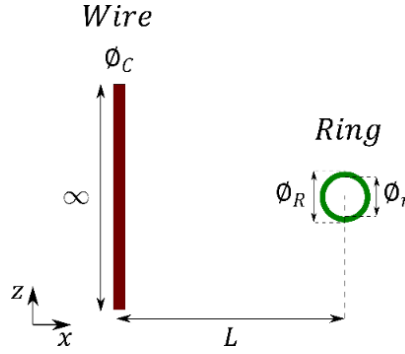


Fig. 3.6 Schematic representation of the analytical test case

The analytical solution in cylindrical coordinates for this system is described by:

$$\vec{H}_{an}(r) = \frac{\sqrt{2}I_{RMS} \sin(\omega t)}{2\pi r_i} \hat{\phi} \quad (3.41)$$

It is important to note that this solution provides an approximates as it does not account for the reverse effect caused to eddy currents induced within the ring. An analytical error can now be computed using the L_2norm , similar to the estimator defined in (3.21):

$$\epsilon_{an} = \|\vec{H}_{an} - \vec{H}_{P_0}\|_{L^2(\Omega)} \quad (3.42)$$

Convergence with mesh size

To initiate the validation of the error estimator defined in (3.21), a mesh sensitivity analysis is performed. Por this purpose, we employed a range of decreasing mesh sizes (h) as illustrated in Fig. 3.7.

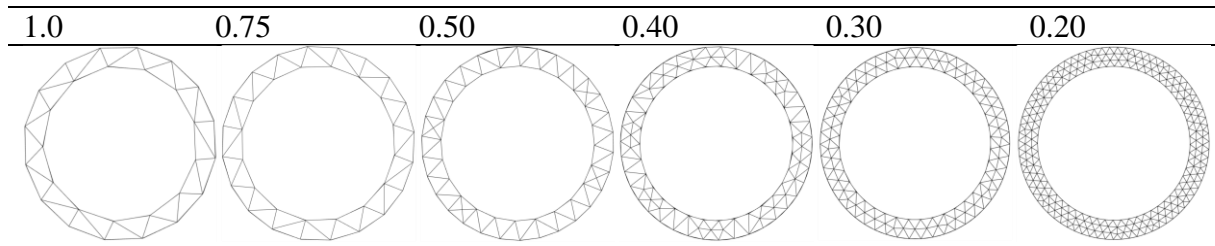


Fig. 3.7 Mesh sensitivity analysis (dimensions in mm)

As a result, a comparison was made between the analytical error (3.42) and the error estimator (3.21). The results, presented in Fig. 3.8, reveal that both the error and the estimator exhibit similar convergence behaviour as the mesh size decreases. This demonstrates that the utilization of the recovery-based error (3.21) offers a reliable approximation of the error discretization within a finite element procedure.

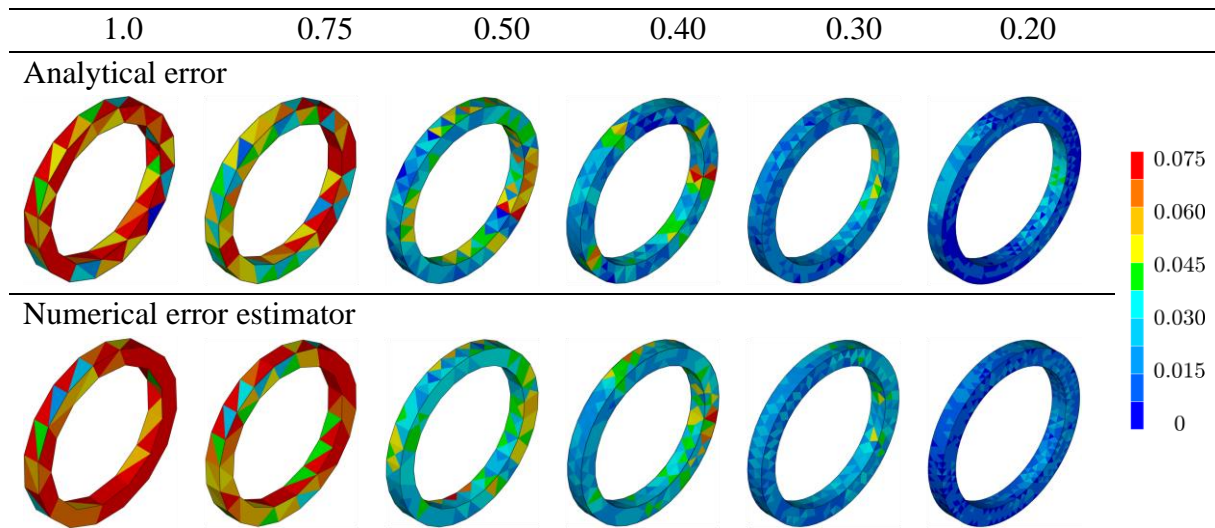


Fig. 3.8 Analytical and numerical error

3.7.2 Convergence rate analysis

To gain a more detailed understanding of the estimator's quality, we conducted a simplified case study. Fig. 3.9 illustrates the workpiece, coil, and the symmetry employed. For the sake of simplicity, we defined an isotropic mesh in which the mesh size uniformly decreases across the entire domain, ranging from 8 to 1 mm.

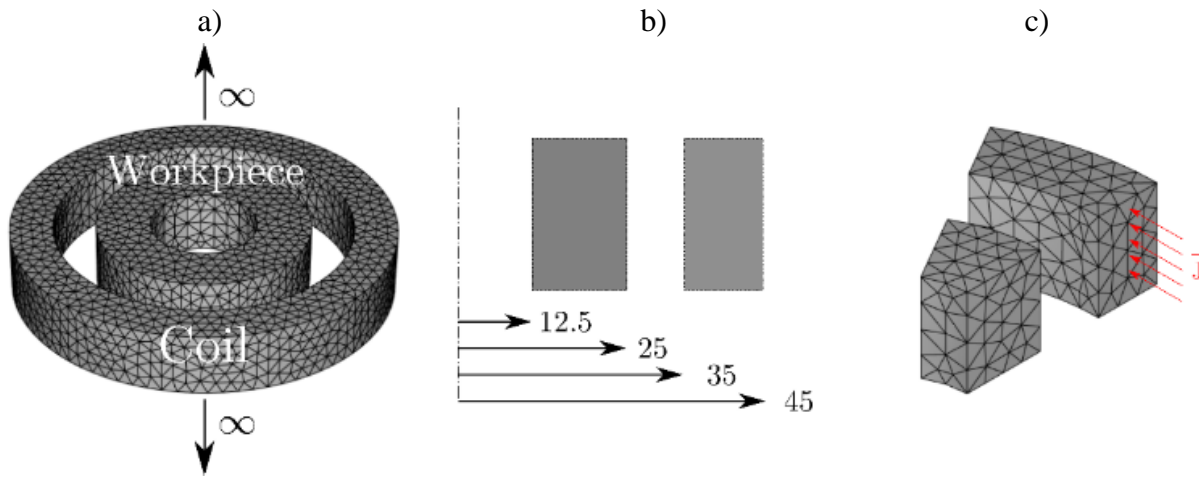


Fig. 3.9 a) Workpiece and inductor. B) dimensions in mm and c) current representation in the axisymmetric part (only 30°).

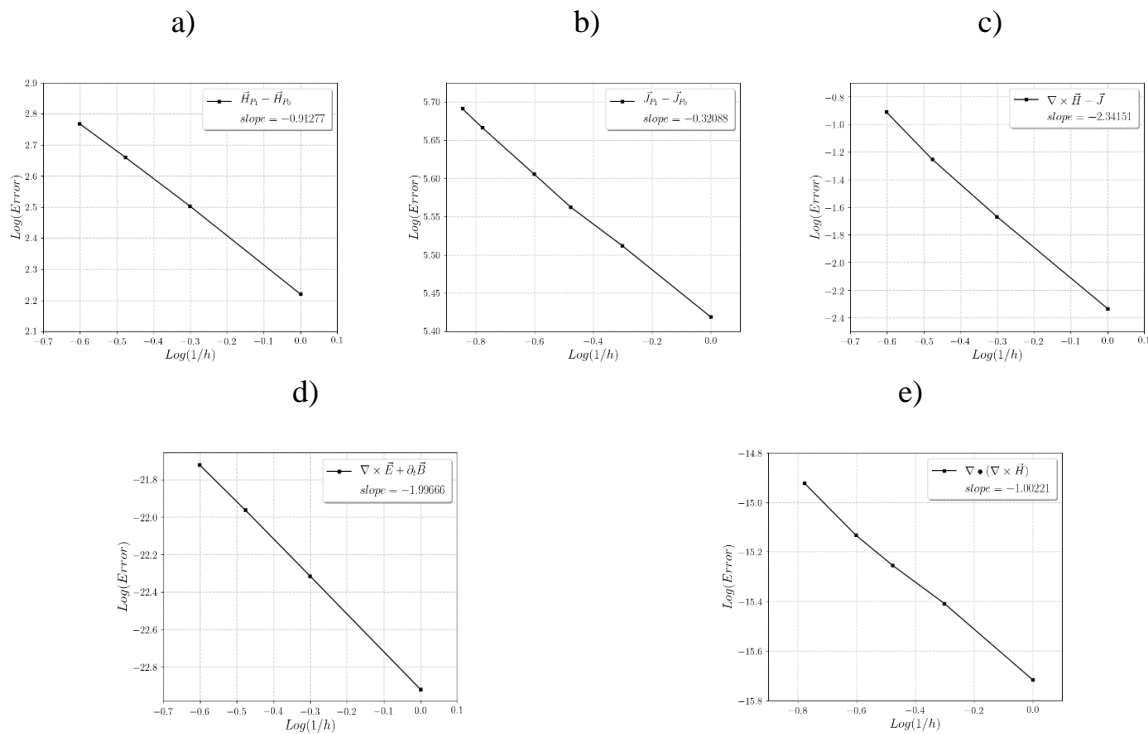


Fig. 3.10 Log-Log plot of the convergence of the estimators based on: a) recovery of magnetic field, b) current conservation, c) the verification of Ampere's law, d) the verification of Faraday's Induction law and e) fundamental calculus principles.

Fig. 3.10 displayed the convergence rates for each estimator defined in sections 3.4 and 3.5. The global error results are presented in a log vs log plot as a function of the mesh size (h). According to (3.6), the slope of the straight line directly indicates the convergence rate. It is noteworthy that the recovery-based estimator and the one based on the fundamental calculus principle exhibit a convergence rate close to unity, while the current density derivation exhibits the lowest convergence rate. On the other hand, the estimators based on the verification of the

Maxwell equations have the highest convergence rates, with a rate of 1.99 for Faraday's law and 2.34 for Ampere's law.

3.7.3 Application to the TEAM7 benchmark case

In order to test the local a posteriori error estimators, a benchmark case has been selected from the TEAM (Testing electromagnetic analysis methods) problems. TEAM represents an international working group dedicated to comparing electromagnetic analysis computer codes. Specifically, we focused on case number 7 [64], which is designed to evaluate the electromagnetic induction phenomenon. This problem entails a thick aluminium plate with a hole positioned off-centre and unsymmetrically within a non-uniform magnetic field. The field is generated by a sinusoidally varying exciting current. The problem setup is shown in Fig. 3.11.

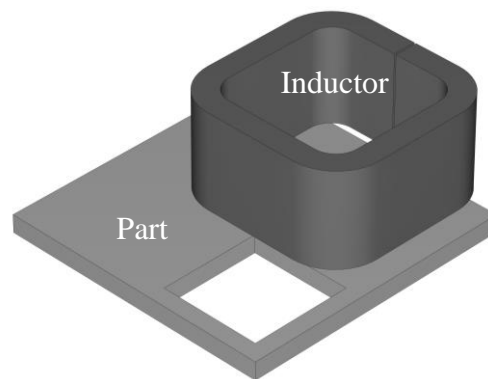


Fig. 3.11 TEAM 7 Benchmark case.

To evaluate the performance of the a posteriori error estimator proposed in section 3.4.2, it's important to assess how it behaves on the benchmark case. For this purpose, we computed the magnetic field using the quasi-steady state electromagnetic model presented in section 2.2. The magnitude and vector field distribution are depicted in Fig. 3.12 and Fig. 3.13, respectively. This information will help us gauge the estimator ability to identify areas with significant changes in the field, essentially where the field gradient is most pronounced.

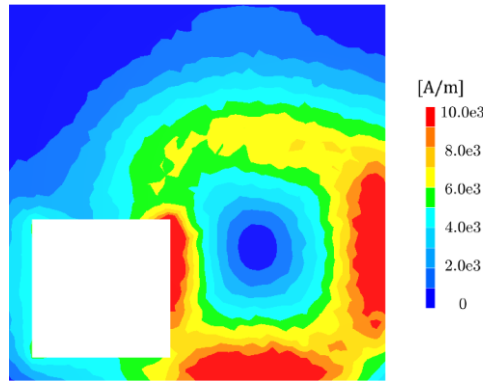


Fig. 3.12 Distribution of magnetic field magnitude on the plate (in A/m)

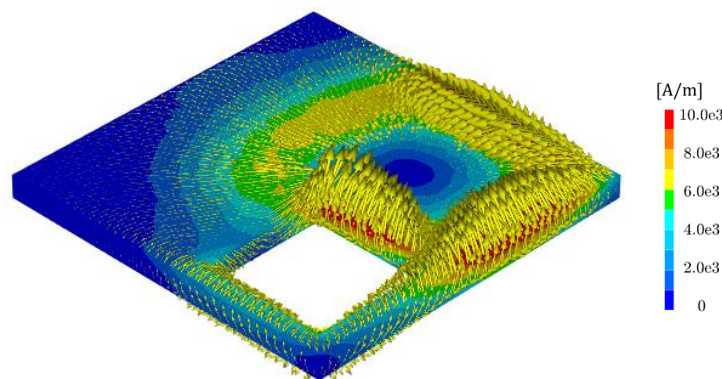


Fig. 3.13 Distribution of magnetic field vectors on the plate (in A/m)

3.7.3.1.1 Convergence with mesh size

According to finite element discretization principle, as established in (3.5), numerical errors should decrease as the mesh size becomes smaller. To evaluate the convergence of each estimator developed in sections 3.4 and 3.5, a mesh sensitivity analysis is performed on the benchmark case. The test was meshed uniformly with element size of 20, 15, 10, 8 and 6 mm, and the results are only shown within the workpiece. To facilitate comprehension, each calculated error result is indicated next to its respective mesh. The error estimators results of are presented individually as follows:

1. Galerkin's recovery-based estimator in Fig. 3.14.
2. Current density derivation-based estimator in Fig. 3.15.
3. Faraday's law verification-based estimator in Fig. 3.16.
4. Ampere's law verification-based estimator in Fig. 3.17.
5. Fundamental conservation principle-based estimator in Fig. 3.18.

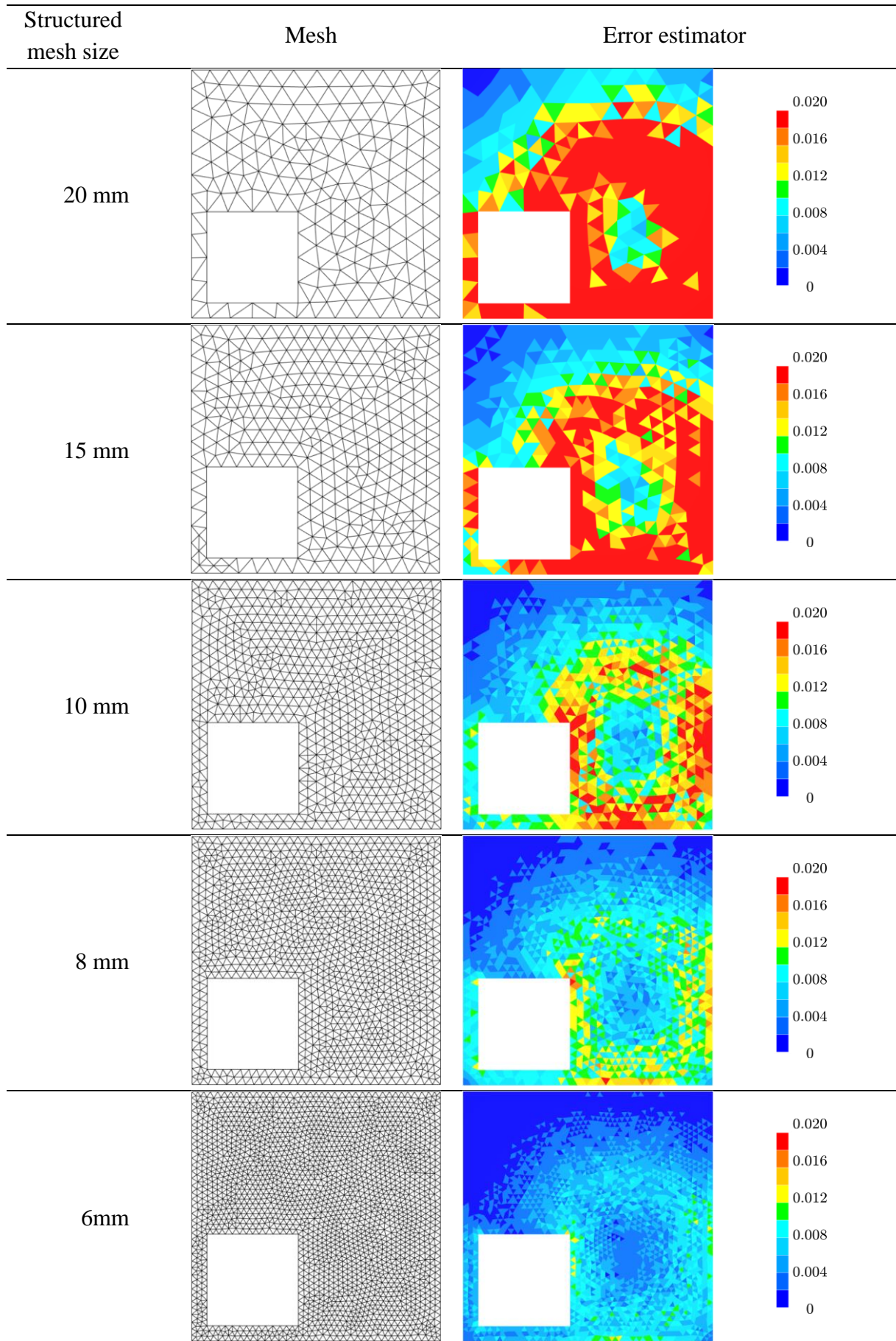


Fig. 3.14 Error distribution on the plate – Recovery technique on the magnetic field

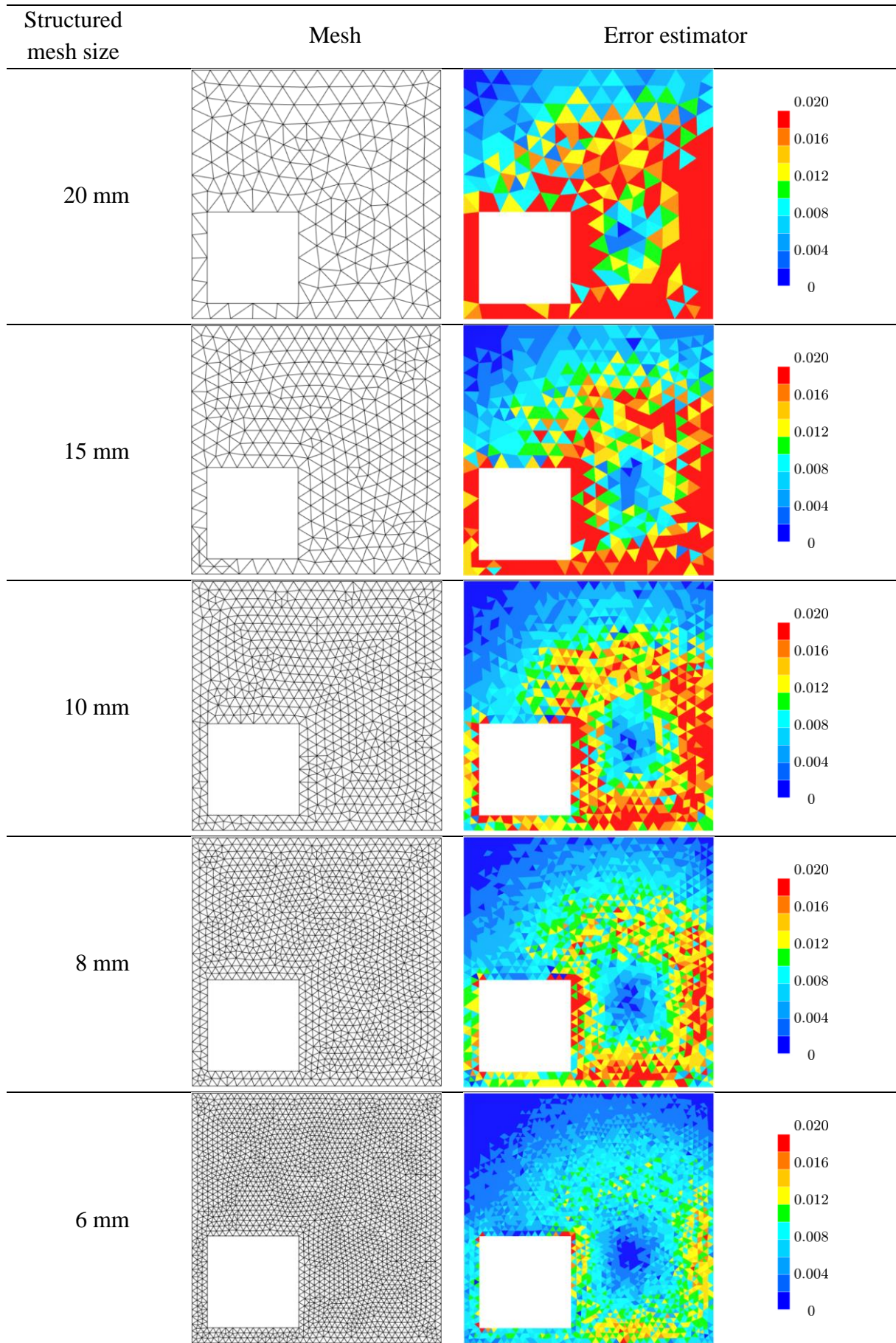


Fig. 3.15 Error distribution on the plate – Current density derivation

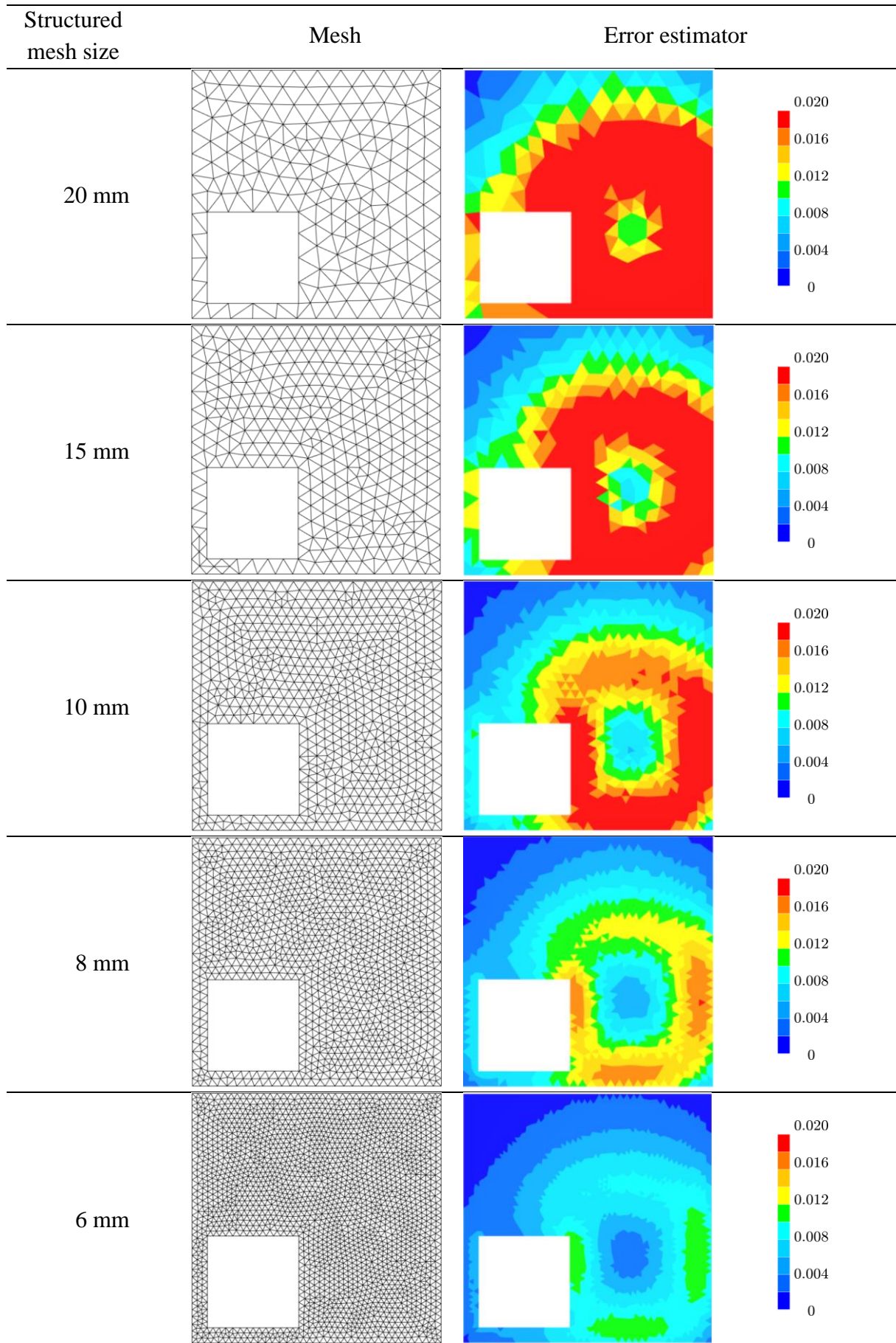


Fig. 3.16 Error distribution on the plate – Faraday law

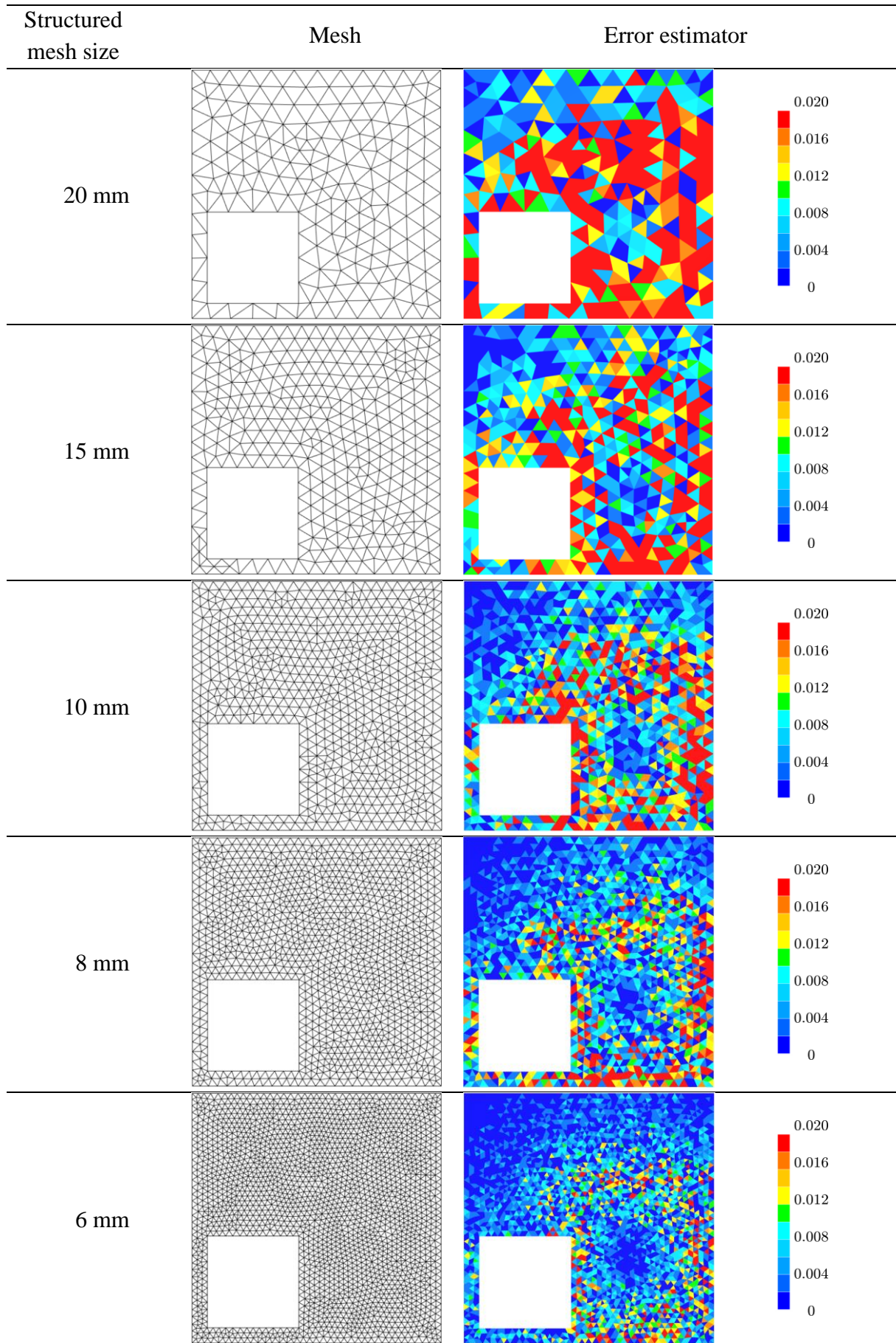


Fig. 3.17 Error distribution on the plate – Ampere Law

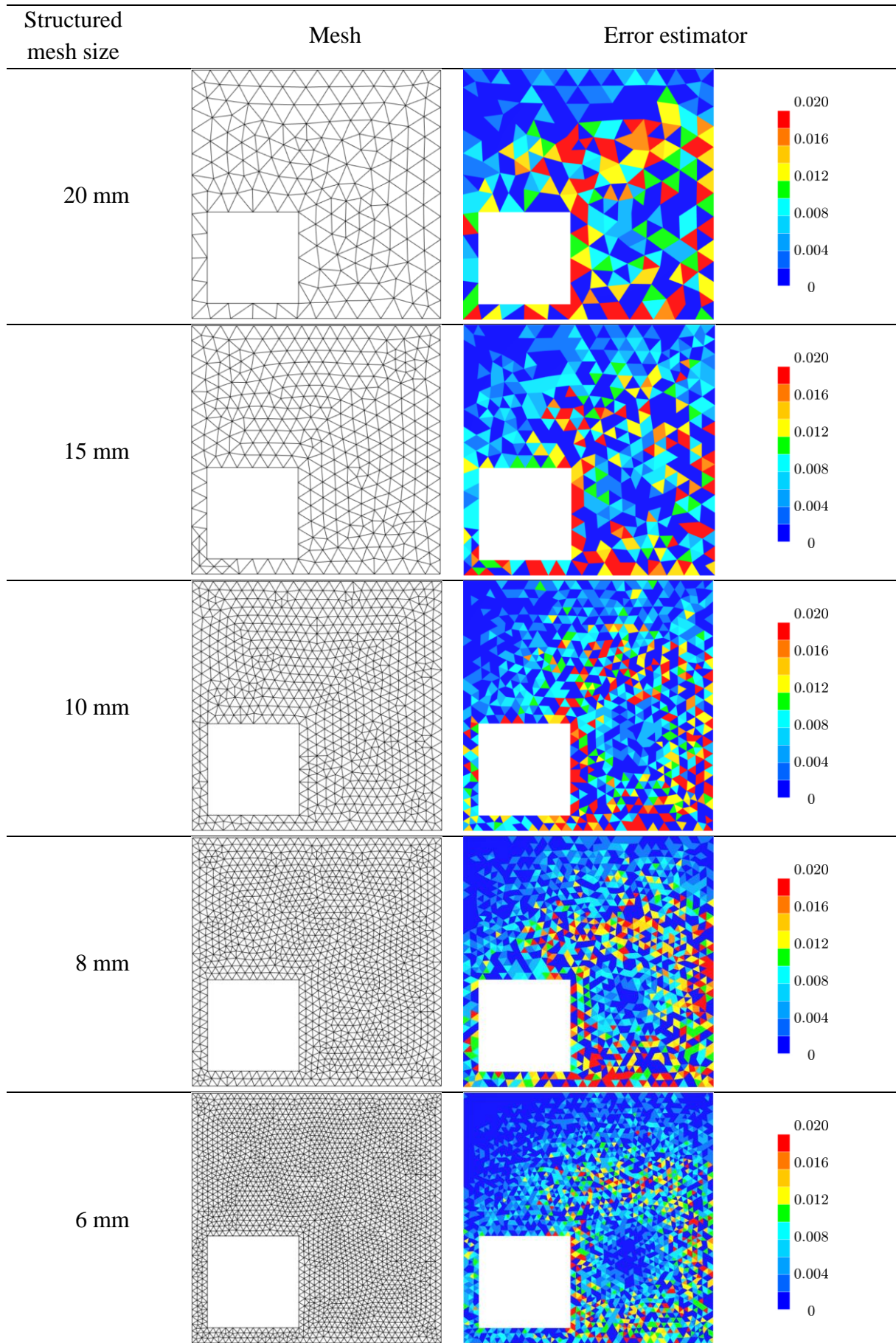


Fig. 3.18 Error distribution on the plate – fundamental conservation principle

Overall, the error analysis for each estimator reveals higher errors in the coarser mesh, which consistently decrease as the meshes become finer. This observed trend signifies a satisfactory convergence of the estimators with mesh refinement. Furthermore, it is worth noting that in each case, the estimator effectively identifies areas with higher solution gradients, as evident when comparing the results displayed alongside the magnetic field shown in Fig. 3.12 and Fig. 3.13.

However, it's essential to recognize that while all the previously presented approaches demonstrate convergence concerning mesh size in terms of relative error reduction, they exhibit significantly different error distribution patterns. These distinctions will have a profound impact on adaptive remeshing procedures built upon them. A clear division can be observed between the first three estimators and the last two, despite the latter demonstrating the highest convergence rates in previous analyses. These estimators exhibit notably sparse error patterns. This distinction arises because the latter two estimators are designed to capture local behaviours at the element level. This localization can be counterproductive when addressing continuity issues or situations where the field's gradient undergoes abrupt changes. In contrast, the first three estimators exhibit a more consistent behaviour due to their utilization of the recovery approach, which effectively leverages the mesh's capacity to capture gradient evolution in the fields.

3.7.3.1.2 Comparison of computational times

As elaborated in the definition of the recovery-based estimator, it involves solving a linear system represented as $Ax = b$. Solving such systems can often be computationally demanding. The primary objective here is to create an estimator that is efficient enough to enhance the computational process, without introducing a system that's equivalent in complexity to the main finite element system. To evaluate this efficiency, a comparison between these two linear systems is conducted, assessing how costly the error estimator is in contrast to the computation expense of FEM.

Table 3.3 presents the comparison of computation times and number of iterations required for finite element analysis and the recovery procedure. It becomes evident that the recovery-based procedure is notably efficient in terms of computational time when compared with the FEM resolution.

Table 3.3 Linear system resolution. Comparison between fem and recovery method

Mesh size (mm)	FEM		Recovery	
	Iterations number	Time (sec)	Iterations number	Time (sec)
20	194	2.985	24	0.375
15	209	3.890	29	0.531
10	222	4.470	30	0.625
8	239	5.938	29	0.797
6	254	9.672	26	1.110
4	305	23.890	29	2.375

3.7.3.1.3 Considering magnetic permeability variation due to the magnetic field and time-averaging estimator.

Magnetic permeability is mainly temperature-dependent, with ferromagnetic materials transitioning to paramagnetic states above a critical temperature, known as the Curie temperature. Additionally, it can vary with the magnetic field strength in ferromagnetic materials. Using a full-time integration approach instead of the harmonic one offers an advantage in addressing the ferromagnetic properties of materials. Magnetic permeability can be precisely defined as the derivative of the magnetic flux density concerning to the total magnetic field intensity ([31], [65]):

$$\mu = \frac{\partial |\vec{B}|}{\partial |\vec{H}|} \quad (3.43)$$

Frohlich-Kenelly ([66], [67], [68]) introduced a model for magnetic permeability as follows:

$$\mu(|\vec{H}|, T) = \mu_0 \left(1 + \frac{\alpha}{\mu_0(\beta + |\vec{H}|)} - \frac{\alpha|\vec{H}|}{\mu_0(\beta + |\vec{H}|)^2} \right) \quad (3.44)$$

Here, α and β are two constant coefficients. In this section, we examine the performance of the recovery-based error estimator under uniform and varying magnetic permeability conditions. A convergence analysis is conducted using the TEAM 7 benchmark case. Notably, most estimators studied in the literature are formulated in the frequency domain, while our model is discretized in the time domain. To deal with that, an average of time is computed to observe the estimator's behaviour.

$$E_e^{average}(x) = \frac{1}{T} \int_0^T |E_e(x, t)|^2 dt \quad (3.45)$$

Similar to previous cases, a mesh sensitivity analysis is performed on a modified version of the TEAM7 benchmark case to analyse how the estimator, based on the recovery of magnetic field, deals with variations in magnetic permeability. Three simulations were performed with varying workpiece magnetic permeabilities: constant $\mu_r = 1$ (uniform case), $\mu_r = 100$ (domain-wise uniform) and H-dependent $\mu_r(\vec{H})$ (non-harmonic case) are compared. The results, shown in Fig. 3.19, indicates a favourable convergence of error as the mesh size decreases for each case. By examining the error distribution within the plate, we observe the necessity for finer meshes when the workpiece material exhibits variable magnetic permeability. It must be noted that, this evaluation does not have extra impact in computation cost. These results underscore the efficiency of the error estimator in dealing with variable properties of materials in electromagnetic modelling, a crucial aspect in simulating industrial manufacturing processes.

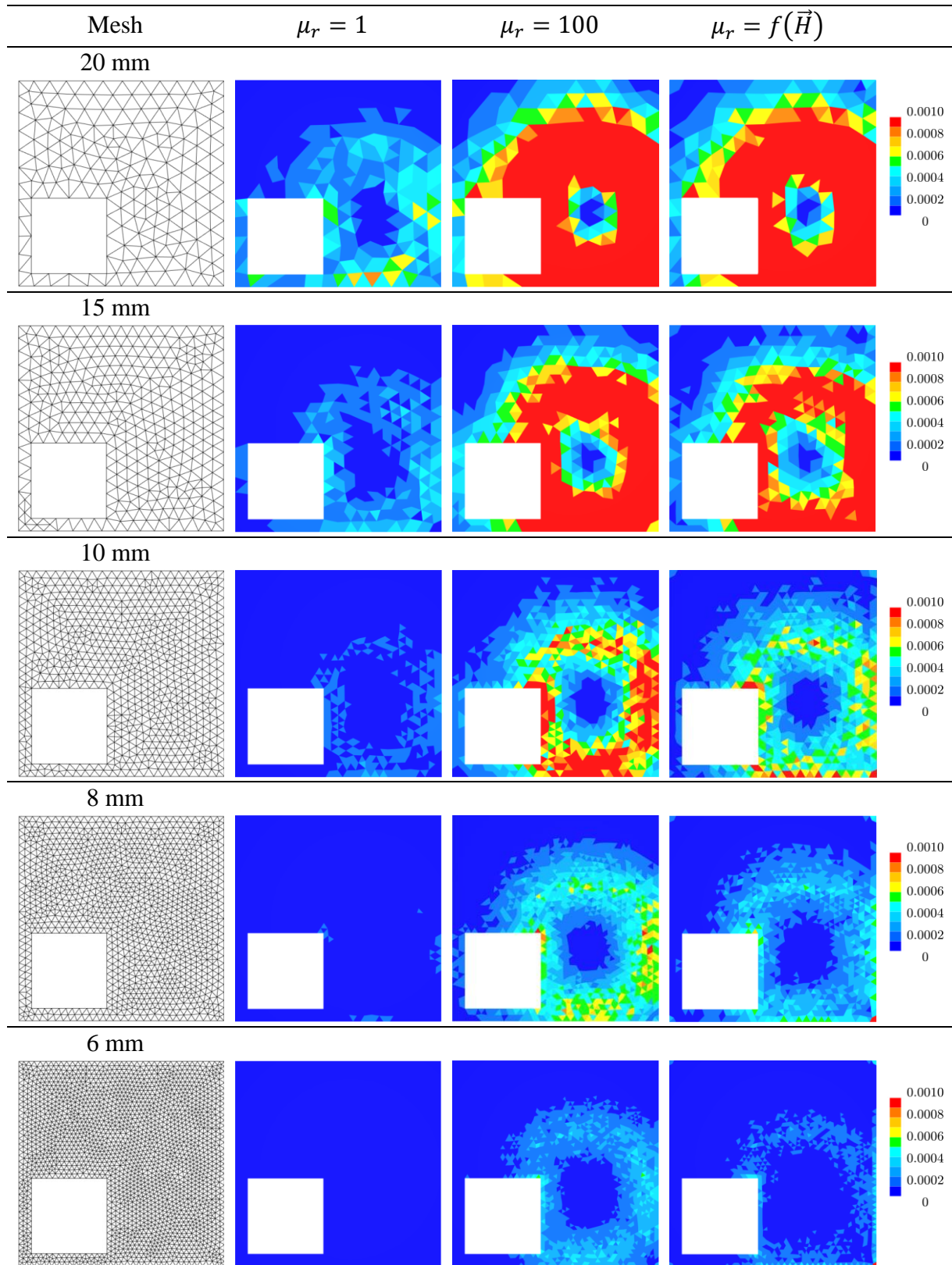


Fig. 3.19 Error distribution in the plate – magnetic permeability

3.7.4 Heat treatment case

As mentioned earlier, the primary objective of this study is to enable dealing with complex geometrical configurations encountered in practical industrial processes. Consequently, we chose to examine a heat treatment case involving a crankpin ([1],[69]) to analyse the capability and effectiveness of our estimator in providing error estimates. Fig. 3.20 illustrates the crankpin and inductor setup.

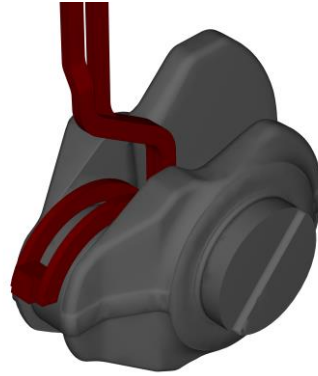


Fig. 3.20 Crankpin (in green) and inductor (in dark red)

The magnitude of the magnetic field at the end of the electric signal period is displayed in Fig. 3.21, providing insight into its distribution across the crankpin.

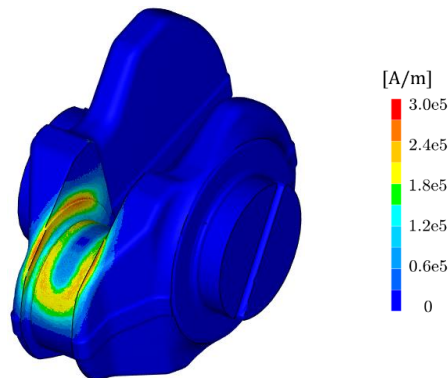


Fig. 3.21 Magnetic field magnitude (in A/m) at the end of the electromagnetic period.

Fig. 3.22 illustrates how the error estimate behaves throughout the electromagnetic period, with 135° and 315° representing time points equivalent to the root mean square (RMS) of the electrical signal over a period, and 360° marking the end of the period. When comparing the magnetic field and the error estimate at 360° , it becomes evident that the estimator effectively tracks the field's variation. Furthermore, the estimator correctly tracks the skin effect, accurately adapting to the complex geometry and the distribution of current circulation,

especially in regions affected by the nearby inductors, as displayed in Fig. 3.23. These regions may be candidates for future mesh size adaptation.

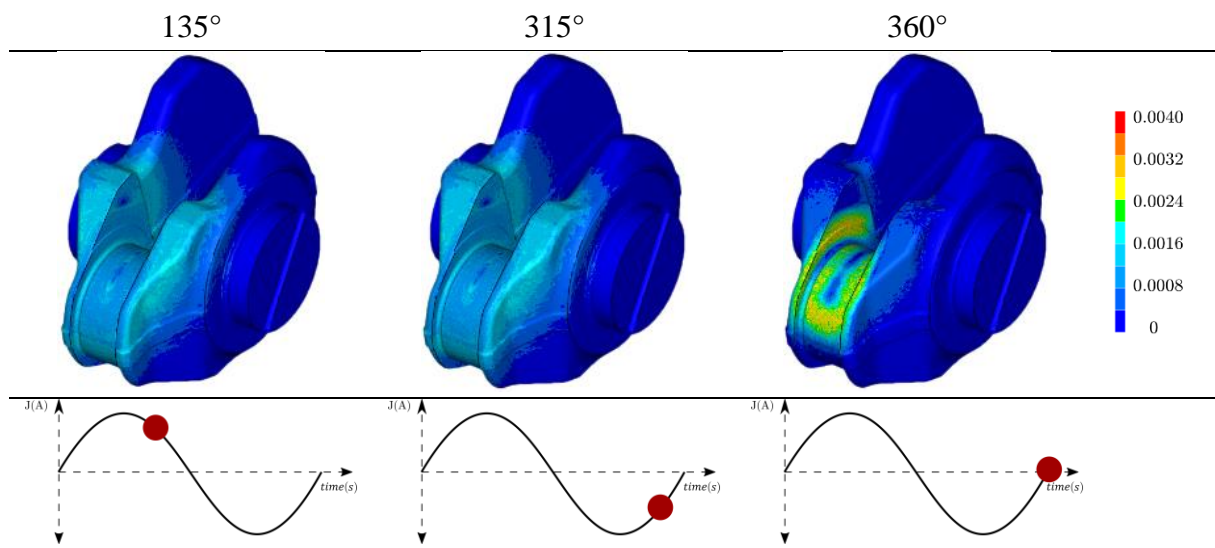


Fig. 3.22 Error distribution at different time steps of the sinusoidal signal

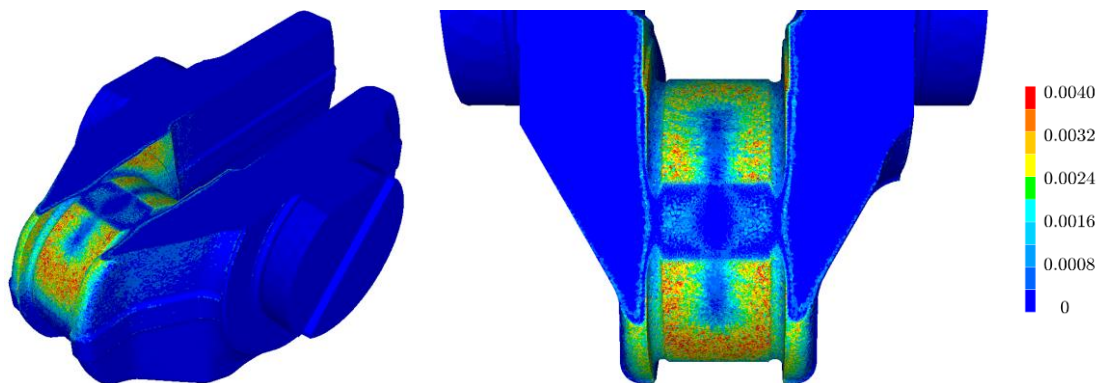


Fig. 3.23 Error distribution on the surface and a cutting plane at the end of the electromagnetic period (360°).

The simulation was executed on a single processor and in parallel using 16 processors, following a SPMD paradigm. Table 3.4 provides insights into the computational time required for the estimator in comparison to the solver's time for solving the entire finite element system. Remarkably, the estimator's computation time is notably lower, accounting for just 14.5% of the total time on a single processor and 10% in parallel.

Table 3.4 CPU Time for linear systems resolution [sec]

Processors	FEM	Recovery method
1	240	35
16	43.25	4.5

3.7.5 Magnetic pulse forming case

The magnetic pulse forming (MPF) technology or electromagnetic forming (EMF) consists in deforming metallic components through the application of an intense electromagnetic pulse. This process enters in the category of high-speed forming processes due to the range of strain rates that are usually attained, typically ranging from $10^3 s^{-1}$ to $10^4 s^{-1}$. Fig. 3.24 illustrates a typical setup for this process, featuring a coil and workpiece. In this setup, the plate has a diameter of 70 mm and a thickness of 1 mm , while the inductor has a diameter of 2 mm . The process utilizes a pulsed discharge signal with a natural frequency of 162 kHz . The primary objective of this case study is to evaluate how the estimator performs under the parameters applied. Notably, the magnetic field in this case is highly concentrated within a small area, as depicted in Fig. 3.25, which is shaped by the inductor's geometry. The aim is to assess how the estimator behaves in such complex configurations and at higher frequencies than those typically used in conventional induction heating processes.

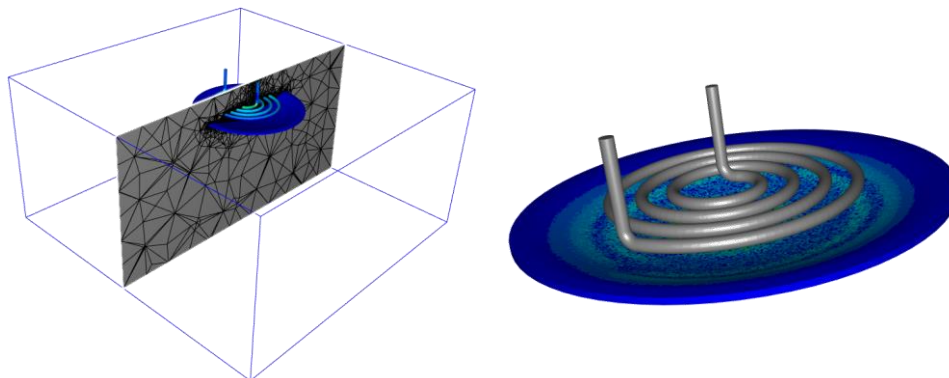
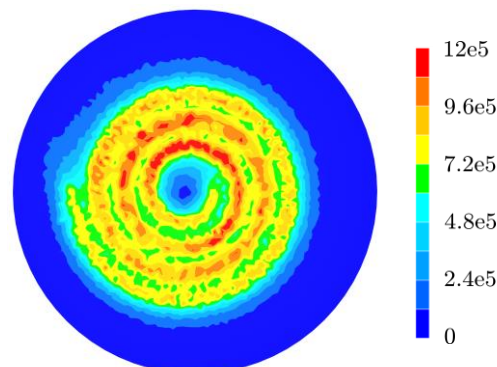


Fig. 3.24 Magnetic pulse forming case.

Fig. 3.25 Magnetic field distribution in A/m .

A convergence analysis has been conducted by progressively decreasing the mesh size across the workpiece. The mesh is uniformly defined with element sizes of 5 mm, 3 mm, and 1 mm. For better understanding, in Fig. 3.26, each mesh is visually represented alongside the corresponding error estimator calculated for that mesh.

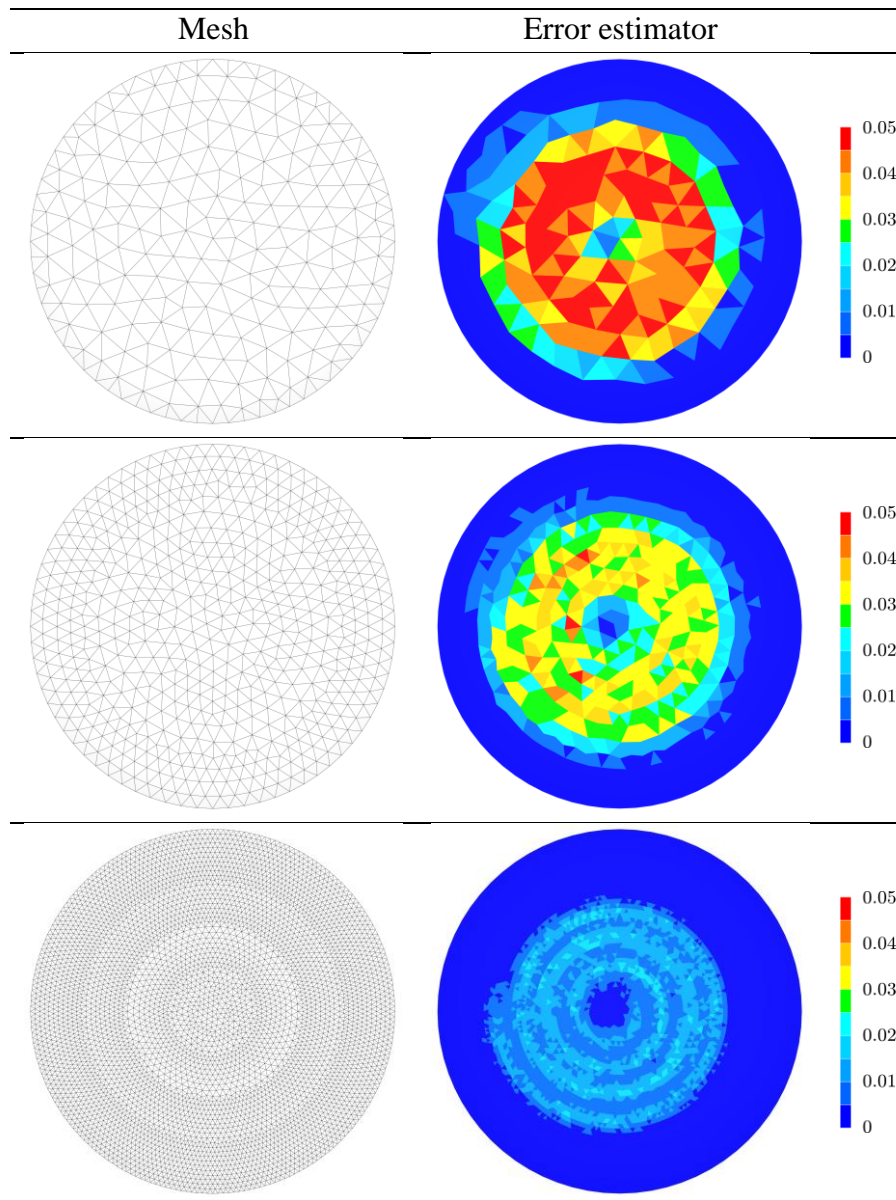


Fig. 3.26 Mesh and associated error distribution.

As illustrated in Fig. 3.26, the estimator effectively captures the magnetic field's variations, underscoring its capacity to handle intricate and complex field distributions.

3.7.6 Electromagnetic stirring case

The electromagnetic stirring process is widely used in the materials forming industry. It consists of using the time-varying electromagnetic field to manipulate the fluid flow within the liquid steel and the stirrer without any physical contact. This technique employs the Lorentz force, similarly to a linear induction motor, to disrupt the fluid flow of molten metal. This disruption leads to a more uniform solidification, preventing the premature growth of dendrites during the casting process and ultimately resulting in a higher quality final ingot. To evaluate the error estimator's performance in this process, a laboratory-scale stirring application of Galinstan melt in a plexiglass mould [70] have been selected. Unlike magnetic pulse forming, this process operates at lower frequencies, 2Hz in this case. The geometry of the melt and the inductor are depicted in Fig. 3.27. The melt geometry has a diameter of 62 mm and a height of 70 mm, while the inductor has a diameter of 8 mm. The distribution of the magnetic field across the inductor, the air, and the melt, is shown in Fig. 3.28.

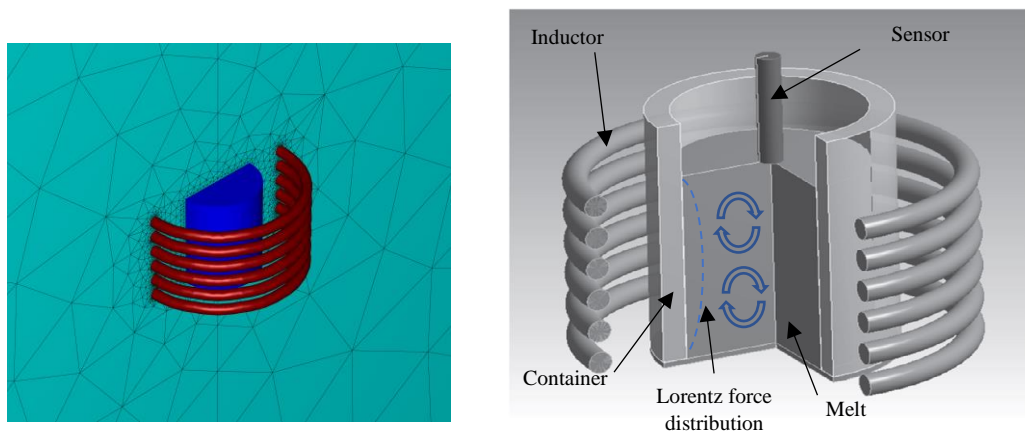


Fig. 3.27 Electromagnetic stirring case. Left: set-up immersed in the air. Right: scheme of the case proposed on [70].

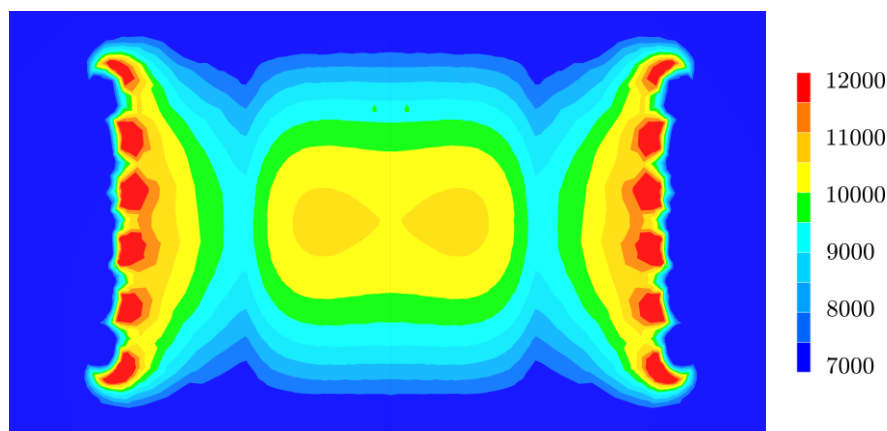


Fig. 3.28 Magnetic field distribution in A/m .

A convergence analysis is carried out by systematically reducing the mesh size on the melt portion. The mesh size uniformly decreases on the melt section with the same element size: 3mm, 2mm, and 1mm, while the mesh size on the inductor and air remains constant. Fig. 3.29 visually presents each mesh configuration alongside its corresponding error estimator.

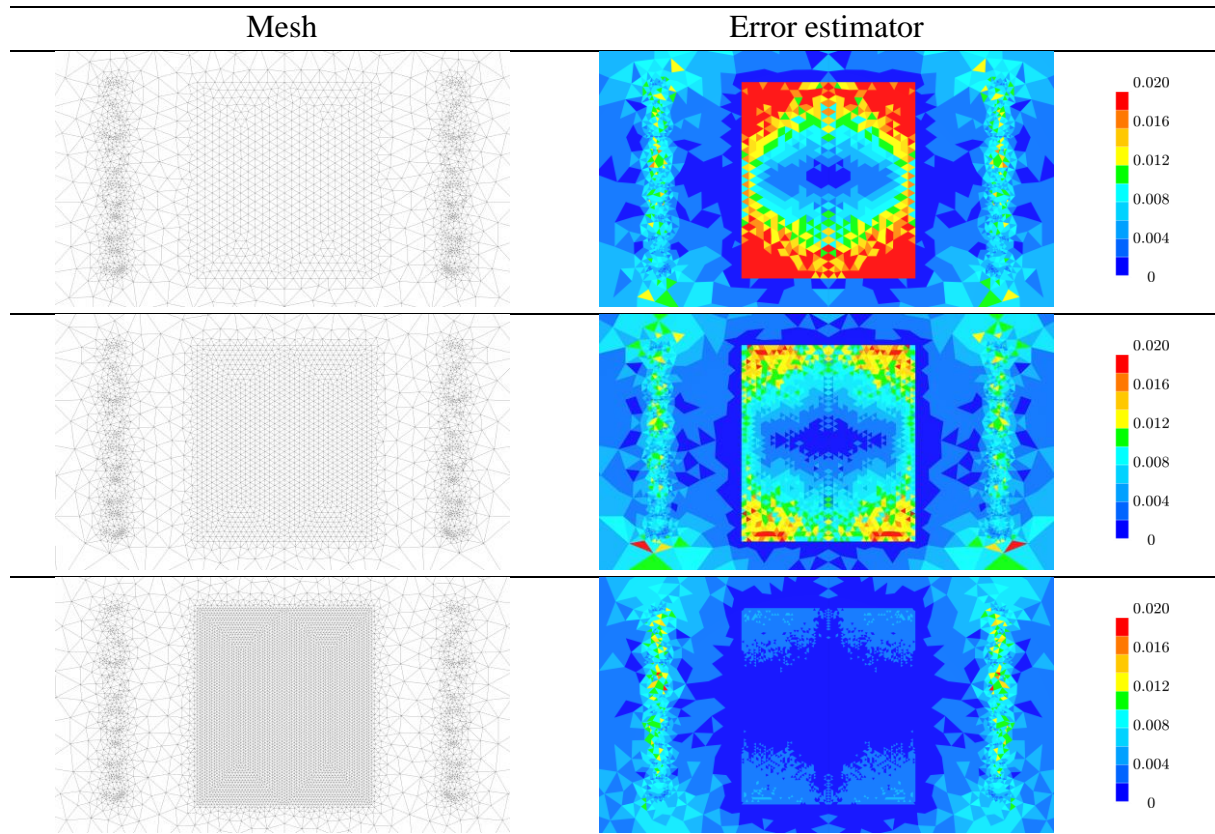


Fig. 3.29 Mesh and associated error distribution

Comparing the magnetic field distribution depicted in Fig. 3.28 with the error estimation presented in Fig. 3.29, it is evident that the estimator adeptly track the magnetic field gradient. Noticeably, larger errors occur in regions with more substantial magnetic field variation. Additionally, as the mesh size decreases, a clear convergence trend emerges, with the error diminishing significantly in the melt region. This performance underscores the estimator's capacity to accurately monitor errors in processes that employ lower frequencies, as exemplified in this stirring application.

3.8 Conclusions

In this chapter, several a posteriori error estimators for the modelling of electromagnetic processing of materials have been presented. Those estimators have been applied to a fully immersed finite element approach, working in conjunction with a full-time integration of the Maxwell equations. These estimators have been applied to the electromagnetic fields governing the induction phenomenon, such as the magnetic field and eddy current.

First, a recovery-based estimator has been developed using the Galerkin method, in order to construct a magnetic field with a higher interpolation order. This estimator has been validated by comparing it with the exact error in an analytical case.

Subsequently, two estimators based on the verification of fundamental principles of the electromagnetic induction phenomenon were developed: one grounded in Ampere's law and the other in Faraday's Induction law.

Additionally, two other estimators were also proposed. In the first, the recovered magnetic field was employed to compute a derived current density, which was then compared with the current density originally computed by the FEM. In the second, a procedure for assessing mesh accuracy was developed. It hinged on the verification of a fundamental vector calculus rule: the divergence of a curl must be zero. This estimator can be applied to any field, although the results were only shown in the magnetic field.

Following the development of these estimators each was subjected to rigorous testing on the TEAM7 benchmark case, focusing on a constant magnetic permeability. Furthermore, the performance of the recovery-based estimator when dealing with a space-dependent magnetic permeability have also been tested. This underscored its efficiency in handling the nonlinearity of material properties coefficients.

To further evaluate the capabilities of recovery-based, various industrial-like scenarios were explored. Firstly, a heat treatment case involving a complex crankpin geometry showcased the estimator's ability to handle intricate geometries. Secondly, we investigated a typical magnetic pulse forming case, pushing the estimator's limits with higher frequencies. Lastly, we delved into an electromagnetic stirring case, mirroring real-world industrial processes.

In conclusion, numerical results have solidified the theoretical foundations of our estimators. They have exhibited commendable convergence rates with the mesh. Despite the current density-based estimator's relatively lower order of convergence, its local convergence aligns well with the other estimators. Conversely, the estimator relying on the validation of Ampere's law and the one rooted in fundamental vector calculus principles exhibit sparse error patterns. This characteristic renders them less suitable for deployment in an adaptive remeshing procedure. We have successfully implemented these estimators in the commercial software FORGE® & THERCAST®, providing a robust foundation for future research. These estimators will be instrumental in conducting adaptive remeshing, advancing the field of electromagnetic material processing modelling.

Chapter 4

Mesh adaptation

4.1	Introduction	101
4.1.1	Electromagnetic-coupled processes and modelling	101
4.1.2	Metric based anisotropic mesh adaptation - basic principles	101
4.2	Anisotropic mesh adaptation	103
4.2.1	Metric based methods.....	103
4.2.1.1	Metric tensor.....	103
4.2.1.2	Evaluation of first and second order derivatives	106
4.2.1.2.1	Hessian from a scalar field ($\text{Hess}(x)$)	106
4.2.1.2.1.1	Hessian symmetrisation	108
4.2.1.2.2	Jacobian from a vector field ($J(x)$).....	109
4.2.1.3	Metric normalisation.....	111
4.2.2	Algorithms proposed	112
4.3	Anisotropy Capturing Comparison	113
4.3.1	Symmetrisation procedure.....	114
4.3.2	Anisotropic behaviour	115
4.4	Application to electromagnetic processing of materials	118
4.4.1	Intrinsic anisotropy.....	119
4.4.2	Isotropic vs Anisotropic performance comparison (model size/error distribution/etc)	120
4.4.3	Skin effect case.....	123
4.4.4	Industrial processes	125
4.4.4.1	Induction heating application	125
4.4.4.2	Magnetic Pulse forming application.....	127
4.4.4.3	Electromagnetic Stirring application	129
4.4.5	Magnetic and electric fields duality	130
4.5	Relation between the Hessian and the Jacobian	132
4.6	Conclusions.....	134

Résumé : Adaptation automatique de maillage pour la modélisation électromagnétique.

Ce chapitre se concentre sur la construction des métriques, une étape essentielle de l'adaptation de maillage en éléments finis. Ces métriques ont pour objectif de capturer le phénomène électromagnétique et servent d'entrée au mailleur pour la construction du maillage adaptatif.

Dans un premier temps, une bibliographie des adaptations de maillage implémentées dans la modélisation électromagnétique est présentée. Ensuite, deux métriques sont définies :

- La première est basée sur le calcul de la Hessien d'un champ scalaire.
- La deuxième est basée sur le calcul du Jacobien d'un champ vectoriel.

La capacité des deux métriques à capturer l'anisotropie des champs est évaluée à l'aide d'exemples concrets. Ensuite, des comparaisons des deux métriques avec des maillages isotropiques sont réalisées, ainsi que des applications aux cas industriels tels que le chauffage par induction, la mise en forme par impulsion magnétique et le brassage électromagnétique.

Finalement, une comparaison entre les deux métriques est également effectuée.

4 Mesh adaptation

Electromagnetic material processing often involves parts with complex geometries and materials with non-linear magnetic behaviour. Efficient modelling of these processes can often be highly demanding in terms of CPU time and resources. Anisotropic mesh adaptation allows capturing the behaviour of complex physical phenomena, as well as improving the accuracy of the numerical solution. Appropriate control of the algorithm ensures a prescribed accuracy with a reduced number of degrees of freedom. The main purpose of this chapter is to construct a metric tensor to carry on an anisotropic mesh adaptation procedure dealing with the electromagnetic phenomenon. This approach will be implemented within our fully immersed computational, thus, allowing for adaptive remeshing across the entire domain.

4.1 Introduction

4.1.1 Electromagnetic-coupled processes and modelling

The continuous improvement of computational processing units (CPUs/GPUs) and the availability of high-performance computing (HPC) infrastructures enables computational models to become increasingly realistic and accurate – thus dealing to an increased numerical complexity. In order to reduce the time from concept to production by improving the engineering design stage, one of the main challenges and opportunities for improving numerical methods is to automatize the generation and adaptation of meshes. In the finite element method, the computational domain is divided into a finite number of elements on which the system of partial differential equations describing the physical phenomena is discretised. To achieve an accurate numerical solution, elements must comply with a minimum geometrical quality criterion in order to limit the influence of round-off errors, intrinsic to finite precision arithmetic. Moreover, a very fine discretization results in a large number of elements leading to a large memory and CPU time requirements. To overcome this situation, mesh adaptation methods have been developed. These methods involve identifying regions where the numerical solution is not sufficiently accurate and proposing local refinements, as well as de-refinements enabling efficiently reallocation of computational resources elsewhere in the domain.

4.1.2 Metric based anisotropic mesh adaptation - basic principles

The relationship between mesh generation and achieving a suitable numerical solution has been a significant research topic in the engineering community for many years. The primary goal is to attain a high level of accuracy in the numerical solution while minimizing the number of degrees of freedom in the mesh.

Anisotropic mesh adaptation is a valuable tool widely employed in mesh generation to optimize the numerical solution. It enables to adapt the size, shape and orientation of elements in order to achieve a specific accuracy of the solution while improving the computational performance. Anisotropic mesh adaptation aims to create an optimal mesh of the computational domain, ensuring that the error of the solution of the considered problem is uniformly distributed throughout the entire domain.

The main requirement of this approach is the correct calculation of the metric, typically based on some error estimate. It is worth mentioning that error estimators based on local error problems can be inaccurate in producing anisotropic meshes [71]. In fact, these estimators usually do not contain enough information about the direction of the solution, which is global in nature. Additionally, their accuracy and efficiency can be sensitive to the aspect ratio of the elements, which can be large for anisotropic meshes. Therefore, it is desirable to define an error estimate using a globally defined error problem. Several methods have been published on the use of a posteriori error estimators to control anisotropic mesh adaptation. Among them we can mention: Huang et al. [72] developed and compared a hierarchical error estimator with a recovery-based method. Cao et al. [73] calculated some scalar monitoring functions to use adaptive mesh motion from interpolation errors and a posteriori error estimates. Apel et al. [74] used the gradients of some a posteriori error estimates for calculating anisotropic meshes. Agouzal et al. [75] calculated a metric tensor from edge-based error estimates.

One approach employed for constructing the metric tensor field to generate adaptive meshes involves computing the Hessian of an exact solution of a scalar field. However, finding an exact solution is in most cases impossible, numerical methods must be used to construct it from the finite element solution. One of the most commonly used methods is based on recovery strategies. In fact, these strategies are quite attractive since they are not tied to a particular numerical scheme or to a specific application and can be applied to a wide range of PDEs, providing high-dimensional information of the solution [76][77]. Most of these recovery techniques, often utilizing discrete least squares or integral formulation, compute nodal values based on the gradients over neighbouring elements. Other recovery techniques include simple weighted average methods [78] and minimization problems [79]. Lipnikov and Vassilevski [80] conducted a comparative analysis of these methods, assessing three of them, a variational method [81] and two projection methods [82][83]. Their findings indicated that the variational method is less expensive and offers the most accurate interpolation solution as well as the most robust behavior on a larger scale of norms compared to the other methods. Additionally, Agouzal and Vassilevski introduced another variation method for the Hessian recovery in [84].

In electromagnetic modelling, research into adaptive remeshing remains relatively underexplored, we can mention the work of Grosgees et al, primarily focusing in 2D and 3D for simple geometries in the calculation of high electromagnetic field gradients [85]–[87]. In this chapter, we develop an adaptive remeshing procedure for finite element methods, based on Hessian or Jacobian recovery strategies, which enables dealing with complex geometries for electromagnetically coupled material processing applications.

4.2 Anisotropic mesh adaptation

Anisotropic mesh generation is based on defining a discrete metric tensor at each node, enabling precise control of size, shape and orientation of mesh elements. This metric tensor is defined as a symmetric positive-definite square matrix. In simple terms, a metric is used to measure locally space, in a different way from the classical identity tensor.

4.2.1 Metric based methods

Among the various strategies for mesh adaptation, metric-based mesh adaptation stands out as the most widely employed approach for achieving anisotropic mesh generation. Its main feature lies in the construction of a metric tensor, which contains the necessary information for guiding the generation of anisotropic meshes. In order to generate such meshes, domain the desired sizes and directions of the final mesh elements is determined at each point of the domain. To accomplish this, a tensor field must be established at each point of the domain, allowing to evaluate the lengths and angles within the mesh. Anisotropic mesh adaptation, based on metric fields, requires the construction of several quantities, These includes an error estimator for controlling mesh size, as well as normalizing the metric, alongside values describing the deformation or distortion of the non-Euclidean manifold resulting from the action of existing physical fields.

4.2.1.1 Metric tensor

The fundamental concept behind a metric-based mesh generator is to create a unit mesh within a prescribed metric space. The key to generate a unit mesh lies in defining a unit element. Specifically, an element K is considered a unit element when each of its edges have a length equal to the unity within the metric \mathcal{M} .

$$l_{\mathcal{M}}(e_i) = 1, \forall i = 1, 2, \dots, n \quad (4.1)$$

Where n is the number of edges. In 2D, $n = 2$ for a triangle, and in 3D, $n = 6$ for tetrahedron.

The metric tensor \mathcal{M} is defined as a symmetric positive-definite square matrix:

- Symmetry

$$\langle u, \mathcal{M}v \rangle = \langle v, \mathcal{M}u \rangle ; \forall (u, v) \in \mathbb{R}^3 \times \mathbb{R}^3$$

- Positive

$$\langle u, \mathcal{M}u \rangle \geq 0 ; \forall u \in \mathbb{R}^3$$

- Definite

$$\langle u, \mathcal{M}u \rangle = 0 \Rightarrow u = 0 ; \forall u \in \mathbb{R}^3$$

The scalar product in a metric space conforming to a metric \mathcal{M} can be defined as:

$$\langle x, x \rangle = x^T \mathcal{M} x \quad (4.2)$$

And its corresponding norm can be defined as follows:

$$\|x\|_{\mathcal{M}} = \sqrt{x^T \mathcal{M} x} \quad (4.3)$$

It is worth mentioning that the geometric representation of \mathcal{M} in \mathbb{R}^3 is an ellipsoid, as illustrated in Fig. 4.1. The ellipsoid's axes align with the eigenvectors \mathcal{R} , and its size given by the eigenvalues Λ by $h_i = \lambda_i^{-1/2}$.

In order to define a desired mesh size in a specific direction, the metric tensor needs to be construct. The primary purpose of the metric \mathcal{M} is to establish a mapping between a Euclidian space and a metric space, and vice versa. In this context, the scalar product in the Euclidian space is defined as:

$$\langle x, x \rangle = x^T x \quad (4.4)$$

And the associated Euclidean norm is given by

$$\|x\| = \sqrt{x^T x} \quad (4.5)$$

In order to comprehend how the metric \mathcal{M} works, Fig. 4.1 outlines its underlying principle.

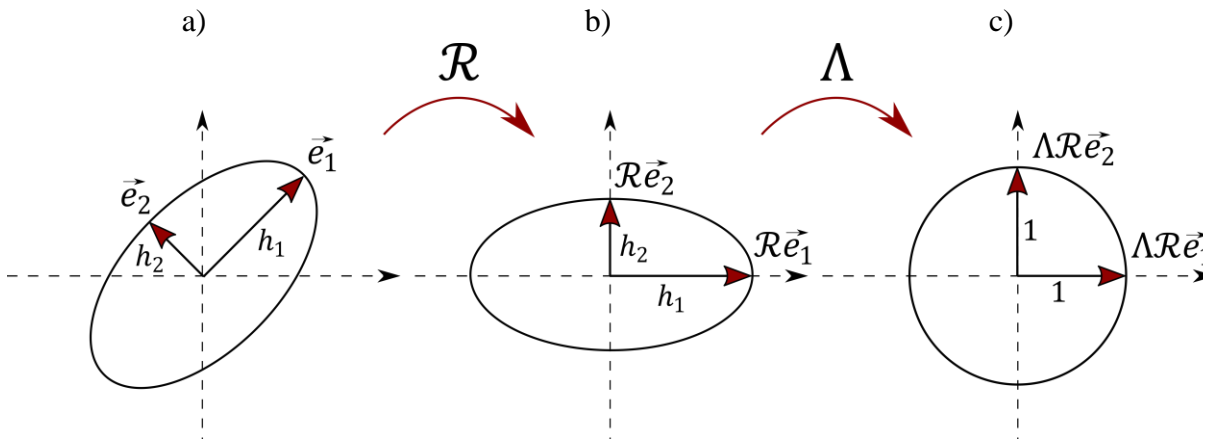


Fig. 4.1 Metric principle: transformation steps from a Euclidean space to a metric space

Fig. 4.1.a shows a Euclidean space represented by an ellipse, in 2D, with principal directions \vec{e}_1 and \vec{e}_2 and respective sizes h_1 and h_2 . These principal directions are assumed to be perpendicular to each other. To map from this Euclidean space to the metric space depicted in Fig. 4.1.c, a transformation is performed. This transformation typically involves a combination of a rotation matrix \mathcal{R} and a scaling matrix Λ . Initially, the rotation matrix \mathcal{R} modifies the direction of \vec{e}_1 and \vec{e}_2 to align with the principal axes of a transformed space shown

in Fig. 4.1.b. Subsequently, the scaling matrix Λ is applied to resize the axes to the unit lengths, as shows in Fig. 4.1.c. The matrix Λ is diagonal with coefficients equal to:

$$\Lambda = \text{diag}(\lambda_i); \quad \lambda_i = 1/h_i \quad (4.6)$$

Having established the framework for space transformation, we can now define a vector x within the interior of the ellipse of Fig. 4.1.a, then its corresponding vector in the metric space $x_{\mathcal{M}}$ is prescribed by:

$$x_{\mathcal{M}} = \Lambda \mathcal{R}x \quad (4.7)$$

Once this transformation is accomplished, the length of the vector $x_{\mathcal{M}}$ can be computed using equation (4.5):

$$l_{x_{\mathcal{M}}} = \sqrt{x_{\mathcal{M}}^T x_{\mathcal{M}}} \quad (4.8)$$

Substituting the transformation of $x_{\mathcal{M}}$ into equation (4.8), we get:

$$l_{x_{\mathcal{M}}} = \sqrt{x^T \mathcal{R}^T \Lambda^T \Lambda \mathcal{R}x} \quad (4.9)$$

Since the scaling matrix Λ is diagonal, the above expression can be represented as:

$$l_{x_{\mathcal{M}}} = \sqrt{x^T \mathcal{R}^T \Lambda^2 \mathcal{R}x} \quad (4.10)$$

The metric \mathcal{M} is then defined as:

$$\mathcal{M} = \mathcal{R} \Lambda \mathcal{R}^T \quad (4.11)$$

Here, $\lambda_i = 1/h_i^2$. In \mathbb{R}^3 , \mathcal{M} is typically represented as a 3×3 matrix:

$$R = \langle \vec{e}_1, \vec{e}_2, \vec{e}_3 \rangle \quad (4.12)$$

And

$$\Lambda = \begin{bmatrix} \lambda_1 & 0 & 0 \\ 0 & \lambda_2 & 0 \\ 0 & 0 & \lambda_3 \end{bmatrix} \quad (4.13)$$

Where $\vec{e}_1, \vec{e}_2, \vec{e}_3$ are the eigenvectors, and $\lambda_1, \lambda_2, \lambda_3$ the eigenvalues of \mathcal{M} .

4.2.1.2 Evaluation of first and second order derivatives

To determine the metric field, a Galerkin recovery or residual minimization recovery procedure is employed. The metric tensor allows the measurement of distances or similarities between objects in a given space., then providing essential information for adapting the mesh according to a predefined field. This chapter explores two distinct methods for calculating the metric tensor. The first method involves deriving a Hessian field from a scalar field, commencing with any field norm. On the other hand, the second method calculates the metric as the Jacobian of a vector field. Both approaches are detailed hereafter.

4.2.1.2.1 Hessian from a scalar field ($\text{Hess}(\|\vec{x}\|)$)

One approach to measuring the anisotropy and mesh size of a given function u is through the calculation of its Hessian. The Hessian is a square matrix of second-order partial derivatives of a scalar-valued function, which measures the local curvature of a function with many variables. This concept was postulated by Alauzet [88], who proposed an estimator for interpolation error from which a metric based on the Hessian of the function u naturally appears. The linear interpolate of the function u , denoted as $\Pi_h u(x)$, used to construct the error estimator is given by:

$$\Pi_h u(x) = \sum_{i=1}^n u(p_i) \varphi_i(x) \quad (4.14)$$

Here, φ is the nodal shape function, and n represents the number of vertices or degrees of freedom of the element, By definition:

$$\Pi_h u(p_i) = u(p_i) \quad (4.15)$$

Let's define a tetrahedral element K with its four vertices are represented by $[a, b, c, d]$ and its six edges by e_j with $[j = 1, \dots, 6]$. Assuming that u is a twice-differentiable function, we aim to bound the interpolation error as:

$$\epsilon = u - \Pi_h u \quad (4.16)$$

A Taylor expansion is used to compute the error estimator at a vertex, e.g. "a", with respect to any internal point of the tetrahedron K . This leads to the expression:

$$\begin{aligned} (u - \Pi_h u)(a) &= (u - \Pi_h u)(x) + \langle ax, \vec{\nabla}(u - \Pi_h u)(x) \rangle \\ &\quad + 1/2 \langle ax, \vec{\nabla}^2(u - \Pi_h u)(x) ax \rangle \end{aligned} \quad (4.17)$$

Where $\vec{\nabla}$ represents the gradient operator and $\vec{\nabla}^2 t$ is the Laplacian, which by definition is the Hessian (Hess) of the interpolation error. Assuming that the maximal error occurs at point x , the gradient vanishes at this point:

$$\vec{\nabla}(u - \Pi_h u)(x) = 0 \quad (4.18)$$

Then, using the definition of linear interpolate (4.15), we have:

$$(u - \Pi_h u)(a) = 0 \quad (4.19)$$

Now, the expression (4.17) can be rewritten as:

$$(u - \Pi_h u)(x) = |\langle ax, \text{Hess}(u - \Pi_h u)(x)ax \rangle| \quad (4.20)$$

This implies that the error at any point x of K is directly related to the Hessian:

$$|\epsilon(x)| = |\langle ax, \text{Hess}(u - \Pi_h u)(x)ax \rangle| \quad (4.21)$$

By using the metric space norm defined in (4.2), it becomes evident that the Hessian can be considerate a metric:

$$\|\epsilon(x)\|^2 = (ax)^T \text{Hess}(u - \Pi_h u)(x)(ax) \quad (4.22)$$

Now, the question arises: how do we compute the Hessian? Similar to the calculation of the a posteriori error estimator, a recovery-based procedure is developed to construct the Hessian field. This procedure is based on the Galerkin minimisation problem and involves the following steps:

Let X_{P_0} be a scalar continuous field, computed by recovery from the error estimator or any field norm $\|X\|$. A recovered field X_{P_1} at the nodes is calculated through a global minimization problem as:

$$\langle \varphi, X_{P_1} - X_{P_0} \rangle = 0 \quad \forall \varphi \in V \quad (4.23)$$

Here, φ is the nodal basis function. Then, a discontinuous gradient vector field $\vec{\nabla}(X)_{P_0}$ is calculated at the Gauss points using the finite element definition:

$$\vec{\nabla}(X)_{P_0} = \sum_{i=1}^{\text{nodes}} \vec{\nabla} \varphi_i X_{P_{1i}} \quad (4.24)$$

In order to construct the Hessian field, the above procedure is repeated. First, a continuous gradient field by recovery \vec{G}_{P_1} is computed by recovery from $\vec{\nabla}(X)_{P_0}$ at the nodes as:

$$\langle \varphi, \vec{G}_{P_1} - \vec{\nabla}(X)_{P_0} \rangle = 0 \quad \forall \varphi \in V \quad (4.25)$$

Using (4.24) again, the discontinuous Hessian tensor field $\overline{\overline{\text{Hess}}}_{P_0}$ is computed at the Gauss points:

$$\overline{\overline{\text{Hess}}}_{P_0} = \sum_{i=1}^{\text{nodes}} \vec{\nabla}\varphi_i \vec{G}_{P_{1i}} \quad (4.26)$$

Finally, the recovery method is employed to compute the continuous Hessian tensor field $\overline{\overline{\text{Hess}}}_{P_1}$ at every node within the mesh.

$$\langle \varphi, \overline{\overline{\text{Hess}}}_{P_1} - \overline{\overline{\text{Hess}}}_{P_0} \rangle = 0 \quad \forall \varphi \in V \quad (4.27)$$

4.2.1.2.1.1 Hessian symmetrisation

The resulting tensor obtained above is typically not positive definite. To address this issue, both symmetry and positive definiteness need to be enforced. Two methods of symmetrisation have been tested. The first one involves taking the average between the tensor and its transpose, (since the purpose of this section is to symmetrize a tensor, the letter T will be used to represent them), represented here as $\overline{\overline{T}}_1$:

$$\overline{\overline{T}}_1 = \frac{1}{2} (\overline{\overline{T}}_1^T + \overline{\overline{T}}_1) \quad (4.28)$$

While this naïve approach is rather straightforward to implement and computationally cheap, it does not guarantee positive definiteness. Therefore, a second approach that ensures both requirements can be achieved using the conjugate product:

$$\overline{\overline{T}}_2 = \overline{\overline{T}}_1^T \overline{\overline{T}}_1 \quad (4.29)$$

Once the symmetrisation methods are applied, the resulting tensor in equation from equation (4.29) requires further processing, thus the eigenvectors and eigenvalues are calculated as follows:

$$\overline{\overline{R}}, \overline{\overline{\Lambda}} = \text{eig}(\text{Hess}(\|\vec{x}\|)) \quad (4.30)$$

The metric $\overline{\overline{M}}$ is then deduced from the eigenvalues and eigenvectors, particularly since the Hessian tensor is square in this case:

$$\overline{\overline{M}} = \overline{\overline{R}} \overline{\overline{\Lambda}} \overline{\overline{R}}^T \text{ with } \overline{\overline{\Lambda}} = \text{diag}(\lambda_i^{1/2}) \quad (4.31)$$

On the other hand, the metric symmetrisation calculated with (4.28) requires no further modification. In both cases, it leads to a metric that is proportional to the inverse of the square of the mesh size:

$$\bar{M} \propto \frac{1}{h^2} \quad (4.32)$$

4.2.1.2.2 Jacobian from a vector field ($J(\vec{x})$)

In our approach to construct an appropriate metric for capturing the anisotropic behaviour of electromagnetic fields, we begin by utilizing the Jacobian for a multivariable vector-valued function. This Jacobian is computed as the transpose of its gradient. When a function at a point is differentiable, the Jacobian matrix describes the local stretching and rotation imposed by the function near that point. The Jacobian of a vector field is expressed as:

$$J(\vec{u}) = \vec{\nabla}^T \vec{u} = \begin{bmatrix} \frac{\partial u_1}{\partial x_1} & \frac{\partial u_1}{\partial x_2} & \frac{\partial u_1}{\partial x_3} \\ \frac{\partial u_2}{\partial x_1} & \frac{\partial u_2}{\partial x_2} & \frac{\partial u_2}{\partial x_3} \\ \frac{\partial u_3}{\partial x_1} & \frac{\partial u_3}{\partial x_2} & \frac{\partial u_3}{\partial x_3} \end{bmatrix} \quad (4.33)$$

In the case of a differentiable vector function “ u ” at a point \vec{x}_0 , the Jacobian matrix ($J(u)$) provides the best linear approximation of “ u ” near the point x_0 . This can be represented through the Taylor expansion of u , as follows:

$$u(\vec{x}) = u(\vec{x}_0) + \vec{\nabla}(u(\vec{x}_0))(\vec{x} - \vec{x}_0) + O(\|\vec{x} - \vec{x}_0\|) \quad (4.34)$$

Rearranging the above expression:

$$u(\vec{x}) - u(\vec{x}_0) = \vec{\nabla}(u(\vec{x}_0))(\vec{x} - \vec{x}_0) + O(\|\vec{x} - \vec{x}_0\|) \quad (4.35)$$

Here, we define an error term for the approximation of \vec{x} :

$$\epsilon(\vec{x}) = u(\vec{x}) - u(\vec{x}_0) \quad (4.36)$$

The norm of this error can be expressed as a dot product:

$$\|\epsilon(\vec{x})\|^2 = \langle \epsilon(\vec{x}), \epsilon(\vec{x}) \rangle \quad (4.37)$$

Substituting the value:

$$\|\epsilon(\vec{x})\|^2 = \left(\vec{\nabla}(u(\vec{x}_0))(\vec{x} - \vec{x}_0) \cdot \vec{\nabla}(u(\vec{x}_0))(\vec{x} - \vec{x}_0) \right) \quad (4.38)$$

The above expression can be reordered as follows:

$$||\epsilon(\vec{x})||^2 = (\vec{x} - \vec{x}_0)^T \vec{\nabla}^T(u(\vec{x}_0)) \vec{\nabla}(u(\vec{x}_0)) (\vec{x} - \vec{x}_0) \quad (4.39)$$

From this, a metric tensor is defined as:

$$\bar{\bar{M}} = \vec{\nabla}^T(u(\vec{x}_0)) \vec{\nabla}(u(\vec{x}_0)) \quad (4.40)$$

Then, the expression can be rewritten as:

$$||\epsilon(\vec{x})||^2 = (\vec{x} - \vec{x}_0)^T \bar{\bar{M}} (\vec{x} - \vec{x}_0) \quad (4.41)$$

In this case, the procedure applied is also based on a recovery procedure. However, this procedure is only applied once to access the gradient (second-order tensor) of the vector field \vec{X} . Since the gradient of any vector field is represented as a matrix, the transpose of this matrix is used as the Jacobian of any vector field to compute the metric tensor.

Let \vec{X}_{P_0} be an elementwise vector field. Then, a recovered continuous vector field \vec{X}_{P_1} at the element nodes can be computed by recovery as follows:

$$\langle \varphi, \vec{X}_{P_1} - \vec{X}_{P_0} \rangle = 0 \quad (4.42)$$

Then, a discontinuous gradient field $\vec{\nabla}(\vec{X})_{P_0}$ at the Gauss points from \vec{X}_{P_1} is calculated using the finite element definition:

$$\vec{\nabla}(\vec{X})_{P_0} = \sum_{i=1}^{\text{nodes}} \vec{\nabla} \varphi_i \vec{X}_{P_{1i}} \quad (4.43)$$

Since $\vec{\nabla}(\vec{X})_{P_0}$ is inherently a tensor field, the recovery procedure is again employed to calculate the continuous Jacobian tensor field $\bar{\bar{J}}_{P_1}$ from $\vec{\nabla}(\vec{X})_{P_0}$ at each node of the mesh:

$$\langle \varphi, \bar{\bar{J}}_{P_1} - \vec{\nabla} \vec{X}_{P_0} \rangle = 0 \quad (4.44)$$

Once the Jacobian is calculated, equation (4.40) is employed to build the metric:

$$\bar{\bar{M}} = \bar{\bar{J}}_{P_1}^T \bar{\bar{J}}_{P_1} \quad (4.45)$$

The metric approximated using the Jacobian is a square tensor of the first derivatives. Expression (4.45) directly ensures the symmetry and positive definiteness of the metric, avoiding the need for further tensor treatment. The eigenvectors and eigenvalues are computed from the Jacobian using:

$$\bar{\mathbf{R}}, \bar{\Lambda} = \text{eig}(\bar{\mathbf{M}}) \quad (4.46)$$

Then, to compute the metric $\bar{\mathbf{M}}$, no linearization is required:

$$\bar{\mathbf{M}} = \bar{\mathbf{R}}\bar{\Lambda}\bar{\mathbf{R}}^T \text{ with } \bar{\Lambda} = \text{diag}(\lambda_i) \quad (4.47)$$

Therefore, as in the case of the Hess($\|x\|$) method, this approach also leads to the same proportionality between the metric and the mesh size:

$$\bar{\mathbf{M}} \propto \frac{1}{h^2} \quad (4.48)$$

4.2.1.3 Metric normalisation

As defined in equation (4.1) the unit element requires that each of its edges has a length equal to unity. In order to achieve this a normalisation of the metric is required. Using the definition of the dot product, the computed error on an element with edge (\vec{e}) can be expressed as:

$$\epsilon = \langle \vec{e}, \mathcal{M} \vec{e} \rangle \quad (4.49)$$

Thus, a metric providing a unit length is defined as:

$$\bar{\mathcal{M}} = \frac{\bar{\mathbf{M}}}{\epsilon} \quad (4.50)$$

The expression in equation (4.49) can be rewritten as:

$$\langle \vec{e}, \bar{\mathcal{M}} \vec{e} \rangle = 1 \quad (4.51)$$

Therefore, the metric $\bar{\mathcal{M}}$ enables the construction of a unit mesh with edge lengths equal to 1:

$$l_{\mathcal{M}}(e_i) = \sqrt{\langle \vec{e}_i, \bar{\mathcal{M}} \vec{e}_i \rangle} = 1 \quad (4.52)$$

This allows for equidistribution of the error over the new mesh.

As illustrated in Fig. 4.1, the scaling step of the transformation is determined by the eigenvalue matrix. In fact, the eigenvalues enable to relate the required mesh size (h) along the eigenvector's directions and the error estimator by using the proportionality ratio.

$$\lambda_i = \frac{1}{h_i^2} \quad (4.53)$$

In order to prevent non-usable metric specifications, such as infinite mesh sizes in an element, caused for instance, by highly single-directional fields, the eigenvalues are rescaled by applying an error tolerance (ϵ_0) computed from equation (3.21), as defined in equation (4.50), and bounding the minimal (h_{min}) and maximal (h_{max}) mesh size values:

$$\tilde{\lambda}_i = \min\left(\max\left(\frac{\lambda_i}{\epsilon_0}, \frac{1}{h_{max}^2}\right), \frac{1}{h_{min}^2}\right) \quad (4.54)$$

In the case of anisotropy loss due to normalization, the ratio between the eigenvalues are stored as:

$$r_{12} = \frac{\lambda_1}{\lambda_2} \quad (4.55)$$

$$r_{13} = \frac{\lambda_1}{\lambda_3} \quad (4.56)$$

Then, once the normalization defined by equation (4.54) has been applied, the eigenvalues are checked to see if their values are the same ($\tilde{\lambda}_1 = \tilde{\lambda}_2 = \tilde{\lambda}_3$), in which case, the eigenvalues are again rescaled according to equations (4.55) and (4.56). This enables maintaining the anisotropy of the solution while ensuring a reasonable mesh size.

Finally, the metric is deduced as:

$$\bar{\bar{\mathcal{M}}}_i = \bar{\bar{\mathbf{R}}}_i \bar{\bar{\Lambda}}_i \bar{\bar{\mathbf{R}}}_i^T \quad (4.57)$$

For the sake of simplicity, the double-bar notation for second-order tensors will not be used for the final metric \mathcal{M} .

4.2.2 Algorithms proposed

The procedures for computing the metric tensor are summarized on the next following algorithms:

Table 4.1 Metric computed from a scalar field

Steps	Description
$\ X\ _{L^2(\Omega)}$: Compute scalar discrete field norm (P_0) from a postprocessed vector field
X	: Compute scalar continuous field (P_1) by recovery on $\ X\ _{L^2(\Omega)}$
$\vec{\nabla}(X)$: Compute discontinuous gradient vector field (P_0) by gradient computation of X
\vec{G}	: Compute continuous gradient vector field (P_1) by recovery on $\vec{\nabla}(X)$

$\vec{\nabla}(\vec{G})$:	Compute discontinuous hessian tensor field (P_0) by gradient computation of \vec{G}
$\overline{\overline{Hess}}$:	Compute continuous hessian tensor Field (P_1) by recovery on $\vec{\nabla}(\vec{G})$
$\overline{\overline{M}}$:	Transform the Hessian into a symmetric positive-definite matrix
$\mathcal{M}(\ x\)$:	Normalize the eigenvalues to construct the metric tensor

Table 4.2 Metric computed from a vector field.

Steps		Description
\vec{X}	:	Vector discrete field (P_0)
$\vec{\nabla}(\vec{X})$:	Compute discontinuous hessian tensor field (P_0) by gradient computation of \vec{X}
$\overline{\overline{J}}$:	Compute continuous Jacobian tensor Field (P_1) by recovery on $\vec{\nabla}(\vec{X})$
$\overline{\overline{M}}$:	Transforming the Jacobian into a symmetric positive-definite matrix
$\mathcal{M}(x)$:	Normalize the eigenvalues to construct the metric tensor

4.3 Anisotropy Capturing Comparison

This section compares the metric calculated from a Hessian field ($\mathcal{M}(\|x\|)$) and the metric calculated from a Jacobian matrix $\mathcal{M}(x)$ of a vector field \vec{x} .

Initially, the symmetrisation procedure for the Hessian is tested, followed by an examination of their ability to capture the anisotropy. To demonstrate this, a simple case is proposed, which is depicted in Fig. 4.2, where the workpiece and the inductor are represented as thin plates.

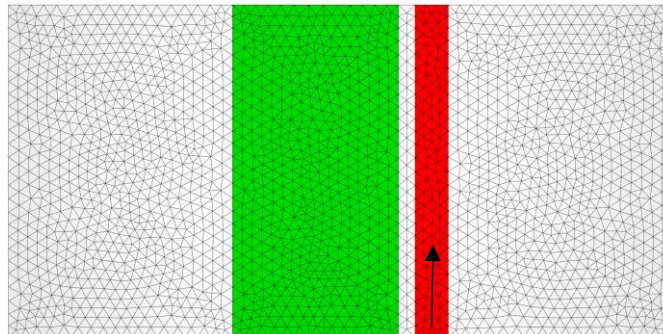


Fig. 4.2. Workpiece (green), Inductor (red) and air (grey)

4.3.1 Symmetrisation procedure

To begin, a comparison is made between the two symmetrisation procedures in order to properly construct the metric $\mathcal{M}(\|x\|)$. Since a metric tensor can be represented as ellipsoid in 3D space, where the principal axes are given by their eigenvectors and their length by the eigenvalues [89], Knowing this, and applying a current density as show in Fig. 4.3, we can expect well-ordered ellipsoids in the same direction. Fig. 4.3 shows the ellipsoids of the metric tensor $\mathcal{M}(\|x\|)$ constructed using the magnetic field (\vec{H}) for both symmetrisation procedure defined in (4.28) and (4.29).

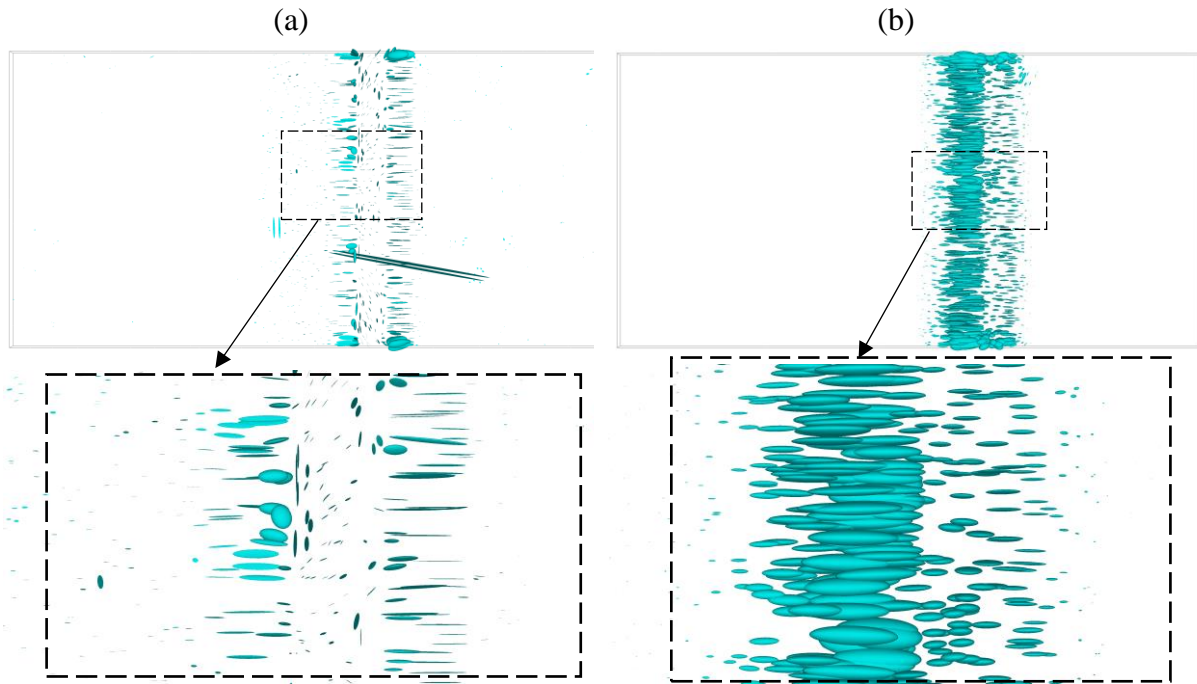


Fig. 4.3 Ellipsoid metric representation on symmetrisation procedure: a) \bar{T}_1 and b) \bar{T}_2

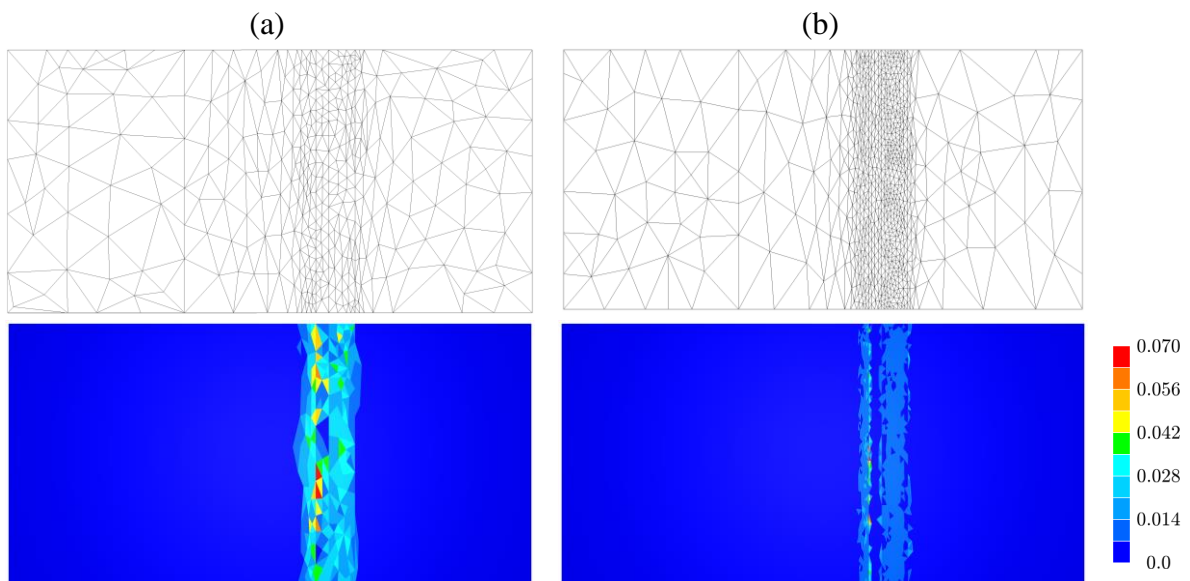


Fig. 4.4 Mesh and error resulting from symmetrisation procedure: a) \bar{T}_1 and b) \bar{T}_2

For each one of the symmetrisation procedures $\bar{\bar{T}}_1$ and $\bar{\bar{T}}_2$ displayed in Fig. 4.3a and Fig. 4.3b respectively, the behaviour found is quite different. It can be seen that, although the $\bar{\bar{T}}_1$ procedure predicts a globally consistent anisotropy behaviour, the ellipsoid distribution does not seem to capture the direction properly. Furthermore, it appears to completely rotate the principal axes in the air between the workpiece and inductor by 90° . It also drastically changes the direction of the axes of the ellipsoid on the surface of the workpiece. In contrast, the metric symmetrized by the $\bar{\bar{T}}_2$ procedure predicts a more uniform behaviour. In fact, the ellipsoids point uniformly in the same direction. Therefore, the $\bar{\bar{T}}_2$ procedure shows to be more suitable for capturing the anisotropy of the direction of the fields.

Fig. 4.4 shows the resulting meshes after computing the metric tensors from the original isotropic mesh, in Fig. 4.2, as well as their respective error estimator distribution over the domain. As predicted by the ellipsoid analysis, the highest element density is located over the inductor region, the workpiece close to the inductor, and the air in between, for both metrics. However, the mesh created from the $\bar{\bar{T}}_1$ procedure shows a change of orientation in the elements between the inductor and the workpiece, as predicted by the ellipsoids and a larger error compared to $\bar{\bar{T}}_2$. Therefore, it is evident that procedure $\bar{\bar{T}}_2$ enables to generate a better suited mesh distribution, since it leads to a further decrease of the error for roughly the same number of degrees of freedom.

In conclusion, following the results shown in Fig. 4.3 and Fig. 4.4, the $\bar{\bar{T}}_2$ procedure appears to be the most suitable. In fact, the positive-definite symmetric matrix found here maintains more accurately the direction of the anisotropy, thus it will be used from here onwards to generate the adaptative mesh.

4.3.2 Anisotropic behaviour

Once the appropriated symmetrisation procedure has been chosen, a second test is performed with both metrics. The anisotropy behaviour is then studied to determine which metric captures the physical phenomenon more accurately. The metric is symmetrized using (4.29), and as in the previous test, the ellipsoid is used to understand how each metric captures anisotropy. For this purpose, the magnetic field (\vec{H}) is used to calculate both metrics. Then, the characteristic ellipsoids of $\mathcal{M}(\|\vec{H}\|)$ and $\mathcal{M}(\vec{H})$ are shown in Fig. 4.5.

Fig. 4.5 illustrates a remarkable difference regarding the anisotropy. Although both metrics point uniformly in the same direction, the shape of the ellipsoid varies, indicating a higher anisotropy in the $\mathcal{M}(\vec{H})$ metric. In order to compare the performance of these metrics, the adaptation is performed for both cases. The resulting meshes are displayed in Fig. 4.6a for $\mathcal{M}(\|\vec{H}\|)$ and Fig. 4.6b for $\mathcal{M}(\vec{H})$. Upon examining the results from these meshes, it becomes evident that the metric calculated from a vector field, $\mathcal{M}(\vec{H})$, is better suited to capture the sharp anisotropy of the field. Wherein contrast, $\mathcal{M}(\|\vec{H}\|)$ also exhibits anisotropic behaviour but to a lesser extent.

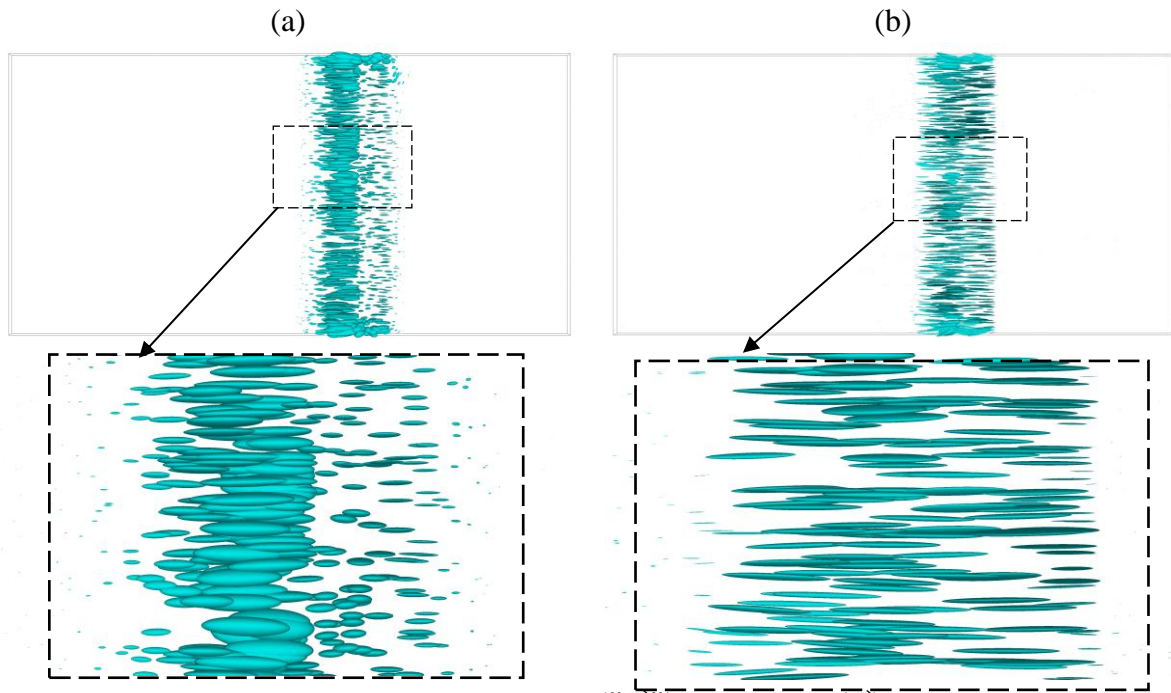


Fig. 4.5 Ellipsoid metric representation: (a): $\mathcal{M}(\|\vec{H}\|)$ and (b): $\mathcal{M}(\vec{H})$

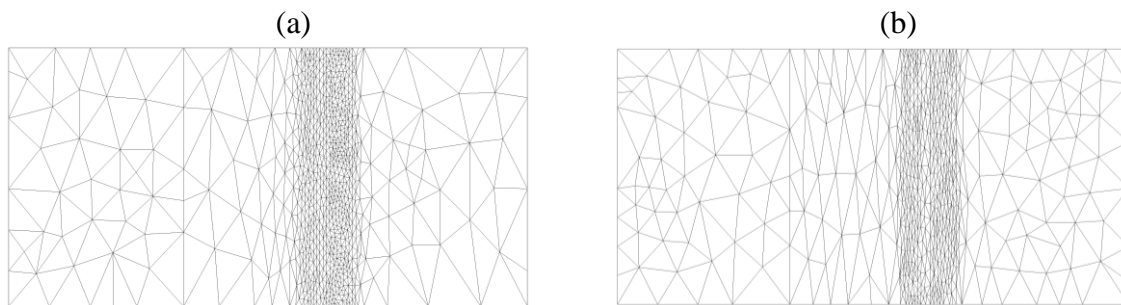


Fig. 4.6 Mesh resulting from (a): $\mathcal{M}(\|\vec{H}\|)$ and (b): $\mathcal{M}(\vec{H})$

The previous example was a quasi 2D case of an unidirectional field. In order to assess both metrics in a more intricate 3D scenario, an axisymmetric induction heating case is examined, as depicted in Fig. 4.7.

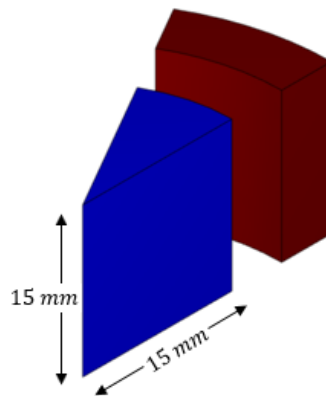


Fig. 4.7 Axisymmetric induction heating case, workpiece in blue and inductor in dark-red.

To further evaluate the metrics, a similar comparison to the previous case is performed in the axisymmetric induction case. By comparing the ellipsoids representing each metric, the anisotropic behaviour contained in the metric before meshing is clearly seen. These results are shown in Fig. 4.8 and Fig. 4.9 for $\mathcal{M}(\|\vec{H}\|)$ and $\mathcal{M}(\vec{H})$ respectively.

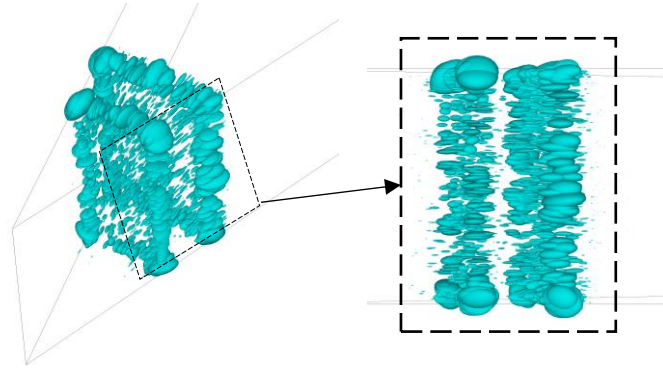


Fig. 4.8 Metric tensor from a scalar field ($\mathcal{M}(\|\vec{H}\|)$)

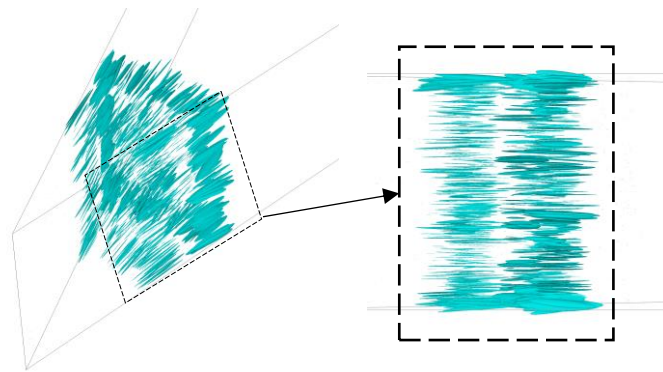


Fig. 4.9 Metric tensor from a vector field ($\mathcal{M}(\vec{H})$)

According to the ellipsoids displayed in Fig. 4.8 and Fig. 4.9, it can be noted that the behaviour captured by $\mathcal{M}(\vec{H})$ exhibits a significantly higher anisotropy compared to $\mathcal{M}(\|\vec{H}\|)$. The ellipsoids of $\mathcal{M}(\|\vec{H}\|)$ leads to be nearly spherical shapes, indicative of a more classical isotropic behaviour.

In order to provide a clearer illustration of this distinction, both metrics are employed to drive the remeshing procedure, resulting in the meshes depicted in Fig. 4.10.

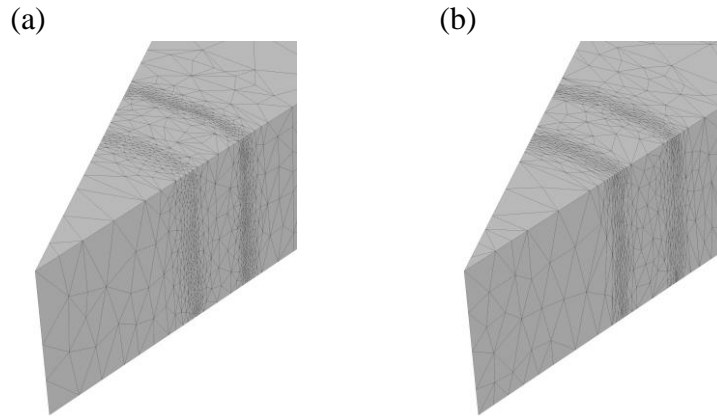


Fig. 4.10 (a): $\mathcal{M}(\|\vec{H}\|)$ and (b): $\mathcal{M}(\vec{H})$ mesh results

Fig. 4.10a and Fig. 4.10b display the meshes generated using $\mathcal{M}(\|\vec{H}\|)$ and $\mathcal{M}(\vec{H})$ respectively. In the same way, as seen in the results with the representative ellipsoids, $\mathcal{M}(\vec{H})$ exhibits a higher degree of anisotropic behaviour. While $\mathcal{M}(\|\vec{H}\|)$ specifies where the mesh needs to be refined or de-refined, its anisotropy is somewhat reduced.

The results presented in this section lead to the conclusion that the symmetrisation procedure involving the conjugate product (4.29) not only symmetrizes and positively defines the tensor but also does not distort the principal direction of anisotropy. Furthermore, although metrics computed as the Hessian of a scalar field have been more extensively studied in the literature, the metric computed from the Jacobian of a vector field appears to better capture the anisotropy of physical phenomena. In this regard, the $\mathcal{M}(\vec{H})$ procedure will be retained and applied to several cases in the next section and results compared with the ones obtained with $\mathcal{M}(\|\vec{H}\|)$.

4.4 Application to electromagnetic processing of materials

In this section, the capabilities of the metrics are explored through a series of electromagnetic coupled processes. Firstly, the intrinsic anisotropy of the electromagnetic phenomena is highlighted, underscoring the advantage of anisotropic mesh adaptation. In the same lines, a benchmark case is used to compare isotropic and anisotropic. Subsequently, the metric's ability to handle automatically with the electromagnetic skin effect is tested. Finally, three industrial cases are presented: an induction heating application for a heat treatment in a wheel bearing piece, a magnetic pulse forming application in a circular sheet and an electromagnetic stirring application with a more complex geometry.

For most cases, the magnetic field (\vec{H}) to construct and compare the proposed metrics is used. However, the skin effect test is analysed with the electrical field (\vec{E}) with the purpose to demonstrate the versatility of both approaches.

4.4.1 Intrinsic anisotropy

In full immersion finite element analysis for solving electromagnetic problem, achieving uniform accuracy across the entire mesh, using a uniform mesh, is unnecessary and computational wasteful. This scenario is commonly encountered in isotropic configurations. Therefore, a more efficient approach involves employing adaptive anisotropic remeshing techniques.

Anisotropic remeshing allows for different regions of the mesh to have varying levels of detail. In regions where electromagnetic fields change abruptly, finer elements are deployed, while regions with minimal field gradients can be discretized using larger elements. This anisotropic structure plays a key role in tracking the behaviour of electromagnetic fields. In scenarios where electromagnetic fields exhibit complete single-directional, a straightforward strategy is to employ larger elements aligned with the field's direction. This strategy will reduce the number of elements within the mesh while preserving a good accuracy.

Consider the example in Fig. 4.11, which depicts a cylindrical inductor and a workpiece, along with the magnetic field lines for clarity of the phenomenon. By observing the magnetic field lines, it is possible to observe common electromagnetic features that introduce anisotropy, such as the skin and proximity effects. The skin effect causes the field to concentrate near the surface of the cylindrical part, while the proximity effect results in a larger field in the vicinity of the inductor.

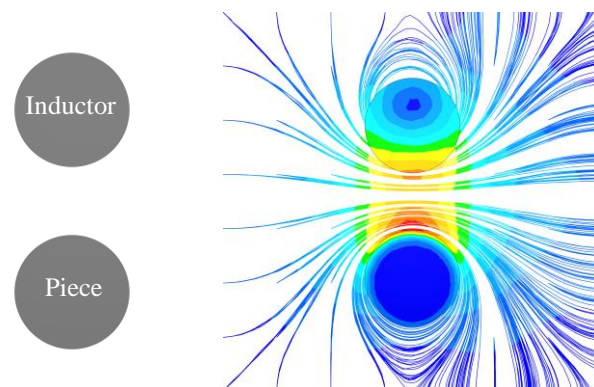


Fig. 4.11: Left: inductor and workpiece, diameter of 5 mm and length of 20mm for both cases. Right: magnetic field lines shown at the beginning of the sine wave.

Efficient mesh adaptation is achieved by refining regions where electromagnetic field variations are significant and allowing elements to grow in areas with lower gradients. It is important to note that choosing an isotropic mesh structure would result in exponential growth in the number of elements as the cylinder length increases. To illustrate this, we conducted experiments with both isotropic and anisotropic meshing, aiming to maintain the same level of error in both cases. The $\mathcal{M}(\vec{H})$ metric has been used to capture the anisotropic behaviour of the magnetic field. Fig. 4.12 displays both the isotropic and the anisotropic generated mesh, where the isotropic mesh required 405000 degrees of freedom to achieve the desired accuracy, the anisotropic mesh only needs 140000 to achieve the same level of accuracy. It is worth mentioning that the anisotropic mesh created using the $\mathcal{M}(\vec{H})$ successfully captured the electromagnetic phenomenon described above.

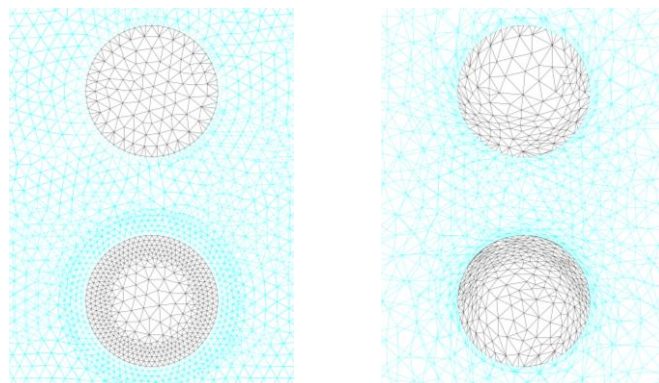


Fig. 4.12: Left: isotropic mesh. Right: anisotropic mesh.

We conducted tests with both meshes to assess the convergence of the finite element solution. In solving the linear system for the electromagnetic problem, we employed the conjugate gradient method along with the Jacobi preconditioner. Table 4.3 presents the degrees of freedom, the CPU time and the number of iterations required to solve the linear system.

Table 4.3 isotropic vs anisotropic mesh

Mesh	Elements	CPU elapsed	Iterations
Isotropic	405000	3s 421ms	167
Anisotropic	140000	2s 140ms	302

Notably, there is an increase in the number of iterations needed for the linear system's solution. This increase may be attributed to the matrix's poor conditioning, which can occur due to the presence of flat elements in anisotropic configurations.

Hence, in this case, it can be concluded that the anisotropic structure significantly optimizes computational resources, reducing by nearly 3, and enhancing computation speed by 40%.

4.4.2 Isotropic vs Anisotropic performance comparison (model size/error distribution/etc)

In order to evaluate and compare the effectiveness of the developed metric tensor in this study with an isotropic mesh adaptation procedure, a benchmark case has been chosen. This benchmark case belongs to the TEAM (Testing electromagnetic analysis methods) problems, which represents an open international working group aiming at comparing electromagnetic analysis computer codes. Specifically, case number 7 [64], which is a pure electromagnetic case, focuses on the induction phenomenon, has been selected for analysis. This case involves a thick aluminium plate with an off-centre hole, positioned asymmetrically within a non-uniform magnetic field generated by a sinusoidal current source. This case is shown in Fig. 4.13

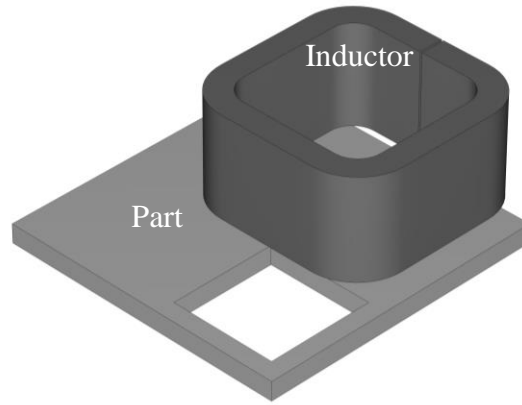


Fig. 4.13 Team 7 benchmark case.

Fig. 4.14 illustrates the mesh and error estimator in the comparison between isotropic and anisotropic mesh adaptation, along with the initial mesh used. In each case the minimal and maximal mesh sizes, denoted as h_{min} and h_{max} , have been defined as the same. Since the fully immersed finite element approach is employed for spatial discretization, the entire domain is adapted, and different minimal and maximal mesh sizes values are assigned for different regions (workpiece, inductor, and air) within the domain. The simulation uses a frequency of 50Hz and a current of 2742.

Upon examining Fig. 4.14 and referring to Table 4.4, it becomes evident that while the isotropic approach succeeds in capturing the underlying physical phenomena, it necessitates nearly twice the number of degrees of freedom as the anisotropic approach. It is worth noting that the anisotropic approach adequately captures the physical phenomena and manages to distribute the error across the workpiece, even including several elements within the plate thickness. The error is evenly distributed in both metric approaches, however the metric $\mathcal{M}(\vec{H})$ achieves a better compromise between the error and number of degrees of freedom required.

Table 4.4 Mesh size and error estimator

Mesh	Initial	Isotropic	$\mathcal{M}(\ \vec{H}\)$	$\mathcal{M}(\vec{H})$
Nodes	4033	30273	19845	15673
elements	22889	165340	113648	89426
Error [%]	10.12×10^{-4}	3.4×10^{-4}	3.7×10^{-4}	4.2×10^{-4}

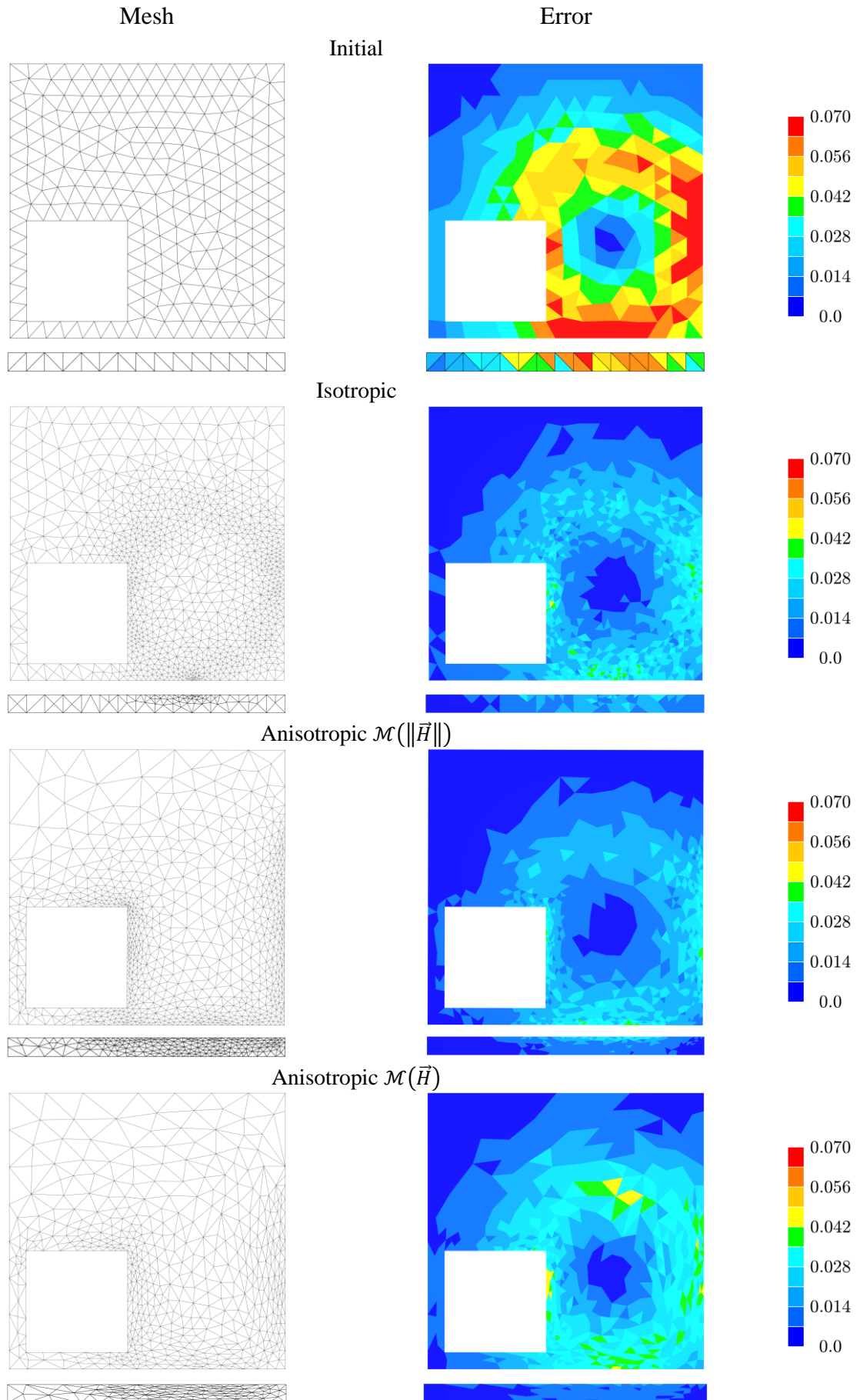


Fig. 4.14 Isotropic vs Anisotropic, mesh and error distribution results

4.4.3 Skin effect case

The metric tensors developed in this chapter are assumed to be adaptable to a wide range of physical phenomena. As previously explained, the skin-depth phenomenon is a significant factor contributing to anisotropy in electromagnetic problems. To illustrate this, we present a straightforward case in Fig. 4.7. The main idea here is to vary the frequency parameter to achieve different skin depths, calculated using the relation (1.7). Frequencies of 350, 1000 and 550 Hz were employed to obtain skin depths of 12mm , 7mm , and 3mm , respectively. Having prior knowledge of the skin depth allows us to assess whether the metric can capture this phenomenon and generate a new mesh to address it. In this case, only the metric calculated from the Jacobian is used, using the electric field (\vec{E}). The results for the three different skin-depths are depicted in Fig. 4.15. It is worth mentioning that the radius of the workpiece is 15mm .

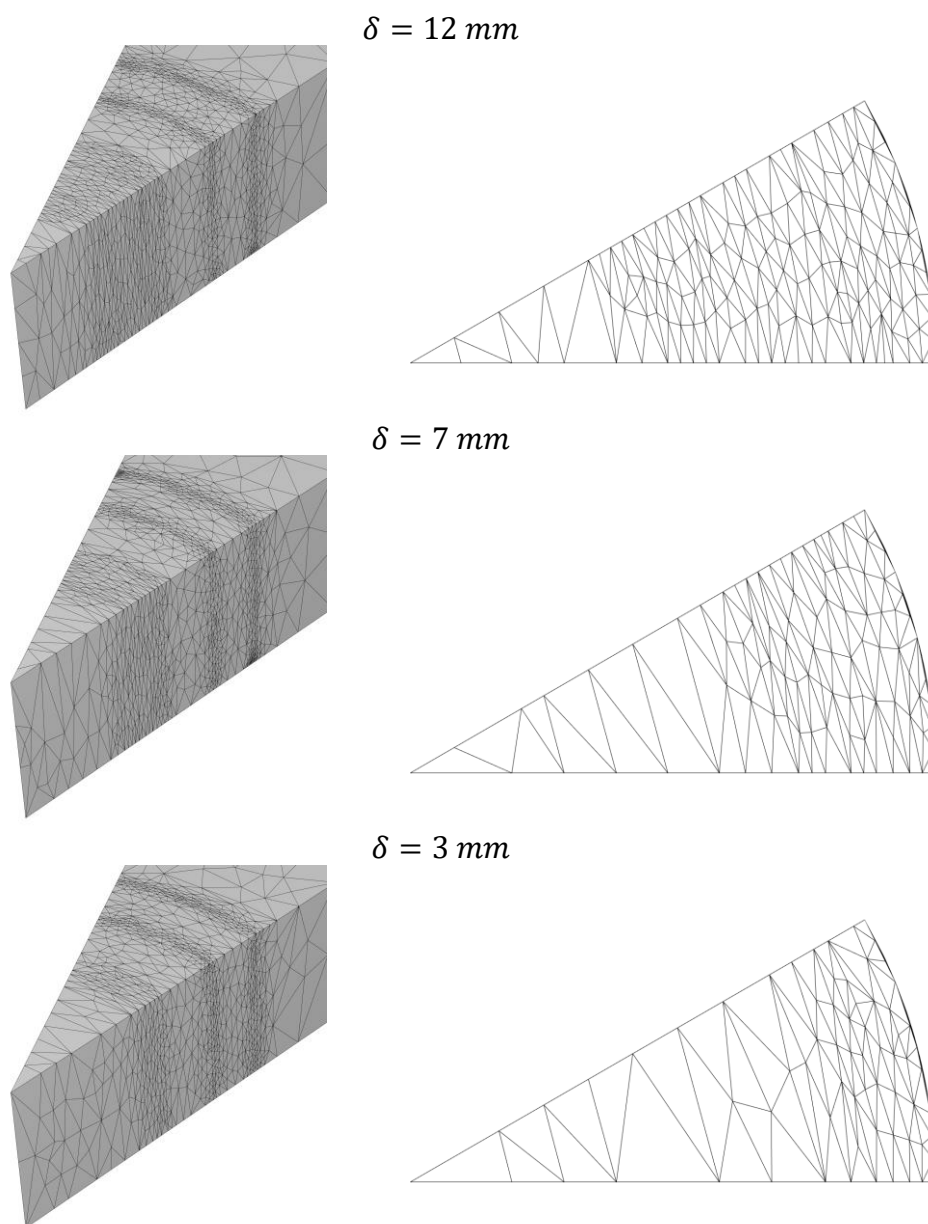


Fig. 4.15 Skin effect meshes after adaptation.

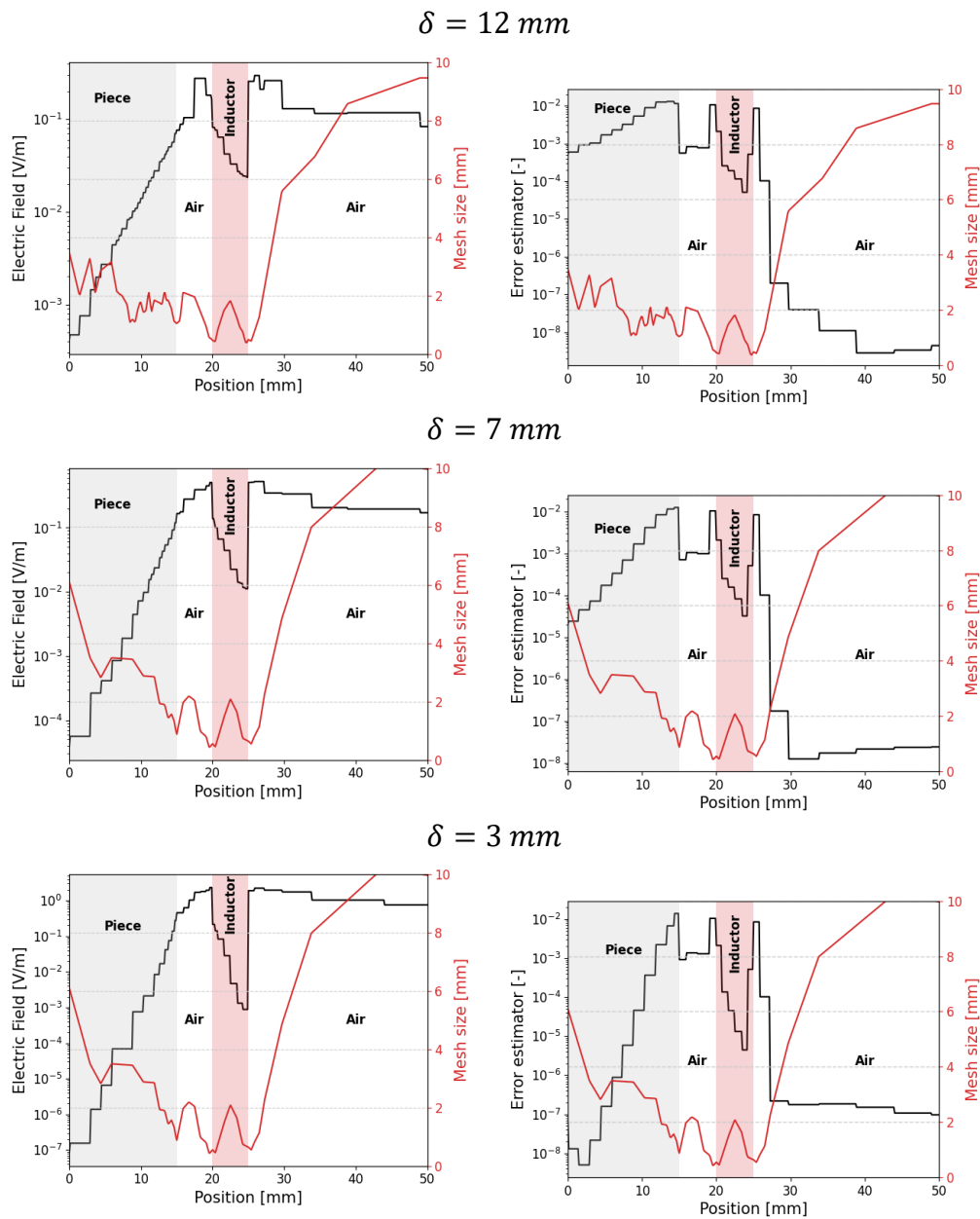


Fig. 4.16 mesh size evolution regarding the electric field and error estimator

Fig. 4.15 displays the generated meshes for each skin depth parameter. It is evident that the metric is able to adequately track this phenomenon, resulting in a higher density of elements within the skin depth region and de-refining where it is no longer necessary. Furthermore, Fig. 4.16 illustrates the evolution of the mesh size along the horizontal axis with respect to the electric field and the error estimator. These results demonstrate a strong correlation between the fields. Specifically, as the electric field gradient increases, the error estimator also increases, and the metric $\mathcal{M}(\vec{E})$ naturally responds to these changes by reducing the mesh size to provide a more accurate representation of the field.

4.4.4 Industrial processes

4.4.4.1 Induction heating application

The metric is put to the test in an induction heat treatment scenario involving a wheel bearing. In this setup, two inductors are strategically positioned in the heat treatment zone, and current concentrators are applied to each inductor to direct the magnetic field towards the part. Due to the symmetrical nature of the wheel bearing, only a section of the geometry is simulated.

At first glance, it's expected that the metric tensor will attempt to adapt the mesh in regions between the part and the inductors, where the magnetic field exerts a significant influence. Additionally, it should capture the specific behaviour introduced by the concentrators. The wheel bearing is shown in Fig. 4.17, and the results of a comparison of experiments and simulation data for prediction of during induction hardening are in Fig. 4.18. Here, the region with the most pronounced treatment influence is clearly visible [90].

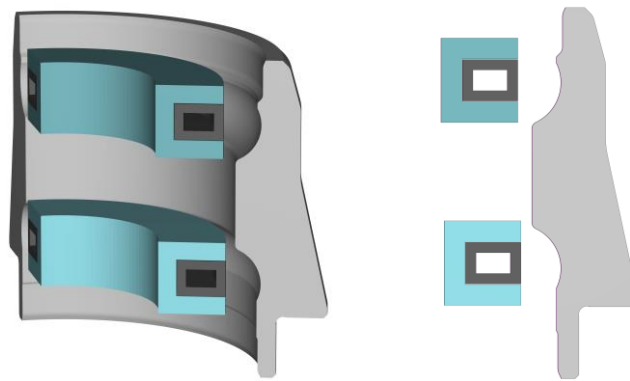


Fig. 4.17 Wheel bearing case.

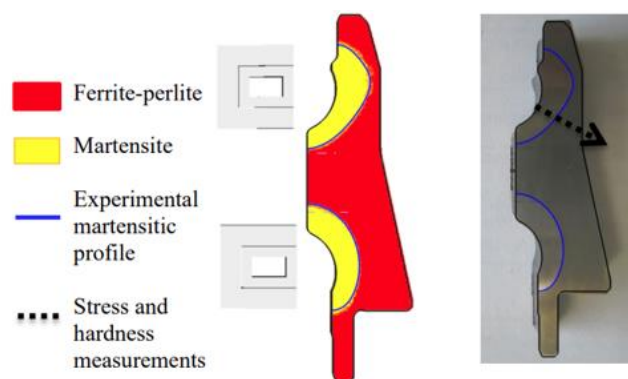


Fig. 4.18 Comparison of microstructure predicted by FEM with experimental data [90].

For this heat treatment simulation, a frequency of 13020 Hz used. The results for this case are presented in Fig. 4.19. At first sight, it reveals that both metrics effectively track the predicted electromagnetic behaviour. They achieve this by appropriately refining the mesh on

the bearing while coarsening it on the rest of the part. Additionally, they successfully capture the functionality of the concentrators and reduces the error on the adapted meshes. Interestingly, although the metric $\mathcal{M}(\|\vec{H}\|)$ appears to yield a mesh with lower error compared to $\mathcal{M}(\vec{H})$, it is important to note the latter requires fewer degrees of freedom, as illustrated in Table 4.5

Table 4.5 Mesh size and error estimator

Mesh	Initial	$\mathcal{M}(\ \vec{H}\)$	$\mathcal{M}(\vec{H})$
Nodes	9303	41476	33252
elements	42670	205843	159722
Error [%]	4.15×10^{-5}	1.38×10^{-5}	1.8×10^{-5}

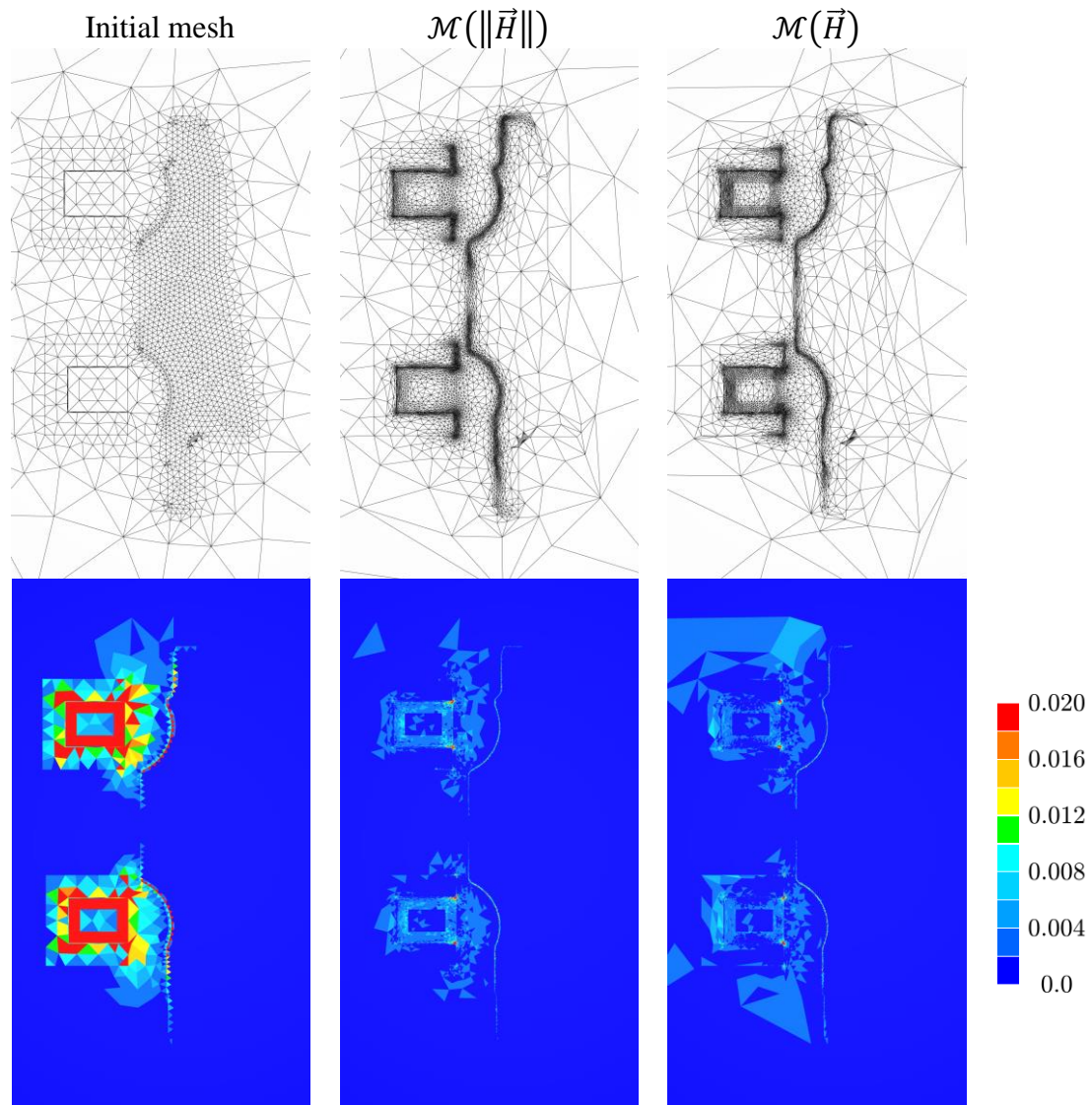


Fig. 4.19 Induction heating case: mesh and error distribution results.

4.4.4.2 Magnetic Pulse forming application.

The magnetic pulse forming (MPF) technology or electromagnetic forming (EMF) consists in deforming metallic components through the application of an intense electromagnetic pulse. This process enters in the category of high-speed forming processes due of the range of strain rates that are usually attained, ranging from $10^3 s^{-1}$ to $10^4 s^{-1}$. A typical coil and workpiece set-up of this process is shown in Fig. 4.20.

The objective of this case is to assess whether the metric tensor is able to effectively capture the magnetic field induced by the circular coil at a high frequency, and how it adapts the mesh accordingly. For this simulation, a pulsed discharge signal with a natural frequency of 162kHz is employed.

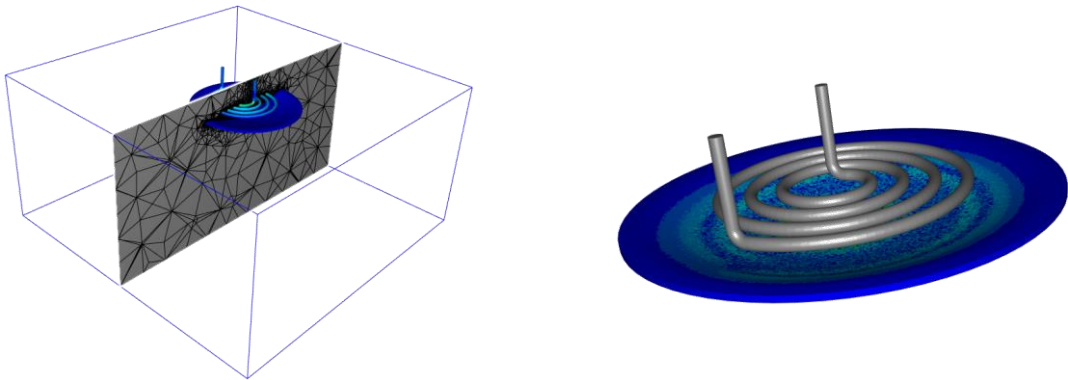


Fig. 4.20 Magnetic pulse forming case.

Fig. 4.21 presents a comparison of the meshes and error distribution for both metrics, along with the initial mesh. Similar to previous case, both metrics are able to accurately capture the physical phenomenon. Notably, $\mathcal{M}(\|\vec{H}\|)$ achieves a smaller final error distribution compared to $\mathcal{M}(\vec{H})$. However, it is important to highlight the substantial difference between in the number of degrees of freedom, as indicated in Table 4.6. Here, $\mathcal{M}(\vec{H})$ requires fewer degrees of freedom to attain a mesh with an acceptable reduction in the error.

Table 4.6 Mesh size and error estimator

Mesh	Initial	$\mathcal{M}(\ \vec{H}\)$	$\mathcal{M}(\vec{H})$
Nodes	67805	79735	54292
elements	438928	465389	309727
Error [%]	1.7×10^{-7}	0.9×10^{-7}	1.0×10^{-7}

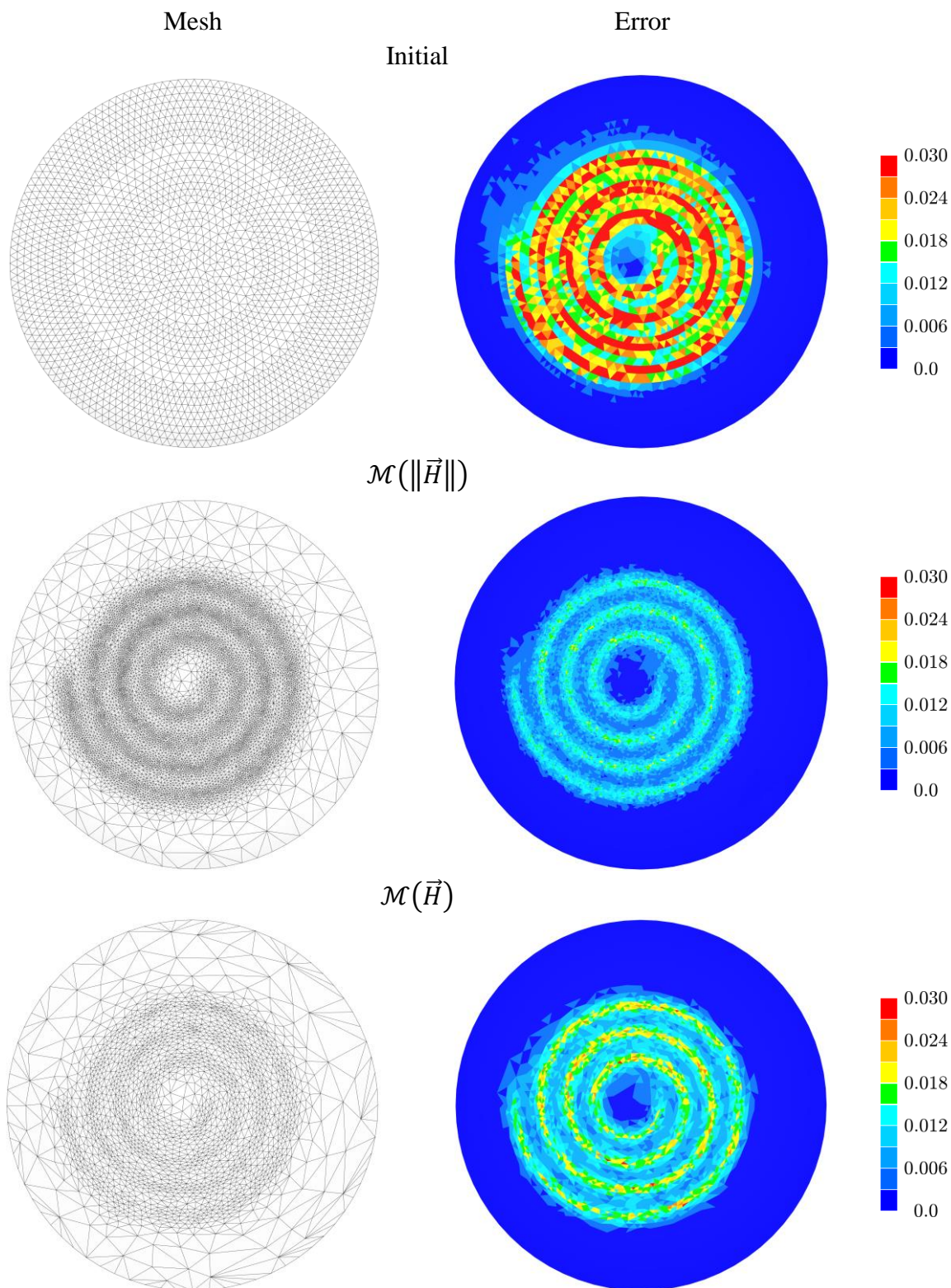


Fig. 4.21 Magnetic pulse forming mesh and error distribution results.

4.4.4.3 Electromagnetic Stirring application

So far, metrics have been used to govern the anisotropic meshing procedure using simple geometries. To evaluate its performance in more complex geometries, the electromagnetic stirring process was selected. This process, extensively employed in the materials forming industry, employs a time-varying electromagnetic field to control the fluid flow within the liquid steel without any physical contact. This process is used to disrupt the molten metal's fluid flow using Lorentz forces, which induce a linear induction motor allowing a more homogeneous solidification, avoiding premature growth of dendrites during the casting process and resulting in a better quality of the final ingot. The geometry used to simulate this process encompasses a steel bar with six inductors supported by a core, as depicted in Fig. 4.22.

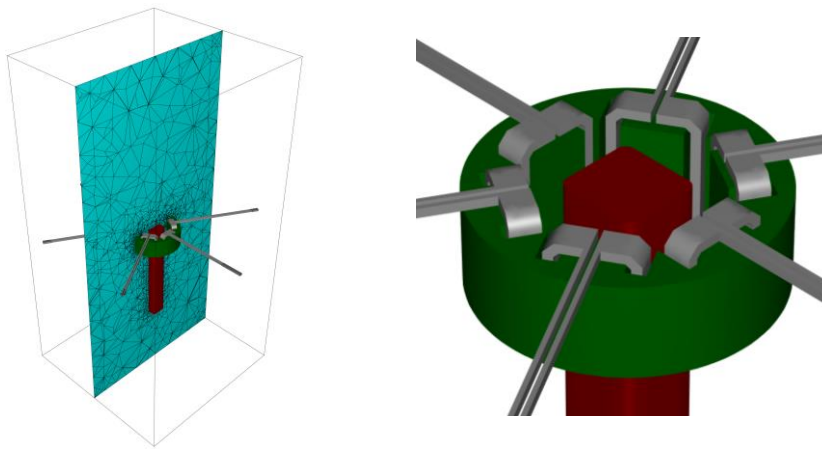


Fig. 4.22 Electromagnetic stirring case

This process operates at a low frequency, specifically 2Hz in this simulation. Fig. 4.23 displays the results for the electromagnetic stirring case. This case serves as an appropriate test to evaluate the performance of the metrics when dealing with complex geometries. Similar to previous cases, the meshes and error distribution are shown to facilitate a comprehensive comparison between the two proposed metrics. It is evident that the anisotropy is more pronounced in the mesh generated using the metric $\mathcal{M}(\vec{H})$, particularly on the workpiece. This leads to a mesh with fewer degrees of freedom, as indicated in Table 4.7. It is worth mentioning that this time the metric $\mathcal{M}(\vec{H})$, with fewer number of elements compared to $\mathcal{M}(\|\vec{H}\|)$ achieves a better distribution of the error across the entire domain.

Table 4.7 Mesh size and error estimator

Mesh	Initial	$\mathcal{M}(\ \vec{H}\)$	$\mathcal{M}(\vec{H})$
Nodes	32669	223097	183749
elements	183749	1291863	964964
Error [%]	15.7×10^{-3}	5.6×10^{-3}	6.5×10^{-3}

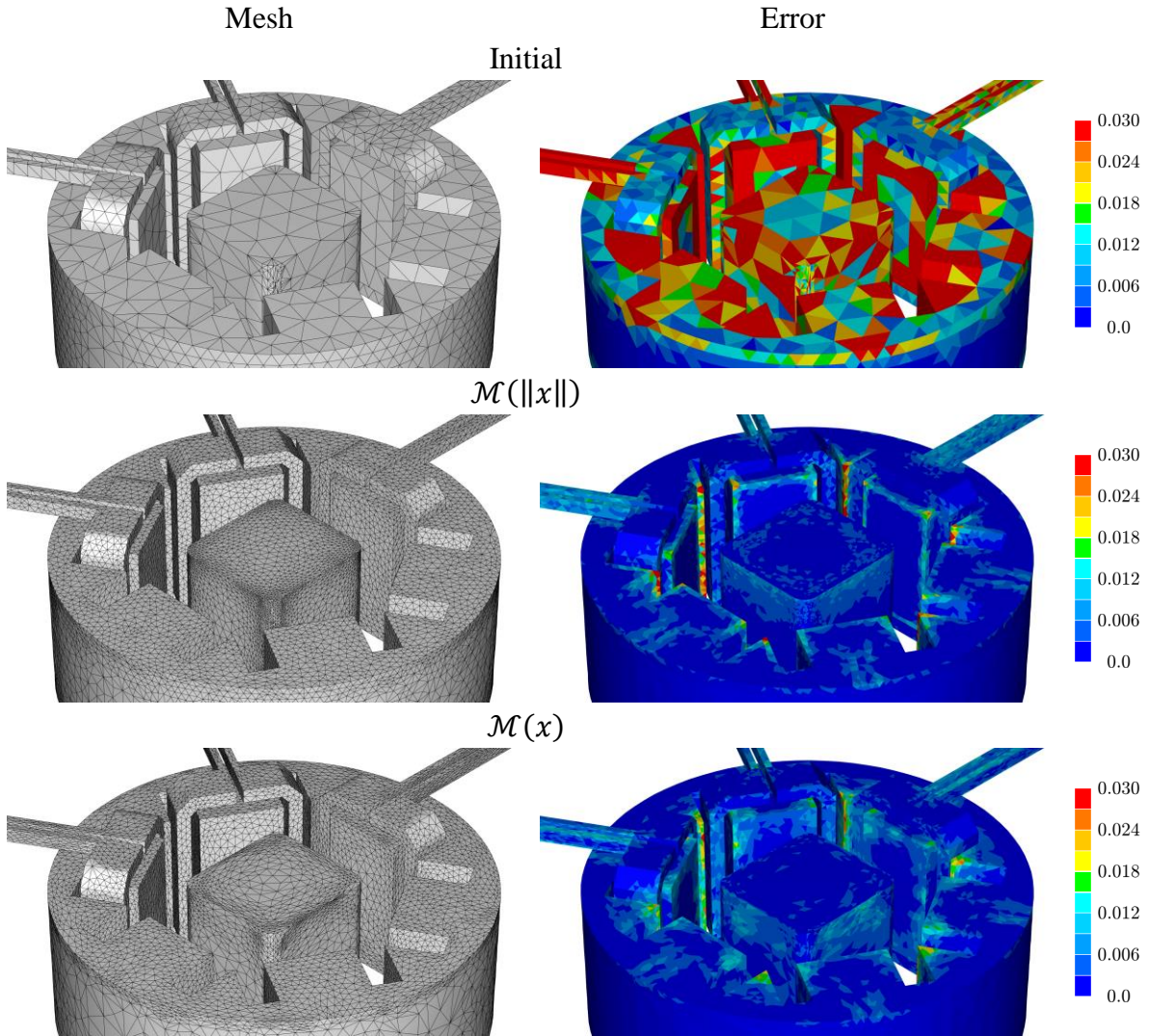


Fig. 4.23 Electromagnetic stirring mesh and error distribution results

4.4.5 Magnetic and electric fields duality

In the electromagnetic phenomena, a duality exists between the magnetic and the electric fields. The classical Maxwell equations, which govern these fields, reveal this duality in this manner:

$$\vec{E} = \frac{1}{\sigma} \vec{\nabla} \times \vec{H} \quad (4.58)$$

$$-\frac{1}{\mu} \frac{\partial \vec{H}}{\partial t} = \vec{\nabla} \times \vec{E} \quad (4.59)$$

The equations can be represented by emphasizing the relationship between the curls of both fields:

$$\vec{E} \approx \vec{\nabla} \times \vec{H} \quad (4.60)$$

$$\vec{H} \approx \vec{\nabla} \times \vec{E} \quad (4.61)$$

The metrics proposed in this chapter offers the flexibility to work with either field. A comparison of the resulting meshes generated by the Jacobian-based metric applied to \vec{H} and \vec{E} vividly illustrates the duality between these fields, as shown in Fig. 4.24. In fact, in some cases constructing the metric for one field automatically adapts the mesh to follow the other field. Fig. 4.24a presents the mesh constructed from the electric field \vec{E} alongside the magnitude of the magnetic field and its vectors fields. While Fig. 4.24b showcases the mesh constructed from the magnetic field \vec{H} along with the magnitude of the electric field and its vector fields. In both cases, it is evident that the mesh is accurately adapted to the characteristics of their dual field.

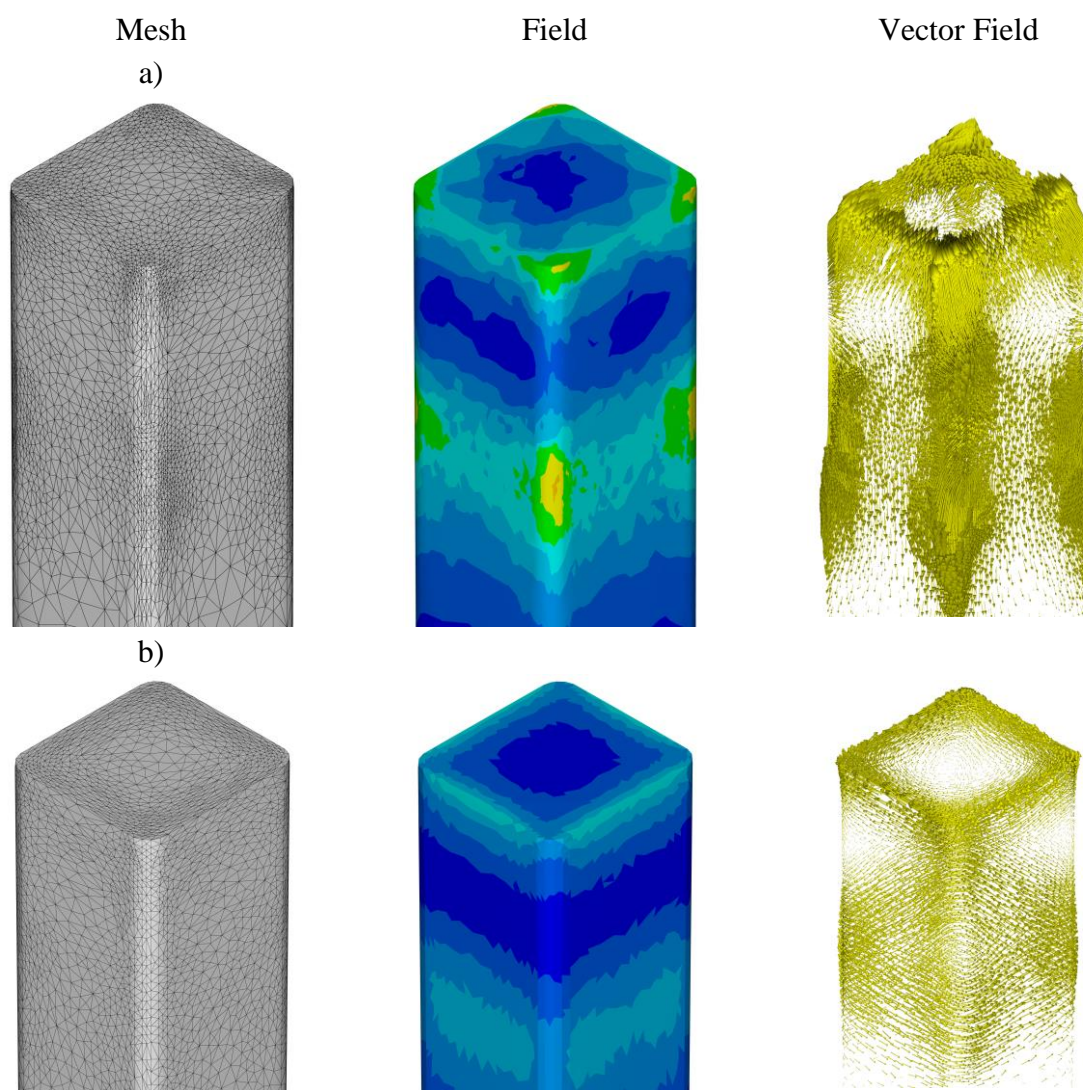


Fig. 4.24 Duality between the magnetic field (\vec{H}) and electric field (\vec{E}). a) Metric constructed with \vec{E} , results of \vec{H} , b) Metric constructed with \vec{H} , results of \vec{E}

4.5 Relation between the Hessian and the Jacobian

Building upon the previously defined relationship between the Hessian and the error estimator (4.21). We propose a connection between the Hessian et Jacobian. Under the assumption of a square norm of a twice-differentiable function, the Hessian can be expressed as follows, using Einstein notation:

$$\text{Hess}(\|x_k\|^2) = (x_k x_k)_{,ij} \quad (4.62)$$

The first-order derivative can be derived as:

$$(\nabla(\|x_k\|^2))_j = 2x_k x_{k,j} \quad (4.63)$$

For the second-order derivative, we have:

$$\frac{1}{2}(\text{Hess}(\|x_k\|^2))_{ij} = x_{k,i} x_{k,j} + x_k x_{k,ji} \quad (4.64)$$

Reordering the first term on the right-hand side:

$$\frac{1}{2}(\text{Hess}(\|x_k\|^2))_{ij} = (x_{i,k})^T x_{k,j} + x_k x_{k,ji} \quad (4.65)$$

Notably, the metric proposed based on the Jacobian appears on the right-hand side of this expression $\mathcal{M}(x)$

$$\mathcal{M}(x)_{ij} = (x_{i,k})^T x_{k,j} \quad (4.66)$$

Recalling the metric based on the Hessian of a scalar field:

$$\mathcal{M}(\|x\|)_{ij} = (\text{Hess}(\|x_k\|^2))_{ij} \quad (4.67)$$

In this chapter, we have numerically evaluated both metrics, enabling us to assess the third term as:

$$\tilde{\mathcal{M}}_{ij} = x_k x_{k,ji} \quad (4.68)$$

Finally, this term is calculated as:

$$\tilde{\mathcal{M}}_{ij} = \frac{1}{2} \mathcal{M}(\|x\|)_{ij} - \mathcal{M}(x)_{ij} \quad (4.69)$$

In order to evaluate this additional term, the TEAM7 benchmark have been selected, where all the three metrics are calculated, and the Frobenius's norm is applied to compare them. The magnetic field is employed to construct and compare the metrics.

To begin, let's first visualize the magnetic field distribution and its respective error estimator on the plate.

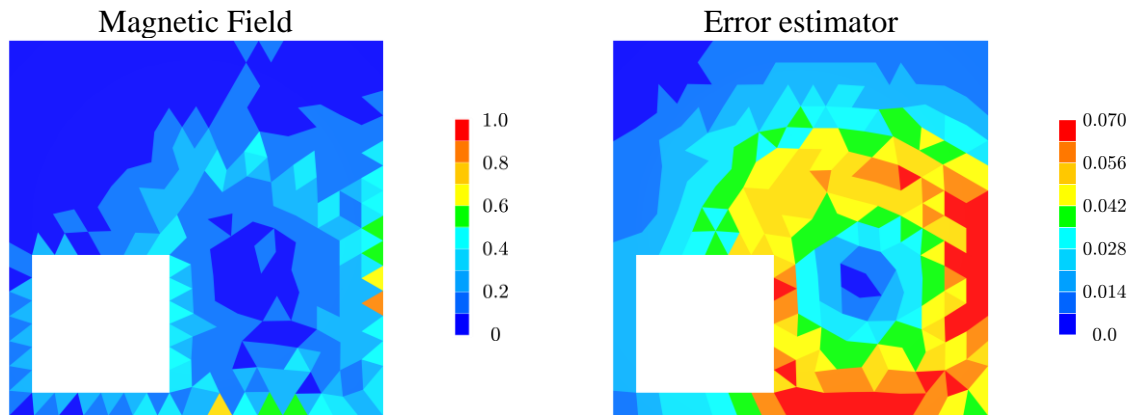


Fig. 4.25 Magnetic field and error distribution on the workpiece

Next, we present the Frobenius norm of each of the metrics.

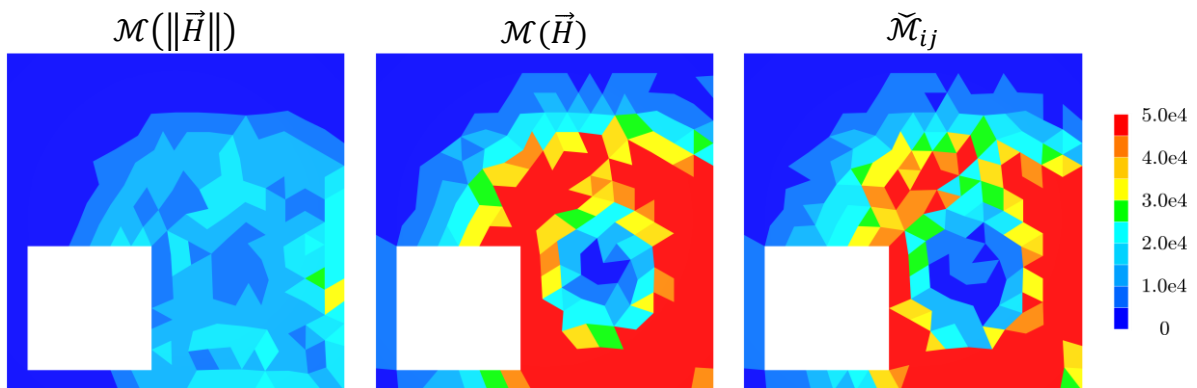


Fig. 4.26 Frobenius norm: left: Hessian, centre: Jacobian and right: Difference

Clearly, the metric calculated from the Jacobian, denoted as $\mathcal{M}(\vec{H})$, more effectively captures the magnetic field's variation and, consequently, the error distribution. Conversely, $\mathcal{M}(\|\vec{H}\|)$ appears to oversmooth the error, leading to a loss of information regarding the field's variation.

4.6 Conclusions

In this chapter, we have explored various strategies for constructing a metric tensor to effectively address electromagnetic phenomena. We began by introducing two methods for symmetrizing the Hessian-based tensor field. Among these, the conjugate product method emerged as the most suitable approach, ensuring both symmetry and positive definiteness of the tensor while preserving the direction of anisotropy contained in the metric.

Next, we showed that the metric field can be obtained as the Hessian of a scalar field or as the Jacobian of a vector field. Both procedures employ a recovery-based approach, in conjunction with gradient operators. The metrics have been tested in different configurations, from comparison with an isotropic mesh procedure, to evaluating their ability to capture the skin effect phenomenon. In all cases, the metrics demonstrated being sufficiently accurate to guarantee a level of refinement where is necessary.

Then, they were applied in industrial applications, specifically in induction heating, magnetic pulse forming, and electromagnetic stirring processes. The results indicated that these strategies effectively accommodated the underlying physics involved in each of these process, allowing good mesh distribution and error reduction.

This work has shown the potential of the Jacobian-based metric for carry out a mesh adaptation procedure. This approach appears to better capture field's anisotropy while keeping a good balance between error reduction and the number of degrees of freedom. Furthermore, it also provides an additional alternative to deal with the average anisotropy of a vector field. Traditionally, this would involve handling the anisotropy of each component individually by computing a metric for each component and then carry out a metric intersection procedure. Such procedures are not only computationally expensive but also dependent on the order in which the intersections are performed.

This development has been exclusively focused on the electromagnetic model, Leaving for the future the perspective of extending these developments to other physics, such as the solid mechanics or fluid mechanics, and their implementation within FORGE® and THERCAST®, respectively.

Chapter 5

Fully coupled multi-physical implementation

5.1	Coupling procedure	138
5.1.1	Current procedure.....	138
5.1.2	Proposed procedure	139
5.1.3	Geometrical metric	140
5.2	Performance test	141
5.2.1	Simple induction case.....	141
5.2.2	A more complex induction case	144
5.3	Industrial applications	146
5.3.1	Wheel bearing Induction heating	146
5.3.2	Magnetic Pulse Forming	149
5.4	Conclusions.....	154

Résumé : Application multiphysique entièrement couplée

Ce chapitre se concentre sur les applications complètement couplées. Tout d'abord, la procédure de couplage actuelle est introduite, ainsi que la nouvelle procédure proposée. Ensuite, une métrique géométrique, capable de reproduire le même maillage d'un setup donné, est développée dans le but d'aider à remplacer la procédure actuelle.

Des tests de performance sont réalisés afin de mesurer l'effet du changement de stratégie de remaillage. Finalement, des cas industriels sont étudiés pour évaluer notre développement sur des situations plus complexes, utilisant le logiciel Forge®.

5 Fully coupled multi-physical implementation

5.1 Coupling procedure

This section aims to explain the existing coupling procedure used in the fully coupled Electromagnetic - Solid/Fluid Mechanics simulation in Forge®. Furthermore, a novel coupling procedure is proposed as a replacement for the current approach.

5.1.1 Current procedure

The procedure being currently used incorporates a remeshing capability in the Solid/Fluid Mechanics solver during the coupling simulation, enabling adaptive meshing if necessary. However, the Electromagnetic solver lacks this feature, resulting in a complete remeshing of the entire domain whenever mesh modifications are required. Furthermore, this remeshing process is carried out by an external mesher (CM2), which operates sequentially. This sequential execution induced a bottleneck in parallel computer architectures, as the entire domain needs to be assembled on a single processor to perform the meshing procedure and partition again to continue the simulation. The algorithm for the multi-physics implementation is illustrated in Fig. 5.1

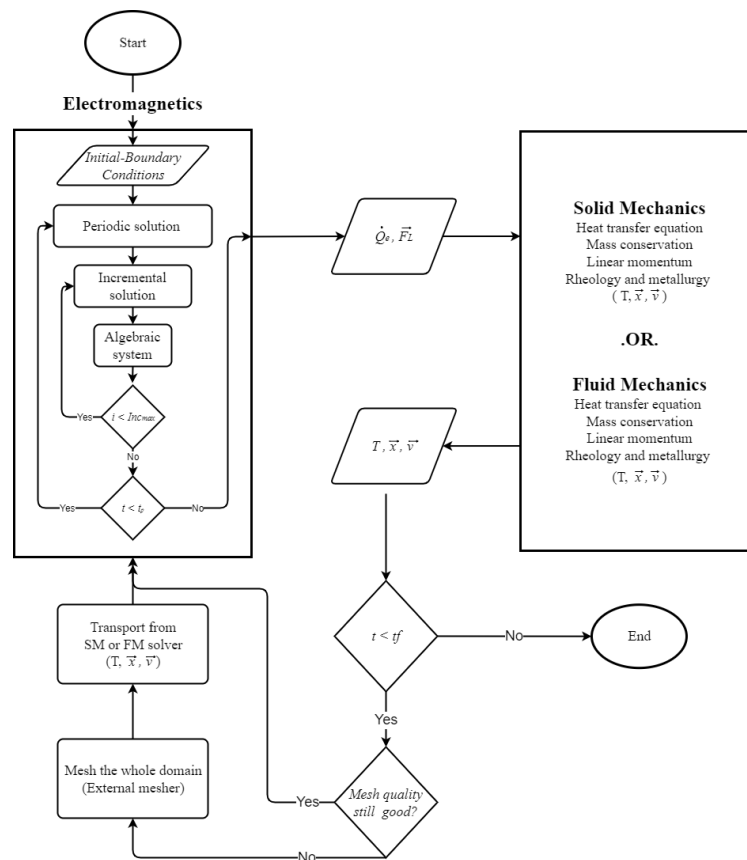


Fig. 5.1 Current algorithm

5.1.2 Proposed procedure

The primary objective of this procedure is to eliminate the dependency on the external CM2 mesher. To achieve this, a new algorithm is proposed, wherein the CM2 mesher is substituted with an internal remeshing procedure. This internal remeshing enables the final step to have complete control over the entire simulation within the solver, offering various advantages such as a more efficient use of parallel architectures, thereby eliminating time and resource waste associated with the external sequential mesher. The algorithm outlining the new strategy is illustrated in Fig. 5.2

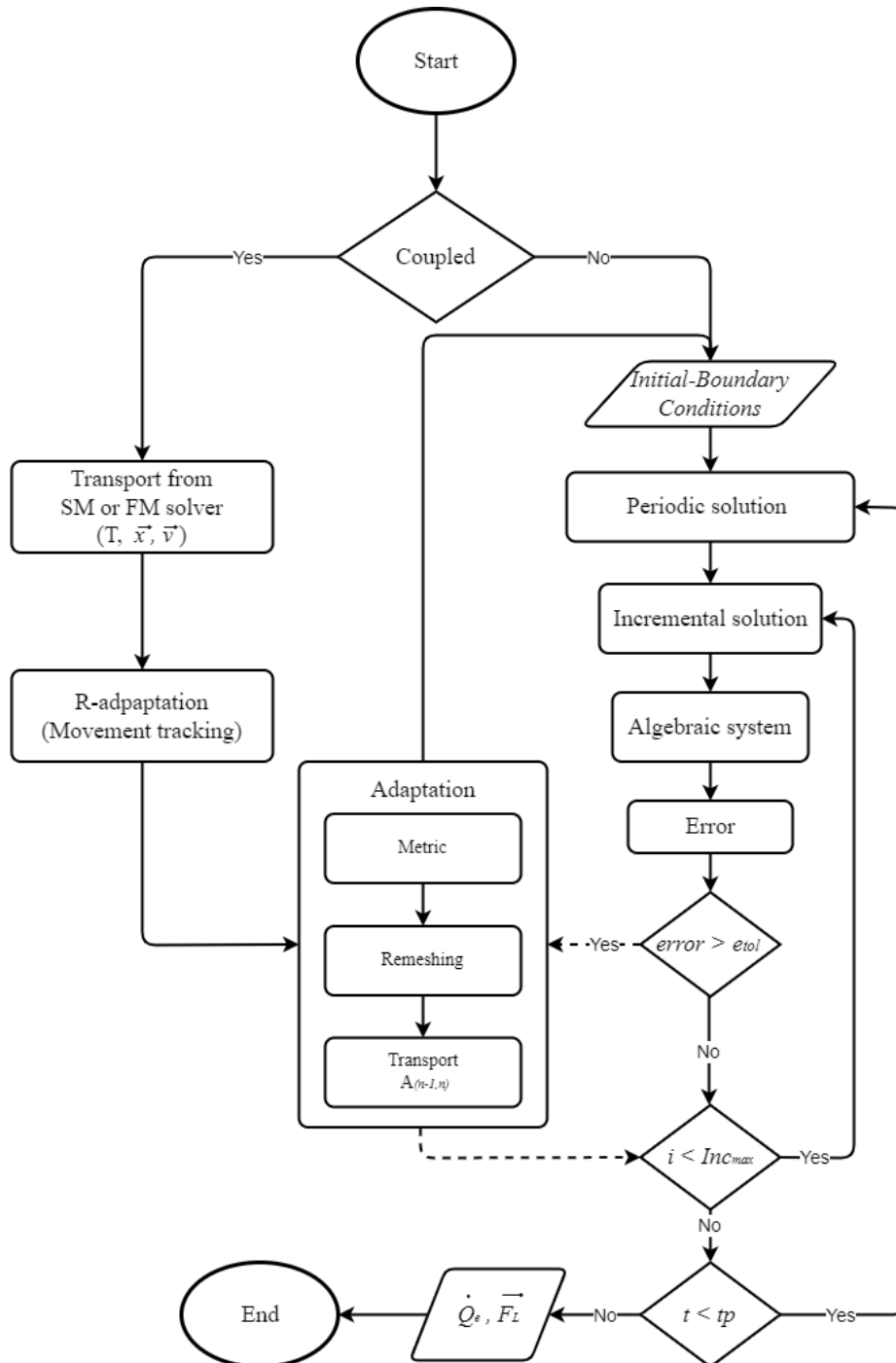


Fig. 5.2 New algorithm

The proposed procedure offers the ability of mesh adaptation either after coupling with another physics or during the simulation itself, guided by the error analysis as illustrated in Fig. 5.2. The adaptation block encompasses a metric calculation step, integrating the metrics outlined in Chapter 0, to drive the remeshing process. Subsequently, the fields are transported from the old mesh to the new adapted mesh.

To address the removal of the external mesher (CM2), after coupling with another physics a novel metric has been developed. The fundamental concept revolves around recreating the identical mesh structure at each coupling step, which serves as the initial mesh for the electromagnetic solver. This is achieved through the development of a geometric metric, proposed by Thierry Coupez [91]. The calculation of the metric follows the procedure outlined below:

5.1.3 Geometrical metric

Considering the metric characteristics discussed in Chapter 0, it is possible to associate a unit metric field with any given mesh. Specifically, this metric is assigned to the element that must have an edge length equal to one. Let's define the edge vector, denoted as \vec{e}_{ij} , formed by nodes i and j . Additionally, let \mathbb{M}_{ij} represent the transformation matrix that converts \vec{e}_{ij} into a vector of unit length:

$$\|\mathbb{M}_{ij}\vec{e}_{ij}\| = 1 \quad (5.1)$$

Then the unit length is calculated as:

$$\langle \mathbb{M}_{ij}\vec{e}_{ij}, \mathbb{M}_{ij}\vec{e}_{ij} \rangle = 1 \quad (5.2)$$

This expression can be rewritten as:

$$\langle \mathbb{M}_{ij}^T \mathbb{M}_{ij} \vec{e}_{ij}, \vec{e}_{ij} \rangle = 1 \quad (5.3)$$

When the metric can be defined as:

$$\bar{\mathcal{M}} = \mathbb{M}_{ij}^T \mathbb{M}_{ij} \quad (5.4)$$

Then, the expression (5.3) can be rewritten as:

$$\langle \vec{e}_{ij}, \bar{\mathcal{M}} \vec{e}_{ij} \rangle = 1 \quad (5.5)$$

Founding the same definition as in the Chapter 0 to calculate the unit length of the edges:

$$l_{\mathcal{M}}(\vec{e}_{ij}) = \sqrt{\langle \vec{e}_{ij}, \bar{\mathcal{M}} \vec{e}_{ij} \rangle} = 1 \quad (5.6)$$

The strategy consists of building the metric field at each node of the mesh taking a path of edges surrounding the node. In order to do this, the expression (5.5) is summed up over the edges:

$$\sum_{j \in \Gamma(i)} \langle \vec{e}_{ij}, \bar{\mathcal{M}}_i \vec{e}_{ij} \rangle = \sum_{j \in \Gamma(i)} 1 \quad (5.7)$$

This expression can be rewritten as:

$$\bar{\mathcal{M}}_i : \left(\sum_{j \in \Gamma(i)} \langle \vec{e}_{ij} \otimes \vec{e}_{ij} \rangle \right) = |\Gamma(i)| \quad (5.8)$$

Here, $|\Gamma(i)|$ is the set of edges sharing the node i . The metric at the node i ($\bar{\mathcal{M}}_i$) can then be expressed as:

$$\bar{\mathcal{M}}_i = \frac{1}{d} \left(\frac{1}{|\Gamma(i)|} \sum_{j \in \Gamma(i)} \langle \vec{e}_{ij} \otimes \vec{e}_{ij} \rangle \right)^{-1} \quad (5.9)$$

Where d represents the dimension of the space.

5.2 Performance test

After eliminating the external mesher (CM2), two performance tests to evaluate the procedure's performance and efficiency have been done. The primary objective of these tests is to determine the extent to which the time could be reduced by transitioning to an internal remesher.

5.2.1 Simple induction case

The geometric metric, denoted as $\bar{\mathcal{M}}_i$, is employed to regenerate a new mesh that closely resembles the original mesh. This metric plays a crucial role in eliminating the need for the external mesher (CM2) by restoring the previous mesh prior to coupling and constructing a new mesh based on the old one. By implementing this procedure, a comparison can be made between the current and the proposed procedures. To facilitate this comparison, a simple induction heating case is presented as an example (see Fig. 5.3).

The test is carried out comparing the schemes illustrated in Fig. 5.1 and Fig. 5.2.

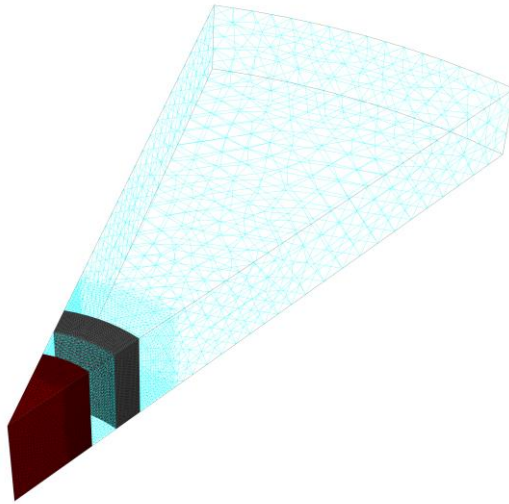


Fig. 5.3 Axisymmetric case: Workpiece and inductor in dark red.

The case depicted in Fig. 5.3 is an axisymmetric induction case, in which the workpiece is surrounded by an inductor; the mesh consists of a system with 150k degrees of freedom. To evaluate the performance, tests are conducted for each scheme using 1, 2, 4, 8, and 10 processors. The results are measured in terms of time and can be summarized as follows:

Current procedure: The process involves the Electromagnetic solver (EM), Thermomechanical solver (TM), External mesher (CM2), and Partitioning (P) for solver initialization and parallel distribution.

Proposed procedure: The process includes the Electromagnetic solver (EM), Thermomechanical solver (TM), and Internal mesher (MTC).

The time required for each procedure is recorded and analysed for the different processor configurations.

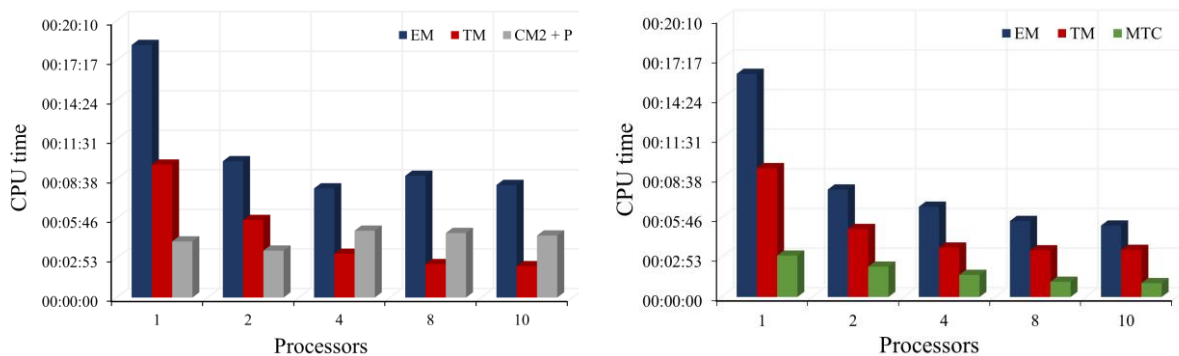


Fig. 5.4 Comparison between the two procedures. Left: current procedure. Right: proposed procedure.

The remeshing procedure is deliberately executed at each coupling step between the thermomechanical (TM) and electromagnetic (EM) solvers throughout the simulation. It also ensures that the same mesh is generated for both the external mesher (CM2) and the internal mesher (MTC). By adopting this methodology, it becomes easier to accurately compare the performance of the simulation between the two procedures.

By using the external mesher, it is apparent that the time dedicated to remeshing remains constant or even increases when comparing a parallel run with a single processor. This clearly indicates the bottleneck associated with the current procedure. Furthermore, it is evident that the remeshing process in the simulation demands more computational resources compared to the thermomechanical calculation, while also taking approximately 50% of the time of the electromagnetic simulation. In contrast, the proposed internal remesher (MTC) effectively utilizes the capabilities of a parallel architecture. The results obtained from this approach demonstrate that the use of additional processors significantly reduces the computational time required for remeshing, removing the bottleneck of the current procedure.

Fig. 5.5 and Table 5.1 illustrate the total time taken by each simulation. It is important to note that the overall computational time is heavily influenced by the duration of the new mesh construction. When employing CM2, the calculation time remains unchanged for 4, 8, and 10 processors. Conversely, with the implementation of MTC, the computation time decreases as the number of processors increases.

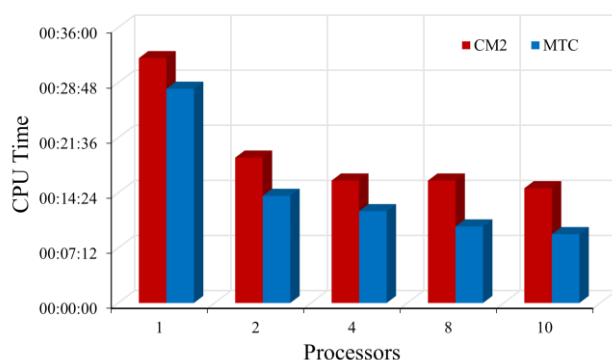


Table 5.1 CPU time

# Proc	CM2	MTC
1	32	28
2	19	14
4	16	12
8	16	10
10	15	9

Time in minutes

Fig. 5.5 Total time spent on each procedure.

The absence of the external mesher has brought significant stabilization. Table 5.2 illustrates the number of linear iterations required to achieve convergence for both procedures, and the maximum temperature in the workpiece. A notable disparity is observed in the electromagnetic solver, when CM2 is used, resulting in a variation of the number of iterations. On the other hand, employing MTC ensures a stable linear solver, with the exact same number of iterations needed for convergence. Additionally, the proposed procedure maintains a nearly invariant maximum temperature. This new approach enhances the stability of the linear system solver.

Table 5.2 Comparison between the two procedures: Linear solver iterations and maximum temperature in the workpiece

# Processors	Thermomechanical solver		Electromagnetic solver		Temperature (°C)	
	CM2	MTC	CM2	MTC	CM2	MTC
1	250	251	320	320	1259.34	1264.34
2	250	251	320	320	1259.46	1264.43
4	255	251	480	320	1278.11	1264.46
8	251	251	640	320	1262.16	1264.39
10	253	251	560	320	1273.11	1264.48

5.2.2 A more complex induction case

In order to evaluate the real CPU time impact on a more realistic application, a more complex case is performed. As observed in the previous test, changing the remeshing procedure within the software can have a significant effect on CPU time. This becomes even more crucial when dealing with a large number of degrees of freedom. Thus, the following induction heating case is presented, as an illustrative example.

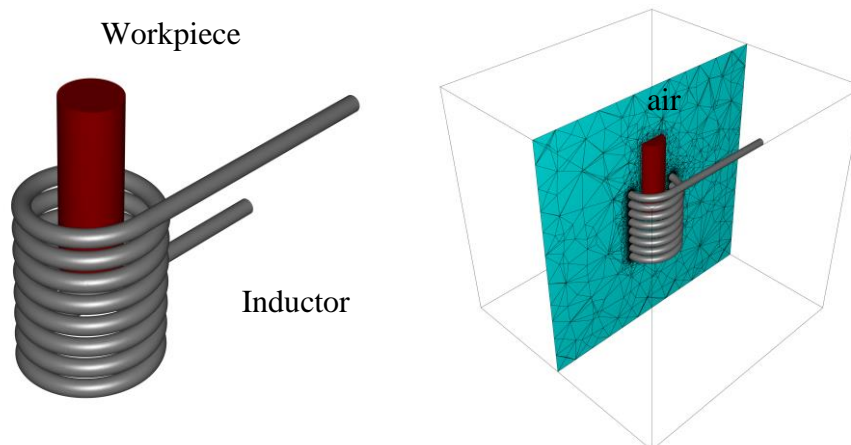


Fig. 5.6 Induction heating case: workpiece in dark red, inductor in grey and air in light green

Fig. 5.6 illustrates a typical industrial induction heating scenario, where a cylinder is heated by a spiral inductor. The corresponding mesh for this case comprises approximately 4 million degrees of freedom, making it a significantly large case to evaluate the difference between using an external and internal mesher.

Similarly, to the previous case, the remeshing procedure is applied after each coupling between the thermomechanical and electromagnetic solvers. In addition, the computation time for each solver is calculated individually, providing a detailed breakdown of the time spent in the simulation. For this particular case, the simulations are conducted using 1, 4, 8, and 16 processors. The time for each step of the simulation is labelled as follows:

Current procedure: The process involves the Electromagnetic solver (EM), Thermomechanical solver (TM), External mesher (CM2), and Partitioning (P) for solver initialization and parallel distribution.

Proposed procedure: The process includes the Electromagnetic solver (EM), Thermomechanical solver (TM), and Internal mesher (MTC).

The results for each step of the simulation are presented in Fig. 5.7.

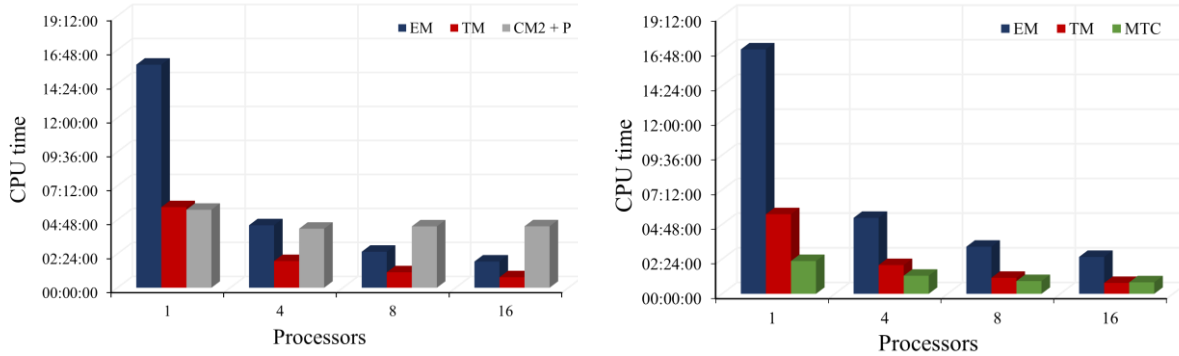
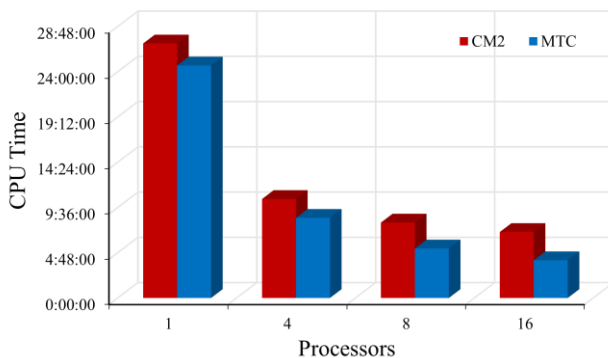


Fig. 5.7 Comparison between the two procedures. Left: current procedure. Right: proposed procedure.

The presented results clearly indicate that the computational resources are more significantly impacted as the number of degrees of freedom in the calculation increases, due to the influence of the external mesh. As depicted in Fig. 5.7, the time spent solely on remeshing is greater than the time spent on the simulation itself, particularly when using more processors in the simulation. The current remeshing procedure appears to take about the same amount of time in each parallel configuration, nullifying the benefits of parallel architecture. Contrarily, the internal mesher overcomes this issue, resulting in a more affordable time spent on remeshing compared to other steps of the simulation. Consequently, the computational time of the calculation is considerably reduced.

Fig. 5.8 and Table 5.3 illustrate the cumulative time for each simulation, indicating noticeable time gains as the number of processors in the simulation increases. There is a reduction of 9% for one processor, while for 16 processors, the time reduction reaches 43%.



# Proc	CM2	MTC
1	27h00	24h40
4	10h30	8h30
8	8h00	5h15
16	7h00	4h00

Time in hours

Fig. 5.8 Total time spent on each procedure.

5.3 Industrial applications

5.3.1 Wheel bearing Induction heating

In this study, we investigate the induction hardening process used in the manufacturing of a wheel bearing [90]. To perform this treatment two inductors and field concentrators are used. They are strategically placed in the area where heat treatment is required to create a concentrated magnetic field towards the part. To optimize the computational efficiency, we have considered the geometry's axial symmetry and only simulated a portion of it as can be seen in the Fig. 5.9

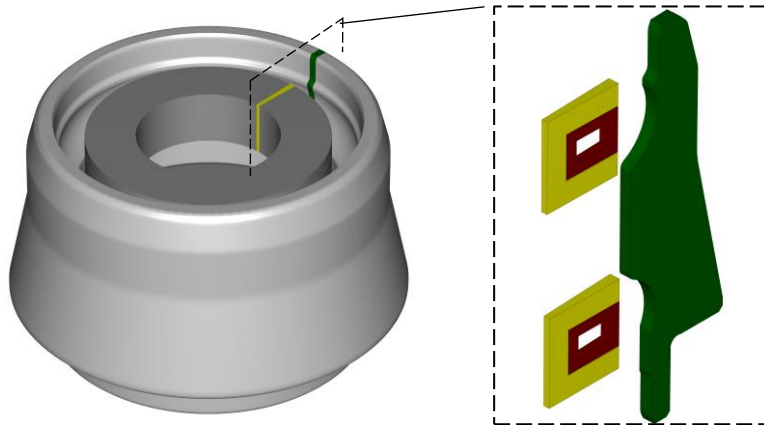


Fig. 5.9 Wheel bearing and symmetry (green: wheel bearing, yellow: concentrators, dark red: inductor)

In order to effectively adapt the mesh to the electromagnetic phenomenon being simulated, we have chosen to focus on the magnetic field distribution throughout the simulation. This is reflected in Fig. 5.10 which illustrates the magnetic field behaviour over the part. By considering this information, we can automate the remeshing so that it effectively captures the critical areas of the simulation while minimizing computational cost and reducing CPU time.

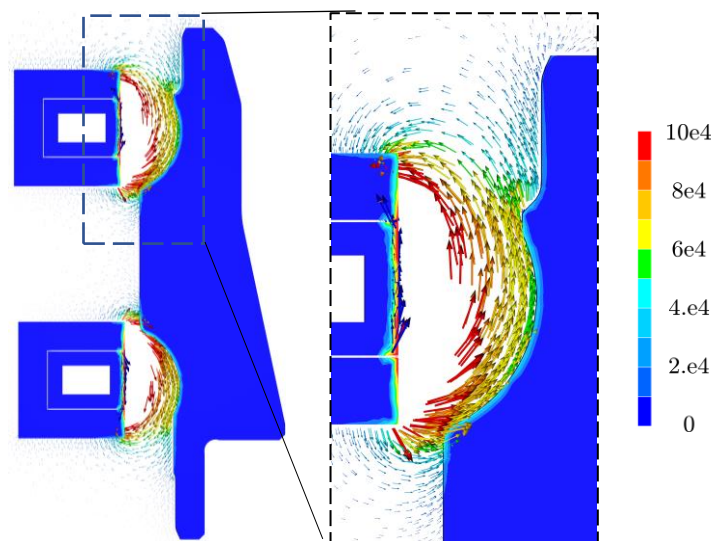


Fig. 5.10 Magnetic field distribution over the wheel bearing

The automatic remeshing procedure using the anisotropic metric tensor, based on Jacobian approximation, introduced in Chapter 0, is expected to adapt the mesh size according to the regions where the magnetic field acts strongly, including the regions influenced by the current concentrators. The simulation results will provide insights into the temperature distribution within the part during the induction heating process, enabling us to optimize the process for improved efficiency and reduced cost.

The distribution of the initial mesh can be observed in Fig. 5.11, where each part is highlighted for easy visualization of the mesh distribution across the geometries and the surrounding air.

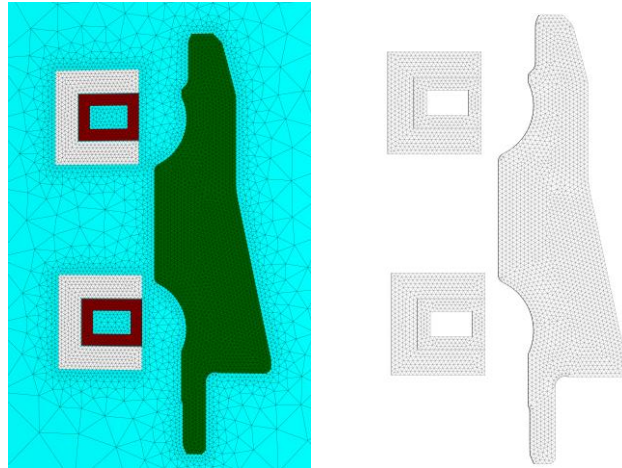


Fig. 5.11 Mesh distribution of the geometries and the surrounding air.

The new mesh is computed using the metric tensor obtained from the anisotropic mesh adaptation procedure. As expected, the adapted mesh distribution is shown in Fig. 5.12; the mesh is refined around the critical areas between the part and the inductors where the magnetic field acts strongly; the surrounding air is also adapted in accordance with the magnetic field. This demonstrates the effectiveness of the proposed automatic remeshing procedure in adapting the mesh size to accurately capture the electromagnetic phenomena.

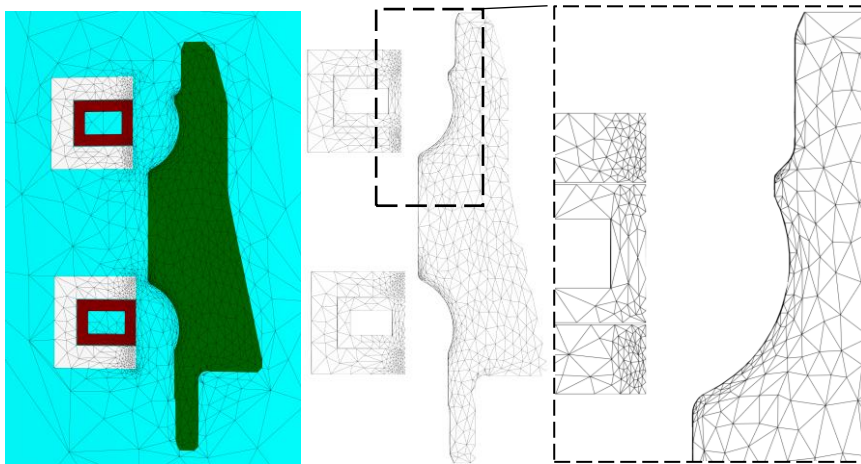


Fig. 5.12 Adapted mesh distribution of the geometries and the surrounding air.

The performance of the initial and adapted meshes were compared to quantify the error and CPU time required for a complete simulation of the hardening process. The initial mesh had 100k degrees of freedom, while the adapted mesh had only 26k degrees of freedom. Resulting in a significant reduction in computational cost. It is worth noting that the adapted mesh had a lower error over the simulation than the initial one, as shown in Fig. 5.13.

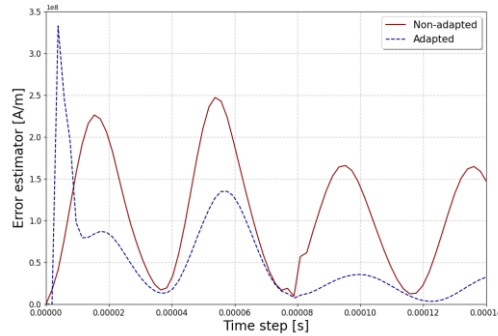


Fig. 5.13 Error estimator comparison over two electromagnetic periods

The CPU time required for the adapted mesh was only 6 minutes, whereas it took 25 minutes for the initial mesh. This substantial reduction in CPU time demonstrates the efficiency of the adapted mesh in the electromagnetic solution, which is approximately four times less computationally expensive.

Finally, in order to compare the temperature distribution on the initial and adapted mesh, we have focused on the temperature at the end of the simulation. Fig. 5.14 illustrates the temperature distribution for both cases, where it is evident that both meshes have a similar temperature profile. The results demonstrate that the proposed anisotropic mesh adaptation procedure can significantly reduce computational cost while maintaining high accuracy in electromagnetic simulations.

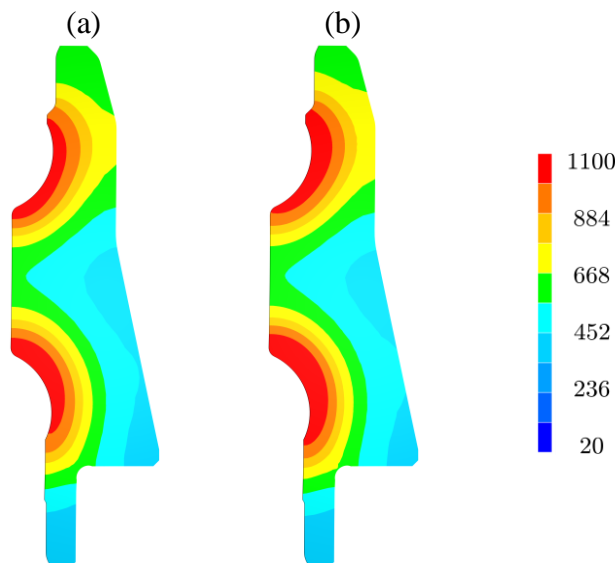


Fig. 5.14 Temperature ($^{\circ}\text{C}$) distribution on the part: (a) adapted mesh, (b) initial mesh.

5.3.2 Magnetic Pulse Forming

To validate the effectiveness of our approach within the context of Magnetic Pulse Forming (MPF), a ring expansion case has been selected. Originally proposed in [92] for plasticity characterization under high-speed loading, this case has later been modified in [93], transitioning from a circular to a square cross-section of the rings. The configuration involves two coaxial copper rings, as illustrated in Fig. 5.15, with the exterior ring (green) serving as the workpiece, and the internal ring representing the inductor (dark red). This choice of case allows us to thoroughly evaluate the performance of our coupled simulation method.

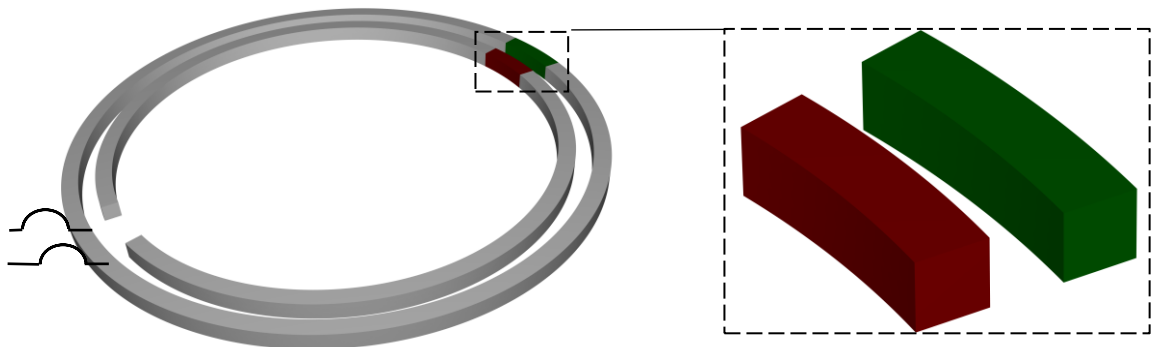


Fig. 5.15 Ring and symmetry used to perform the simulation (dark red: inductor, green: workpiece).

The MPF machine is directly connected to the inductor, acting as the power source that delivers the electric load necessary to generate the pulse. This pulse is responsible for deforming the external ring, resulting in its expansion. The machine parameters, including key variables such as voltage, capacitance, resistance, and inductance, are detailed in Table 5.4. Additionally, Table 5.5 provides specific information regarding the geometry of the parts involved in the ring expansion process.

Table 5.4 Machine parameter	
Parameters	
V_0 [Volts]	5000
C_m [μF]	126
R_m [$m\Omega$]	48
L_m [nH]	115.7

Table 5.5 Geometry dimensions	
Geometry	
Inductor radius [mm]	14
Inductor cross-section [mm]	1
Ring radius [mm]	16
Ring cross-section [mm]	1

Fig. 5.16 illustrates the mesh configuration for the inductor, ring, and surrounding air in the setup. An isotropic structured mesh has been employed to ensure an accurate representation of the geometries.

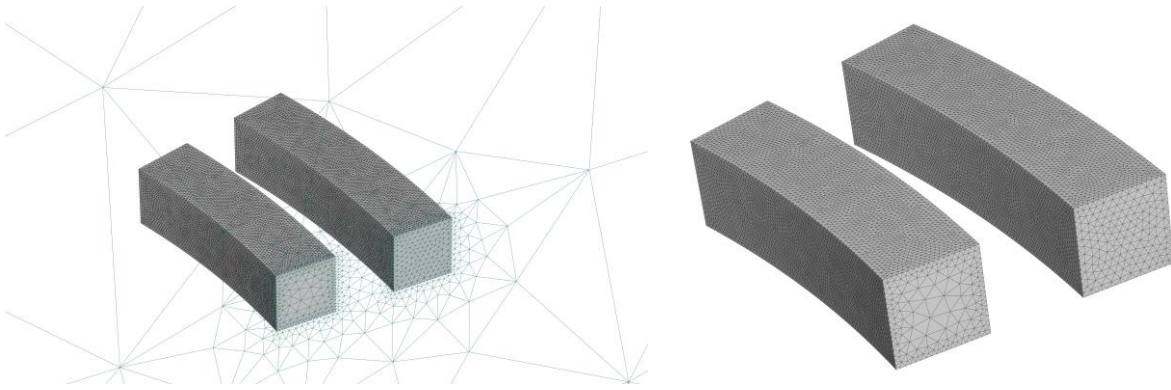


Fig. 5.16 Initial mesh in the set-up

Magnetic field and current density are computed, based on the mesh configuration presented above, and depicted in Fig. 5.17. The figure displays both the magnitude and vector representation of the fields. Observing the magnetic field and current density distribution we can notice the symmetric behaviour within the inductor, and a higher magnitude on the side of the part adjacent to the inductor. This phenomenon is attributed to the proximity effect of the electromagnetic phenomena. This information on the field distribution serves as a guide for adapting the mesh, in order to minimize the number of degrees of freedom while maintaining the accuracy of the solution.

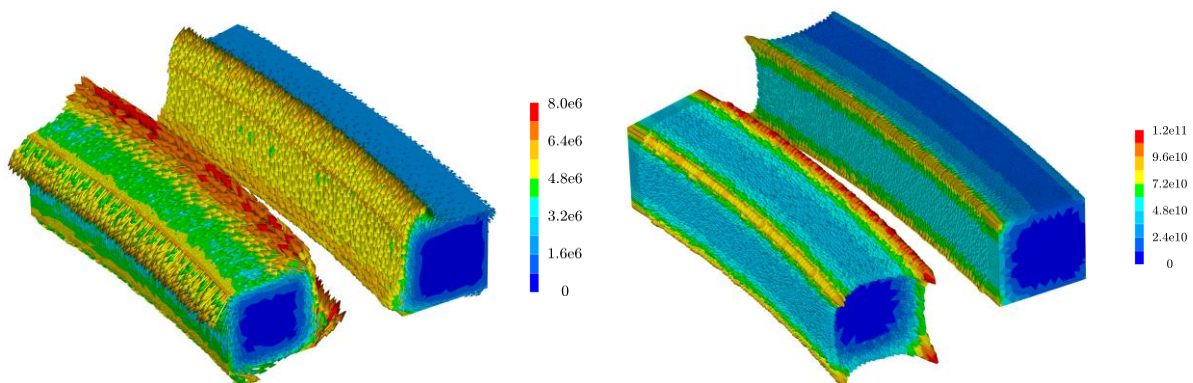


Fig. 5.17 Magnetic field $[A/m]$ and Current density $[A/m^2]$ distribution over the inductor and workpiece

The mesh adaptation procedure introduced in Chapter 0 is employed to dynamically adjust the mesh based on the behaviour of the magnetic field. In accordance with the duality effect explained in the section 4.4.5 the mesh will adapt to follow the anisotropy of the electric field, which is similar to the current density in conductive parts. The metric is calculated using the Jacobian procedure, which enables to reduce the number of degrees of freedom and to accurately capture the electromagnetic phenomena. By utilizing this approach, we can effectively optimize the mesh to accurately represent the field variation throughout the simulation domain. Fig. 5.18 depicts the adapted mesh, providing the representation of the inductor, ring and surrounding air.

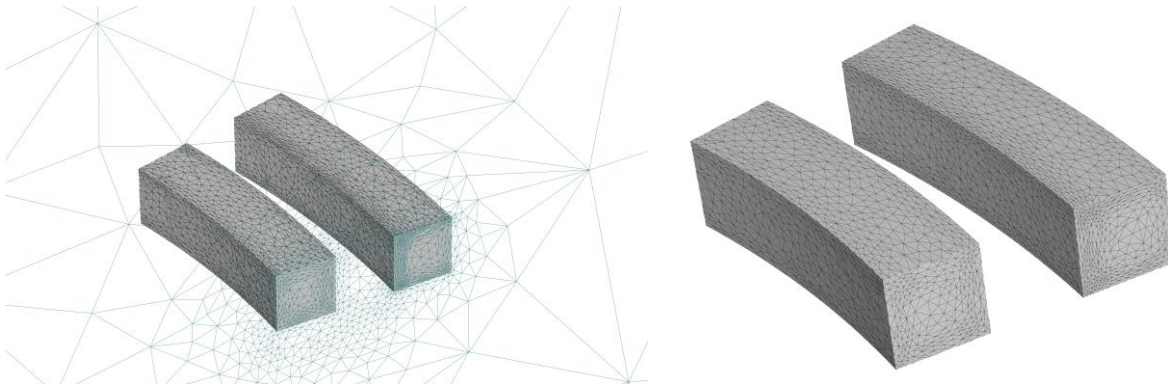


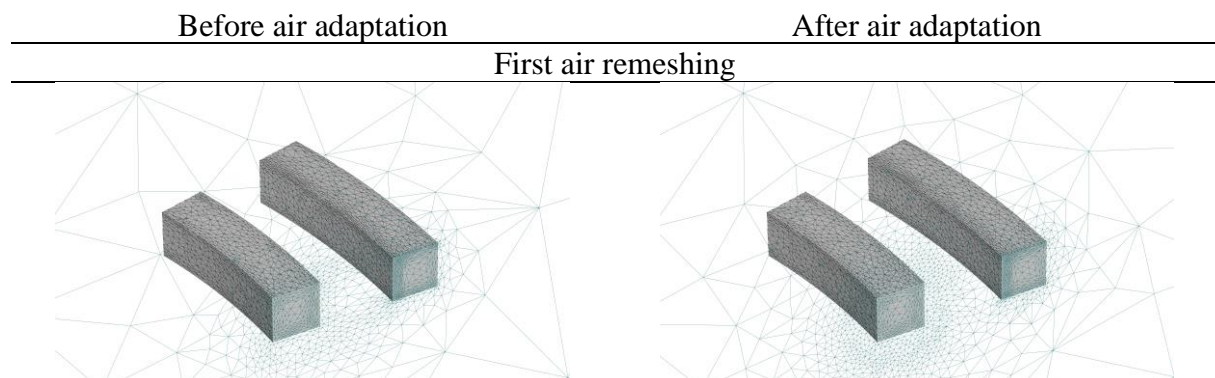
Fig. 5.18 Mesh after adaptation

The mesh adaptation procedure effectively refines and adjusts the mesh to closely capture the intricate electromagnetic phenomenon. Notably, the conductive parts exhibit adaptation in accordance with the anisotropy of the current density, as it was expected. Additionally, the surrounding air domain seems to follow the behaviour of the magnetic field.

The MPF simulation involves a coupled computation at each time step, where the electromagnetic solving step is followed by the thermomechanical solving step, and iteration between the two solvers until the simulation is finished. Additionally, as the ring expands, it necessitates mesh modifications to accurately capture the evolving parts. To effectively manage this, the following methodology was implemented:

- 1) Initially, the mesh is adapted based on the anisotropy of the field, as explained earlier, ensuring an optimal representation of the electromagnetic phenomenon.
- 2) At each coupling, an r-adaptation procedure is applied to dynamically move the mesh in accordance with the displacement of the parts, ensuring a consistent mesh alignment.
- 3) A mesh quality test is performed to determine if a remeshing procedure is required, ensuring the mesh maintains its integrity and accuracy throughout the simulation.
- 4) To avoid an unnecessary increase in element count, the surrounding air is only adapted periodically, finding a balance between accuracy and computational efficiency.

This methodology ensures that the mesh adapts precisely to the evolving physical phenomenon.



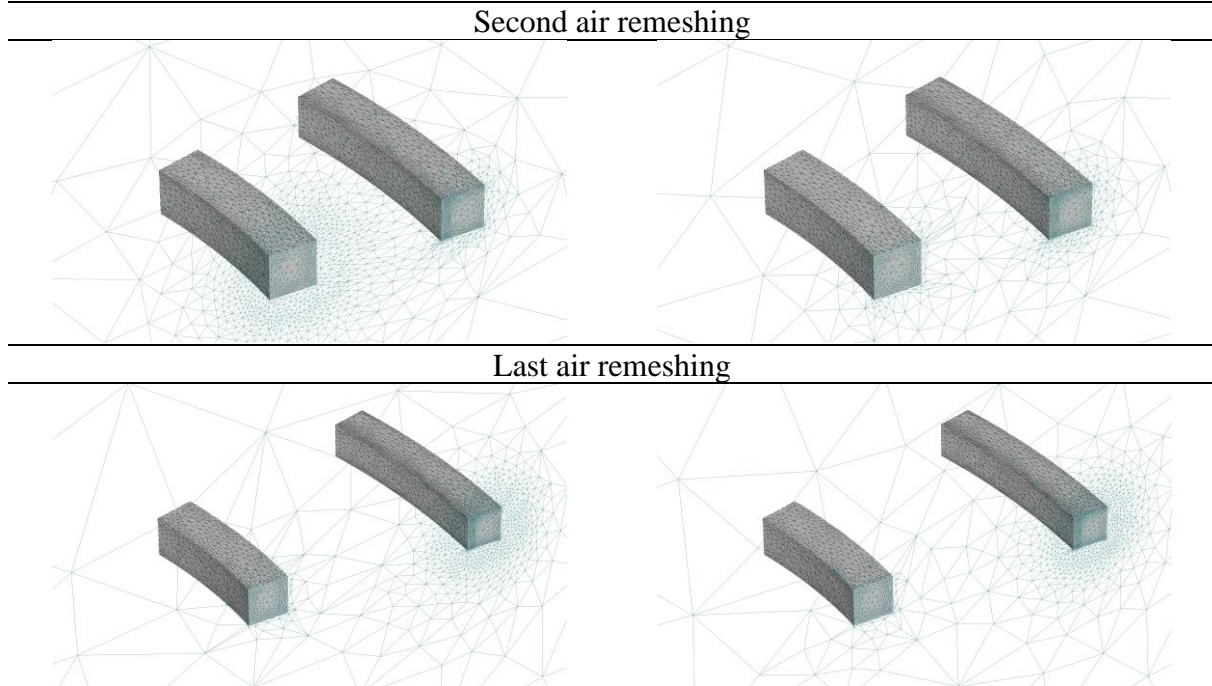


Fig. 5.19 air adaptation during the simulation

The fourth point of the methodology is exemplified through the results obtained during the simulation. Fig. 5.19 shows the meshes where only the surrounding air is periodically adapted, presenting the mesh before and after the air adaptation process. Upon observation, it is evident that prior to adaptation, the elements in the air region appear elongated. However, the subsequent remeshing procedure effectively addresses this issue while simultaneously reducing the number of degrees of freedom. Fig. 5.19 demonstrates three stages of the simulation: the initial air remeshing, followed by the second and final adaptations.

A comparison is made between the meshes depicted in Fig. 5.16 and Fig. 5.18 to evaluate the behaviour of the adapted mesh in relation to a fully isotropic mesh. The initial mesh (Fig. 5.16) consists of a total of 329399 DoF, while the adapted mesh reduces the DoF to 137749. Fig. 5.20 illustrates the global error estimator of the magnetic field throughout the simulation, clearly demonstrating that the non-adapted mesh exhibits significantly larger error compared to the adapted mesh. Therefore, the adapted mesh achieves a fine balance between accurately representing the physical phenomenon and minimizing use of computational resources.

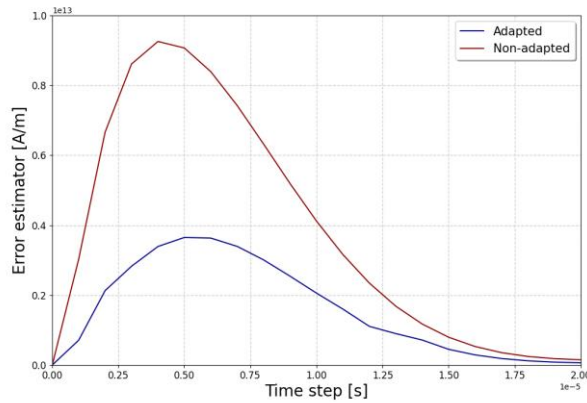
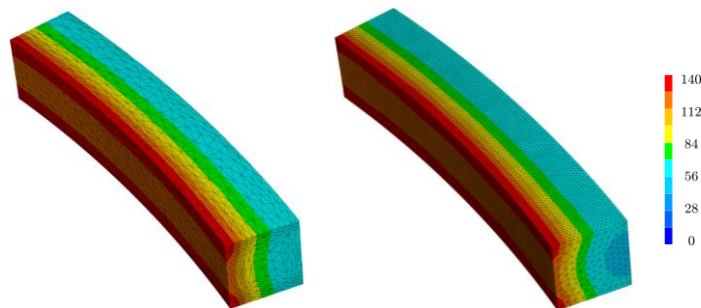


Fig. 5.20 Error estimator comparison

Following the simulation, the time required in the electromagnetic solver is significantly reduced by 46% when comparing the non-adapted mesh with the adapted one. The non-adapted mesh took approximately 37 minutes, while the adapted mesh reduced the time to 20 minutes. Furthermore, the temperature distribution over the ring, depicted in Fig. 5.21, demonstrates a good agreement at the end of the simulation. It is also seen that the adapted mesh employed in the electromagnetic solver effectively captures the temperature evolution.

Fig. 5.21 Temperature ($^{\circ}\text{C}$) distribution of the ring

5.4 Conclusions

This chapter was dedicated to the fully coupled multi-physics simulation of electromagnetic-based industrial processes. We provided an overview of the current coupling scheme used in Forge® and proposed modifications to implement the developed mesh adaptation procedure. First, a geometric metric capable of recreating a mesh was developed, eliminating the need for an external mesher (CM2).

Once the coupling was fully implemented, we conducted performance tests. The first case involved a simple induction heating scenario, where we showcased the primary advantages of transitioning from an external mesher to the internal mesher (MTC). The second case was more industrially relevant and demonstrated a significant reduction in computational time using the proposed procedure.

Furthermore, we simulated two industrial cases. The first case involved an induction hardening process applied to a wheel bearing. The results demonstrated not only a considerable reduction in numerical errors, CPU time, and memory usage but also the preservation of accuracy when adapting the mesh according to the underlying physical phenomenon.

The second case was a magnetic pulse forming test using a ring expansion scenario. As the workpiece was in motion, we explained the procedure to track the movement on the piece. In this case as well, the procedure showed a substantial reduction in numerical errors and computational resources, along with a well-fitted mesh adaptation based on temperature.

Chapter 6

Conclusions and perspectives

6 Conclusions

The main goal of this Ph.D. research was to achieve efficient and accurate modelling of electromagnetic-based processes by developing automated anisotropic meshing procedures in conjunction with error estimators. The key focus was on adapting the mesh effectively based on the underlying physical phenomena, ensuring robustness in dealing with complex industrial processes. To achieve this, we implemented these methods in the commercial software Forge® and Thercast® and testing them on complex industrial cases.

The motivation behind this work stems from the significant time investment required by the electromagnetic solver during the coupling simulation with heat transfer, solid or fluid mechanics solvers. It has been observed that the remeshing phase for the electromagnetic solver often consumes more time than the actual simulation, particularly in the case of complex geometries.

To address this challenge, we identified two key focal points that required attention.

The first involved the development of an error estimator. This component needs to meet several criteria, including its ability to effectively identify and quantify the errors in the solution. The estimator has to be versatile enough to adapt to the varying characteristics of the electromagnetic phenomena. Furthermore, it needed to possess a general applicability, enabling its implementation for various electromagnetic quantities. Lastly, it is crucial for the estimator to be computationally efficient, minimizing the required computational time for its implementation.

The second point entailed the development of a metric tensor. This component played a pivotal role in capturing the electromagnetic phenomena accurately. Its purpose is to track the anisotropy exhibited by the electromagnetic phenomena, thereby guiding the mesh adaptation process. By effectively utilizing the information provided by the metric tensor, the mesh can be dynamically adjusted in order to align with the evolving characteristics of the electromagnetic simulation.

Since this work focuses on the simulation of electromagnetic-based processes. We provide in Chapter 1 an introduction to the main processes which include Induction Heating, Magnetic Pulse Forming, and Electromagnetic Stirring. Furthermore, we explain the underlying physical phenomena associated with these processes, emphasizing important effects such as the skin depth effect, proximity effect, and the influence of magnetic fields on material properties.

Additionally, we have discussed the behaviour of ferromagnetic and paramagnetic materials in relation to the Curie temperature.

Chapter 2 has explored the Multiphysics numerical model, encompassing electromagnetic, heat transfer, solids, and fluid mechanics problems. The primary focus of this chapter is to analyse the electromagnetic phenomena, thus emphasizing their significance for this work. An explanation of the finite element approach used here was provided, covering essential aspects such as the $A - \phi$ potential formulation, its variational resolution, vector edge elements, and the employed time integration scheme. Additionally, the coupling procedure is highlighted to show the overall simulation framework.

Chapter 3 focused on addressing the first requirements for constructing an adaptive mesh adaptation procedure, which involves the error estimator development. A literature review has been conducted, with specific emphasis on electromagnetic modelling and various existing methods. In order to meet the specified criteria, an error estimator based on the recovery approach, specifically the variational Galerkin approach, was selected. This method offered distinct advantages over other recovery-based methods, as it uses a global linear system resolution. Consequently, the recovered field is directly computed as an unknown of the linear system, eliminating the need for case-specific developments and ensuring robustness. Additionally, alternative estimators were developed in this chapter, aiming to verify physical phenomena such as the Ampere and Faraday equations. Validation tests were performed, encompassing a range of scenarios from purely electromagnetic cases to representative industrial processes, to evaluate the performance of the estimators.

Chapter 4 was the cornerstone of this work, focusing on the development of the metric tensor. The numerical determination of the tensor was discussed, and two distinct metrics were proposed. The first metric was a commonly used tensor in adaptive procedures, constructed based on the Hessian of the studied scalar field. This tensor was based on the computation of the second derivatives of a scalar field. The second method involved the development of a metric based on the Jacobian, which was directly computed from first derivative of a vector field. These methods were thoroughly tested across various scenarios to evaluate their ability to capture the anisotropy of electromagnetic phenomena and reduction of the error in the solution. Additionally, industrial cases involving Induction Heating, Magnetic Pulse Forming, and Electromagnetic Stirring were simulated to assess the performance of the metrics in these specific applications. The results reveal that the metric based on the Jacobian captures more effectively the anisotropy of the phenomena, leading to a reduction in the number of degrees of freedom for almost the same reduction in error. This can be attributed to the utilization of linear basis functions, where an approximation of the second order derivative of the vector field solution may mask the anisotropy and then the neglected term may contain the lost anisotropy, whereas the first derivative provides a better means of tracking it. For more details see Appendix 7.4.

Chapter 5 focused on the implementation of the automatic mesh procedure within a fully coupled simulation. The chapter started by comparing the current strategy used in the commercial software Forge® with our new strategy. Performance tests were conducted on two induction heating cases: a simple case with 150k degrees of freedom and a more complex case

with around 4 million of degrees of freedom. Our procedure has demonstrated a significant improvement in CPU time compared to the existing strategy. The second part of the chapter was dedicated to industrial processes. The first industrial case involved the induction heating of a wheel bearing, where our methodology successfully reduces solution errors while simultaneously reducing CPU time. And the second case examined an expansion ring, yielding promising results.

Perspectives

The direct numerical model for electromagnetic computations has now been greatly enhanced. Several extensions of this work can be foreseen.

One extension can deal with expansion of the applicability of the method to a broader range of scenarios, including heating and hardening processes with moving parts close to the inductors; efficient interaction of remeshing with part motion should be investigated.

Our methods have been tested on linear elements. Another extension could deal with the investigation of the behaviour of the error estimator and the remeshing procedure with higher-order elements.

As these developments have been carried out for the benefit of Multiphysics computations it would be required to study the impact of the electromagnetic mesh adaptation on the accuracy of the thermo-mechanical computations. Furthermore, as the core of the metric computation strategy has been done in an agnostic manner with respect to the physical fields it would greatly benefit to transfer the methodology back into the remeshing procedures currently implemented for the standard mechanical solvers in FORGE® and THERCAST®.

APPENDIX

Appendices

7.1	Solid mechanics problem	161
7.1.1	Mass conservation	161
7.1.2	Linear momentum conservation.....	162
7.1.3	Angular momentum conservation	163
7.1.4	Constitutive laws	165
7.1.4.1	Elasticity:.....	165
7.1.4.2	Compressibility:.....	166
7.1.4.3	Plasticity:	166
7.2	Fluids Mechanics problem.....	167
7.2.1	Mass continuity equation	168
7.2.2	Momentum conservation.....	168
7.2.3	Constitutive laws	169
7.3	Edge element – Coulomb gauge demonstration.....	170
7.4	Hessian – Jacobian analytical and numerical test	171
7.4.1	Numerical solution	173
7.4.1.1	Hessian.....	173
7.4.1.2	Jacobian	176
7.4.2	Analytical solution	178
7.4.2.1	Hessian.....	178
7.4.2.2	Jacobian	178
7.4.3	Analytical vs numerical solution.....	179

7 Appendices

7.1 Solid mechanics problem

7.1.1 Mass conservation

Considering a domain Ω , the mass inside of it is defined by

$$m = \int_{\Omega} \rho(\vec{x}, t) d\Omega \quad (7.1)$$

Where ρ is the density of matter at any point of Ω . Then, assuming no diffusion, nor production of mass. The mass variation can be expressed by

$$\frac{dm}{dt} = \frac{d}{dt} \int_{\Omega} \rho dV = \int_{\Omega} \frac{\partial \rho}{\partial t} dV \quad (7.2)$$

The transfer of the time derivative to the inside of the integral causes no problems as the volume of the domain Ω is fixed. Then, the time derivative inside becomes a partial derivative ($\partial/\partial t$), since ρ is a variable of position and time.

Following the above assumptions, the mass variation inside of the domain must be due to transfer of mass across their faces. Which is described as the mass flux of a transported material. It is defined as the product of the density by the material velocity field \vec{v} . The quantity of material going out through each face (Γ) of Ω is given by the normal component (\hat{n}) of Γ , multiplied by the corresponding area, that is:

$$\int_{\Omega} \frac{\partial \rho}{\partial t} dV = \int_{\Gamma} \rho \vec{v} \cdot \hat{n} dS \quad (7.3)$$

Applying the divergence theorem at the rhs of the above equation, the mass flux can be expressed as integral of volume and the mass conservation equation is then expressed as:

$$\int_{\Omega} \frac{\partial \rho}{\partial t} dV = \int_{\Omega} \vec{\nabla} \cdot (\rho \vec{v}) d\Omega \quad (7.4)$$

Then, assuming the continuity of the above expression and using the fact that this equality is true not only in the whole system Ω , but also for its very single subdomain, the following PDE is obtained:

$$\frac{\partial \rho}{\partial t} + \vec{\nabla} \cdot (\rho \vec{v}) = 0 \quad (7.5)$$

Finally, two particular situations can occur:

In the first, is the stationary case (steady state), which meant that nothing changes over time. This implies that the partial derivative with respect to time is zero. Then, the equation (7.5) becomes:

$$\vec{\nabla} \cdot (\rho \vec{v}) = 0 \quad (7.6)$$

In the second situation implies a material density constant in the Ω . In this case the material is said to be incompressible. Then, (7.5) can be rewritten as:

$$\vec{\nabla} \cdot \vec{v} = 0 \quad (7.7)$$

7.1.2 Linear momentum conservation

The velocity \vec{v} that appears in the equation of mass conservation can be determined from the conservation of momentum. Mostly the variations of this momentum are due volume forces and contact forces acting in a body. Then, the total forces are given by

$$f(t) = \int_{\Omega} \rho \vec{b} dV + \int_{\Gamma} \vec{t} dS \quad (7.8)$$

The force \vec{t} is the contact force on the Γ and it is exerted by the neighboring elements. This force is decomposed into normal and tangential components, being the first the tensile stress and the second the shear stress. Generalizing, it can be measured in a surface defined by the normal \hat{n} , and it is given in term of the Cauchy stress tensor as:

$$\vec{t} = \underline{\underline{\sigma}} \cdot \hat{n} \quad (7.9)$$

Using the divergence theorem, the Cauchy stress tensor can be expressed in a volume integral as:

$$\int_{\Gamma} \underline{\underline{\sigma}} \cdot \hat{n} dS = \int_{\Omega} \vec{\nabla} \cdot \underline{\underline{\sigma}} dV \quad (7.10)$$

Here, the momentum density ($\rho \vec{v}$) is introduced. In the general expression of conservation of momentum, in addition to the variation of momentum being equal to the sum of the external forces. The flux of momentum entering or leaving of the domain must also be considered. In other words, the velocity transports not only mass but also the momentum itself. That is expressed as

$$\int_{\Gamma} \rho \vec{v} (\vec{v} \cdot \hat{n}) dS = \int_{\Omega} \vec{\nabla} \cdot ((\rho \vec{v}) \vec{v}) dV \quad (7.11)$$

Finally, the general expression of the momentum conservation can be written as

$$\int_{\Omega} \frac{\partial}{\partial t} (\rho \vec{v}) dV + \int_{\Omega} \vec{\nabla} \cdot ((\rho \vec{v}) \vec{v}) dV = \int_{\Omega} \rho \vec{b} dV + \int_{\Omega} \vec{\nabla} \cdot \underline{\underline{\sigma}} dV \quad (7.12)$$

Again, assuming the continuity of the above expression and using the fact that this equality is true not only in the whole system Ω , but also for its very single subdomain. The momentum conservation is given by

$$\frac{\partial}{\partial t} (\rho \vec{v}) + \vec{\nabla} \cdot ((\rho \vec{v}) \vec{v}) = \rho \vec{b} + \vec{\nabla} \cdot \underline{\underline{\sigma}} \quad (7.13)$$

Using the rules for partial derivation from vector calculus, the left-size term cans also be written:

$$\frac{\partial}{\partial t} (\rho \vec{v}) + \vec{\nabla} \cdot ((\rho \vec{v}) \vec{v}) = \vec{v} \left(\frac{\partial \rho}{\partial t} + \vec{\nabla} \cdot (\rho \vec{v}) \right) + \rho \left(\frac{\partial \vec{v}}{\partial t} + \vec{v} \cdot \vec{\nabla} \vec{v} \right) \quad (7.14)$$

From the conservation of mass (7.5), the first term in parenthesis is equal to zero. Therefore, the conservation of momentum is rewritten as

$$\rho \left(\frac{\partial \vec{v}}{\partial t} + \vec{v} \cdot \vec{\nabla} \vec{v} \right) = \rho \vec{b} + \vec{\nabla} \cdot \underline{\underline{\sigma}} \quad (7.15)$$

The stress tensor is normally decomposed into a deviatoric and a hydrostatic component, which are defined by

$$\text{Hydrostatic pressure: } p = -\frac{1}{3} \text{Tr}(\underline{\underline{\sigma}}) \quad (7.16)$$

$$\text{Deviatoric component: } \underline{\underline{S}} = \underline{\underline{\sigma}} + p \underline{\underline{I}} \quad (7.17)$$

After this modification, momentum conservation is given by

$$\frac{\partial}{\partial t} (\rho \vec{v}) + \vec{v} \cdot \vec{\nabla} (\rho \vec{v}) = \vec{\nabla} \cdot \underline{\underline{S}} - \vec{\nabla} p + \rho \vec{b} \quad (7.18)$$

The term \vec{b} in electromagnetic based industrial processes represents the Lorenz force, which is the coupling term with the electromagnetic model.

7.1.3 Angular momentum conservation

Conservation of angular momentum for a continuum requires that the Cauchy stress must be symmetric, then

$$\sigma_{ij} = \sigma_{ji} \quad (7.19)$$

Taking the variations of this momentum are only due to the sum of external forces, (7.13) can be written as

$$\int_{\Omega} \frac{\partial}{\partial t} (\rho \vec{v}) dV = \int_{\Omega} \rho \vec{b} dV + \int_{\Omega} \vec{\nabla} \cdot \underline{\underline{\sigma}} dV \quad (7.20)$$

The balance of angular momentum for the domain Ω is defined by

$$\int_{\Omega} \vec{x} \times \frac{\partial}{\partial t} (\rho \vec{v}) dV = \int_{\Omega} \vec{x} \times \rho \vec{b} dV + \int_{\Omega} \vec{x} \times \vec{\nabla} \cdot \underline{\underline{\sigma}} dV \quad (7.21)$$

Writing the above expression in index notation

$$\frac{\partial}{\partial t} \int_{\Omega} \varepsilon_{ijk} x_j v_k \rho dV = \int_{\Omega} \varepsilon_{ijk} x_j b_k \rho dV + \frac{\partial}{\partial x_m} \int_{\Omega} \varepsilon_{ijk} x_j \sigma_{mk} dV \quad (7.22)$$

$$\frac{\partial}{\partial t} \int_{\Omega} \varepsilon_{ijk} x_j v_k \rho dV = \int_{\Omega} \varepsilon_{ijk} x_j b_k \rho dV + \int_{\Omega} \varepsilon_{ijk} \left(\delta_{jm} \sigma_{mk} + x_j \frac{\partial \sigma_{mk}}{\partial x_m} \right) dV \quad (7.23)$$

Reordering the comment terms

$$\int_{\Omega} \varepsilon_{ijk} \delta_{jm} \sigma_{mk} dV = - \int_{\Omega} \varepsilon_{ijk} x_j \left(\frac{\partial \sigma_{mk}}{\partial x_m} + b_k \rho - \frac{\partial v_k \rho}{\partial t} \right) dV \quad (7.24)$$

The integral on the right-hand side of this expression is zero, because the stresses must satisfy the linear momentum balance equation. Since this holds for any volume Ω .

$$\begin{aligned} \varepsilon_{ijk} \delta_{jm} \sigma_{mk} &= 0 \\ \varepsilon_{ijk} \sigma_{jk} &= 0 \\ \varepsilon_{imn} \varepsilon_{ijk} \sigma_{jk} &= 0 \\ (\delta_{jm} \delta_{kn} - \delta_{km} \delta_{nj}) \sigma_{jk} &= 0 \\ \sigma_{mn} - \sigma_{nm} &= 0 \\ \sigma_{mn} &= \sigma_{nm} \end{aligned} \quad (7.25)$$

Which proves the stress tensor symmetric.

7.1.4 Constitutive laws

In order to take into account the mechanical behaviour of materials, constitutive laws are traduced to relate the stress tensor to the strain tensor.

$$\underline{\underline{\sigma}} = E \underline{\underline{\varepsilon}} \quad (7.26)$$

Forge® uses a formulation based on strain rates rather than directly on the strain. The linear superposition of the strain is used; this means that each individual term is added to compute the total deformation.

$$\underline{\underline{\dot{\varepsilon}}} = \underline{\underline{\dot{\varepsilon}}}^{el} + \underline{\underline{\dot{\varepsilon}}}^{vp} + \underline{\underline{\dot{\varepsilon}}}^{th} \quad (7.27)$$

Where $\underline{\underline{\dot{\varepsilon}}}^{el}$, $\underline{\underline{\dot{\varepsilon}}}^{vp}$ and $\underline{\underline{\dot{\varepsilon}}}^{th}$ are the elastic, viscoelastic and thermal strain rate tensors respectively. They can be computed as

$$\underline{\underline{\dot{\varepsilon}}}^{el} = D^{-1} \underline{\underline{\dot{\sigma}}} \quad (7.28)$$

$$\underline{\underline{\dot{\varepsilon}}}^{vp} = \frac{3}{2} \frac{\dot{\varepsilon}}{\bar{\sigma}} \underline{\underline{S}} \quad (7.29)$$

$$\underline{\underline{\dot{\varepsilon}}}^{th} = \alpha \dot{T} \underline{\underline{I}} \quad (7.30)$$

Where D is the stiffness fourth order tensor, $\underline{\underline{\dot{\sigma}}}$ is a time derivative for the stress tensor, $\dot{\varepsilon}$ and $\bar{\sigma}$ are the Von Mises equivalent strain rate and stress respectively, α is the thermal expansion coefficient and \dot{T} the temperature rate of change.

The Von Mises equivalent strain rate and stress are defined as

$$\dot{\varepsilon} = \sqrt{\frac{2}{3} \underline{\underline{\dot{\varepsilon}}} : \underline{\underline{\dot{\varepsilon}}}} \quad (7.31)$$

$$\bar{\sigma} = \sqrt{\frac{3}{2} \underline{\underline{S}} : \underline{\underline{S}}} \quad (7.32)$$

Those quantities are linked to the material properties as

7.1.4.1 Elasticity:

The stress tensor is related to the strain using the Hooke's law

$$\underline{\underline{\underline{\varepsilon}}}^{el} = \frac{1 + \nu}{E} \underline{\underline{\underline{\sigma}}} - \frac{\nu}{E} tr(\underline{\underline{\underline{\sigma}}}) \underline{\underline{\underline{I}}} \quad (7.33)$$

The strain rate tensor is computed taking the time derivatives of the strain tensor, then it takes the form

$$\underline{\underline{\underline{\dot{\varepsilon}}}}^{el} = \frac{1 + \nu}{E} \underline{\underline{\underline{\dot{\sigma}}}} - \frac{\nu}{E} tr(\underline{\underline{\underline{\dot{\sigma}}}}) \underline{\underline{\underline{I}}} \quad (7.34)$$

Where ν and E are the Poisson's coefficient and the elastic modulus respectively.

7.1.4.2 Compressibility:

The bulk modulus (κ) defines the resistance of a material on uniform compression.

$$\kappa = \rho \frac{dp}{d\rho} \quad (7.35)$$

Where p is the pressure in a differential volume element. In compressible materials, the compressibility is defined as

$$\vec{\nabla} \cdot \vec{v} = -\frac{1}{\kappa} \dot{p} \quad (7.36)$$

In the particular case of isotropic elasticity, it is defined as

$$\vec{\nabla} \cdot \vec{v} = -\frac{3(1 - 2\nu)}{E} \dot{p} \quad (7.37)$$

Therefore, the bulk modulus can be expressed in term of the material properties as

$$\kappa = \frac{E}{3(1 - 2\nu)} \quad (7.38)$$

For incompressible materials the Poisson's coefficient $\nu = 0.5$. which complies with (7.8) ($\vec{\nabla} \cdot \vec{v} = 0$).

7.1.4.3 Plasticity:

The essential characteristic of the deformation in elastic materials is its reversibility: when the loads is released, the material returns to its initial conditions. On other hand, when the stress applied exceeds the flow stress (σ_0) irreversible plastic deformation appears; it means that the return to its original condition does not occur when the load is released, and a plastic

strain is created. The evolution of the flow stress depends on the plastic strain (ε^{pl}) experienced by the material and can be described by a strain-hardening function $\sigma_0(\varepsilon^{pl})$.

Given a stress tensor σ at a point in the material, it is necessary to decide if the state of the stress corresponds to the elastic domain or the plastic domain. Several criteria have been created to define this, between them it can be mentioned: the plasticity criterion for the multi axial case, Tresca's, Von Mises, etc; for more information see chapter 6 of [94].

In the EMF process, deformation occurs under high strain rates, around $10^3 s^{-1}$ to $10^4 s^{-1}$. For this reason, an adequate description of the stress under these conditions is required. Several authors have developed various plastic models taking into account high strain rates. On can mention:

Johnson-Cook model

$$\sigma_y = (A + B\bar{\varepsilon}_{pl}^n) \left[1 + C \log \left(\frac{\dot{\varepsilon}}{\dot{\varepsilon}_0} \right) \right] \left[1 - \left(\frac{T - T_0}{T_m - T_0} \right)^m \right] \quad (7.39)$$

Where σ_y is the Yield stress, $\bar{\varepsilon}_{pl}^n$ the equivalent plastic strain, $\dot{\varepsilon}$ the strain rate, T the temperature and A, B, C, n and m are empirical material parameters.

Hollomon model

$$\sigma_y = \sigma_0 \bar{\varepsilon}_{pl}^n \quad (7.40)$$

Takatsu model

$$\sigma_y = K_1 \bar{\varepsilon}_{pl}^{n1} + K_2 \bar{\varepsilon}_{pl}^{n2} \ln \left(\frac{\dot{\varepsilon}}{\dot{\varepsilon}_0} \right) \quad (7.41)$$

7.2 Fluids Mechanics problem

A Newtonian fluid motion in a domain Ω and a time period $[0; T]$ can be described as in solid mechanics problem. Where the fluid behaviour satisfies conservation of momentum and mass of the system:

$$\frac{\partial \rho}{\partial t} + \vec{\nabla} \cdot (\rho \vec{v}) = s_1 \quad (7.42)$$

$$\frac{\partial}{\partial t} (\rho \vec{v}) + \vec{\nabla} \cdot ((\rho \vec{v}) \vec{v}) = s_2 \quad (7.43)$$

Where ρ is the fluid mass density, s_1 and s_2 are the source values for the mass and momentum conservation respectively. The fields velocity $\vec{v}(\vec{x}, t)$ and pressure $p(\vec{x}, t)$ describe the motion.

7.2.1 Mass continuity equation

The equation (7.43), representing the mass conservation inside a domain, can be rewrite as

$$\frac{\partial \rho}{\partial t} - \vec{v} \cdot \vec{\nabla} \rho + \rho \vec{\nabla} \cdot \vec{v} = s_1 \quad (7.44)$$

Where the derivative of the fluid mass density is related to the compressibility of the fluid. A fluid is incompressible if the condition is satisfied.

$$\mathcal{M} = \frac{v}{c} < 0.3 \quad (7.45)$$

Where \mathcal{M} is the Mach number and c the speed of sound in the domain. This speed is deduced from the material's compressibility at isentropic (the entropy of the system studied remains constant) conditions βs .

$$c = \sqrt{\frac{1}{\rho \beta s}} \quad (7.46)$$

Having this in consideration, then assuming constant mass density over the domain, expression (7.45) is rewritten as follows.

$$\rho \vec{\nabla} \cdot \vec{v} = s_1 \quad (7.47)$$

Finally, assuming no mass source, the incompressible expression for the fluid becomes.

$$\vec{\nabla} \cdot \vec{v} = 0 \quad (7.48)$$

7.2.2 Momentum conservation

Let develop the equation (7.43) as follows:

$$\vec{v} \frac{\partial \rho}{\partial t} + \rho \frac{\partial \vec{v}}{\partial t} + \rho \vec{v} \cdot \vec{\nabla} \vec{v} + \rho \vec{v} \vec{\nabla} \cdot \vec{v} = s_2 \quad (7.49)$$

Equation (7.46) can be re-ordered in the form:

$$\vec{v} \left(\frac{\partial \rho}{\partial t} + \vec{\nabla} \cdot (\rho \vec{v}) \right) + \rho \left(\frac{\partial \vec{v}}{\partial t} + \vec{u} \cdot \vec{\nabla} \vec{v} \right) = s_2 \quad (7.50)$$

For the definition of mass conservation (7.42), the equation (7.50) becomes.

$$\rho \left(\frac{\partial \vec{v}}{\partial t} + \vec{u} \cdot \vec{\nabla} \vec{v} \right) = s_1 \quad (7.51)$$

Where the source term s_1 can be defined for Newtonian fluids as follows.

$$s_1 = \vec{\nabla} \cdot \underline{\underline{\sigma}} + \vec{f} \quad (7.52)$$

Where $\underline{\underline{\sigma}}$ is the Cauchy stress tensor and \vec{f} an external volumetric force. Taking the source term in consideration, the momentum conservation equation is expressed as

$$\rho \left(\frac{\partial \vec{v}}{\partial t} + \vec{u} \cdot \vec{\nabla} \vec{v} \right) = \vec{\nabla} \cdot \underline{\underline{\sigma}} + \vec{f} \quad (7.53)$$

7.2.3 Constitutive laws

The constitutive equation of a Newtonian fluid is written based on the following considerations.

- The fluid obeys the laws of statics.
- The fluid behaviour is independent of the reference frame as well as of the observer.
- The stress tensor is a function of the strain rate tensor.
- The fluid is an isotropic medium, that is, independent of coordinate system axes orientation.

Following these assumptions, the stress tensor can be expressed by.

$$\underline{\underline{\sigma}} = 2\mu \underline{\underline{\dot{\epsilon}}}(\vec{v}) - p \underline{\underline{I}} \quad (7.54)$$

Where μ is the fluid dynamic viscosity, p is the pressure, $\underline{\underline{I}}$ the identity tensor, and the strain rate tensor is defined as:

$$\underline{\underline{\dot{\epsilon}}}(\vec{v}) = \frac{1}{2} \left(\vec{\nabla} \vec{v} + (\vec{\nabla} \vec{v})^T \right) \quad (7.55)$$

Substituting the stress tensor found into the momentum conservation equation.

$$\rho \left(\frac{\partial \vec{v}}{\partial t} + \vec{v} \cdot \vec{\nabla} \vec{v} \right) = \vec{\nabla} \cdot \left(2\mu \underline{\underline{\dot{\epsilon}}}(\vec{v}) - p \underline{\underline{I}} \right) + \vec{f} \quad (7.56)$$

Rearranging the above expression and leaving only the source term in the right-hand measure size, the momentum conservation equation becomes

$$\rho \left(\frac{\partial \vec{v}}{\partial t} + \vec{u} \cdot \vec{\nabla} \vec{v} \right) - 2\mu \vec{\nabla} \cdot \left(\underline{\underline{\dot{\epsilon}}}(\vec{v}) \right) + \vec{\nabla} p = \vec{f} \quad (7.57)$$

As in solid mechanics, the source term \vec{f} is the coupling term with the electromagnetic model.

7.3 Edge element – Coulomb gauge demonstration

The Nedelec element has the advantage of implicitly guaranteeing the Coulomb gauge

$$\vec{\nabla} \cdot \vec{A} = 0 \quad (7.58)$$

It can be demonstrated by using the definition of the vector field in the edge basis functions (2.70) and substituting \vec{A} in the Coulomb gauge (2.73)

$$\vec{\nabla} \cdot \sum_e a_e(t) \vec{\Psi}_e(\vec{x}) = 0 \quad (7.59)$$

By rearranging the terms of the equation, one arrives at

$$\sum_e a_e(t) \vec{\nabla} \cdot \vec{\Psi}_e(\vec{x}) = 0 \quad (7.60)$$

Note that by solving only the divergence of the basis function $\vec{\Psi}_e(\vec{x})$ it is possible to demonstrate the Coulomb gauge

$$\begin{aligned} \vec{\nabla} \cdot \vec{\Psi}_e(\vec{x}) &= \vec{\nabla} \cdot \left(\varphi_i(\vec{x}) \vec{\nabla} \varphi_j(\vec{x}) - \varphi_j(\vec{x}) \vec{\nabla} \varphi_i(\vec{x}) \right) \\ \vec{\nabla} \cdot \vec{\Psi}_e(\vec{x}) &= \vec{\nabla} \cdot \left(\varphi_i(\vec{x}) \vec{\nabla} \varphi_j(\vec{x}) \right) - \vec{\nabla} \cdot \left(\varphi_j(\vec{x}) \vec{\nabla} \varphi_i(\vec{x}) \right) \\ \vec{\nabla} \cdot \vec{\Psi}_e(\vec{x}) &= \varphi_i(\vec{x}) \vec{\nabla} \cdot \vec{\nabla} \varphi_j(\vec{x}) + \vec{\nabla} \varphi_j(\vec{x}) \cdot \vec{\nabla} \varphi_i(\vec{x}) - \varphi_j(\vec{x}) \vec{\nabla} \cdot \vec{\nabla} \varphi_i(\vec{x}) - \nabla \varphi_i(\vec{x}) \cdot \vec{\nabla} \varphi_j \quad (7.61) \\ \vec{\nabla} \cdot \vec{\Psi}_e(\vec{x}) &= [\vec{\nabla} \varphi_j(\vec{x}) \cdot \vec{\nabla} \varphi_i(\vec{x}) - \vec{\nabla} \varphi_i(\vec{x}) \cdot \vec{\nabla} \varphi_j] + [\varphi_i(\vec{x}) \vec{\nabla} \cdot \vec{\nabla} \varphi_j(\vec{x}) - \varphi_j(\vec{x}) \vec{\nabla} \cdot \vec{\nabla} \varphi_i(\vec{x})] \\ \vec{\nabla} \cdot \vec{\Psi}_e(\vec{x}) &= [\vec{\nabla} \varphi_j(\vec{x}) \cdot \vec{\nabla} \varphi_i(\vec{x}) - \vec{\nabla} \varphi_i(\vec{x}) \cdot \vec{\nabla} \varphi_j] + [\varphi_i(\vec{x}) \nabla^2 \varphi_j(\vec{x}) - \varphi_j(\vec{x}) \nabla^2 \varphi_i(\vec{x})] \end{aligned}$$

The first rhs term of the last expression is equal to zero and the second one is null due to the use of P_1 linear elements. Then, it is seen that the Coulomb gauge is naturally implicitly on the Nedelec elements.

$$\vec{\nabla} \cdot \vec{\Psi}_e(\vec{x}) = 0 \quad (7.62)$$

7.4 Hessian – Jacobian analytical and numerical test

In this section, a comparative analysis of two approaches introduced in Chapter 0 is performed. The main objective is to gain a deeper understanding of the intermediate steps involved in the calculation of the metric. Specifically, it aims to examine how the Hessian approach may diffuse the anisotropy of the field and identify any potential loss of information. To achieve this, a simple test case involving a single element - a perfect tetrahedron with an edge length of unity - is proposed. This test case will allow to explore and evaluate the nature of the results of the Hessian and Jacobian obtained in Section 4.5

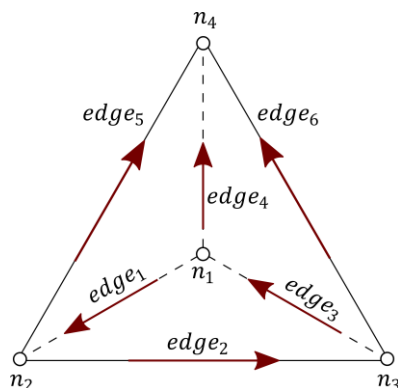


Fig. 7.1 Perfect tetrahedron.

The node coordinates are defined by

$n_1 = (0,0,0)$	$n_2 = (1,0,0)$	$n_3 = (0,1,0)$	$n_4 = (0,0,1)$
-----------------	-----------------	-----------------	-----------------

The Gauss integration points are then defined on the tetrahedron shown in Fig. 7.1 as follows:

$$a = 0.25 * \left(1 - \frac{1}{\sqrt{5}}\right) = 0.1382$$

$$b = 1 - 3 * a = 0.5854$$

$x_{g1} = (a, a, a)$	$x_{g2} = (a, a, b)$	$x_{g3} = (a, b, a)$	$x_{g4} = (b, a, a)$
----------------------	----------------------	----------------------	----------------------

In order to investigate the nature of the results found in this chapter, the numerical calculation for the Hessian and the Jacobian is carried out in detail in this section. First, let's define the Galerkin recovery procedure, which is used to go from constant fields at the Gauss points to linear wise fields at the nodes.

Let's denote the nodes by the character i and the Gauss integration point by x_g and define a scalar function $f(x_g)$ evaluated at the Gauss points. The recovery approach consists of solving the following linear system:

$$\langle f - f(x_g), \varphi \rangle = 0 \quad (7.63)$$

Where φ represents the nodal basis function. The field f is then expressed by

$$f = \sum_{i=1}^4 f_i \varphi_i \quad (7.64)$$

Introducing the above expression into the equation (7.63) and shifting $f(x_g)$ to the right-hand side, it results in:

$$\sum_{i=1}^4 \langle \varphi_i, \varphi_j \rangle f_i = \langle f(x_g), \varphi_j \rangle \quad (7.65)$$

On the left-hand side a matrix of mass is defined with nodal basis functions of the element

$$m_{ij} = \sum_{i=1}^4 \langle \varphi_i, \varphi_j \rangle \quad (7.66)$$

The matrix of mass is inversible and constant over the element, then the expression (7.65) can be rewritten as

$$f_i = m_{ij}^{-1} \langle f(x_g), \varphi_j \rangle \quad (7.67)$$

Let's construct this matrix in the tetrahedral element by:

$$m_{ij} = \begin{bmatrix} \langle \varphi_1, \varphi_1 \rangle & \langle \varphi_2, \varphi_1 \rangle & \langle \varphi_3, \varphi_1 \rangle & \langle \varphi_4, \varphi_1 \rangle \\ \langle \varphi_1, \varphi_2 \rangle & \langle \varphi_2, \varphi_2 \rangle & \langle \varphi_3, \varphi_2 \rangle & \langle \varphi_4, \varphi_2 \rangle \\ \langle \varphi_1, \varphi_3 \rangle & \langle \varphi_2, \varphi_3 \rangle & \langle \varphi_3, \varphi_3 \rangle & \langle \varphi_4, \varphi_3 \rangle \\ \langle \varphi_1, \varphi_4 \rangle & \langle \varphi_2, \varphi_4 \rangle & \langle \varphi_3, \varphi_4 \rangle & \langle \varphi_4, \varphi_4 \rangle \end{bmatrix} \quad (7.68)$$

The components of the matrix are integrals which can be expressed as:

$$\langle \varphi_i, \varphi_j \rangle = \int_K \varphi_i \varphi_j dV \quad (7.69)$$

And solved numerically by:

$$\langle \varphi_i, \varphi_j \rangle = \sum_{g=1}^4 \varphi_i(x_g) \varphi_j(x_g) w_g$$

Then, calculating each of the components, the matrix of mass is given by:

$$m_{ij} = \begin{bmatrix} 0.01667 & 0.00833 & 0.00833 & 0.00833 \\ 0.00833 & 0.01667 & 0.00833 & 0.00833 \\ 0.00833 & 0.00833 & 0.01667 & 0.00833 \\ 0.00833 & 0.00833 & 0.00833 & 0.01667 \end{bmatrix} \quad (7.70)$$

And therefore, its inverse:

$$m_{ij}^{-1} = \begin{bmatrix} 96 & -24 & -24 & -24 \\ -24 & 96 & -24 & -24 \\ -24 & -24 & 96 & -24 \\ -24 & -24 & -24 & 96 \end{bmatrix} \quad (7.71)$$

Finally, the vector on the right-hand side is expressed as:

$$\langle f(x_g), \varphi_j \rangle = \int_K f(x_g) \varphi_j dV \quad (7.72)$$

The integral is then calculated numerically at each node as follows:

$$\langle f(x_g), \varphi_j \rangle = \sum_{g=1}^4 f(x_g) \varphi_j(x_g) w_g \quad (7.73)$$

Since the Galerkin recovery procedure is defined, let's calculate the Hessian and the Jacobian.

First, let's define a vector field function:

$$\vec{f} = \langle z^4, 0, 0 \rangle \quad (7.74)$$

Which norm is equal to:

$$\|\vec{f}\| = z^4 \quad (7.75)$$

7.4.1 Numerical solution

7.4.1.1 Hessian

The Hessian tensor is commonly calculated as the second derivative of the norm of a function \vec{f} defined at the integration points.

From the norm of \vec{f} (7.75) evaluated at the Gauss points $f(x_g)$, the steps to calculate the Hessian are explained as follows:

$f(x_{g1}) = 0.0003647$	$f(x_{g2}) = 0.1174467$	$f(x_{g3}) = 0.0003647$	$f(x_{g4}) = 0.0003647$
-------------------------	-------------------------	-------------------------	-------------------------

I. Galerkin recovery procedure:

The expression in (7.67) is used to build the function f_i at the nodes:

$$f_i = m_{ij}^{-1} \langle f(x_g), \varphi_j \rangle \quad (7.76)$$

The vector on the right-hand side given by the expression (7.73) is equal to:

$$\langle f(x_g), \varphi_j \rangle = \begin{pmatrix} 0.0006894 \\ 0.0006894 \\ 0.0006894 \\ 0.0028711 \end{pmatrix} \quad (7.77)$$

Substituting the result in (7.77) into (7.76), the recovered field at the nodes is equal to:

$$f_i = \begin{pmatrix} -0.035815 \\ -0.035815 \\ -0.035815 \\ 0.225988 \end{pmatrix} \quad (7.78)$$

II. Gradient computation:

The gradient at the Gauss points is given by:

$$\vec{\nabla}(f(x_g)) = \sum_{i=1}^4 \vec{\nabla} \varphi_i f_i \quad (7.79)$$

The Gradient is constant over the tetrahedron, therefore:

$$\vec{\nabla}(f(x_g)) = \vec{\nabla}(f(x_{g1})) = \vec{\nabla}(f(x_{g2})) = \vec{\nabla}(f(x_{g3})) = \vec{\nabla}(f(x_{g4})) \quad (7.80)$$

Then, the result of the gradient at each Gauss point is:

$$\vec{\nabla}(f(x_g)) = \begin{pmatrix} -1.388x10^{-17} \\ -2.082x10^{-17} \\ 0.261803 \end{pmatrix} \quad (7.81)$$

III. Galerkin recovery procedure:

The recovery procedure is carried out once again to construct the gradient at the nodes $\vec{\nabla}(f_i)$, As the gradient is a vectorial field, the linear system is solved three times once for each component. Then applying the expression in (7.67):

$$\vec{\nabla}(f_i) = m_{ij}^{-1} \langle \vec{\nabla}(f(x_g)), \varphi_j \rangle \quad (7.82)$$

The vector on the right-hand side given by the expression (7.73) is equal to:

$$\langle \vec{\nabla}(f(x_g)), \varphi_j \rangle = \begin{pmatrix} -5.782x10 - 19 \\ -5.782x10 - 19 \\ 0.010908 \end{pmatrix} \quad (7.83)$$

Substituting the result in (7.83) into (7.82), the recovered field at the nodes is equal to:

$$\vec{\nabla}(f_i) = \begin{pmatrix} -1.388x10^{-17} \\ -2.082x10^{-17} \\ 0.261803 \end{pmatrix} \quad (7.84)$$

It should be noted that the results are the same for all nodes, so the result is only given for one node.

IV. Gradient computation:

Having the gradient at the nodes, the Hessian is calculated by applying the gradient operator as follows:

$$\bar{\bar{H}}(f(x_g)) = \sum_{i=1}^4 \vec{\nabla}\varphi_i \vec{\nabla}(f_i) \quad (7.85)$$

The result at each Gauss point is equal to:

$$\bar{\bar{H}}(f(x_g)) = \begin{bmatrix} -7.70x10^{-33} & -1.54x10^{-33} & 1.08x10^{-32} \\ 9.24x10^{-33} & 1.54x10^{-32} & 1.54x10^{-32} \\ -5.55x10^{-17} & -5.55x10^{-17} & -5.55x10^{-17} \end{bmatrix} \quad (7.86)$$

V. Galerkin recovery procedure:

As the mesher needs an input at the nodes, the recovery procedure is applied again. Then applying the expression in (7.67):

$$\bar{\bar{H}}(f_i) = m_{ij}^{-1} \langle \bar{\bar{H}}(f(x_g)), \varphi_j \rangle \quad (7.87)$$

The vector on the right-hand side given by the expression (7.73) is equal to:

$$\langle \bar{H}(f(x_g)), \varphi_j \rangle = \begin{pmatrix} -3.21x10^{-34} \\ -6.42x10^{-35} \\ 4.49x10^{-34} \\ 3.85x10^{-34} \\ 6.42x10^{-34} \\ 6.42x10^{-34} \\ -2.31x10^{-18} \\ -2.31x10^{-18} \\ -2.31x10^{-18} \end{pmatrix} \quad (7.88)$$

Finally, the Hessian tensor at each node is equal to

$$\bar{H}(f_i) = \begin{bmatrix} -7.70x10^{-33} & -1.54x10^{-33} & 1.07x10^{-32} \\ 9.24x10^{-33} & 1.54x10^{-32} & 1.54x10^{-32} \\ -5.55x10^{-17} & -5.55x10^{-17} & -5.55x10^{-17} \end{bmatrix} \quad (7.89)$$

7.4.1.2 Jacobian

The Jacobian matrix is calculated as the first derivative of a vector function. In this case, the function \vec{f} (7.74) is evaluated at each Gauss point, given the following values:

$\vec{f}(x_{g1}) = \begin{pmatrix} 0.0003647 \\ 0 \\ 0 \end{pmatrix}$	$\vec{f}(x_{g2}) = \begin{pmatrix} 0.117447 \\ 0 \\ 0 \end{pmatrix}$	$\vec{f}(x_{g3}) = \begin{pmatrix} 0.0003647 \\ 0 \\ 0 \end{pmatrix}$	$\vec{f}(x_{g4}) = \begin{pmatrix} 0.0003647 \\ 0 \\ 0 \end{pmatrix}$
---	--	---	---

I. Galerkin recovery procedure:

The recovery approach is used here to construct a vector field at the nodes from $\vec{f}(x_g)$. Then applying the expression in (7.67):

$$\vec{f}_i = m_{ij}^{-1} \langle \vec{f}(x_g), \varphi_j \rangle \quad (7.90)$$

The vector on the right-hand side given by the expression (7.73) is equal to:

$$\vec{B}_j = \langle \vec{f}(x_g), \varphi_j \rangle \quad (7.91)$$

$\vec{B}_1 = \begin{pmatrix} 0.0006894 \\ 0 \\ 0 \end{pmatrix}$	$\vec{B}_2 = \begin{pmatrix} 0.0006894 \\ 0 \\ 0 \end{pmatrix}$	$\vec{B}_3 = \begin{pmatrix} 0.0006894 \\ 0 \\ 0 \end{pmatrix}$	$\vec{B}_4 = \begin{pmatrix} 0.002871 \\ 0 \\ 0 \end{pmatrix}$
---	---	---	--

Substituting the result of (7.91) into (7.90), the recovered field at the nodes is equal to:

$$\vec{f}_1 = \begin{pmatrix} -0.03589 \\ 0 \\ 0 \end{pmatrix}; \vec{f}_2 = \begin{pmatrix} -0.03589 \\ 0 \\ 0 \end{pmatrix}; \vec{f}_3 = \begin{pmatrix} -0.03589 \\ 0 \\ 0 \end{pmatrix}; \vec{f}_4 = \begin{pmatrix} 0.2260 \\ 0 \\ 0 \end{pmatrix} \quad (7.92)$$

II. Gradient computation:

The Jacobian matrix is calculated as the gradient of the vector field at the nodes:

$$\bar{J}(x_g) = \sum_{i=1}^4 \bar{\nabla} \varphi_i \vec{f}_i \quad (7.93)$$

Since the Jacobian is constant in the tetrahedron, only one Gauss point is shown.

$$\bar{J}(x_g) = \begin{bmatrix} -2.77x10^{-17} & -1.39x10^{-17} & 0.2618 \\ 0 & 0 & 0 \\ 0 & 0 & 0 \end{bmatrix} \quad (7.94)$$

III. Galerkin recovery procedure:

As it is necessary to define the Jacobian at the nodes as input to the mesher, the recovery procedure is applied again. Then applying the expression in (7.67):

$$\bar{J}_i = m_{ij}^{-1} \langle \bar{J}(x_g), \varphi_j \rangle \quad (7.95)$$

The vector on the right-hand side given by the expression (7.73) is equal to:

$$\langle \bar{J}(x_g), \varphi_j \rangle = \begin{pmatrix} -5.78x10^{-19} \\ -8.67x10^{-19} \\ 0.010908 \\ 0 \\ 0 \\ 0 \\ 0 \\ 0 \\ 0 \end{pmatrix} \quad (7.96)$$

Finally, the Jacobian matrix at the nodes is equal to:

$$\bar{J}_i = \begin{bmatrix} -1.39x10^{-17} & -2.08x10^{-17} & 0.2618 \\ 0 & 0 & 0 \\ 0 & 0 & 0 \end{bmatrix} \quad (7.97)$$

IV. Metric construction

To construct the metric based on the Jacobian, it is necessary to multiply it by its transpose matrix.

$$\bar{J} = \bar{J}_i^T \bar{J}_i \quad (7.98)$$

Then the Jacobian tensor is equal to:

$$\bar{\vec{J}} = \begin{bmatrix} 1.92x10^{-34} & 2.89x10^{-34} & -3.63x10^{-18} \\ 2.89x10^{-34} & 4.33x10^{-34} & -5.45x10^{-18} \\ -3.63x10^{-18} & -5.45x10^{-18} & 0.06854 \end{bmatrix} \quad (7.99)$$

Let's eliminate some components as their values are numerical noise, so the Jacobian can be rewritten as:

$$\bar{\vec{J}} = \begin{bmatrix} 0 & 0 & 0 \\ 0 & 0 & 0 \\ 0 & 0 & 0.06854 \end{bmatrix} \quad (7.100)$$

7.4.2 Analytical solution

7.4.2.1 Hessian

The Hessian is defined as the second derivative of a scalar field. We can then express it in matrix form as:

$$\bar{\bar{H}}(f) = \begin{bmatrix} \frac{\partial^2 f}{\partial x^2} & \frac{\partial^2 f}{\partial x \partial y} & \frac{\partial^2 f}{\partial x \partial z} \\ \frac{\partial^2 f}{\partial y \partial x} & \frac{\partial^2 f}{\partial y^2} & \frac{\partial^2 f}{\partial y \partial z} \\ \frac{\partial^2 f}{\partial z \partial x} & \frac{\partial^2 f}{\partial z \partial y} & \frac{\partial^2 f}{\partial z^2} \end{bmatrix} \quad (7.101)$$

Then, using the norm of \vec{f} defined in (7.75) the analytical Hessian of \vec{f} is equal to:

$$\bar{\bar{H}}(f) = \begin{bmatrix} 0 & 0 & 0 \\ 0 & 0 & 0 \\ 0 & 0 & 12z^2 \end{bmatrix} \quad (7.102)$$

Evaluating the above result at each integration point, it results in:

$\bar{\bar{H}}(f_1) = \begin{bmatrix} 0 & 0 & 0 \\ 0 & 0 & 0 \\ 0 & 0 & 0.229 \end{bmatrix}$	$\bar{\bar{H}}(f_2) = \begin{bmatrix} 0 & 0 & 0 \\ 0 & 0 & 0 \\ 0 & 0 & 4.112 \end{bmatrix}$	$\bar{\bar{H}}(f_3) = \begin{bmatrix} 0 & 0 & 0 \\ 0 & 0 & 0 \\ 0 & 0 & 0.229 \end{bmatrix}$	$\bar{\bar{H}}(f_4) = \begin{bmatrix} 0 & 0 & 0 \\ 0 & 0 & 0 \\ 0 & 0 & 0.229 \end{bmatrix}$
--	--	--	--

Finally, calculating the value at the barycenter of the element by the mean of the analytical Hessian over the tetrahedron it arrives at:

$$\bar{\bar{H}}(f_1) = \begin{bmatrix} 0 & 0 & 0 \\ 0 & 0 & 0 \\ 0 & 0 & 1.19975 \end{bmatrix} \quad (7.103)$$

7.4.2.2 Jacobian

The Jacobian is defined as the derivative of a vector field \vec{f} . We can then express it in matrix form as:

$$\bar{J}(\vec{f}) = \vec{v}^T \vec{f} = \begin{bmatrix} \frac{\partial f_1}{\partial x} & \frac{\partial f_1}{\partial y} & \frac{\partial f_1}{\partial z} \\ \frac{\partial f_2}{\partial x} & \frac{\partial f_2}{\partial y} & \frac{\partial f_2}{\partial z} \\ \frac{\partial f_3}{\partial x} & \frac{\partial f_3}{\partial y} & \frac{\partial f_3}{\partial z} \end{bmatrix} \quad (7.104)$$

Then, using the function \vec{f} defined in (7.74), the analytical Jacobian is equal to

$$\bar{J}(\vec{f}) = \vec{v}^T \vec{f} = \begin{bmatrix} 0 & 0 & 4z^3 \\ 0 & 0 & 0 \\ 0 & 0 & 0 \end{bmatrix} \quad (7.105)$$

The metric based on the Jacobian must be multiplied by its transpose, which leads to:

$$\bar{J} = \bar{J}(\vec{f})^T \bar{J}(\vec{f}) \quad (7.106)$$

Finally, the analytical expression for the Jacobian tensor is given by:

$$\bar{J} = \begin{bmatrix} 0 & 0 & 0 \\ 0 & 0 & 0 \\ 0 & 0 & 16z^6 \end{bmatrix} \quad (7.107)$$

Evaluating the above expression at each integration point, it results in:

$$\bar{J}_1 = \begin{bmatrix} 0 & 0 & 0 \\ 0 & 0 & 0 \\ 0 & 0 & 0.000111 \end{bmatrix} \quad \bar{J}_2 = \begin{bmatrix} 0 & 0 & 0 \\ 0 & 0 & 0 \\ 0 & 0 & 0.6439 \end{bmatrix} \quad \bar{J}_3 = \begin{bmatrix} 0 & 0 & 0 \\ 0 & 0 & 0 \\ 0 & 0 & 0.000111 \end{bmatrix} \quad \bar{J}_4 = \begin{bmatrix} 0 & 0 & 0 \\ 0 & 0 & 0 \\ 0 & 0 & 0.000111 \end{bmatrix}$$

Finally, calculating the value at the barycenter of the element by the mean of the analytical Jacobian over the tetrahedron it arrives at:

$$\bar{J}_1 = \begin{bmatrix} 0 & 0 & 0 \\ 0 & 0 & 0 \\ 0 & 0 & 0.1611 \end{bmatrix} \quad (7.108)$$

7.4.3 Analytical vs numerical solution

Table 7.1. presents a comparison of the analytical and numerical tensor solutions. It can be seen that the numerical Jacobian procedure successfully captures the anisotropy present in the analytical solution, while the Hessian approach falls short in following the anisotropy adequately. However, when considering the order of magnitudes in the components, the numerical Hessian does attempt to maintain the anisotropy to some extent but does not fully recover it. This may be attributed to the use of linear basis functions in our approximation, which offer a good approximation when only one derivative is involved, as seen in the Jacobian case. However, the information is lost when calculating a second derivative, as in the case of the Hessian.

Table 7.1 Comparison between analytical and numerical

Method	Analytical	Numerical
Hessian	$\begin{bmatrix} 0 & 0 & 0 \\ 0 & 0 & 0 \\ 0 & 0 & 1.19975 \end{bmatrix}$	$\begin{bmatrix} -7.70x10^{-33} & -1.54x10^{-33} & 1.07x10^{-32} \\ 9.24x10^{-33} & 1.54x10^{-32} & 1.54x10^{-32} \\ -5.55x10^{-17} & -5.55x10^{-17} & -5.55x10^{-17} \end{bmatrix}$
Jacobian	$\begin{bmatrix} 0 & 0 & 0 \\ 0 & 0 & 0 \\ 0 & 0 & 0.1611 \end{bmatrix}$	$\begin{bmatrix} 0 & 0 & 0 \\ 0 & 0 & 0 \\ 0 & 0 & 0.06854 \end{bmatrix}$

Bibliography

- [1] D. Cardinaux, “Étude et modélisation numérique 3D par éléments finis d’un procédé de traitement thermique de tôles embouties après chauffage par induction : Application à un renfort de pied central automobile,” Ecole Nationale Supérieure des Mines de Paris, 2008. [Online]. Available: <https://tel.archives-ouvertes.fr/tel-00345259/>
- [2] J. R. Alves Zapata, “Magnetic pulse forming processes : Computational modelling and experimental validation,” Université de recherche Paris Sciences et Lettres, 2016. [Online]. Available: <https://pastel.archives-ouvertes.fr/tel-01417196>
- [3] L. Marioni, “Computational Modelling and Electromagnetic-CFD Coupling in Casting Processes,” Université Paris sciences et lettres, 2017. Accessed: May 10, 2021. [Online]. Available: <https://pastel.archives-ouvertes.fr/tel-01774582>
- [4] V. Rudnev, D. Loveless, R. Cook, and M. Black, *Handbook of Induction Heating*. New York: Marcell Dekker Inc, 2003. doi: 10.4236/me.2019.101007.
- [5] S. Lupi, M. Forzan, and A. Aliferov, *Induction and direct resistance heating: Theory and numerical modeling*. Springer International Publishing, 2015. doi: 10.1007/978-3-319-03479-9.
- [6] F. Dughiero, M. Forzan, M. Garbin, C. Pozza, and E. Sieni, “A 3D numerical FEM model for the simulation of induction welding of tubes,” *COMPEL - Int. J. Comput. Math. Electr. Electron. Eng.*, vol. 30, no. 5, pp. 1570–1581, 2011, doi: 10.1108/03321641111152720.
- [7] V. Psyk, D. Risch, B. L. Kinsey, A. E. Tekkaya, and M. Kleiner, “Electromagnetic forming - A review,” *J. Mater. Process. Technol.*, vol. 211, no. 5, pp. 787–829, May 2011, doi: 10.1016/j.jmatprotec.2010.12.012.
- [8] U. Müller and L. Bühler, “Magnetofluidynamics in Channels and Containers,” in *Magnetofluidynamics in Channels and Containers*, Springer Berlin Heidelberg, 2001, pp. 1–7. doi: 10.1007/978-3-662-04405-6_1.
- [9] V. Psyk, M. Linnemann, and G. Sebastiani, *Electromagnetic pulse forming*. LTD, 2020. doi: 10.1016/B978-0-12-818232-1.00004-7.
- [10] H. Zhang *et al.*, “Experimental Evaluation of MHD Modeling of EMS During Continuous Casting,” *Metall. Mater. Trans. B Process Metall. Mater. Process. Sci.*, vol. 53, no. 4, pp. 2166–2181, 2022, doi: 10.1007/s11663-022-02516-3.
- [11] O. Espinosa and A. Reisenegger, “The magnetic stress tensor in magnetized matter,” pp. 1–6, 2003, [Online]. Available: <http://arxiv.org/abs/astro-ph/0307134>
- [12] O. Bíró, “Edge element formulations of eddy current problems,” *Comput. Methods Appl. Mech. Eng.*, vol. 169, no. 3–4, pp. 391–405, Feb. 1999, doi: 10.1016/S0045-7825(98)00165-0.
- [13] Y. Le Menach, “Contribution à la modélisation numérique tridimensionnelle des systèmes électrotechniques,” Université des Sciences et Technologies de Lille, 1999.
- [14] O. Biro and K. Preis, “On the use of the magnetic vector potential in the finite element analysis of 3D eddy currents,” *IEEE Trans. Magn.*, vol. 25, pp. 3145–3159, 1989.

- [15] J.-M. Jin, *The finite element method in electromagnetics*. New York: John Wiley & Sons, 2002.
- [16] J. C. Nedelec, “Mixed finite elements in \mathbb{R}^3 ,” *Numer. Math.*, vol. 35, no. 3, pp. 315–341, 1980, doi: 10.1007/BF01396415.
- [17] J. C. Nédélec, “A new family of mixed finite elements in \mathbb{R}^3 ,” *Numer. Math.*, vol. 50, no. 1, pp. 57–81, Jan. 1986, doi: 10.1007/BF01389668.
- [18] A. Bossavit, *Computational Electromagnetism*. Elsevier, 1998. doi: 10.1016/B978-0-12-118710-1.X5000-4.
- [19] S. J. Salon and J. M. Schneider, “A hybrid finite element-boundary integral formulation of the eddy current problem,” *IEEE Trans. Magn.*, vol. 18, no. 2, pp. 461–466, 1982, doi: 10.1109/TMAG.1982.1061891.
- [20] P. L’Eplattenier and I. Çaldichoury, “A BEM method for electromagnetics in complex 3D geometries,” *Bound. Elem. Other Mesh Reduct. Methods XXXVIII*, vol. 61, pp. 311–326, 2015, doi: 10.2495/bem380251.
- [21] J. Bai, Y. Cao, X. He, H. Liu, and X. Yang, “Modeling and an immersed finite element method for an interface wave equation,” *Comput. Math. with Appl.*, vol. 76, no. 7, pp. 1625–1638, Oct. 2018, doi: 10.1016/j.camwa.2018.07.015.
- [22] Y. Gong, B. Li, and Z. Li, “Immersed-interface finite-element methods for elliptic interface problems with nonhomogeneous jump conditions,” *SIAM J. Numer. Anal.*, vol. 46, no. 1, pp. 472–495, Jan. 2007, doi: 10.1137/060666482.
- [23] W. Feng, X. He, Y. Lin, and X. Zhang, “Immersed finite element method for interface problems with algebraic multigrid solver,” *Commun. Comput. Phys.*, vol. 15, no. 4, pp. 1045–1067, 2014, doi: 10.4208/cicp.150313.171013s.
- [24] J. Alves, J. Barlier, S. Marie, C. Beraudo, and F. Bay, “Modelling of large displacements and large strains in coupled electromagnetic/solid mechanics/heat transfer problems”, Accessed: Jan. 27, 2022. [Online]. Available: <https://hal.archives-ouvertes.fr/hal-01334238>
- [25] K. Fujimoto and S. Machida, “Electromagnetic full particle code with adaptive mesh refinement technique: Application to the current sheet evolution,” *J. Comput. Phys.*, vol. 214, no. 2, pp. 550–566, May 2006, doi: 10.1016/J.JCP.2005.10.003.
- [26] H. Usui, M. Nunami, T. Moritaka, T. Matsui, and Y. Yagi, “A multi-scale electromagnetic particle code with Adaptive Mesh Refinement and its parallelization,” *Procedia Comput. Sci.*, vol. 4, pp. 2337–2343, 2011, doi: 10.1016/J.PROCS.2011.04.254.
- [27] S. J. Salon, L. Ovacik, and J. F. Bailey, “Finite Element Calculation of Harmonic Losses in AC Machine Windings,” *IEEE Trans. Magn.*, vol. 29, no. 2, pp. 1442–1445, 1993, doi: 10.1109/20.250674.
- [28] V. Hill, O. Farle, and R. Dyczij-Edlinger, “A stabilized multilevel vector finite-element solver for time-harmonic electromagnetic waves,” *IEEE Trans. Magn.*, vol. 39, no. 3 I, pp. 1203–1206, May 2003, doi: 10.1109/TMAG.2003.810379.
- [29] R.-U. Börner, O. G. Ernst, and K. Spitzer, “Fast 3-D simulation of transient electromagnetic fields by model reduction in the frequency domain using Krylov

- subspace projection,” *Geophys. J. Int.*, vol. 173, no. 3, pp. 766–780, Jun. 2008, doi: 10.1111/j.1365-246X.2008.03750.x.
- [30] L. Marioni, J. R. Alves Z., E. Hachem, and F. Bay, “A new approach to solve complex valued systems arising from the solution of Maxwell equations in the frequency domain through real-equivalent formulations,” *Numer. Linear Algebr. with Appl.*, vol. 24, no. 2, p. e2079, Mar. 2017, doi: 10.1002/nla.2079.
- [31] C. Chaboudez, S. Ciain, R. Glardon, D. Mari, J. Rappaz, and M. Swierkosz, “Numerical modeling in induction heating for axisymmetric geometries,” *IEEE Trans. Magn.*, vol. 33, no. 1 PART 2, pp. 739–745, 1997, doi: 10.1109/20.560107.
- [32] V. Labbé, “Modélisation numérique du chauffage par induction : approche éléments finis et calcul parallèle,” Ecole des Mines de Paris, 2002. Accessed: Apr. 23, 2021. [Online]. Available: <https://pastel.archives-ouvertes.fr/tel-00443740>
- [33] N. SOYRIS-MACAIRE, “Modelisation tridimensionnelle du couplage thermique en forgeage a chaud,” Paris, ENMP, 1990. Accessed: Apr. 15, 2021. [Online]. Available: <http://www.theses.fr/1990ENMP0224>
- [34] C. Pelissou, “Discretisation spatio-temporelle du problème thermique à deux champs : application au procédé de forgeage à chaud,” Ecole Nationale Supérieure des Mines de Paris, 2006. Accessed: Apr. 15, 2021. [Online]. Available: <https://pastel.archives-ouvertes.fr/pastel-00001503>
- [35] J. Alves, F. Bay, U. Ripert, J. Barlier, and N. Poulain, “Advancements in the Simulation of Magnetic Pulse Forming Processes with FORGE®,” *Miner. Met. Mater. Ser.*, pp. 1217–1230, 2021, doi: 10.1007/978-3-030-75381-8_101.
- [36] T. Coupez and S. Marie, “Parallel Simulation Of 3D Forming Processes,” in *EUROSIM 96, HPCN Challenges in Telecomp and Telecom: Parallel Simulation of Complex Systems and Large-Scale Applications, Proceedings of the EUROSIM 1996 International Conference, 10-12 June 1996, Delft, The Netherlands*, 1996, no. Simulation Practice and Theory, pp. 221–228.
- [37] I. Babuska and A. K. Aziz, *The Mathematical Foundations of the Finite Element Method with Applications to Partial Differential Equations*. New York: Academic Press Inc., 1972.
- [38] M. Ainsworth and J. T. (John T. Oden, *A posteriori error estimation in finite element analysis*. Wiley, 2000.
- [39] I. Babuška and W. C. Rheinboldt, “A-posteriori error estimates for the finite element method,” *Int. J. Numer. Methods Eng.*, vol. 12, no. 10, pp. 1597–1615, Jan. 1978, doi: 10.1002/nme.1620121010.
- [40] F. Izsák, D. Harutyunyan, and J. J. W. van der Vegt, “Implicit a posteriori error estimates for the Maxwell equations,” *Math. Comput.*, vol. 77, no. 263, pp. 1355–1386, Sep. 2008, doi: 10.1090/s0025-5718-08-02046-2.
- [41] R. Beck, R. Hiptmair, R. H. W. Hoppe, and B. Wohlmuth, “Residual based a posteriori error estimators for Eddy current computation,” *Math. Model. Numer. Anal.*, vol. 34, no. 1, pp. 159–182, 2000, doi: 10.1051/m2an:2000136.
- [42] S. Nicaise and E. Creusé, “A posteriori error estimation for the heterogeneous Maxwell equations on isotropic and anisotropic meshes,” *Calcolo*, vol. 40, no. 4, pp. 249–271,

- 2003, doi: 10.1007/s10092-003-0077-y.
- [43] L. Zhong, S. Shu, L. Chen, and J. Xu, “Convergence of adaptive edge finite element methods for $H(\text{curl})$ -elliptic problems,” *Numer. Linear Algebr. with Appl.*, vol. 17, no. 2–3, pp. 415–437, Apr. 2010, doi: 10.1002/nla.694.
- [44] D. Braess and J. Schöberl, “Equilibrated residual error estimator for edge elements,” *Math. Comput.*, vol. 77, no. 262, pp. 651–673, Nov. 2007, doi: 10.1090/s0025-5718-07-02080-7.
- [45] J. Gedicke, S. Geevers, and I. Perugia, “An Equilibrated a Posteriori Error Estimator for Arbitrary-Order Nédélec Elements for Magnetostatic Problems,” *J. Sci. Comput.*, vol. 83, p. 58, 2020, doi: 10.1007/s10915-020-01224-x.
- [46] J. Gedicke, S. Geevers, I. Perugia, and J. Schöberl, “A polynomial-degree-robust a posteriori error estimator for Nedelec discretizations of magnetostatic problems,” *SIAM J. Numer. Anal.*, vol. 59, no. 4, pp. 2237–2253, Apr. 2020, doi: 10.48550/arxiv.2004.08323.
- [47] S. Nicaise, “On Zienkiewicz–Zhu error estimators for Maxwell’s equations,” *Comptes Rendus Math.*, vol. 340, no. 9, pp. 697–702, May 2005, doi: 10.1016/j.crma.2005.03.016.
- [48] I. Babuška and W. C. Rheinboldt, “Error Estimates for Adaptive Finite Element Computations,” *SIAM J. Numer. Anal.*, vol. 15, no. 4, pp. 736–754, Aug. 1978, doi: 10.1137/0715049.
- [49] K. Eriksson and C. Johnson, “An adaptive finite element method for linear elliptic problems,” *Math. Comput.*, vol. 50, no. 182, pp. 361–383, May 1988, doi: 10.1090/s0025-5718-1988-0929542-x.
- [50] C. Johnson and P. Hansbo, “Adaptive finite element methods in computational mechanics,” *Comput. Methods Appl. Mech. Eng.*, vol. 101, no. 1–3, pp. 143–181, Dec. 1992, doi: 10.1016/0045-7825(92)90020-K.
- [51] F. A. Bornemann, B. Erdmann, and R. Kornhuber, “A posteriori error estimates for elliptic problems in two and three space dimensions,” *SIAM J. Numer. Anal.*, vol. 33, no. 3, pp. 1188–1204, Aug. 1996, doi: 10.1137/0733059.
- [52] P. Monk, *Finite Element Methods for Maxwell’s Equations*. New York, 2003. Accessed: Mar. 23, 2020. [Online]. Available: <https://www.oxfordscholarship.com/view/10.1093/acprof:oso/9780198508885.001.0001/acprof-9780198508885>
- [53] E. Creusé, S. Nicaise, Z. Tang, Y. Le Menach, N. Nemitz, and F. Piriou, “Residual-based a posteriori estimators for the a - φ magnetodynamic harmonic formulation of the maxwell system,” *Math. Model. Methods Appl. Sci.*, vol. 22, no. 5, 2012, doi: 10.1142/S021820251150028X.
- [54] E. Creusé, S. Nicaise, and R. Tittarelli, “Residual-based a posteriori estimators for the T/Ω magnetodynamic harmonic formulation of the maxwell system,” *Comput. Methods Appl. Math.*, vol. 10, no. 2, pp. 411–429, 2013, doi: 10.1515/cmam-2014-0015.
- [55] R. Tittarelli, “Estimateurs d’erreur a posteriori pour les équations de Maxwell en formulation temporelle et potentielle,” Université Lille1 - Sciences et Technologies, 2016. Accessed: Apr. 12, 2021. [Online]. Available: <http://ori.univ-lille1.fr/notice/view/univ-lille1-ori-444518>

- [56] M. Ainsworth and A. Craig, “A posteriori error estimators in the finite element method,” *Numer. Math.*, vol. 60, no. 1, pp. 429–463, Dec. 1991, doi: 10.1007/BF01385730.
- [57] O. C. Zienkiewicz and J. Z. Zhu, “The superconvergent patch recovery (SPR) and adaptive finite element refinement,” *Comput. Methods Appl. Mech. Eng.*, vol. 101, no. 1–3, pp. 207–224, Dec. 1992, doi: 10.1016/0045-7825(92)90023-D.
- [58] O. C. Zienkiewicz and J. Z. Zhu, “The superconvergent patch recovery and a posteriori error estimates. Part 1: The recovery technique,” *Int. J. Numer. Methods Eng.*, vol. 33, no. 7, pp. 1331–1364, May 1992, doi: 10.1002/nme.1620330702.
- [59] O. C. Zienkiewicz and J. Z. Zhu, “The superconvergent patch recovery and a posteriori error estimates. Part 2: Error estimates and adaptivity,” *Int. J. Numer. Methods Eng.*, vol. 33, no. 7, pp. 1365–1382, May 1992, doi: 10.1002/nme.1620330703.
- [60] Z. Cai and S. Cao, “A recovery-based a posteriori error estimator for H(curl) interface problems,” *Comput. Methods Appl. Mech. Eng.*, vol. 296, pp. 169–195, Nov. 2015, doi: 10.1016/j.cma.2015.08.002.
- [61] E. Creusé, S. Nicaise, R. Tittarelli, and R. A. Tittarelli, “A guaranteed equilibrated error estimator for the $A-\Phi$ and $T-\Omega$ magnetodynamic harmonic formulations of the Maxwell system A guaranteed equilibrated error estimator for the $A - \phi$ and $T - \Omega$ magnetodynamic harmonic formulations of the Maxwell system,” OUP, 2017. Accessed: Mar. 23, 2020. [Online]. Available: <https://hal.archives-ouvertes.fr/hal-01110258>
- [62] E. Creusé, Y. Le Menach, S. Nicaise, F. Piriou, and R. Tittarelli, “Two guaranteed equilibrated error estimators for Harmonic formulations in eddy current problems,” *Comput. Math. with Appl.*, vol. 77, no. 6, pp. 1549–1562, 2019, doi: 10.1016/j.camwa.2018.08.046.
- [63] S. Kumar, L. Fourment, and S. Guerdoux, “Parallel, second-order and consistent remeshing transfer operators for evolving meshes with superconvergence property on surface and volume,” *Finite Elem. Anal. Des.*, vol. 93, no. C, pp. 70–84, Jan. 2015, doi: 10.1016/j.finel.2014.09.002.
- [64] “TEAM Workshops, Test Problems,” 1998. Accessed: Mar. 25, 2021. [Online]. Available: <https://www.osti.gov/servlets/purl/7179128>
- [65] C. Guérin, “Détermination des pertes par courants de Foucault dans les cuves de transformateurs. Modélisation de régions minces et prise en compte de la saturation des matériaux magnétiques en régime harmonique,” Institut National Polytechnique de Grenoble - INPG, Grenoble, 1994. Accessed: Apr. 26, 2021. [Online]. Available: <https://tel.archives-ouvertes.fr/tel-00526516>
- [66] D. Labridis and P. Dokopoulos, “Calculation of Eddy Current Losses in Nonlinear Ferromagnetic Materials,” *IEEE Trans. Magn.*, vol. 25, no. 3, pp. 2665–2669, 1989, doi: 10.1109/20.24506.
- [67] A. Bossavit and J. C. Vérité, “The ‘TRIFOU’ code: Solving the 3-D eddy-currents problem by using H as state variable,” *IEEE Trans. Magn.*, vol. 19, no. 6, pp. 2465–2470, 1983, doi: 10.1109/TMAG.1983.1062817.
- [68] F. Bay, V. Labbe, Y. Favennec, and J. L. Chenot, “A numerical model for induction heating processes coupling electromagnetism and thermomechanics,” *Int. J. Numer. METHODS Eng. Int. J. Numer. Meth. Engng*, vol. 58, pp. 839–867, 2003, doi:

10.1002/nme.796.

- [69] G. G. F. Bay, J. Barlier, T. Sourmail, P. De Cagny, M. Courteaux, B. Paya, B. Denand, V. A. Esin, J. Teixeira, E. Aeby-Gautier, S. Denis M. Dehmas, “Modelling Distorsions in induction heat treatment processes.” Accessed: Jul. 07, 2022. [Online]. Available: <https://hal.archives-ouvertes.fr/hal-01259189>
- [70] D. A. Musaeva, V. K. Ilyin, V. Geža, and E. Baake, “Experimental investigation of low-frequency pulsed Lorentz force influence on the motion of Galinstan melt,” *St. Petersburg Polytech. Univ. J. Phys. Math.*, vol. 2, no. 3, pp. 193–200, 2016, doi: 10.1016/j.spjpm.2016.08.002.
- [71] M. Dobrowolski, S. Gräf, and C. Pflaum, “On a posteriori error estimators in the finite element method on anisotropic meshes,” *ETNA. Electron. Trans. Numer. Anal.*, vol. 8, pp. 36–45, 1999.
- [72] W. Huang, L. Kamenski, and J. Lang, “A new anisotropic mesh adaptation method based upon hierarchical a posteriori error estimates,” *J. Comput. Phys.*, vol. 229, no. 6, pp. 2179–2198, Mar. 2010, doi: 10.1016/j.jcp.2009.11.029.
- [73] W. Cao, W. Huang, and R. D. Russell, “Comparison of two-dimensional r-adaptive finite element methods using various error indicators,” *Math. Comput. Simul.*, vol. 56, no. 2, pp. 127–143, 2001, doi: 10.1016/S0378-4754(01)00285-3.
- [74] T. Apel, S. Grosman, P. K. Jimack, and A. Meyer, “A new methodology for anisotropic mesh refinement based upon error gradients,” *Appl. Numer. Math.*, vol. 50, no. 3–4, pp. 329–341, Sep. 2004, doi: 10.1016/j.apnum.2004.01.006.
- [75] A. Agouzal, K. Lipnikov, and Y. Vassilevski, “Generation of Quasi-optimal Meshes Based on a Posteriori Error Estimates.”
- [76] J. Peraire, M. Vahdati, K. Morgan, and O. C. Zienkiewicz, “Adaptive remeshing for compressible flow computations,” *J. Comput. Phys.*, vol. 72, no. 2, pp. 449–466, 1987, doi: 10.1016/0021-9991(87)90093-3.
- [77] O. C. Zienkiewicz and J. Wu, “Automatic directional refinement in adaptive analysis of compressible flows,” *Int. J. Numer. Methods Eng.*, vol. 37, no. 13, pp. 2189–2210, 1994, doi: 10.1002/nme.1620371304.
- [78] R. C. Almeida, R. A. Feijóo, A. C. Galeão, C. Padra, and R. S. Silva, “Adaptive finite element computational fluid dynamics using an anisotropic error estimator,” *Comput. Methods Appl. Mech. Eng.*, vol. 182, no. 3–4, pp. 379–400, 2000, doi: 10.1016/S0045-7825(99)00200-5.
- [79] F. Alauzet, P. Frey, F. Alauzet, and P. Frey, “Estimateur d ’ erreur géométrique et métriques anisotropes pour l ’ adaptation de maillage . Partie I: aspects théoriques,” 2006.
- [80] K. Lipnikov and Y. Vassilevski, “Analysis of Hessian Recovery Methods for Generating Adaptive Meshes,” in *Proceedings of the 15th International Meshing Roundtable*, 2006, no. January. doi: 10.1007/978-3-540-34958-7.
- [81] G. C. Buscaglia and E. A. Dari, “Anisotropic mesh optimization and its application in adaptivity,” *Int. J. Numer. Methods Eng.*, vol. 40, no. 22, pp. 4119–4136, 1997, doi: 10.1002/(SICI)1097-0207(19971130)40:22<4119::AID-NME254>3.0.CO;2-R.

- [82] A. Mathematics, S. Journal, and N. Analysis, “Asymptotically Exact a Posteriori Error Estimators , Part I : Grids with Superconvergence,” *SIAM J. Numer. Anal.*, vol. 41, no. 6, pp. 2294–2312, 2010.
- [83] J. Z. Zhu and O. C. Zienkiewicz, “Superconvergence recovery technique and a posteriori error estimators,” *Int. J. Numer. Methods Eng.*, vol. 30, no. 7, pp. 1321–1339, 1990, doi: 10.1002/nme.1620300707.
- [84] A. Agouzal and Y. Vassilevski, “On a discrete Hessian recovery for P1 finite elements,” *J. Numer. Math.*, vol. 10, no. 1, pp. 1–12, 2002, doi: 10.1515/JNMA.2002.1.
- [85] H. Borouchaki, T. Grosge, and D. Barchiesi, “Improved 3D adaptive remeshing scheme applied in high electromagnetic field gradient computation,” *Finite Elem. Anal. Des.*, vol. 46, no. 1–2, pp. 84–95, 2010, doi: 10.1016/j.finel.2009.06.026.
- [86] T. Grosge, H. Borouchaki, and D. Barchiesi, “New adaptive mesh development for accurate near-field enhancement computation,” *J. Microsc.*, vol. 229, no. 2, pp. 293–301, 2008, doi: 10.1111/j.1365-2818.2008.01903.x.
- [87] T. Grosge, H. Borouchaki, and D. Barchiesi, “Improved scheme for accurate computation of high electric near-field gradients,” *Opt. Express*, vol. 15, no. 3, p. 1307, 2007, doi: 10.1364/oe.15.001307.
- [88] F. Alauzet, “Metric-based anisotropic mesh adaptation,” p. 66, 2007.
- [89] A. Loseille and F. Alauzet, “Continuous mesh framework part I: Well-posed continuous interpolation error,” *SIAM J. Numer. Anal.*, vol. 49, no. 1, pp. 38–60, 2011, doi: 10.1137/090754078.
- [90] V. Lejay *et al.*, “FEM Simulation of induction hardening : from the generator behavior to the quenched microstructure prediction . Comparison of experiments vs simulations .,” no. 1, pp. 1–12.
- [91] T. Coupez, “Metric construction by length distribution tensor and edge based error for anisotropic adaptive meshing,” *J. Comput. Phys.*, vol. 230, no. 7, pp. 2391–2405, 2011, doi: 10.1016/j.jcp.2010.11.041.
- [92] G. K. Fenton, “Development of numerical tools to model plasticity in aluminum due to electromagnetic forces,” *Master’s thesis, Dep. Mater. Sci. Eng. Ohio State Univeristy*, no. July, 1996.
- [93] J. R. Alves Z and F. Bay, “Magnetic pulse forming: simulation and experiments for high-speed forming processes,” *Adv. Mater. Process. Technol.*, vol. 1, no. 3–4, pp. 560–576, 2015, doi: 10.1080/2374068X.2015.1132723.
- [94] M. Bellet and M. Deville, *Numerical Modeling in Materials Science and Engineering*, vol. 6, no. 3. 2003. doi: 10.1016/s1369-7021(03)00336-5.

RÉSUMÉ

Les procédés de fabrication utilisant l'électromagnétisme impliquent de forts couplages multiphysiques entre l'électromagnétisme et d'autres champs physiques. Leur conception et leur optimisation sont donc assez complexes et reposent largement sur des modèles numériques efficaces. Cependant, ces modèles nécessitent souvent de très importantes ressources informatiques ; réduire le temps de calcul tout en garantissant un niveau de précision donné des résultats numériques est donc l'un des principaux défis.

L'objectif de ce travail de doctorat est donc de relever ce défi en développant des procédures de maillage anisotrope automatisées en lien avec des estimateurs d'erreur spécifiques pour les calculs électromagnétiques. Ce travail a été réalisé en plusieurs étapes.

La première étape est le développement d'un estimateur d'erreur robuste - capable d'identifier et de quantifier efficacement les erreurs de la solution numérique dans le cas de modèles industriels complexes.

La deuxième étape concerne le remaillage anisotrope adaptatif et le développement d'un nouveau cadre pour calculer le tenseur métrique, qui doit être capable de capturer l'anisotropie inhérente aux phénomènes électromagnétiques.

La troisième et dernière étape concerne la modélisation de cas industriels complexes, basée sur une implémentation des méthodes développées dans les logiciels Forge® & Thercast®, permettant des couplages multiphysiques avec les phénomènes thermodynamiques.

MOTS CLÉS

Procédés de fabrication utilisant l'électromagnétisme, méthode des éléments finis, estimateurs d'erreur, adaptation de maillage.

ABSTRACT

Electromagnetic-coupled manufacturing processes involve strong multiphysics couplings between electromagnetism and other physical fields. Their design and optimisation are quite complex and relies heavily on efficient computational models. However, these models are often highly demanding in terms of resources; reducing CPU time while preserving a specified accuracy of numerical results is one of the main challenges.

The purpose of this PhD work is thus to address this challenge by developing automated anisotropic meshing procedures in conjunction with specific error estimators for the electromagnetic computations. This work has been carried out in several stages.

The first stage is the development of a robust error estimator – able to effectively identify and quantify the errors of the numerical solution in the case of complex industrial models.

The second stage deals with adaptive anisotropic remeshing and the development of a novel framework to compute the metric tensor, which needs to enable capturing the inherently anisotropic behaviour of the electromagnetic phenomena.

The third and last stage deals with modelling of complex industrial cases, based on the implementation of the developed methods in the Forge® & Thercast® software enabling multiphysical couplings with the thermodynamical phenomena.

KEYWORDS

Electromagnetic-coupled manufacturing processes, finite element method, error estimators, mesh adaptation.